

# Design Report Update 2020

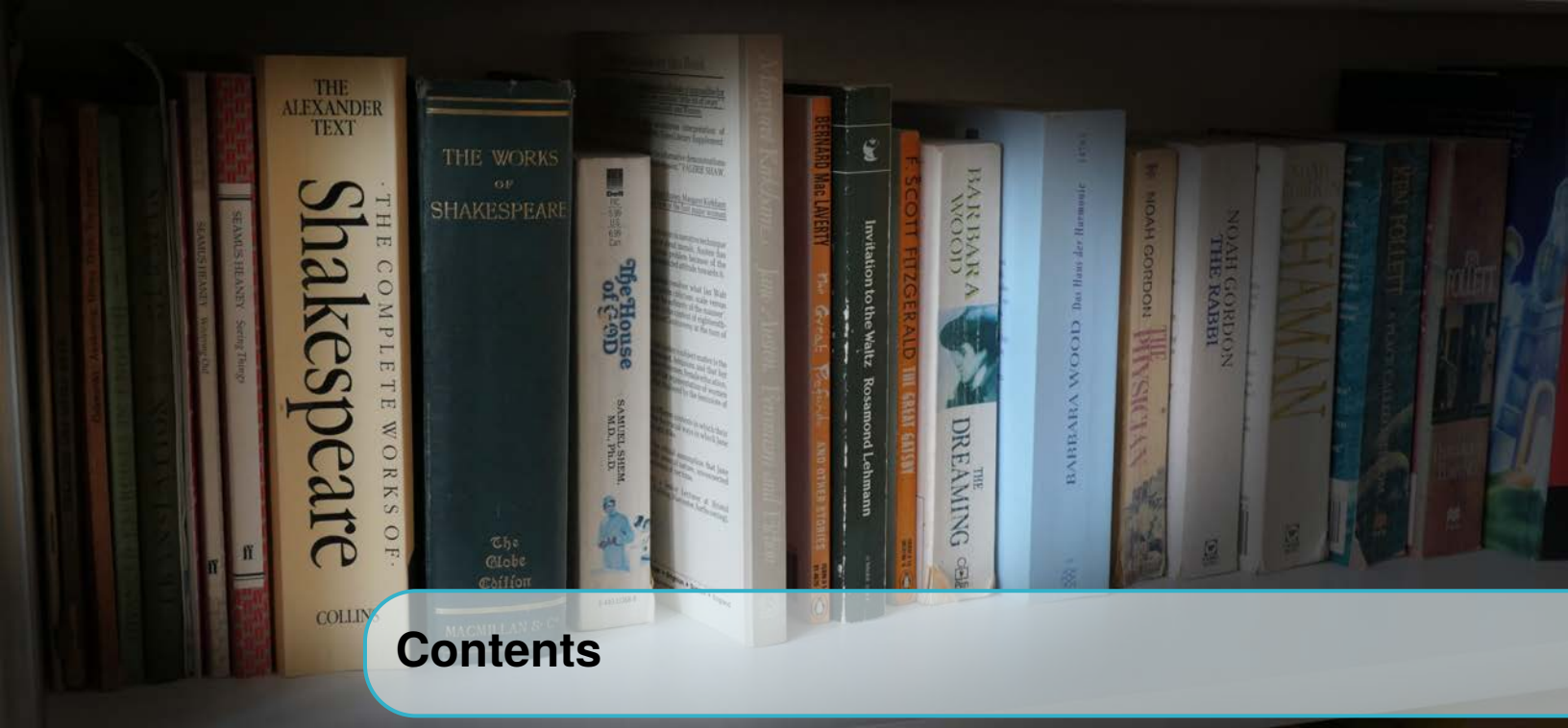
## for the Einstein Telescope

ET Steering Committee Editorial Team  
released September 2020



ET EDITORIAL TEAM

*First release, September 2020*



# Contents

<b>Nomenclature</b>	<b>19</b>
<b>1 Introduction</b>	<b>29</b>
1.1 The basics of gravitational wave detectors	30
1.2 Scientific targets of the ET observatory	37
1.3 Design of the ET observatory	39
1.3.1 Size, shape and layout	39
1.3.2 Quantum noise	40
1.3.3 Thermal noise	42
1.3.4 Seismic isolation	43
1.3.5 Terrestrial gravitational noise	45
1.3.6 Vacuum	45
1.3.7 Noise budget	45
1.3.8 Layout of the observatory	47
<b>I SCIENCE CASE</b>	<b>49</b>
<b>2 Introduction</b>	<b>51</b>
<b>3 Astrophysics</b>	<b>55</b>
3.1 Black hole binaries	55
3.2 Neutron stars	57
3.2.1 Coalescing neutron star binaries	58

3.2.2	Continuous waves from spinning neutron stars . . . . .	60
3.2.3	Burst signals from neutron stars . . . . .	62
3.3	<b>Multi-band and multi-messenger astrophysics: synergies with other gravitational-wave detectors and electromagnetic/neutrino observatories</b>	<b>63</b>
3.3.1	Networks of ground-based gravitational-wave detectors . . . . .	63
3.3.2	Joint gravitational-wave and electromagnetic observations . . . . .	65
3.3.3	Nucleosynthesis, nuclear physics and kilonovae . . . . .	66
3.3.4	Relativistic astrophysics and short GRBs . . . . .	67
3.3.5	Core collapse supernovae . . . . .	69
3.3.6	Multi-messenger astrophysics with neutrinos and cosmic rays . . . . .	70
3.3.7	Multi-band gravitational-wave observations with LISA . . . . .	71
<b>4</b>	<b>Fundamental Physics and Cosmology . . . . .</b>	<b>73</b>
4.1	<b>Physics near the black hole horizon: from tests of GR to quantum gravity</b>	<b>74</b>
4.1.1	Testing the GR predictions for space-time dynamics near the horizon . . . . .	74
4.1.2	Exotic compact objects and signals from quantum gravity . . . . .	76
4.2	The nature of dark matter	77
4.3	The nature of dark energy	79
4.4	<b>Toward the big bang: stochastic gravitational-wave backgrounds</b>	<b>82</b>
4.4.1	Cosmological backgrounds . . . . .	83
4.4.2	Astrophysical backgrounds . . . . .	86
<b>5</b>	<b>Summary of key science objectives . . . . .</b>	<b>87</b>
<b>II</b>	<b>SITE, INFRASTRUCTURE AND INSTRUMENTATION</b>	<b>91</b>
<b>6</b>	<b>Detector . . . . .</b>	<b>93</b>
6.1	<b>Optical layout</b>	<b>93</b>
6.1.1	A xylophone design for ET . . . . .	94
6.1.2	Arm cavity design . . . . .	97
6.1.3	Central interferometer design . . . . .	97
6.2	<b>Core optics</b>	<b>98</b>
6.2.1	<b>The substrate materials</b>	<b>98</b>
6.2.1.1	Fused silica . . . . .	99
6.2.1.2	Silicon . . . . .	99
6.2.2	<b>Surface polishing</b>	<b>100</b>
6.2.3	<b>Other core optics</b>	<b>101</b>
6.3	<b>Coatings</b>	<b>101</b>
6.3.1	Coating procurement . . . . .	101
6.3.2	Coating thermal noise - full treatment . . . . .	102

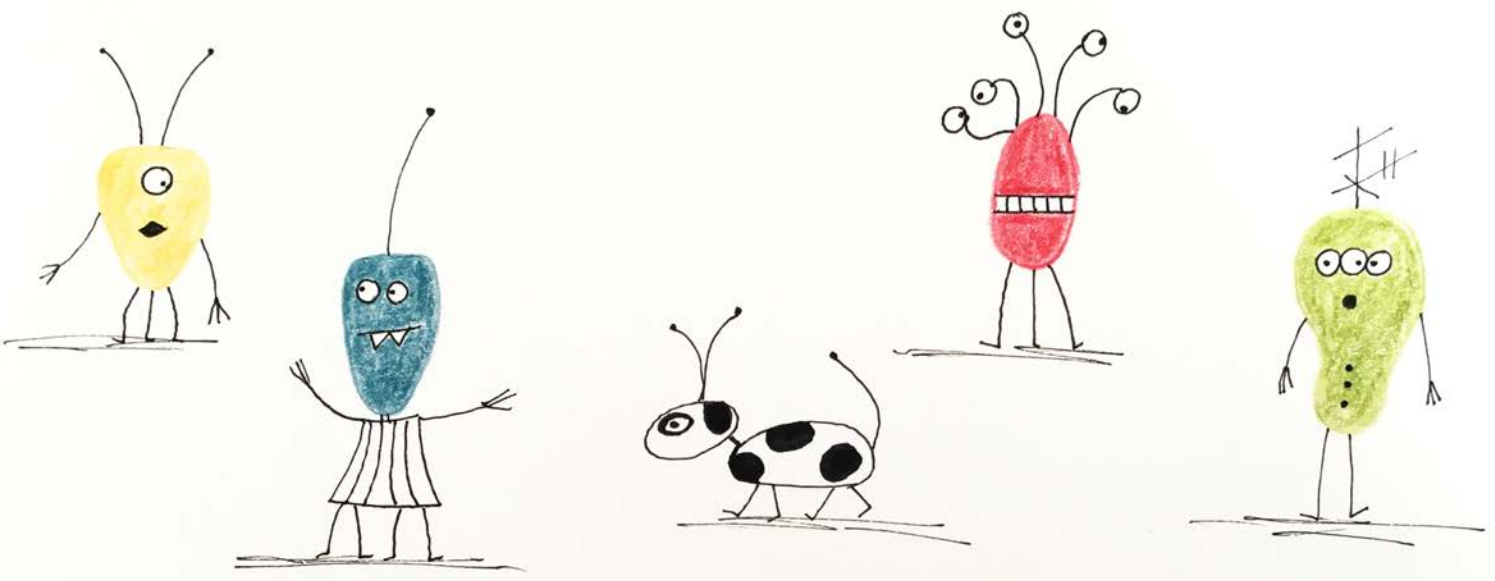
<b>6.3.3</b>	<b>Coating requirements</b>	<b>103</b>
6.3.3.1	ET-LF	103
6.3.3.2	ET-HF	103
6.3.3.3	Other requirements	103
<b>6.3.4</b>	<b>Coating design solutions</b>	<b>104</b>
6.3.4.1	Multimaterial coatings	104
6.3.4.2	Nanolayer coatings	105
6.3.4.3	Coating structure and mechanical loss	105
<b>6.3.5</b>	<b>Possible coating materials</b>	<b>105</b>
6.3.5.1	Amorphous silicon	105
6.3.5.2	Alternative cryogenic low-index layers	106
6.3.5.3	Silicon nitride	106
6.3.5.4	Silica-doped hafnia	107
6.3.5.5	Alumina	107
6.3.5.6	Other amorphous coatings	107
6.3.5.7	Crystalline coatings	107
6.3.5.8	Coating deposition	108
<b>6.3.6</b>	<b>Coating strategy for ET</b>	<b>108</b>
<b>6.4</b>	<b>Light sources</b>	<b>109</b>
<b>6.4.1</b>	<b>Requirements</b>	<b>109</b>
<b>6.4.2</b>	<b>High power laser</b>	<b>110</b>
<b>6.4.3</b>	<b>Prestabilization</b>	<b>111</b>
<b>6.5</b>	<b>Quantum noise reduction</b>	<b>112</b>
<b>6.5.1</b>	<b>Review of quantum non-demolition topology options</b>	<b>114</b>
<b>6.5.2</b>	<b>Frequency dependent squeezing</b>	<b>116</b>
6.5.2.1	Filter cavity	117
6.5.2.2	Squeezed light sources	120
<b>6.6</b>	<b>Input and output optics</b>	<b>122</b>
<b>6.6.1</b>	<b>Input optics</b>	<b>122</b>
<b>6.6.2</b>	<b>Output optics</b>	<b>123</b>
<b>6.7</b>	<b>Scattered light mitigation</b>	<b>124</b>
<b>6.7.1</b>	<b>Lessons learned</b>	<b>125</b>
<b>6.7.2</b>	<b>Stray light control</b>	<b>125</b>
<b>6.7.3</b>	<b>New and future developments for stray light reduction</b>	<b>126</b>
<b>6.8</b>	<b>Interferometer control</b>	<b>127</b>
<b>6.8.1</b>	<b>Longitudinal control</b>	<b>127</b>
<b>6.8.2</b>	<b>Lock acquisition</b>	<b>129</b>
<b>6.8.3</b>	<b>Steady state control</b>	<b>130</b>
<b>6.8.4</b>	<b>Alignment control</b>	<b>130</b>
<b>6.9</b>	<b>Calibration</b>	<b>132</b>
<b>6.9.1</b>	<b>Science-driven calibration requirements</b>	<b>132</b>
<b>6.9.2</b>	<b>State of the art</b>	<b>132</b>
6.9.2.1	Photon calibrators	132
6.9.2.2	Newtonian calibrators	133

6.9.2.3	Other calibration methods	133
<b>6.10</b>	<b>Seismic isolation and suspension</b>	<b>133</b>
<b>6.10.1</b>	<b>Seismic isolation systems</b>	<b>133</b>
6.10.1.1	ET requirements	134
6.10.1.2	Seismic platform	134
6.10.1.3	Super-Attenuator modifications for Low-Frequency ET	134
6.10.1.4	Inter-platform motion	135
6.10.1.5	Sensor development	136
<b>6.10.2</b>	<b>Test mass suspension systems</b>	<b>137</b>
6.10.2.1	Suspension thermal noise of the mirror	137
6.10.2.2	High-frequency suspension	138
6.10.2.3	R&D required for High-Frequency suspension	139
6.10.2.4	Low-Frequency suspension	140
6.10.2.5	R&D required for Low-Frequency suspension	142
<b>6.11</b>	<b>Cryogenics</b>	<b>144</b>
<b>6.11.1</b>	<b>The ET cryostats</b>	<b>144</b>
<b>6.11.2</b>	<b>The LF-interferometer cryotrap</b>	<b>146</b>
<b>6.11.3</b>	<b>R&amp;D on cryogenics: lowering the temperature with Helium II</b>	<b>147</b>
<b>6.12</b>	<b>Vacuum system</b>	<b>147</b>
<b>6.12.1</b>	<b>Overview and requirements</b>	<b>147</b>
<b>6.12.2</b>	<b>The arm pipes</b>	<b>148</b>
6.12.2.1	Pipe assembly	153
6.12.2.2	Pipe pumping system	156
6.12.2.3	Pipe bake-out system	157
<b>6.12.3</b>	<b>Cryotrap</b>	<b>157</b>
<b>6.12.4</b>	<b>Towers</b>	<b>158</b>
6.12.4.1	Tower pumping system	159
<b>6.12.5</b>	<b>Valves</b>	<b>159</b>
<b>7</b>	<b>Site and Infrastructure</b>	<b>161</b>
<b>7.1</b>	<b>Infrastructure and site requirements</b>	<b>161</b>
<b>7.1.1</b>	<b>Infrastructure reference design</b>	<b>161</b>
<b>7.1.2</b>	<b>Site conditions</b>	<b>162</b>
7.1.2.1	Surface	163
7.1.2.2	Underground	163
7.1.2.3	Seismicity	164
7.1.2.4	Human safety	165
7.1.2.5	Lifetime	165
<b>7.2</b>	<b>Environmental noise</b>	<b>166</b>
<b>7.2.1</b>	<b>Seismic noise</b>	<b>166</b>
7.2.1.1	Anthropogenic seismic noise	167
7.2.1.2	Wind generated seismic noise	167
<b>7.2.2</b>	<b>Magnetic noise</b>	<b>168</b>

---

<b>7.2.3</b>	<b>Newtonian noise</b> .....	<b>169</b>
7.2.3.1	Seismic gravity noise .....	169
7.2.3.2	Atmospheric gravity noise .....	170
7.2.3.3	Considerations on detector depth .....	170
<b>7.2.4</b>	<b>Newtonian-noise cancellation</b> .....	<b>172</b>
7.2.4.1	Coherent noise cancellation .....	173
7.2.4.2	Site properties relevant to Newtonian-noise cancellation .....	173
7.2.4.3	Optimized sensor arrays for seismic Newtonian-noise cancellation .....	175
<b>7.3</b>	<b>Underground construction</b> .....	<b>177</b>
<b>7.3.1</b>	<b>Tunnels and caverns</b> .....	<b>177</b>
7.3.1.1	Access to the underground infrastructure .....	177
7.3.1.2	Caverns .....	178
7.3.1.3	Tunnels .....	188
<b>7.4</b>	<b>Surface facilities</b> .....	<b>191</b>
<b>7.4.1</b>	<b>Road network</b> .....	<b>191</b>
<b>7.4.2</b>	<b>Visitor centre</b> .....	<b>192</b>
<b>7.4.3</b>	<b>Environmental impact</b> .....	<b>192</b>
<b>8</b>	<b>Computing Infrastructure</b> .....	<b>193</b>
<b>8.1</b>	<b>Computing challenges and strategies</b> .....	<b>193</b>
8.1.1	Data analysis challenges .....	194
8.1.2	Low-latency infrastructure .....	195
8.1.3	Computing strategies .....	195
<b>8.2</b>	<b>On-site computing infrastructure</b> .....	<b>196</b>
<b>8.3</b>	<b>Global computing infrastructure</b> .....	<b>196</b>
	<b>Image credits</b> .....	<b>200</b>
	<b>Bibliography</b> .....	<b>202</b>





## List of Figures

- 1.1 Schematic representation of an interferometric gravitational wave detector. Subsystems are indicated by the colored backgrounds. The borders between subsystems are not sharply defined and somewhat arbitrary. . . . . 31
- 1.2 The effect of gravitational waves on the distances between objects. While the mirrors remain locally at rest the metric gets changed by the gravitational wave. The figure shows the effect of a sinusoidal gravitational wave with period  $\tau$ , for different times  $t$ . The distances measured between the mirrors change by  $\pm\delta\ell$ . . . . . 32
- 1.3 Michelson interferometer principle for gravitational wave detection, showing three different interference conditions resulting in different brightness at the output port. . . 32
- 1.4 Antenna pattern of ET (right panel) compared to that of Virgo (left panel). ET is assumed to be at the same location as Virgo. Note that Virgo is a *single* L-shaped detector while ET consists of *three* V-shaped interferometers rotated relative to one other by 120 deg . The combined antenna pattern of the three detectors in ET (defined as  $F^2 = \sum_{A=1}^3 F_A^2$ , where  $F_1, F_2, F_3$  are the individual antenna pattern functions) makes the response the same for all sources whose sky location makes the same angle to the plane formed by ET (see *e.g.* contours marked 0.6). . . . . 33
- 1.5 Design noise budget for advanced Virgo for the next observation run O4. For details see e.g. [1] . . . . . 34
- 1.6 Example noise budget for the advanced Virgo detector in Italy, February 2020. Shown are amplitude noise spectral densities of individual noise sources contributing to the overall noise of the detector as a function of frequency. The noises are scaled to gravitational wave strain. The figure clearly shows that in the low frequency region many different noise sources contribute at comparable levels and consequently at low frequencies many different sources have to be considered and minimised. . . . . 35

1.7	Design sensitivities of the advanced and the third generation gravitational wave detectors. The various colour shades represent different sets of source locations and orientations. . . . .	39
1.8	The Einstein Telescope's geometry will be a triangular arrangement fo three nested detectors, each consisting of two interferometers. . . . .	39
1.9	The normalised antenna pattern (amplitude sensitivity) of the combined three detectors of the Einstein Telescope for unpolarised waves, i.e. the quadrature sum of "x" and "+" polarised waves. . . . .	40
1.10	Sensitivity of the Einstein Telescope in the 'xylophone' configuration. The sensitivity of the low-frequency cryogenic interferometer is shown in the dashed dark blue curve and the one of the high-frequency room temperature one in a dashed blue-green tone. The sum of both is given by the solid bright red curve. Shown here is the sensitivity for a single detector with 10 km arm length and an angle of 90. (In some of the earlier documents this curve was labelled <i>ET-D</i> sensitivity curve.) . . . . .	41
1.11	Scheme for cooling the mirrors. Front view of the mirror. For details see section 6.11.1	42
1.12	Schematic view of a Virgo Superattenuator, similar to the ones proposed for ET. See also section 6.10.1 . . . . .	44
1.13	Noise budget for the low-frequency (top) and high-frequency (bottom) interferometer for the parameters stated in table 6.1. Shown in black is the amplitude spectral density of a gravitational wave required to produce a signal with the same strength as the total noise of the interferometers. The total noise is decomposed into the individual noise sources, which being statistically independent add up quadratically. . . . .	46
1.14	Artistic view of the ET layout. . . . .	47
1.15	Artistic impression of the underground arrangement of tunnels and caverns. For details see section 7.3.1. . . . .	47
2.1	Astrophysical reach for equal-mass, nonspinning binaries for Advanced LIGO, Einstein Telescope and Cosmic Explorer (from ref. [2, 3]). . . . .	52
3.1	Black holes detected through electromagnetic observations (purple), black holes measured by gravitational-wave observations (blue), neutron stars measured with electromagnetic observations (yellow), and neutron stars detected through gravitational waves (orange). GW190521 is highlighted in the middle of the graphic as the merger of two black holes that produced a remnant that is the most massive black hole observed yet in gravitational waves. Image credit: LIGO-Virgo/Northwestern U. / Frank Elavsky and Aaron Geller. Image taken from <a href="https://www.ligo.caltech.edu/image/ligo20200902a">https://www.ligo.caltech.edu/image/ligo20200902a</a> . . . . .	56
3.2	Left: Conjectured interior structure of a neutron star. Right: Matter encountered in neutron stars and binary mergers explores a large part of the QCD phase diagram in regimes that are inaccessible to terrestrial collider experiments. . . . .	57
3.3	Gravitational wave signal from a NS-NS merger at a distance 100 Mpc, as it sweeps across the detector-accessible frequency range. From [4] (figure courtesy of Jocelyn Read, based on results presented in [5]). . . . .	59

- 3.4 Minimum ellipticity detectable by ET at 90% confidence level in a full coherent search of continuous waves from known pulsars, assuming an observation time  $T_{\text{obs}} = 5$  yr. . . . . 61
- 3.5 Maximum distance at which a continuous wave source would be detected in a full coherent search over  $T_{\text{obs}} = 5$  yr as a function of the source ellipticity, for three different values of the initial signal frequency, for the ET detector. Here we make the assumption that source spin-down is dominated by the emission of GWs and that matched filtering is used in the analysis. . . . . 62
- 3.6 Localization errors of BNSs and BBHs per redshift bin. Top: BNS. Bottom: BBH. Left: ET alone. Right: ET together with currently foreseen future upgrades of Advanced LIGO Hanford, Livingston, India, Advanced Virgo, and KAGRA. We impose a conservative ET detection threshold SNR of 12, and for the plots in the right column that at least one 2G detector has SNR  $> 4$  to include 2G data for the sky localization. Duty cycle is taken 100% for all detectors. . . . . 64
- 4.1 Probing gravity at all scales: illustration of the reach in spacetime curvature versus potential energy targeted by different kinds of observations.  $M$  and  $L$  are the characteristic mass and length involved in the system or process being observed. The genuinely strong-field dynamics of spacetime manifests itself in the top right of the diagram. The label EHT refers to the Event Horizon Telescope. From ref. [3, 6]. . . . . 74
- 4.2 Testing the nature of black holes by using two quasi-normal modes and checking that the characteristic frequencies  $f_{22}$  and  $f_{33}$  and the damping time  $\tau_{22}$  are consistent with each other, given that for ordinary black holes these can only depend on two numbers, namely the final mass  $M$  and final spin  $j$ . The estimates are for the “ringdown” of the remnant black hole arising from a binary similar to the source of GW150914. The dashed curves marked HLV are the 95% confidence regions one would obtain from the current Virgo and LIGO detectors, while the colored bands are for ET. The star indicates the true values of  $M$  and  $j$ . Figure from ref. [3]. . . . . 75
- 4.3 Left panel: an example of the ratio of the gravitational to electromagnetic luminosity distance in a modified gravity model, for different values of a parameter of the model. In the upper curve, at large redshift the deviations of  $d_L^{\text{gw}}(z)$  from  $d_L^{\text{em}}(z)$  reaches 60% (from ref. [7]). Right panel: constraints on the parameters  $(\Xi_0, w_0)$  that describe a non-trivial dark energy sector. Modified GW propagation is not accessible by electromagnetic observations from CMB, Baryon Acoustic Oscillations, and Supernovae, whose contours (red) are flat along the  $\Xi_0$  direction. Standard sirens at ET (gray), combined with these electromagnetic probes allow a determination of  $\Xi_0$  to better than 1% (blue). (From ref. [8]). . . . . 80
- 4.4 Total correction to luminosity distance estimates due to perturbations, as a function of  $z$ . The dotted, dashed and dot-dashed lines show Doppler, lensing and ISW-like contributions, respectively, while the solid line shows the total effect. The green points show the predicted precision in measurements of the luminosity distance of ET. Adapted from [9]. . . . . 82
- 4.5 Spectrum of GWs today,  $h^2\Omega_{\text{GW}}$ , for a model of quadratic inflaton potential, with inflaton - gauge field coupling  $f = M_{\text{Pl}}/34$  vs ET and LISA Power Law Sensitivity (PLS) curves. . . . . 84

- 4.6 The 95% confidence detection region of ET for stochastic backgrounds assuming one year of observation time (shaded area), compared with the prediction for the stochastic GW background from cosmic strings, for two different models of the loop distribution discussed in ref. [10] (left panel) and [11] (right panel). (Figure provided by A.C. Jenkins). . . . . 85
- 6.1 Three nested detectors in a triangular arrangement will form the final Einstein Telescope geometry. . . . . 93
- 6.2 Schematic overview of the corner caverns and central interferometers of one of the three ET detectors. (Used acronyms: LF = low frequency; HF = high frequency; ITM = input mirror; ETM = end mirror; BS = beam splitter; PRM = power recycling mirror); SRM = Signal recycling; FC = filter cavity; x/y = x/y-arm). . . . . 96
- 6.3 Simplified sketch of the ET low and high frequency interferometers of a single ET-detector. 96
- 6.4 Sketch of the optical layout in one corner of the triangle of ET. One can notice in particular the geometrical design of the recycling cavities featuring folded telescopes between the beam splitter and input mirrors. The acronyms used are detailed in the text. 98
- 6.5 A multilayer coatings design for (a) an ETM and (b) an ITM. This design uses an upper stack of  $\text{SiO}_2/\text{Ta}_2\text{O}_5$  on top of a  $\text{SiO}_2:\text{HfO}_2/\text{aSi}$  lower stack [12]. The blue lines show the electric field intensity as a function of depth in the coating. . . . . 104
- 6.6 Maximum effective squeezing level as function of phase noise and optical loss. In order to reach the goal of 10 dB detected squeezing, the optical loss needs to be smaller than 10 % while the phase noise must not exceed 10 mrad. . . . . 117
- 6.7 Illustration of frequency dependent and independent squeezed light injection . . . . . 118
- 6.8 *Left:* Ratio between the ET-LF sensitivity with and without frequency dependent squeezing injection for 1 km length filter cavities. The round trip losses are assumed to range between 10 and 40 ppm (pink belt). The blue line represents the case of lossless cavities which can be approached by using longer cavities. *Right:* Expected cavity round trip losses as a function of the radius of curvature (RoC) of the mirrors for a 300 m long linear cavity, equipped with Virgo-like mirrors (left plot) 200 mm in diameter. The background value derives from the light scattered outside the cavity, while the peaks originate from scattered light that couple to the high order modes of the cavity. The calculation is based on the method used in [13]. . . . . 119
- 6.9 *Left:* Ratio between the quantum noise with and without squeezed light injection for a 300 meter long cavity. Several (colored curves) degradation mechanisms contribute to the total squeezing degradation budget (black curve). The FC assumed round trip losses range between 40 ppm to 10 ppm (yellow belt in the plot) corresponding to different values of the total squeezing degradation budget (dark shadow in the plot). *Right:* Ratio between the ET-HF sensitivity with and without frequency dependent squeezing injection. At low frequencies the additional non-quantum noise sources make the overall sensitivity improvement lower than the corresponding quantum noise suppression (left plot). The overall sensitivity is therefore less affected by the change on the FC parameters (pink belt). . . . . 119

- 6.10 *Left*: Schematic for the generation and coherent control of squeezed vacuum states of light. Laser 1 provides the light field for homodyne detection and for frequency doubling in a second harmonic generator (SHG). The SHG provides the pump field required for the generation of squeezed vacuum states in an optical parametric amplifier (OPA) operated below threshold. The squeezed vacuum states are extracted via a dichroic beam splitter (DBS) and send towards the interferometer. Alternatively, the squeezing level can be characterized by means of a balanced homodyne detector (BHD). A Faraday isolator is implemented in the squeezing path to protect the OPA from light scattered back from the interferometer. *Right*: Quantum noise squeezing as reported in [14]. Trace (a) represents the shot noise reference (normalized to 0 dB) measured with a homodyne detector. In reference to this trace the measured quantum noise powers for squeezing (b) and the corresponding anti-squeezing (c) are shown. Up to 12 dB squeezing and 19.6 dB anti-squeezing was observed, which is consistent with a theoretical model assuming a residual phase noise of 3.5 mrad rms and an overall optical loss of 5.3 % for the squeezed field. This includes 2.5 % optical loss due to the homodyne detection which needs to be subtracted to deduce the squeezing level available for the injection into a gravitational wave detector. This level is indicated by the blue area and corresponds to a squeezing factor of 14 dB. . . . 121
- 6.11 A comparison between the performance of the LIGO and Virgo instruments during the 03 observing run and the ET design sensitivity. The coloured windows show the important frequency regions, and the arrows show the regions where ET must have improved performance in order to reduce the corner-frequency of the ‘seismic wall’. . . 135
- 6.12 Simulation of the SA open-loop horizontal transfer function (Mirror Motion/Ground Motion), along the beam axis, in different configurations. Advanced Virgo SA (blue curve) is compared with two longer versions: 17 m (red curve) and 12 m (orange curve). 136
- 6.13 The simulated mirror displacement obtained using a 17 m-SA and 12-m SA installed on ideal sensor limited-inertial platform with different requirements (blue curve and red curve respectively) is compared with ET-LF, ET-HF, and the combined ET sensitivities (orange, magenta, and black curves respectively). . . . . 137
- 6.14 Strain sensitivity due to suspension thermal noise for the room temperature and cryogenic suspensions; red: room temperature silica, blue 120 K silicon, green 20 K silicon, black ET-D baseline . . . . . 141
- 6.15 Scheme of the cryo-links and cryo-tank needed for cooling a test-mass of the LF-interferometer. Upper image: mirror frontal view. Lower image: mirror side view. . . . . 145
- 6.16 Phase noise given by the residual gases compared to the expected sensitivity, computed for the appropriate beam profile for different gas compositions. (Goal gas composition: Hydrogen [ $1 \cdot 10^{-10}$  mbar], Water [ $5 \cdot 10^{-11}$  mbar], Nitrogen [ $1 \cdot 10^{-11}$  mbar]) . . . . . 149
- 6.17 One corner of the ET vacuum system: LF detector (blue); HF detector (red); filter cavities (yellow). . . . . 150
- 6.18 As an example the cross-section of a Virgo a mirror tower is shown. . . . . 151
- 6.19 Arrangement of the vacuum pipes in the tunnel cross-section. . . . . 152
- 6.20 Schematic layout of the LF interferometer filter cavity auxiliary beam tube. . . . . 152
- 6.21 As an example the Virgo pipe conical baffles are shown. . . . . 153

6.22	3D view of a pumping station: the blue objects represent the pumps and sensors, the yellow ones the cabinets for pumps control and baking power supply (1 cabinet for all). A separate small room is reserved for the high voltage electrical transformer. . . . .	154
6.23	The assembly sequence of one vacuum pipe. . . . .	155
6.24	A liquid nitrogen cryotrap. . . . .	158
7.1	Underground infrastructure near one of the three detector vertices. The main hall hosts the majority of seismic-isolation towers, and is the cross-road between two detector arms (towards upper left and right), a tunnel for the filter cavity (towards lower right), and an access tunnel (towards lower left). . . . .	162
7.2	Overlay of network station spectra used in Peterson's background noise study [15] together with straight-line segments fitted to the high-noise and low-noise envelopes of the overlay. . . . .	166
7.3	Suppression of Rayleigh-wave NN with depth. In this model, it is assumed that wave speed falls from 1.8 km/s at 1 Hz to 500 m/s at 10 Hz. These suppression curves are used in the right plot of Figure 7.4. . . . .	171
7.4	Estimates of seismic NN for ET. Left: ET constructed at the surface. Right: ET constructed underground. . . . .	172
7.5	Suppression of body-wave NN as a function of number of seismometers with optimal placement. The seismometers measure seismic signals with an SNR of 15. The black curve shows the lowest possible residual determined by the seismometer SNR without considering properties of the seismic field. Plot from [16]. . . . .	176
7.6	Suppression of NN from body waves with 15 single-axis (ch1) and three-axis (ch3) seismometers. Sensor locations of 500 arrays for each histogram are derived from the optimal array by adding random numbers to all optimal coordinates drawn from Gaussian distributions of width $\sigma$ . Vertical lines mark the residual of the optimal arrays. Plot from [16]. . . . .	177
7.7	Underground infrastructure of ET. Cavern groups (shown in cyan) are connecting by the long tunnels forming the ET triangle. About 1 km long de-watering shafts also contain Filter Cavities. Each corner station is accessible by an access shaft or tunnel. The image shows the lengths of the various sections. Although accurate numeric values are shown here, the detail led length requirements need to be determined in the technical design phase. Image source Implenia. . . . .	180
7.8	3D impression of the overall tunnel and cavern arrangement for ET. The long tunnels are not shown to scale. . . . .	181
7.9	Sketch of a layout with inclined tunnels for access to the vertex stations. "TBM Tunnel" indicates the arm tunnels of the triangle, produced with a Tunnel Boring Machine. . . . .	181
7.10	Sketch of a layout with vertical shafts for access to the vertex stations. Image source Implenia. . . . .	182
7.11	Perspective view of the underground infrastructure at the corners of the triangle. The curved tunnels connecting the caverns are for construction purposes. . . . .	182
7.12	CAD rendering of a birds view of cavern A. The cut-off view shows the access basement underneath the vacuum towers and a few people for comparison in size. . . . .	183
7.13	Example layout of the basement level of Cavern A with entrance rooms and reinforcement walls giving a solid support for the vacuum tank bases. . . . .	183

---

7.14	CAD rendering of a birds view of cavern B. The entrances to the basement underneath the vacuum towers and a few people for comparison in size are shown. . . . .	184
7.15	Cross section of Cavern A, image source Implenla. . . . .	185
7.16	Sizes of Caverns. . . . .	186
7.17	CAD rendering of the corner station with the tall suspension towers of ET-LF (blue) and ET-HF (red) . . . . .	186
7.18	CAD rendering of the cavern assembly C-E. . . . .	187
7.19	CAD rendering of the caverns C and D. The cut-off view shows the access basement underneath the vacuum towers. Cavern C also contains the vacuum tank of the ET-HF filter cavity (grey). . . . .	187
7.20	Single-shielded tunnel boring machine. . . . .	188
7.21	Open (Gripper) tunnel boring machine. . . . .	189
7.22	Sizes of connection tunnels. Image source Implenla. . . . .	190
8.1	A simplified view of a preliminary Global Computing Infrastructure for the Einstein Telescope. . . . .	197

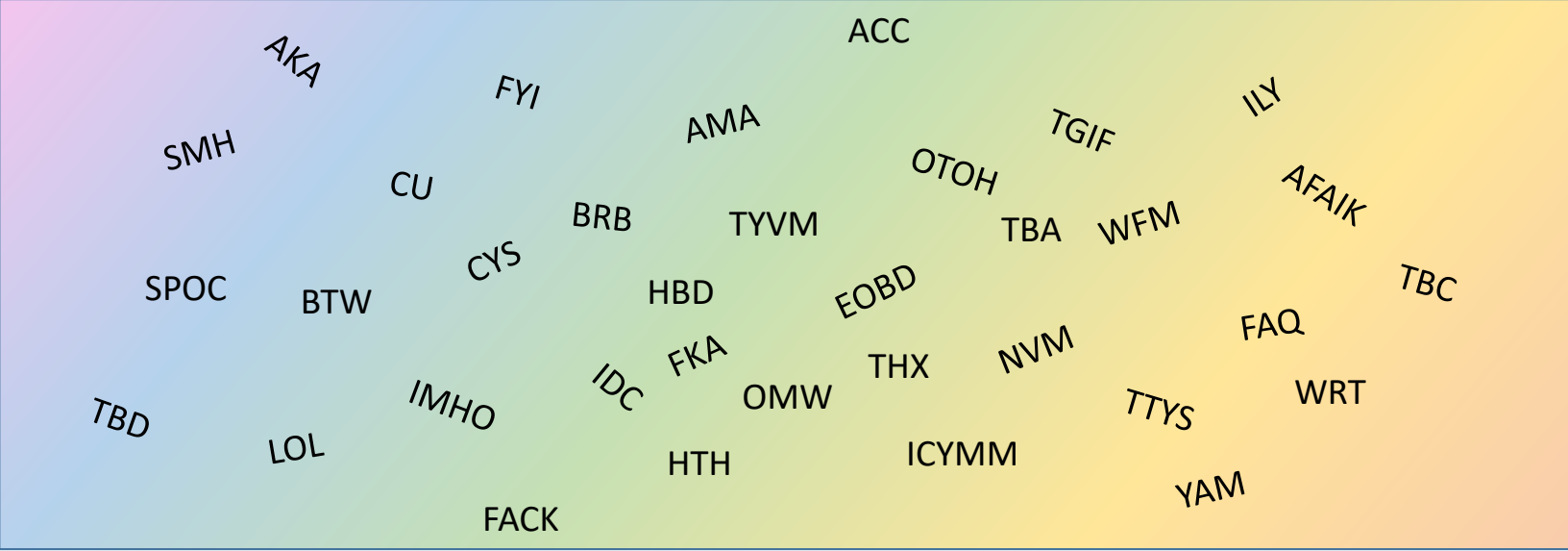




## List of Tables

- |     |   |     |
|-----|---|-----|
| 6.1 | Summary of the most important parameters of the ET high and low frequency interferometers. SA = super attenuator, freq. dep. squeez. = squeezing with frequency dependent angle. . . . .  | 95  |
| 6.2 | Proposed design parameters for the High Frequency suspension: $r_{end}$ and $r_{middle}$ are the radii of the fibre at end and mid sections; $\kappa$ and $C$ are, respectively, thermal conductivity and specific heat of fused silica at room temperature; $h\phi_s$ is the product of the mechanical loss of the material surface, $\phi_s$ , and the depth, $h$ , over which surface loss mechanisms are believed to occur; $\phi_{weld}$ is the loss angle associated with the material losses localized at the welding spots. . . . . | 139 |
| 6.3 | Proposed design parameters for the Low-Frequency suspension: $r_{fibre}$ is the radius of the fibre; $\kappa$ and $C$ are, respectively, the thermal conductivity and specific heat quoted at two possible operating temperatures; $h\phi_s$ is the product of the mechanical loss of the material surface, $\phi_s$ , and the depth, $h$ , over which surface loss mechanisms are believed to occur. . . . .   | 143 |





## Nomenclature

---

### Abbreviations

---

AIGO	Australian International Gravitational Observatory
aLIGO	The advanced LIGO observatory
ALS	Arm Length Stabilisation
ALU	Arithmetic and Logical Unit
APU	Accelerated Processing Unit
ASE	Amplified Spontaneous Emission
BBH	Binary Black Hole
BBN	Big Bang Nucleosynthesis
BH	Black Hole
BHD	Balanced Homodyne Detector
BNS	Binary Neutron Star
BS	(main) beam splitter
CARM	Common Mode Arm Length
CCD	Charge-Coupled Device
CCSN	Core Collapse Supernova
CERN	European Organization for Nuclear Research

---

CLIO	Cryogenic Laser Interferometer Observatory: A prototype gravitational wave detector in Japan
CMB	Cosmic Microwave Background radiation
CMP	Chip-Level Multiprocessing
CP	Compensation Plate
CPU	Central Processing Unit
CTE	Coefficient of Thermal Expansion
cWB	coherent Wave Burst
CW	Continuous Waves
CZ	Czochralski
DARM	Differential Arm Length
DE	Dark Energy
DEG	Digital Enterprise Group
DESY	German Electron Synchrotron
DM	Dark Matter
DNA	Displacement Noise Amplitude spectral density
DOF	Degree(s) Of Freedom
EA	Electrostatic Actuators
EC2	Amazon Elastic Compute Cloud
EDM	Electric Discharge Machining
EM	Electromagnetic
EMRI	Extreme Mass Ratio Inspiral
EOM	Electro-Optic Modulator
EoS	Equation of State
ESFRI	European Strategy Forum on Research Infrastructures
ET	Einstein Telescope
ETM	End Test Mass
FDT	Fluctuation Dissipation Theorem
FEA	Finite Element Analysis
FC	Filter Cavity

---

FFT	Fast Fourier Transform
FI	Faraday Isolator
Flops	Floating point operations per second (a common measure of the computing system speed)
FNA	Force Noise Amplitude spectral density
FP7	Seventh Framework Programme: “Framework programmes (FPs) are the main financial tools through which the European Union supports research and development activities covering almost all scientific disciplines ( <a href="http://cordis.europa.eu/fp7/home_en.html">http://cordis.europa.eu/fp7/home_en.html</a> ).
FP	Folded Pendulum
FPU	Floating Point Unit
FS	Fused Silica
FZ	Float Zone
GAE	Google App Engine
GA	Genetic Algorithm
GAS	Geometric Anti-Spring
GIPC	Global Inverted-Pendulum Control
GPU	Graphic Processing Unit
GRB	Gamma-Ray Burst
GR	General Relativity
GWD	Gravitational Wave Detector
GW	Gravitational Wave
GWIC	Gravitational Wave International Committee ( <a href="https://gwic.ligo.org/">https://gwic.ligo.org/</a> )
HADES	High Activity Disposal Experimental Site, an underground research facility studying geological disposal of radioactive waste
HF	High Frequency
HPC	High Performance Computer
HTT	Hyper-Threading Technology, called also HT
IBS	Ion Beam Sputtering
IFO	Interferometer
ILC	International Linear Collider
IMBH	Intermediate Mass Black Hole

---

IMC	Input Mode Cleaner
IMRI	Intermediate Mass Ratio Inspiral
IO	Input Optics
IO	Input/Output
IP	Inverted Pendulum
ITM	Input Test Mass
KNMI	Royal Dutch Meteorological Institute
kpc	Kiloparsec, $1 \text{ kpc} = 10^3 \text{ pc}$
LF	Low Frequency
LG	Laguerre-Gauss
LHC	Large Hadron Collider
LIGO	Laser Interferometer Gravitational-Wave Observatory
LISA	Laser Space Interferometer Antenna
LMA	Large Mode Area (fibre)
LMXB	Low Mass X-ray Binaries
LNGS	Laboratori Nazionali del Gran Sasso
LSM	Laboratory for Surface Modification
LSO	Last Stable Orbit
LSS	Last Stage Suspension
LVDT	Linear Variable Differential Transformers
MBH	Massive Black Hole
MCMC	Markov Chain Monte Carlo method
MEMS	Micro-Electric Mechanical Systems
MFC	Multifilament-Core (fibre)
MHMC	Metropolis Hastings Monte Carlo method
MIC	Many Integrated Core
MI	Michelson Interferometer
Mpc	Megaparsec, $1 \text{ Mpc} = 10^6 \text{ pc}$
MRM	Marionette Reference Mass
MWIR	Mid Infrared

---

NHNM	New High Noise Model of Peterson
NIR	Near Infrared
NLNM	New Low Noise Model of Peterson
NSBH	Neutron Star – Black Hole
NS	Neutron Star
OMC	Output Mode Cleaner
OM	Output Mirror
OPA	Optical Parametric Amplification
OPL	Optical Path Length
ORFEUS	Observatories and Research Facilities for EUropean Seismology
PCF	Photonic Crystal Fibre
pc	Parsec, a unit of distance; $1 \text{ pc} = 3.086 \times 10^{16} \text{ m}$
PLL	Phase Locked Loop
PN	Post-Newtonian, an approximation to Einstein's field equations
ppm	Parts per million
PRC	Power Recycling Cavity
PRM	Power Recycling Mirror
PR	Power Recycling
PSD	Power Spectral Density
PT	Pulse Tube cryogenic refrigerator
QCD	Quantum Chromodynamics
QND	Quantum Non-Demolition
QNM	Quasi-normal mode
R&D	Research and Development
RDF	Reduced Density Function
RF	Radio Frequency
RIN	Relative Intensity Noise
RM	Recoil Mass or Reference Mass
RMS	Root Mean Squared
rms	Root-mean-square

---

ROC	Radius Of Curvature
RPSD	Root PSD
RSE	Resonant Sideband Extraction
S3	Amazon Simple Storage Service
SAN	Storage Attached Network
SA	Super-Attenuator
SBS	Stimulated Brillouin Scattering
SFR	Star Formation Rate
SGR	Soft Gamma Repeaters
SHG	Second Harmonic Generation
SIMD	Single Instruction, Multiple Data
SI	Sagnac Interferometer
SLM	Spatial-Light modulator
SMBH	Super Massive Black Hole
SMT	Simultaneous multithreading
SNR	Signal to Noise Ratio
SN	Supernova
SQL	Standard Quantum Limit
SQUID	Superconducting Quantum Interference Device, a magnetometer based on Josephson effect
SRC	Signal Recycling Cavity
SRM	Signal Recycling Mirror
SR	Signal Recycling
SRS	Stimulated Raman Scattering
SSE4	Streaming SIMD Extensions version 4
SSE	intel's Streaming SIMD Extension
TBM	Tunnel Boring Machine
TCS	Thermal Compensation System
TEM	Transverse Electromagnetic
TE	Thermo-Elastic

UHV	Ultra-high vacuum
WLCG	Worldwide LHC Computing Grid

---

### Glossary

---

Top500	Top500 is a project which ranks and details twice a year the 500 (non-distributed) most powerful known computer systems in the world.
Compact binary	A compact binary is an astronomical binary consisting of a pair of compact stars
Compact star	Throughout this document a compact star stands for a neutron star or a black hole
CMOS	Complementary metal-oxide-semiconductor is a technology for constructing integrated circuits like microprocessors, static RAM, . . .
Dual Recycling	Using Power- and Signal-Recycling at the same time
ET-HF	The high frequency ET detector in the xylophone design
ET-LF	The low frequency ET detector in the xylophone design
FLRW	The Friedmann-Lemaitre-Robertson-Walker metric is an exact solution of Einstein's field equations of general relativity
G1	The GEO600 detector near Hannover in Germany
GEO600	The GEO600 detector located near Hannover in Germany
H1	The LIGO 4-kilometre interferometer at Hanford, USA
H2	The LIGO 2-kilometre interferometer at Hanford, USA
Horizon Distance	The distance at which a gravitational wave detector would measure a matched-filter signal-to-noise ratio of 8 for an optimally oriented (i.e. face-on) compact binary source located in a direction perpendicular to the plane of the detector
InfiniBand	is a switched fabric communications link used in high-performance computing and enterprise data centers. It is especially used in connections between processor nodes and high performance I/O nodes such as storage device.
L1	The LIGO 4-kilometre interferometer at Livingston Parish, Louisiana, USA
Multi-Core	Multi-core processors are single components with two or more independent actual processors, called cores
Power Recycling	Re-using the light reflected back to the interferometer input by placing a mirror there and resonantly enhancing the circulating light power. Has the same effect as using a more powerful laser.
QND	Typically the term quantum nondemolition (QND) measurement is used to describe a measurement of a quantum system which preserves the integrity of the system and the value of the measured observable. In the literature on gravitational wave detectors

this term is often used to describe a variety of interferometer schemes in which shot noise and radiation pressure noise can be simultaneously suppressed. Such systems are typically not performing a strict QND measurement, thus they may more appropriately be referred to as Quantum Noise Reduction (QNR) systems.

**Resonant Sideband Extraction** The same technique as SR but operated anti-resonant, i.e. widening and/or detuning the bandwidth by reducing the reflectivity of the compound mirror formed by the inboard cavity mirror and the SR mirror.

**shot-crete** a concrete spray-on lining of tunnel and cavern walls. Can either be done as a single layer or with some water-tight foil between two layers. It typically results in a uneven, rough surface.

**Signal Recycling** Resonantly enhancing the GW signals exiting the interferometer through the output port by placing a mirror there. This increases the sensitivity at the cost of the bandwidth. With a different (anti-resonant) tuning the same technique can be used for widening the bandwidth at the expense of the sensitivity (RSE). SR can optimize the sensitivity for an arbitrary frequency.

**V1** The Virgo gravitational wave detector in Italy

**Vacuum fluctuations** Fluctuations that result from the quantum nature of an electromagnetic field even at the lowest possible energy level (zero mean energy = vacuum).

**Virgo** Virgo is a 3-kilometre gravitational wave detector located near Pisa, Italy

**Wigner function** The Wigner function is a quasi-probability density distribution in phase space describing the probability of an outcome of a measurement of phase and amplitude of a quantized harmonic oscillator. For a light field in a quantum noise limited classical state, i.e. a coherent state, the fluctuations are equally distributed between amplitude and phase. Equi-probability lines of the Wigner function would be circles. In a squeezed state fluctuations in one quadrature are decreased at the cost of increased fluctuations in the other quadrature thereby obeying Heisenberg's Uncertainty relation. For squeezed states, the equi-probability lines of the Wigner function become ellipses.

---

### Symbols

---

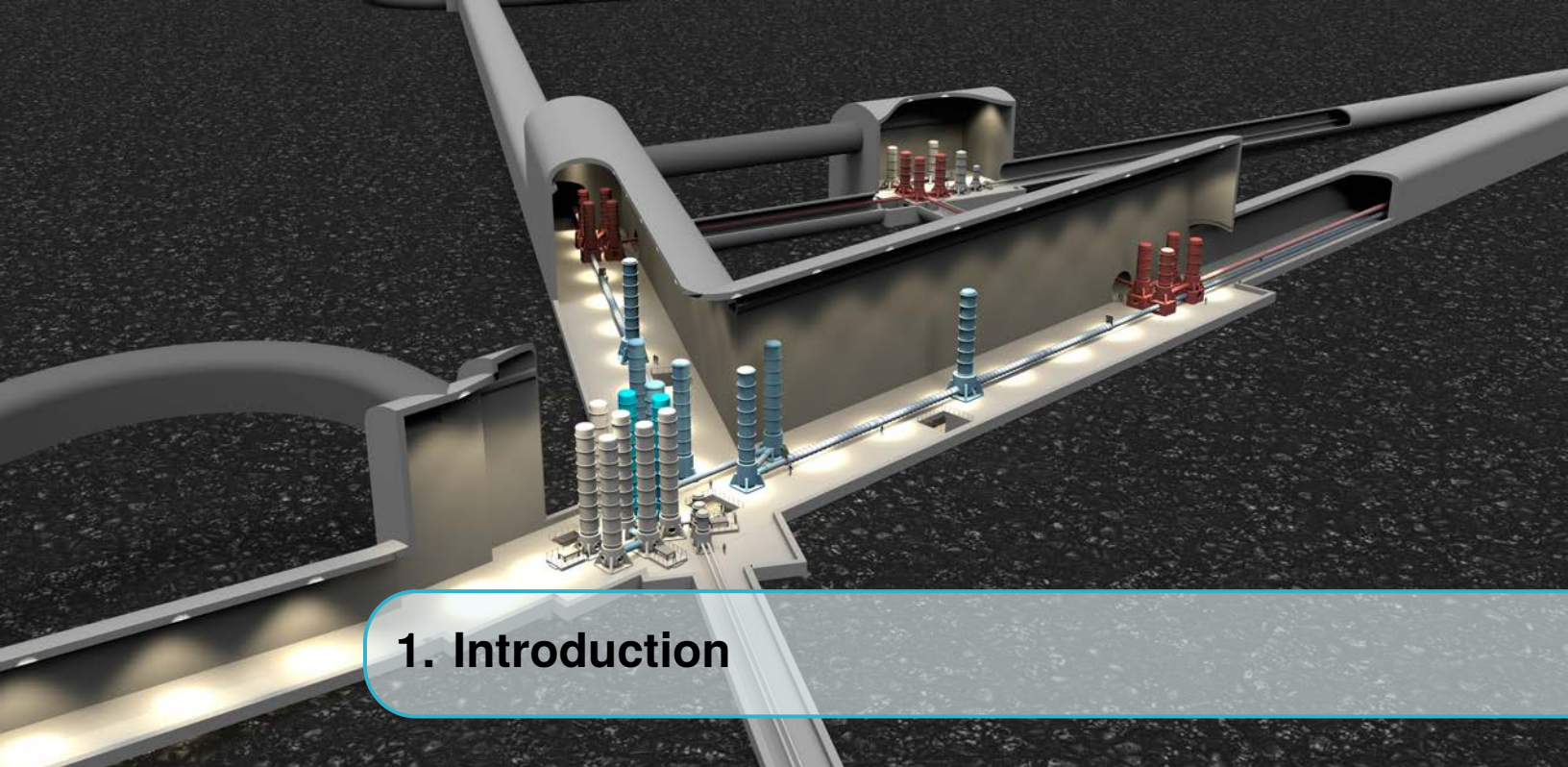
Please note that some symbols might stand for more than one quantity depending on the context

$c$	Speed of light
$D_L$	Luminosity distance to the source
$\mathcal{F}'$	$\pi/\mathcal{F}_{fc}$
$\mathcal{F}_{fc}$	Finesse of a filter cavity
$\Phi_{fc}$	Detuning of a filter cavity

---

$f_{\text{res}}$	Resonance frequency
$F_{\times}$	Detector response to $\times$ polarized GWs
$F_{+}$	Detector response to $+$ polarized GWs
$\gamma_{\text{fc}}$	Half-bandwidth (pole-frequency) of a filter cavity
$h$	Gravitational wave amplitude, usually denoting the detector response
$i$	Imaginary unit
$\lambda(\Omega)$	Frequency-dependent squeezing angle
$L$	Geometric length
$L_{\text{fc}}$	Baseline length of a filter cavity
$l_{\text{rt,fc}}$	Optical amplitude round-trip loss in a filter cavity
$L_{\text{cc}}$	Critical length of a filter cavity
$L_{\text{min}}$	Minimum possible length of a filter cavity that can be realised to match the target bandwidth in presence of optical loss
$M$	Total mass of a binary or a black hole
$\nu$	Symmetric mass ratio: for a binary composed of compact stars of masses $m_1$ and $m_2$ the symmetric mass ratio is $\nu = m_1 m_2 / (m_1 + m_2)^2$ .
$\Omega$	Angular sideband frequency
$P$	Probability distribution
$\rho_{\text{c}}$	Amplitude reflectance factor of a filter cavity's coupling mirror
$R_{\text{c}}$	Power reflectance factor ( $\rho_{\text{c}}^2$ ) of a filter cavity's coupling mirror
$\sigma$	Standard deviation
$\mathbf{T}$	$2 \times 2$ -matrix describing the input-output relation of an optical device
$\tau_{\text{c}}$	Amplitude transmittance of a cavity's coupling mirror
$V$	Variance
$V_a$	Variance in the anti-squeezed quadrature
$V_s$	Variance in the squeezed quadrature
$W$	Wigner function
$X_1$	Amplitude quadrature
$X_2$	Phase quadrature
$\zeta$	Homodyning angle
$z$	Cosmological redshift to the source





# 1. Introduction

The sensitivity increase that resulted from the upgrade of the gravitational wave detectors (GWDs) LIGO [17] and Virgo [18] from their first to the second (advanced) generation (2G) [19],[20] not only led to the first direct detection of gravitational waves on September 14, 2015 [21], but it also enabled the detection of a large number of coalescing binaries in the subsequent observation runs O1, O2 and O3, with ground-breaking scientific results and insights into astrophysical processes.

The impressive sensitivity achieved now results in weekly gravitational wave candidates from binary black holes. And yet the signal-to-noise ratio (SNR) of all previous and the vast majority of the expected detections does not begin to exploit the full potential of gravitational wave (GW) astronomy. The observation rate and SNR of many highly interesting sources (e.g. neutron star mergers or supernovae) is still too low at the current detection range.

Long before the first gravitational wave detection, the GW community started investigating a new (third) generation of detectors. In particular, the European Commission supported the European GW community to perform a conceptual design study within the Seventh Framework Programme (FP7-Capacities) in the period 2008 - 2011.

With a considerably improved sensitivity, new detectors of the third-generation will open the era of precision GW astronomy and with the Einstein Telescope (ET) project Europe will lead this scientific revolution. The **detection** of gravitational waves had been the goal of the "advanced detectors", the current generation. Now the focus is shifting to astrophysical **observations**.

To build a third-generation GW observatory with significantly improved sensitivity, it is necessary to overcome the limitations of the technologies used in the current interferometers, which would limit next-generation machines. The Einstein Telescope will use such new technologies, as outlined in this report. As a target for the next, i.e. the third generation of gravitational wave detectors, we have defined a sensitivity ten times better over a wide frequency range compared to the design sensitivities of current detectors.

The main objective of this document is the definition of the requirements and of the main characteristics of the site hosting ET, and the design of the key elements of the research infrastructure.

The next generation of gravitational wave observatories will need new infrastructures for the following reasons:

- The first and second generation GWDs use the same infrastructure, which is already over 25 years old and will have reached an age of 40 years by the time the Einstein Telescope is expected to be operational. To continue to rely on this infrastructure, a complete overhaul of it would be necessary, with the associated costs and long downtimes.
- The sensitivity that can be achieved in the existing infrastructures by implementing new technologies will be limited by the constraints of the site and infrastructure (arm length, local seismic noise, the lack of flexibility to accommodate cryogenic technology, vacuum pipe size . . .).
- Incremental upgrades to the existing infrastructures can be done in a staged way, allowing for a more or less continuous series of observation runs, with only moderately long interruptions. Radical upgrades of the existing detectors (e.g. going to cryogenic operation at a different wavelength) would require down-times of more than five years.

It is crucial that the infrastructure of the Einstein Telescope will last for many decades to host several generations of detectors and to be versatile enough to host different configurations of detectors. Several such configurations have been studied. The current most suitable configuration, detailed in this document, is compatible with the opportunities and constraints presented by the planned infrastructure and is able to reach the science goals presently envisaged. Upgrades of the detectors over the lifetime of the facility will profit from progress in R&D and will allow the observatory to remain well suited to address the evolving scientific goals

The feasibility of building a third-generation observatory is also being investigated in the United States. Under the name "Cosmic Explorer" (CE), a design study is currently being carried out with the aim of designing an above-ground detector that would exceed the sensitivity of Advanced LIGO by about one order of magnitude. The current concept envisages a detector up to 40 km in length, using conventional, i.e. 2G technologies, in the first phase of deployment planned for the mid thirties and later, in the early forties, switching to cryogenic technologies and other wavelengths.

## 1.1 The basics of gravitational wave detectors <sup>1</sup>

Gravitational waves induce tiny changes in separation between widely spaced 'test masses' (see Infobox 1.1). The instrumental challenge is to measure these tiny changes. Audio band detectors use laser interferometry, where the interferometer mirrors are the test masses at the ends of long baselines whose length changes are measured. The basis of all present and next generation gravitational wave detectors is a dual recycled Fabry-Perot arm cavity Michelson interferometer as sketched in figure 1.1. Being quadrupolar radiation, a passing GW alternately expands and then contracts one arm (e.g.  $L_x$ ) of the interferometer whilst it contracts and then expands the arm perpendicular to it ( $L_y$ ) as indicated in figure 1.2. The effect is extremely small: expressed as a relative length change,  $\delta L/L$ , it is less

<sup>1</sup>This section on the basics of gravitational wave detectors is taken from the GWIC 3G R&D report and has been modified to suit the purposes of this report.

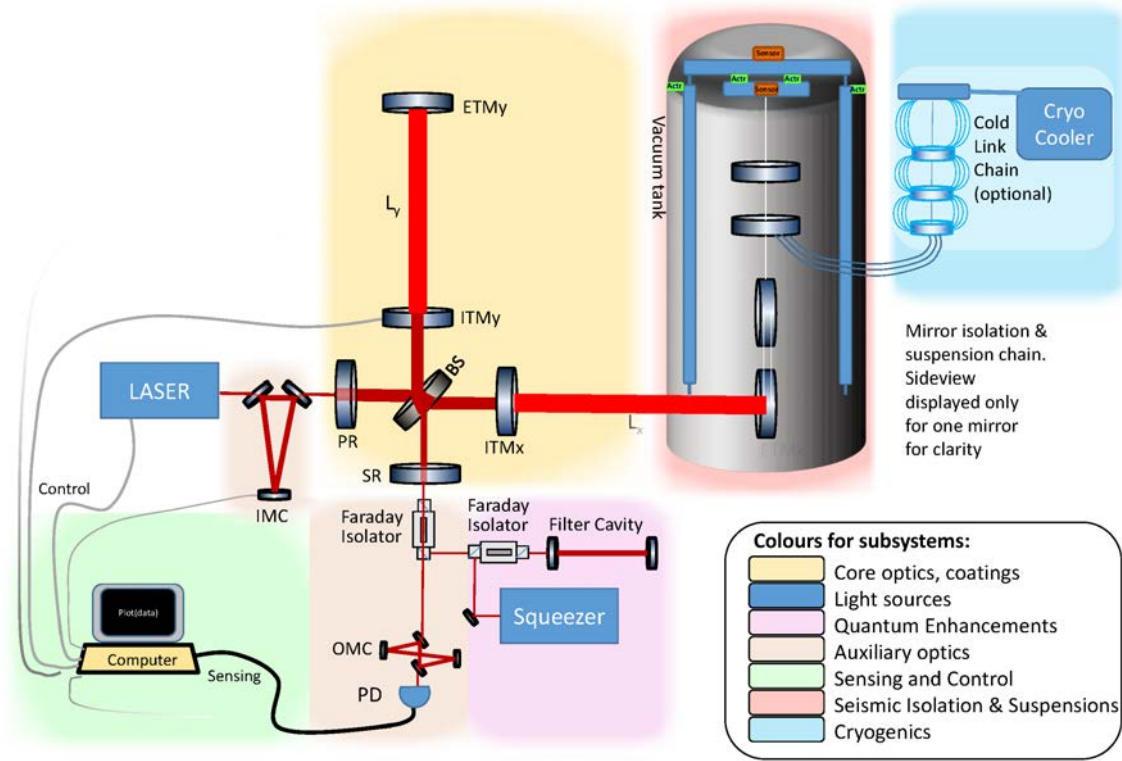


Figure 1.1: Schematic representation of an interferometric gravitational wave detector. Subsystems are indicated by the colored backgrounds. The borders between subsystems are not sharply defined and somewhat arbitrary.

than  $10^{-22}$ ! The arm cavities increase the phase change imposed on the light. Interfering the single frequency light beams from the two arms at the beamsplitter (BS) cancels common noise whilst the signal adds. Extra elements (PR and SR mirrors, squeezing, filter cavities etc) further increase sensitivity and optimise the response. Especially the transmission and the microscopic positioning of the Signal Recycling mirror can be used to either narrow the bandwidth of the detector and increase its peak sensitivity (Signal Recycling mode) or to widen it at the expense of peak sensitivity (Resonant Sideband Extraction (RSE) mode) [22, 23]. The core optics (test mass mirrors) are hung from sophisticated suspensions systems as indicated in figure 1.1 (in the vacuum tank on the right) so that, above resonance frequencies, they are effectively free to move [24]. The main optics can be cooled to cryogenic temperatures to minimise thermal noise (see also Infobox 1.1). In addition to the core optics there are a host of auxiliary optics to condition and match (in angle and size) the laser beam into the interferometer and the signal field out of the interferometer and into the photodetection system.

Once technical noises, such as laser frequency and intensity noise, acoustic noise and seismic noise, have been reduced there are three basic processes limiting the interferometer sensitivity: thermal, Newtonian (gravity gradient), and quantum noise. In Figure 1.5 we demonstrate the typical frequency distributions of these processes using the advanced Virgo design curve [1].

### Infobox 1: Detecting Gravitational Waves

Gravitational waves change distances between objects, while the objects themselves locally remain at rest, by changing the metric of space-time. These changes occur with opposing sign for orthogonal directions, as illustrated in figure 1.2 for one polarisation of a gravitational wave incident perpendicular to the paper ( $h_+$ : see box 1.1 for more details).

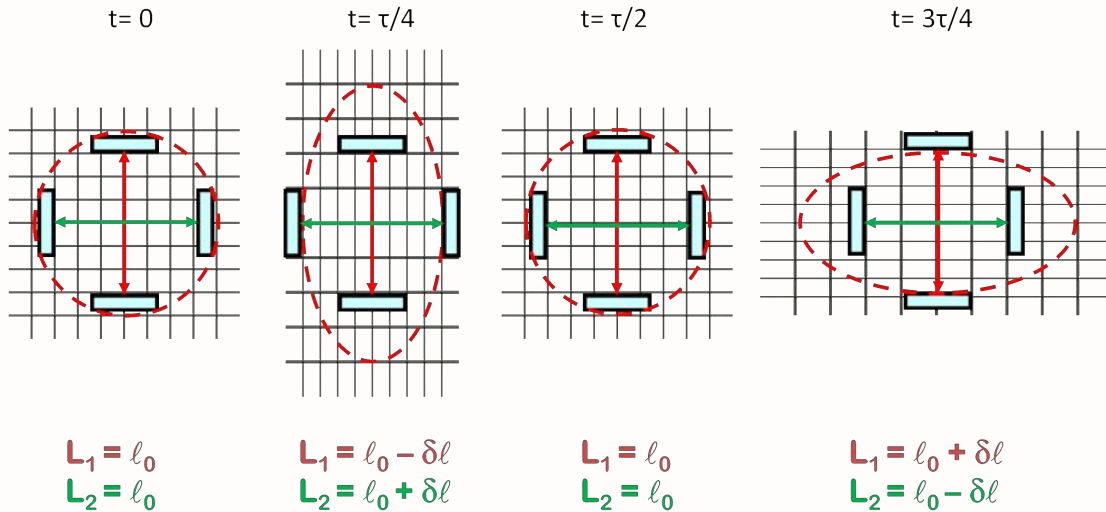


Figure 1.2: The effect of gravitational waves on the distances between objects. While the mirrors remain locally at rest the metric gets changed by the gravitational wave. The figure shows the effect of a sinusoidal gravitational wave with period  $\tau$ , for different times  $t$ . The distances measured between the mirrors change by  $\pm\delta l$ .

A Michelson interferometer is ideally suited to measuring this effect. The measurement principle is shown in figure 1.3. A laser beam is split into two partial beams, sent along the interferometer arms, where it experiences a phase shift by the metric change of the gravitational wave, is reflected at the end and returns to the beam splitter, where it is recombined. The interference condition at the beam splitter, i.e. the phase relation of the two returning beams, determines the intensity on the photo detector. Three different phase relations are shown in figure 1.3. The relative length change of the interferometer arms can hence be detected by measuring the power at the output port. Although the measurement principle is very simple, for getting the best possible sensitivity all influences that change the geometrical or optical arm length or that cause a signal in the detected photo-current mimicking a gravitational wave have to be minimised, resulting in very sophisticated and complex instruments.

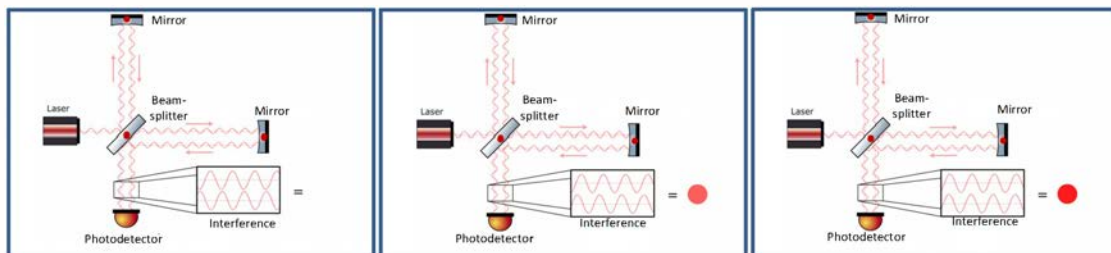


Figure 1.3: Michelson interferometer principle for gravitational wave detection, showing three different interference conditions resulting in different brightness at the output port.

### Infobox 2: ET's Response to Gravitational Waves

A single interferometric gravitational-wave detector cannot measure both polarizations of GW, but only a linear combination of the two, called the *response*  $h(t)$ , given by

$$h(t) = F_+(\theta, \varphi, \psi)h_+(t) + F_\times(\theta, \varphi, \psi)h_\times(t). \quad (1.1.1)$$

Here,  $F_+$  and  $F_\times$  are the detector antenna pattern functions,  $\psi$  is the polarization angle, and  $(\theta, \varphi)$  are angles describing the location of the source on the sky (see *e.g.* Ref. [25] for details). The various angles can be treated as constants for transient sources, but must be taken to be time-dependent for sources that last for more than about 30 min, after which Doppler modulation of the signal due to the relative motion of the source and detector cannot be neglected.

It is expedient to write the response as

$$h(t) = F(t) (\cos \xi h_+ + \sin \xi h_\times), \quad F = \sqrt{F_+^2 + F_\times^2}, \quad \tan \xi = F_\times/F_+. \quad (1.1.2)$$

It turns out that  $F$  is independent of the polarization angle and so measures the sensitivity of the detector to different locations on the sky. Figure 1.4 below plots  $F(\theta, \varphi)$  for an L-shaped interferometer such as Virgo (panel on the left) and for a triangular ET (panel on the right). Since ET consists of a triangle of three detectors, it is a factor  $\sqrt{3}$  more sensitive than a single detector; but, since the opening angles of the arms are  $\pi/3$ , the sensitivity is smaller by a factor  $\sin(\pi/3) = \sqrt{3}/2$  compared to an L-shaped detector—an overall factor of  $3/2$ , as can be seen in Fig. 1.4.

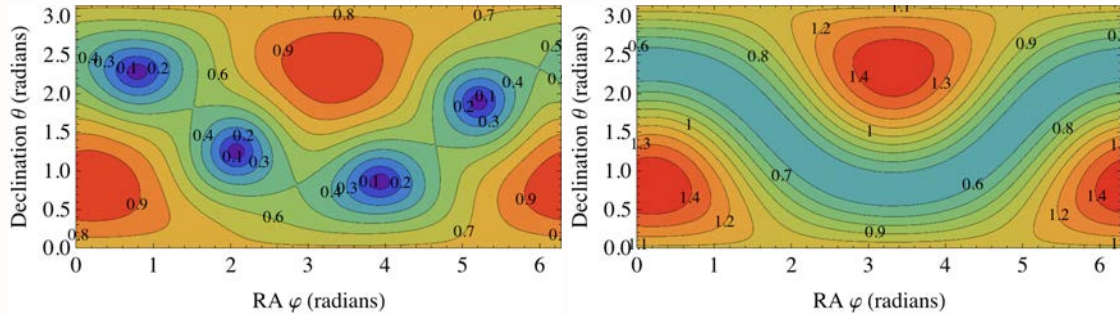


Figure 1.4: Antenna pattern of ET (right panel) compared to that of Virgo (left panel). ET is assumed to be at the same location as Virgo. Note that Virgo is a *single* L-shaped detector while ET consists of *three* V-shaped interferometers rotated relative to one other by 120 deg. The combined antenna pattern of the three detectors in ET (defined as  $F^2 = \sum_{A=1}^3 F_A^2$ , where  $F_1, F_2, F_3$  are the individual antenna pattern functions) makes the response the same for all sources whose sky location makes the same angle to the plane formed by ET (see *e.g.* contours marked 0.6).

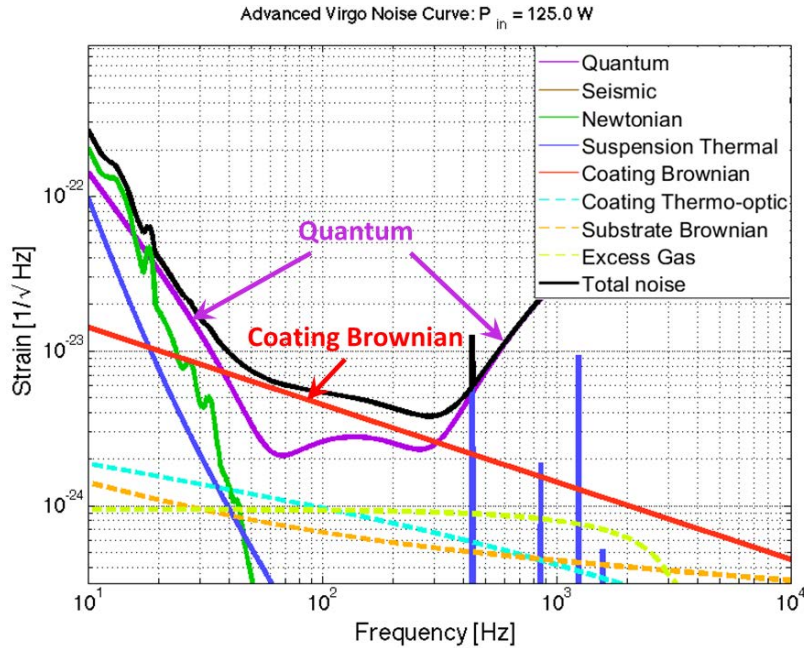


Figure 1.5: Design noise budget for advanced Virgo for the next observation run O4. For details see e.g. [1]

Thermal noise (see also Infobox 1.1) [26] is produced by random displacements of the mirror surfaces in response to thermally fluctuating stresses in the mirror coatings, substrates, and suspensions and it typically dominates at mid-band frequencies (ca. 50-200 Hz). Quantum noise can be roughly divided into quantum radiation pressure noise (QRPN) and quantum phase noise or shot noise (SN)[27]. QRPN, or quantum back-action noise, arises from the random buffeting of the suspended interferometer mirrors by the quantum mechanical amplitude fluctuations of the light field being used to sense the arm-length. Shot noise results from quantum phase uncertainty: there is a limit to how well the phase difference between two light fields returning from the interferometers arms can be determined. Radiation pressure noise dominates at low frequencies (ca. 10Hz to 50 Hz) while shot noise dominates at higher frequencies (above ca. 200 Hz). The standard quantum limit is the noise floor for which the QRPN and shot noise are equal at a given power level (typically around 100 Hz). Newtonian Noise (NN) arises from the direct gravitational forces exerted on the interferometer mirrors by nearby changing mass distributions primarily caused by density fluctuations of the surrounding earth due to seismic waves as well as low frequency atmospheric density changes [28]. The test masses cannot be shielded against these fluctuating forces. In addition to the noise sources discussed above, another important issue is the suppression of instabilities that arise from photon pressure at high optical power.

In reality there are a myriad of technical noise sources that need to be suppressed in order to reveal the 'fundamental limitations' (scattered light, electronic noise, various other control noises). This is dramatically demonstrated in figure 1.6 which shows the noise anatomy for the advanced Virgo (adVirgo) detector close to Pisa, Italy, circa March 2020. Much of the effort and focus when commissioning a detector is devoted to suppressing such "technical" noise.

From Figure 1.5 it is clear that the impact on the sensitivity of reducing one noise source depends

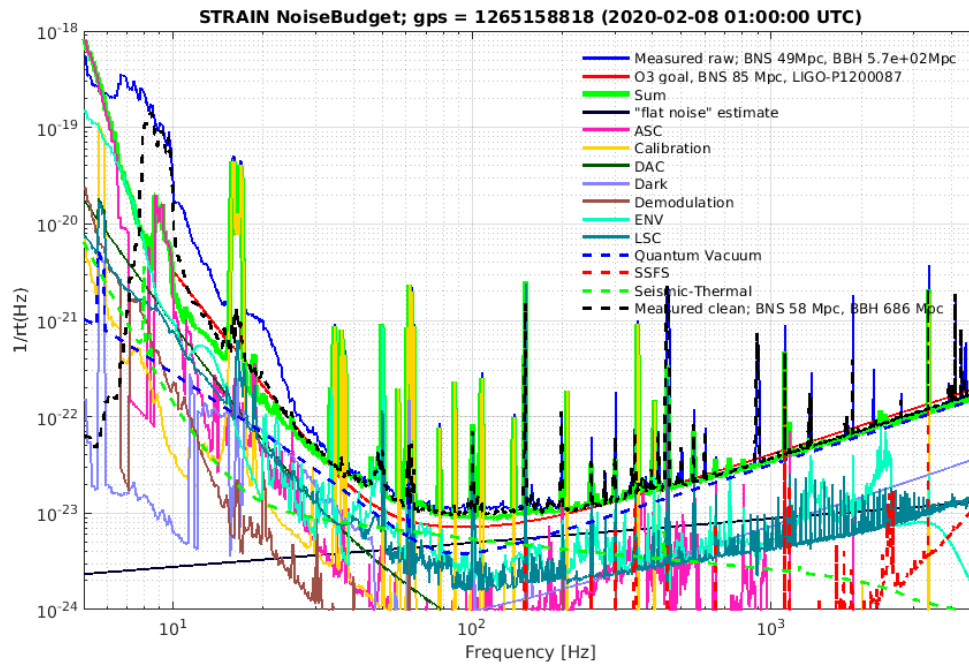


Figure 1.6: Example noise budget for the advanced Virgo detector in Italy, February 2020. Shown are amplitude noise spectral densities of individual noise sources contributing to the overall noise of the detector as a function of frequency. The noises are scaled to gravitational wave strain. The figure clearly shows that in the low frequency region many different noise sources contribute at comparable levels and consequently at low frequencies many different sources have to be considered and minimised.

on other noise contributions at relevant frequencies. For example, lowering quantum noise around 100 Hz will have little impact unless coating Brownian noise is similarly reduced. The low frequency band below 20 Hz is far more complex. In this report we will review each noise source and the R&D that needs to be done, independently of other constraints. It is beyond the scope of this report to reflect on what may happen if progress on a particular subsystem is slower than expected. Such impact on the science that can be done will be considered in trade studies that will be carried out in the various detector collaborations.

Infobox 2: Thermal Noise<sup>a</sup>

<sup>a</sup>This box is taken from the GWIC 3G R&D report and has been modified to suit the purposes of this report.

Thermal noise is one of the fundamental noise sources limiting 2G detectors over a considerable frequency range. The main contributions come from Brownian noise of the mirror suspensions, substrates and coatings and thermo-optic (thermo-elastic plus thermo-refractive) noise of substrates and coatings. The relation between the dissipation and the power spectrum (single sided) of the noise is described by Callen's Fluctuation-Dissipation Theorem [29–31] and is given by:

$$S_x(\omega) = \frac{4k_B T}{\omega^2} |\operatorname{Re}[Y(\omega)]|. \quad (1.1.3)$$

with  $k_b$  the Boltzmann constant,  $\omega$  the angular frequency, T the temperature and Y defined as

$$Y(\omega) = i\omega \frac{X(\omega)}{F(\omega)}, \quad (1.1.4)$$

where  $X(\omega)$  and  $F(\omega)$  are the Fourier components of the displacement of the system and force applied leading to the displacement, respectively. The real part of the admittance is proportional to mechanical losses, hence low noise requires low mechanical losses. Operating the mirrors and suspensions at reduced temperature reduces thermal noise since the  $\sqrt{S_x(\omega)}$  scales with  $\sqrt{T}$ . More significantly, many material properties of mirror substrates and coatings depend on temperature, and hence influence the temperature dependence of thermal noise. Fused silica, like most other glasses, has increased mechanical losses at cryogenic temperatures, making it unsuitable as substrates at cryogenic temperatures. Crystalline materials (Sapphire, Silicon) are therefore the prime candidates for low temperature operation. Most amorphous oxide coatings show higher mechanical losses at cryogenic temperatures while the losses of crystalline or semiconductor coatings improve. However, the latter may suffer from other drawbacks, e.g. increased optical absorption. Further dependence of coating thermal noise on coating parameters is shown in this equation:

$$S_x(f) = \frac{4k_B T}{\pi^2 f Y} \frac{d}{r_0^2} \left( \frac{Y'}{Y} \phi_{\parallel} + \frac{Y}{Y'} \phi_{\perp} \right)$$

Labels in the diagram:

- Temperature (green arrow pointing to  $T$ )
- Boltzmann constant (blue arrow pointing to  $k_B$ )
- Geometrical coating thickness (purple arrow pointing to  $d$ )
- Loss angle of coating (light blue arrow pointing to  $\phi_{\parallel}$  and  $\phi_{\perp}$ )
- Young's modulus of mirror substrate (red arrow pointing to  $Y$ )
- laser beam radius (orange arrow pointing to  $r_0$ )
- Young's modulus of coating (pink arrow pointing to  $Y'$ )
- PSD of displacement (light blue arrow pointing to the left side of the equation)

Coating parameters contributing to thermal noise in GWDs. Equation from [32]

## 1.2 Scientific targets of the ET observatory

GW detection has literally opened a new window on the Universe. With new third-generation observatories such as ET we will begin to look far out through this window. As with any scientific enterprise of this scale, there will be certain questions for which, based on our current understanding, we can say that ET is guaranteed to provide the answers, but ET will also be a discovery machine. It will venture into unexplored territories where further surprises are expected. The following is a summary of the key science capabilities:

(1) ET will **detect BBH coalescences up to cosmological distances**. For a total mass of the system between a few tens and a few hundreds solar masses, as typical of the population of black hole (BH) binaries revealed by 2G detectors, ET will be able to detect their coalescence up to redshift  $z \sim 20$  and beyond, see Fig. 2.1 on page 52. The corresponding rates will be in the order of  $10^5 - 10^6$  events per year. This will provide a census of the population of BHs across the whole epoch of star formation and beyond, answering crucial questions on the progenitors, formation, binary evolution and demographics of stellar BHs. The astrophysical potential in this direction is guaranteed. An observatory network of two or more 3rd-generation observatories would of course be beneficial, in particular for source localization, but even ET as a single observatory is adequate to uncover much of this compelling science.

(2) ET will **extend the region of BH masses** compared to that explored by 2G detectors, including sources of several hundreds of solar masses, that could be detected up to redshifts of order 10 or more, and sources of several thousands solar masses, that could be detected up to  $z \sim 1 - 5$  (see Fig. 2.1). This would provide the first clear evidence for the existence of BHs in this mass range, would allow us to study them as a population and to investigate the possibility that they are the seeds of the supermassive BHs in the center of galaxies. On the low-mass side, ET would detect, up to  $z \sim 0.5 - 1$ , the coalescence of hypothetical binary BHs with a total mass of order one solar mass; any BH with such a mass would necessarily be of primordial, rather than stellar, origin.

(3) ET will **detect the coalescence of BNS up to  $z \simeq 2 - 3$** , with a rate of about  $6 \times 10^4$  events per year. This range reaches the peak of the star formation rate and therefore covers the vast majority of neutron star (NS) binaries coalescing throughout the Universe. This will allow us to investigate their formation mechanisms, evolution, and demographics. The sensitivity of ET in the high-frequency regime will allow us to access the GW signal of the merger phase that is inaccessible to 2G detectors and carries detailed information on the internal structure of neutron stars and on their equation of state. This will have important implications also for fundamental physics, allowing us to study Quantum Chromodynamics (QCD) at ultra-high density and the possibility of phase transitions in the NS core, such as a transition to deconfined quarks or the formation of exotic states of matter. These detections, and a rich science output coming from them, are guaranteed. Again, these goals can be obtained even by ET as a single observatory. A network of three 3G observatories would bring, on top of this, the possibility of accurate localization of the source, allowing to give information to electromagnetic telescopes necessary to identify an electromagnetic counterpart and perform multi-messenger studies.

(4) ET could **detect several new astrophysical sources of GWs**, such as signals emitted during core collapse supernovae, continuous signals from isolated rotating NSs, and possibly burst signals from NSs. While not guaranteed, these signals would bring rich information. Detecting the GWs from supernovae would elucidate the mechanisms of supernova explosions and its post-collapse phase.

The detection of continuous GWs from NSs would allow us to explore the condition of formation and evolution of isolated NS, providing information on their spin, thermal evolution and magnetic field. ET will be able to detect ‘mountains’ on the surface of a NS as small as  $10^{-3}$  mm, which in turn would again give us information on the inner structure of NS and on the corresponding aspects of nuclear and particle physics, such as the existence of exotic matter in the NS core.

(5) The waveform from the loudest BH-BH and NS-NS coalescences will be **observed by ET with exquisite precision**. This will allow accurate tests of General Relativity (GR), both in the inspiral phase, where one can test the validity of the post-Newtonian expansion of GR to sub-permille accuracy, and in the merger and post-merger phase. The latter is particularly interesting since it would allow us to test the nature of BHs and the dynamics of space-time close to the horizon of the final BH, through the observation of the frequencies and lifetimes of its longest-lived quasi-normal modes. This would allow us to perform new accurate quantitative tests of the predictions of GR in this extreme domain. The possibility of performing such accurate tests is guaranteed, and can be performed by ET as a single observatory, also thanks to the triangle configuration that will allow the measurement of the individual polarization amplitudes and more stringent tests on the existence of extra, non-GR, polarizations. These tests could also in principle lead to surprises, such as revealing the existence of exotic compact objects, and could even carry observable imprints of quantum gravity effects. While the latter goals are more speculative, their impact would be revolutionary.

(6) ET will **test several dark matter candidates**, such as primordial black holes, ultralight scalars or vector fields, or dark matter particles accreting on compact objects. ET will be able to explore these possibilities even as a single observatory.

(7) ET will **explore the nature of dark energy** and the possibility of modifications of GR at cosmological distances. The crucial point here is again the ability to detect compact binary coalescences up to cosmological distances, providing an absolute measurement of their distance. The relation between luminosity distance and redshift, in the range of redshifts explored by ET, carries very distinctive signature of the dark energy sector of a modified gravity theory, through the dark energy equation of state and, especially, through an observable related to modified GW propagation. The latter is a particularly powerful probe of dark energy, which is accessible only by GW observations. From the point of view of cosmology, ET is guaranteed to obtain important results (alternative precision measurements of  $H_0$ , significant limits on the equation of state of dark energy), complementing measurements obtained with electromagnetic probes. The possibility of detecting modifications of General Relativity at cosmological scales and understanding the origin of dark energy is not guaranteed, but would be revolutionary.

(8) ET will **search for stochastic backgrounds of GWs**, which are relics of the earliest cosmological epochs. Such a background, if detected, would carry information of the earliest moment of the Universe (much earlier than from the cosmic microwave background observations), and on physics at the corresponding high-energy scales, that is inaccessible by electromagnetic (or neutrino) observations or with particle accelerators. Stochastic backgrounds of cosmological origin in the ET frequency window and sensitivity depend on physics beyond the Standard Model. Thus, the predictions are unavoidably uncertain, and the gain from a successful detection would be correspondingly high, allowing us to explore the earliest moments after the Big Bang.

### 1.3 Design of the ET observatory

The sensitivity of gravitational wave detectors improved considerably from the bar detectors through the first generation (1G) of interferometric detectors to the currently operating *advanced*, second generation (2G) detectors. To achieve the scientific goals stated above, the sensitivity in comparison to the second generation of gravitational wave detectors must be improved by about an order of magnitude over the entire detection frequency band accessible to ground-based detectors currently ranging from some 10 Hz to a few kHz. Frequent and precise observation of low-frequency sources, e.g. intermediate mass black holes, additionally requires an extension of the detection range towards lower frequencies.

The sensitivity goal for the Einstein Telescope is driven by the need to get frequent high SNR events for routine precision gravitational wave astronomy. The high-frequency sensitivity is determined by the maximum feasible laser power in the interferometer arms, the mid-frequency range is governed by thermal noises and the low-frequency range by a variety of noise sources including thermal and external noises, e.g. seismic noise.

The sensitivities of the second and third generation are shown in figure 1.7.

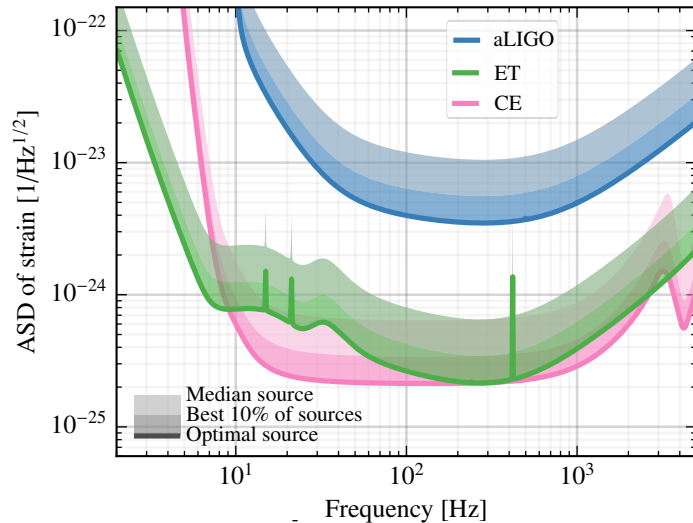


Figure 1.7: Design sensitivities of the advanced and the third generation gravitational wave detectors. The various colour shades represent different sets of source locations and orientations.

#### 1.3.1 Size, shape and layout

In order to achieve the sensitivity that the Einstein Telescope project aims for, it will be necessary to exploit all state-of-the-art technologies and drive them to their technical limits.

The sensitivity goal can only be reached by significantly increasing the size of the detector beyond the size of currently available instruments (i.e. 3 km for Virgo and 4 km for LIGO) and going to an underground location (see chapter 7, where the seismic noise and especially its coupling via gravity gradients is lower than at the surface). Only by increasing the arm length to 10 km can the influence of unavoidable displacement noises be lowered to a tolerable level.

In its final configuration the Einstein Telescope will consist

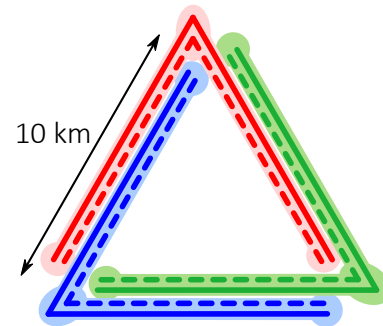


Figure 1.8: The Einstein Telescope's geometry will be a triangular arrangement for three nested detectors, each consisting of two interferometers.

of three nested detectors, which will be arranged in a triangular pattern as shown in figure 1.8 (see also section 6.1).

In contrast to the traditional L-shaped geometry of the first and second generation detectors this arrangement is equally sensitive to both polarisations of the gravitational wave. Additionally, it shows a more isotropic antenna pattern compared to the L-shaped detectors, as shown in figure 1.9. The overall frequency range covered will reach from 3 Hz to several kHz.

Each individual detector in turn will comprise two interferometers, one specialised for detecting low-frequency gravitational waves and the other one for the high-frequency part. The sensitivity goal for each interferometer is shown in figure 1.10. Each individual interferometer has a classical dual-recycled Michelson topology with Fabry-Perot arm cavities. This technique is currently used in Advanced LIGO and about to be installed in Advanced Virgo. Alternative topologies are under study and they, or newer approaches may prove to be great "future" candidates for implementation in this observatory. They are not qualified for "initial" detectors yet.

The sensitivity curve shown in figure 1.10 gives the sensitivity for a single detector with 10 km arm length and an angle of  $90^\circ$  between the arms. This is done for better comparison with the existing and planned detectors. ET will in fact have three 10 km detectors and the angles between the arms will be  $60^\circ$ . The resulting sensitivity in comparison to a single  $90^\circ$  detector depends on the source location in the sky and its orientation, as the angular antenna pattern (see figure 1.9) and the polarization dependence (independent in the triangular case) influence the signal strength differently for different detector layouts. On average the sensitivity of the triple  $60^\circ$  detector is slightly better than a single, optimally oriented  $90^\circ$  one.

### 1.3.2 Quantum noise

In order to achieve a sufficient sensitivity at high frequencies the light power in the arms of the interferometer needs to be increased to the megawatt range. Thermal noise considerations on the other hand require cryogenic optics to reach the sensitivity goal at low frequencies.

Large and heavy mirrors will be used to keep radiation pressure effects low and also allow larger sized beam spots on the mirror surfaces for lowering thermal noise effects.

Operating cryogenic optics at a level of several megawatt of light power presents a serious technological challenge which cannot be mastered with technologies in reach. Even for the best mirrors that

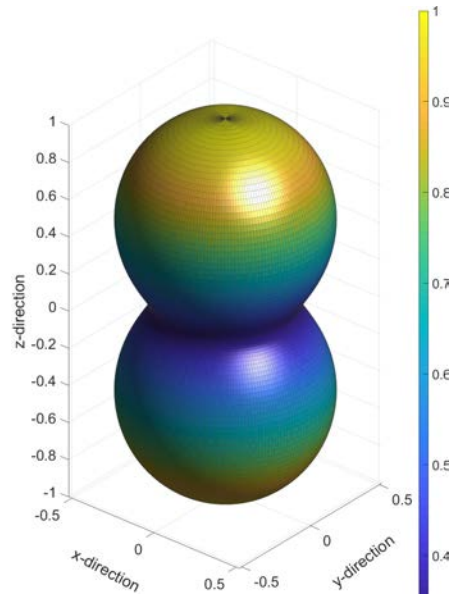


Figure 1.9: The normalised antenna pattern (amplitude sensitivity) of the combined three detectors of the Einstein Telescope for unpolarised waves, i.e. the quadrature sum of "x" and "+" polarised waves.

state-of-the-art coating technology can produce, the residual absorption in the order of one ppm leads to an absorbed power of several Watt at a circulating light power level in the megawatt range. The resulting thickness of the suspension fibres, which would be needed to remove the heat, would spoil the thermal noise performance required of the ultra low loss suspension. The Einstein Telescope will therefore be realised in what we call a ‘xylophone’ arrangement, where each single detector is split into two complementary interferometers, leading to sensitivities as shown in figure 1.10. This split detector arrangement also offers an elegant solution for the challenge that radiation pressure noise and shot noise scale in opposite ways with light power and cannot individually be optimised in a single interferometer. In an interferometer using classical states of light the so-called Standard Quantum Limit (SQL) determines the lower limit for the quantum noise. For each frequency there is a different optimal compromise between shot noise and radiation pressure noise, meaning that in a single interferometer the SQL cannot be reached for all frequencies simultaneously. It can be overcome if non-classical light with correlations between the phase and the amplitude quadratures is used, so-called squeezed light. In the shot noise dominated frequency range squeezed light is used, which shows lower phase fluctuations at the cost of the amplitude fluctuations in comparison to classical laser light in the interferometer arms.

The interferometer dedicated for detecting high-frequency gravitational waves in the range from about 30 Hz to several kHz will be operated at room temperature, use fused silica optics with a diameter of about 60 cm and a mass of about 200 kg each, have a light power of about 3 MW in the interferometer arms, and run in the broadband Resonant Sideband Extraction mode.

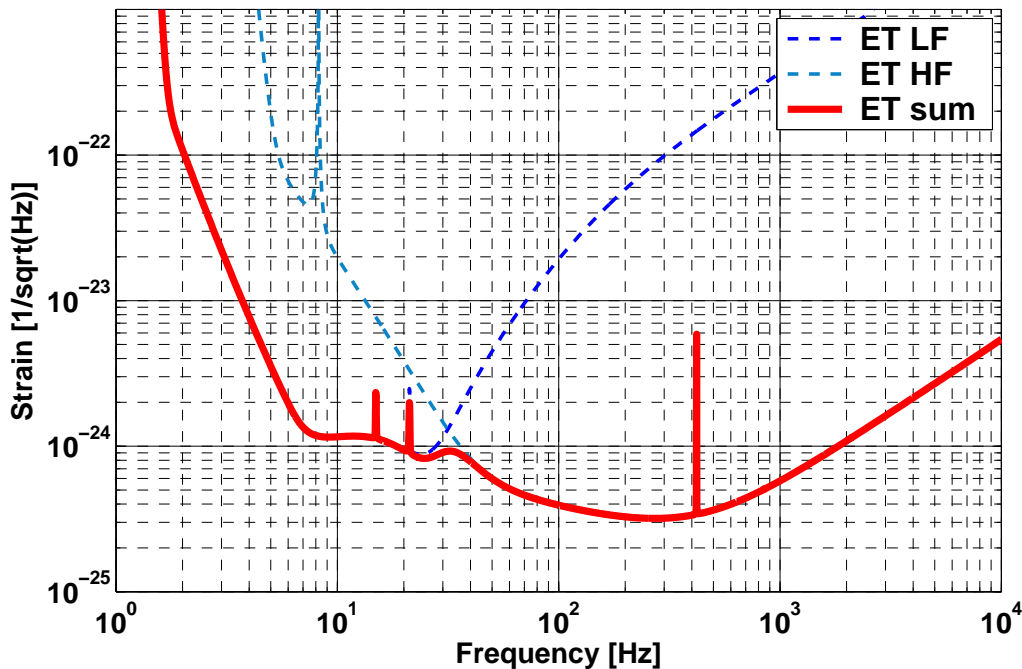


Figure 1.10: Sensitivity of the Einstein Telescope in the ‘xylophone’ configuration. The sensitivity of the low-frequency cryogenic interferometer is shown in the dashed dark blue curve and the one of the high-frequency room temperature one in a dashed blue-green tone. The sum of both is given by the solid bright red curve. Shown here is the sensitivity for a single detector with 10 km arm length and an angle of 90. (In some of the earlier documents this curve was labelled *ET-D* sensitivity curve.)

The cryogenic, low-frequency interferometer, operated at a temperature of 10 - 20 K and aimed at the frequency range from 3 Hz to 30 Hz, will use detuned signal recycling, have a light power of 18 kW in the interferometer arms, and silicon mirrors with a diameter of about 45 cm and a mass of about 200 kg. The cryogenic optics will be made of silicon, necessitating to move to a longer laser wavelength of 1550 nm, because silicon is not transparent at the wavelength of 1064 nm currently used in all gravitational wave detectors with an angle of  $90^\circ$  between the arms.. The dimensions will partly be determined by the maximum available bulk material size and otherwise be comparable to the room temperature ones. A summary of the main parameters for the high and low temperature interferometers is given in table 6.1.

In the low-frequency range, radiation pressure dominated range the fluctuations need to be lowered in the amplitude quadrature. This goal can be achieved by reflecting squeezed light off a filter cavity (see figure 6.3). Noise reduction with squeezed light is currently applied in the existing gravitational wave detectors, resulting in a noise reduction in the shot noise limited regime of about 3 dB in advanced LIGO and advanced Virgo. Squeezing levels of up to 15 dB at the squeezing source have been demonstrated [33] and long term stable noise reduction in the shot noise limited regime with a maximum of 6 dB around 5 kHz has been demonstrated at GEO 600 [34]. For the Einstein Telescope we assume an initial squeezing level at the squeezing source of 15 dB and an effective squeezing level of 10 dB to be available (equivalent in shot noise reduction to a laser power increase of a factor of 10).

### 1.3.3 Thermal noise

Reaching the sensitivity goal at low frequencies requires a significant reduction of thermal noise sources compared to the advanced gravitational-wave detectors, which can be achieved by operating the mirrors at cryogenic temperatures as low as 10 - 20 K.

Cryogenic operation is also used in the Japanese gravitational wave detector KAGRA. At these low temperatures fused silica has a low mechanical quality factor and becomes unusable. Silicon and sapphire show excellent low-temperature behaviour (see section 6.11.1) and are good candidates for cryogenic gravitational wave detectors. Its availability in large quantities and good

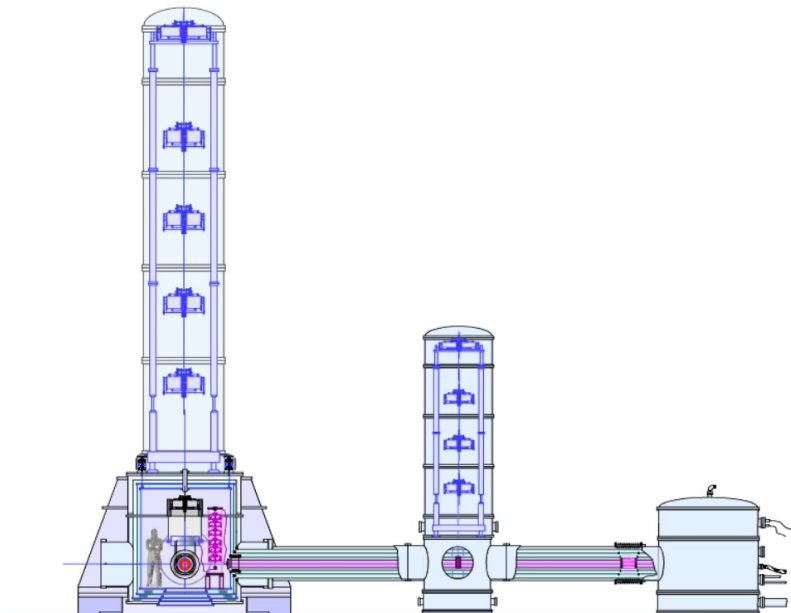


Figure 1.11: Scheme for cooling the mirrors. Front view of the mirror. For details see section 6.11.1

candidates for cryogenic gravitational wave detectors. Its availability in large quantities and good

purity through the semiconductor industry makes silicon a promising candidate for the Einstein Telescope cryogenic optics.

Removing the heat generated by laser light being absorbed at the mirror surfaces without introducing excess vibration levels poses another technical challenge. As thermal radiation does not provide sufficient coupling at cryogenic temperatures this heat removal has to be done by thermal conduction of the suspension fibres. The resulting requirement for the thickness of the silicon suspension fibres needs to be balanced against good seismic isolation properties of thin fibres. The vibration level of cryo coolers, which could be placed close to the optics, threatens the low-frequency sensitivity (see section 6.11.1). R&D in low vibration cryocoolers is still required to sufficiently cut the remaining noise level down for use in the Einstein Telescope.

Cryogenic fluids which are cooled down above ground are available as a seismically more quiet alternative (see section 6.11.1). The final operating temperature for ET remains to be fixed in a technical design phase. The cooling capabilities foreseen so far will allow mirror temperatures as low as 10 K.

#### 1.3.4 Seismic isolation

The main optics for the Einstein Telescope need to be very well isolated against seismic ground motion. In this respect, the approach taken by LIGO and Virgo, in their advanced configurations, is similar, with both observatories employing a combination of active and passive vibration isolation techniques to reduce the contribution of the direct coupling to seismic noise well below the sensitivity of the instruments at 10 Hz. Nonetheless, the details of the implementation are different: LIGO uses a more aggressive active control while Virgo employs both gravitational and mechanical anti-spring systems to achieve very low normal-mode frequencies that are the key to passive (or inertial) attenuation. The strategy employed at the Virgo detector has demonstrated an excellent performance over the full frequency range of the Einstein Telescope and has been chosen as the reference solution.

The baseline configuration consists in a longer Virgo-style Superattenuator (SA) (see figure 1.12) in which horizontal seismic isolation is achieved by means of a six-stage pendulum system, whereas for the vertical degree of freedom cantilever springs are used. The pendulum suspension chain itself is supported by a platform resting on an inverted pendulum (IP), which provides additional horizontal seismic attenuation at very low frequency. The IP stage is also instrumented with actuators and position and inertial sensors for active damping of the chain modes and for augmented attenuation performance via active vibration isolation. Inertial tilt control is handled at the level of the base ring which is mounted on piezoelectric actuators. At the lower end of the chain the test mass suspension system suspended has also to minimize thermal noise, while keeping the capability of precisely controlling the mirror linear and angular position. There are two different test mass suspension systems as one operates at room temperature and the other one in cryogenic conditions. The overall height of the suspension system is about 17 m, requiring correspondingly tall vacuum chambers and caverns.

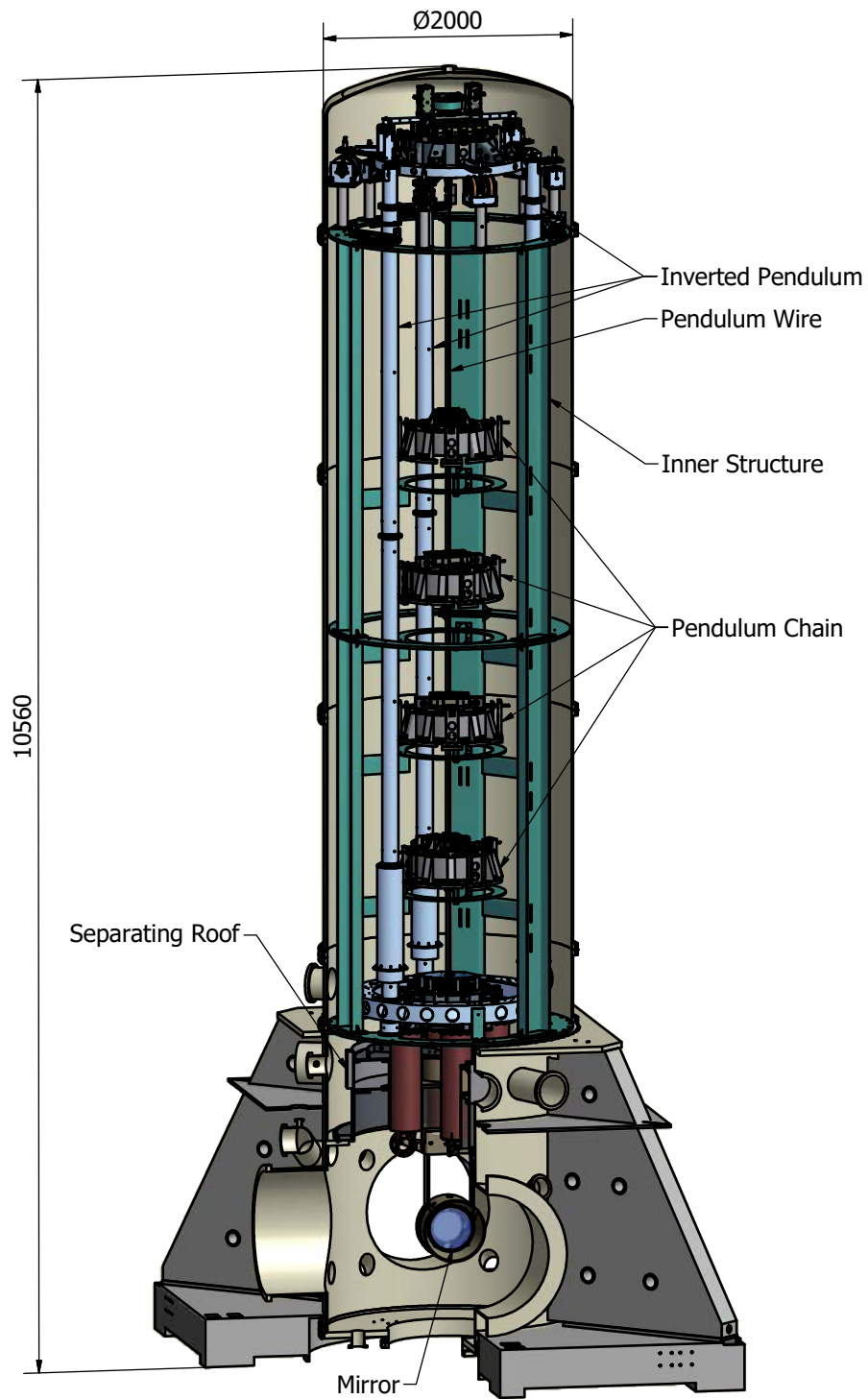


Figure 1.12: Schematic view of a Virgo Superattenuator, similar to the ones proposed for ET. See also section 6.10.1

### 1.3.5 Terrestrial gravitational noise

Newtonian gravitational interactions between the optics and the surrounding soil provide a direct coupling mechanism of ground motion to the interferometer test masses (see also section 7.2.4). As the resulting, so-called gravity gradient noise cannot be shielded from the mirrors, a location has to be found where this seismic motion is minimal and the surrounding soil as homogeneous as possible. This goal can be achieved in an underground location in a seismically quiet region. Preliminary measurements show that a depth of 200 to 300 m in a remote location with low population density provides sufficiently low seismic motion. The potential of measuring the ambient seismic motion, feeding it into a gravity gradient noise model, and then subtracting the predicted effect from the interferometer output signal has been investigated. Initial results are promising, and are interesting also for the current generation of gravitational wave detectors, but investigations need to be continued in an R&D programme.

### 1.3.6 Vacuum

The space between the mirrors in the interferometer arms has to be evacuated to very low residual partial gas pressures to keep the apparent length changes caused by fluctuations of the refractive index sufficiently low. The tolerable maximum total pressure is on the order of  $10^{-8}$  Pa (see paragraph 6.12.1). The more detailed technical design of the vacuum system still needs to be defined in the technical design phase.

### 1.3.7 Noise budget

The xylophone strategy, i.e. splitting each detector into a low-frequency and a high-frequency interferometer, allows the pursuit of different strategies in optimising the noise for each frequency range. The noise budget for the high-frequency interferometer is shown in the bottom part of figure 1.13. In the frequency range from about 7 Hz to 30 Hz the sensitivity is limited by suspension thermal noise, resulting from the interferometer being operated at room temperature. At frequencies above 500 Hz the dominating noise source is photon shot noise. Between these two frequency ranges mirror thermal noise is limiting the overall sensitivity.

In the noise budget for the low-frequency interferometer, shown in the upper part of figure 1.13, quantum noise is limiting the sensitivity over the entire frequency range above 7 Hz. The operation at cryogenic temperatures reduces the influence of suspension thermal noise in the frequency range above 7 Hz to below the quantum noise. Below 7 Hz the sensitivity is limited by comparable amounts of quantum noise, gravity gradient noise, and suspension thermal noise. Due to the good performance of the multistage pendulum suspensions the influence of seismic noise can be limited to the frequency range below 2 Hz. If the heat extraction by the suspension fibers can be increased, a higher tolerable laser power would lead to a further reduction of the quantum noise in the frequency range above 7 Hz.

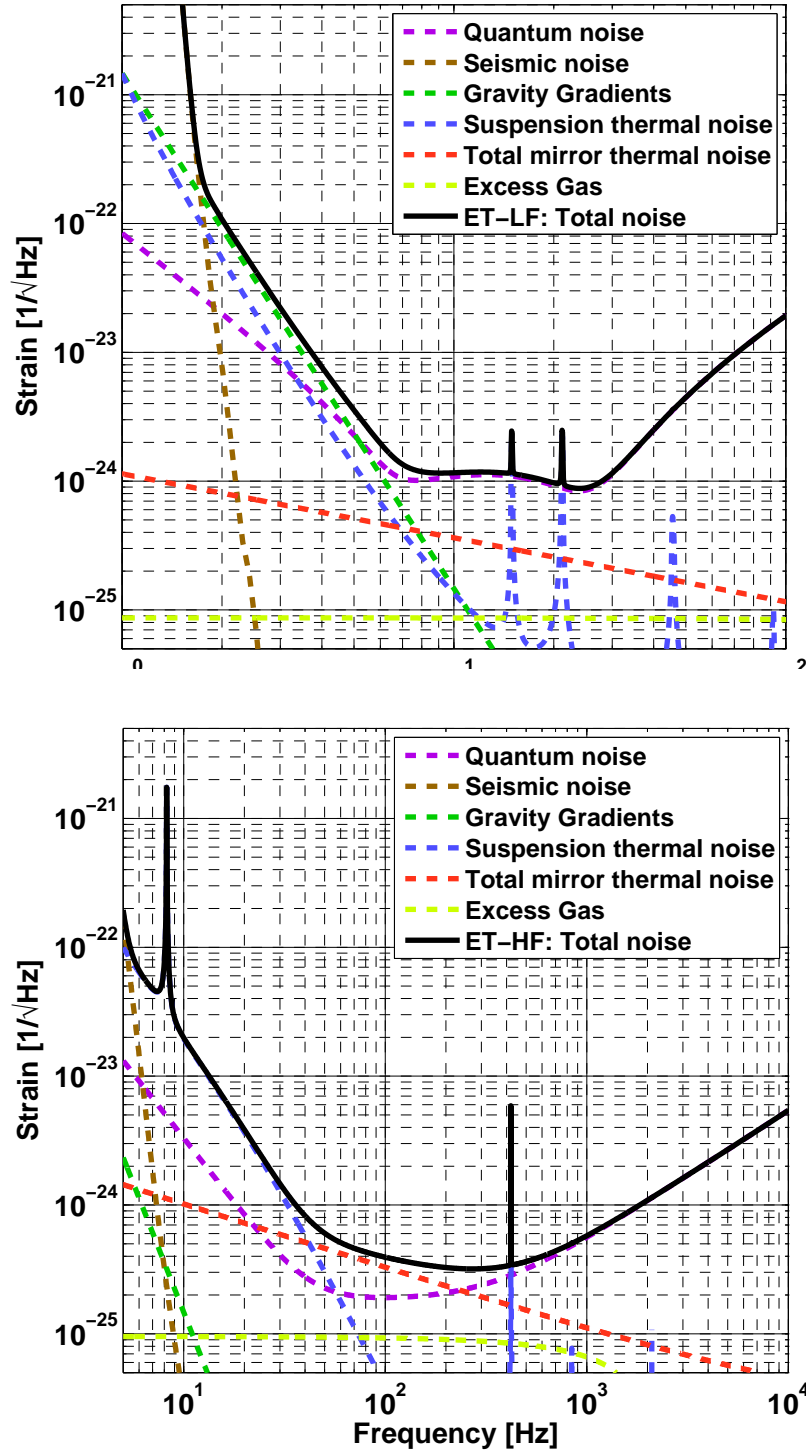


Figure 1.13: Noise budget for the low-frequency (top) and high-frequency (bottom) interferometer for the parameters stated in table 6.1. Shown in black is the amplitude spectral density of a gravitational wave required to produce a signal with the same strength as the total noise of the interferometers. The total noise is decomposed into the individual noise sources, which being statistically independent add up quadratically.

### 1.3.8 Layout of the observatory

As a consequence of the extremely demanding seismic requirements the Einstein Telescope will be located underground at a depth of about 200 m to 300 m. In the complete configuration it will consist of three nested detectors, each in turn composed of two interferometers. Selecting the geometry of an equilateral triangle, where each side of the triangle is simultaneously used by two detector arms, allows the determination of the polarisation of the gravitational wave (for a given source location) and optimises the usage of the tunnels. The topology of each interferometer will be the dual-recycled Michelson layout with Fabry-Perot arm cavities. An artist's impression of the Einstein Telescope is shown in figure 1.14.

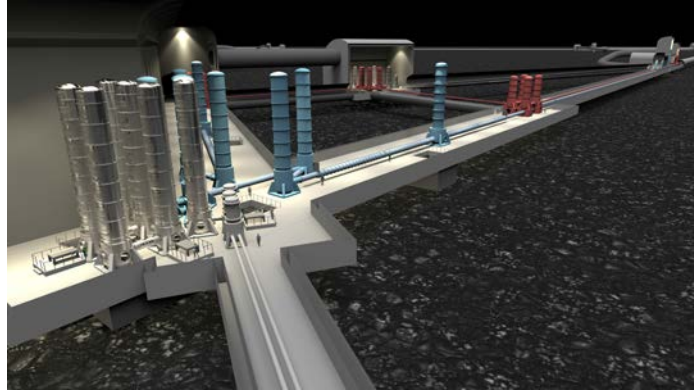


Figure 1.14: Artistic view of the ET layout.

The final site selection will be based on geological surveys and other nonscientific factors of influence (e.g. political, financial, interest of local parties, vicinity to research institutions).

For the desired sensitivity an overall length of arm cavities of about 10 km is required. More specifically, as depicted in figure 7.8, in this document we assume 10 km for the arm cavity length, a separation between the end mirrors of the cavities of one interferometer and the inner cavity mirrors of the other "tunnel-sharing" detector of approximately 300 m and some space for cryogenic baffles and mode matching telescopes of about 100 m (matching the large beam size from the interferometer arms to smaller beams in the beam splitter area). This gives a total triangle side length of about 10.5 km and an overall tunnel length for the Einstein Telescope Observatory of 31.5 km. Another tunnel of almost 1 km in length serves for remote placing of water pumps and hosting filter cavities for generating frequency dependent squeezed light.

The main, about 10 km long tunnels along the observatory arms will have an inner diameter of 6.5 m (see section 7.3.1). Access to the underground detectors is foreseen via vertical shafts (see figure 7.10, 7.9) or inclined access ramp tunnels, which will be determined in a technical design phase after site selection. Inclined tunnel access may be favourable if local regulations prevent the surface entrance to be close to the vertex stations.

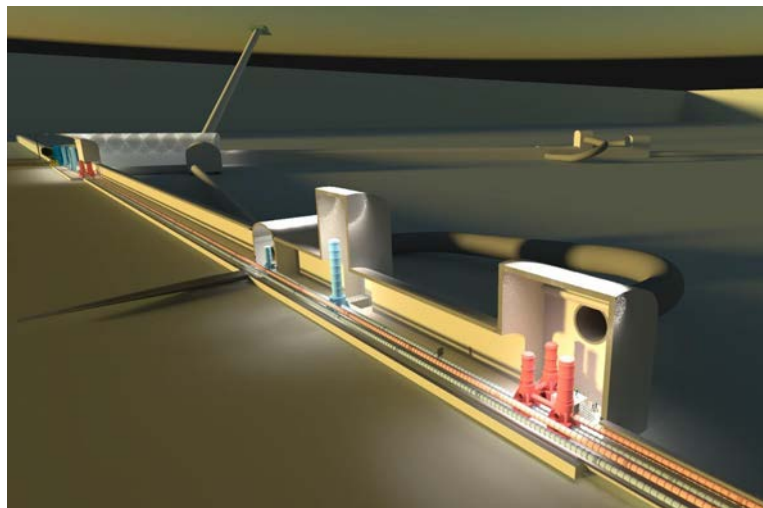


Figure 1.15: Artistic impression of the underground arrangement of tunnels and caverns. For details see section 7.3.1.

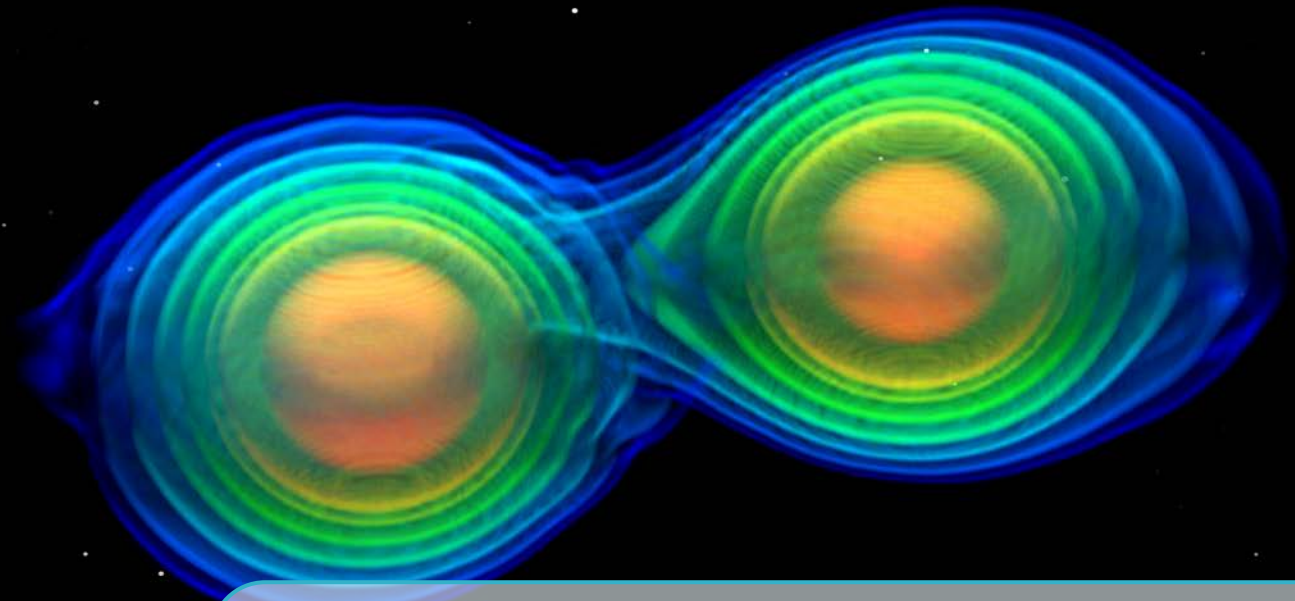
The ET infrastructure will house the observatory for several decades, during which the interferometers will be upgraded as technology advances. Some of these changes may mean that the positions of mirrors and with it the vacuum tank positions will have to be shifted, as we have seen in the upgrades from the 'initial' to the 'advanced' generation of detectors. Within the limits of feasibility the size and shape of the caverns must grant this flexibility.

Above ground, at the entrances to the underground infrastructure, facilities housing workshops, offices, apartments, technical facilities providing cryogenic fluids, air conditioning and venting, emergency electricity generators, etc. will be set up. One major aspect of the design of the total infrastructure is to provide an environment able to house not only the basic initial version of the Einstein Telescope that we describe in this document but also be versatile enough to accommodate upgraded versions in the decades to come.

**Part I**

**SCIENCE CASE**





## 2. Science case introduction

The gravitational-wave (GW) detectors of second generation (2G), the Virgo and LIGO detectors, have truly opened a new window on the Universe. The first direct detection of GWs from a binary black hole (BH) coalescence, in September 2015 [21], was a historic moment, and the culmination of decades of efforts from a large community. Another historic moment was the first detection of a neutron star (NS) binary coalescence, together with the simultaneous detection of the associated gamma-ray burst, and the subsequent observation of the electromagnetic counterpart in all bands of the electromagnetic spectrum [35–42]. A number of additional detections have taken place since, to the extent that, at the current level of sensitivity of 2G detectors, BH-BH detections take place on a weekly basis. Many remarkable results in astrophysics and in fundamental physics have already been obtained thanks to these first detections. To mention only a few highlights, the observation of the NS-NS binary coalescence GW170817 solved the long-standing problem of the origin of (at least some) short gamma ray bursts [35, 43, 44]; the observations of the associated kilonova revealed that NS-NS mergers are a major formation site of the heaviest elements through r-process nucleosynthesis [45–48]; the observation of tens of BH-BH coalescences has revealed a previously unknown population of stellar-mass BHs, much heavier than those detected through the observation of X-ray binaries [49], and has shown that BH-BH binaries exist, and coalesce within a Hubble time at a detectable rate. Concerning fundamental physics, cosmology and General Relativity (GR), the observation of the GWs and the gamma-ray burst from the NS-NS binary GW170817 proved that the speed of GWs is the same as the speed of light to about a part in  $10^{15}$  [38]; the GW signal, together with the electromagnetic determination of the redshift of the source, provided the first measurement of the Hubble constant with GWs [50]; the tail of the waveform of the first observed event, GW150914, showed oscillations consistent with the prediction from General Relativity for the quasi-normal modes of the final BH [51]; several possible deviations from GR (graviton mass, post-Newtonian coefficients, modified dispersion relations, etc.) could be tested and bounded [51–53].

Extraordinary as they are, these results can however be considered only as a first step toward our exploration of the Universe with GWs. Third-generation (3G) GW detectors, like the Einstein

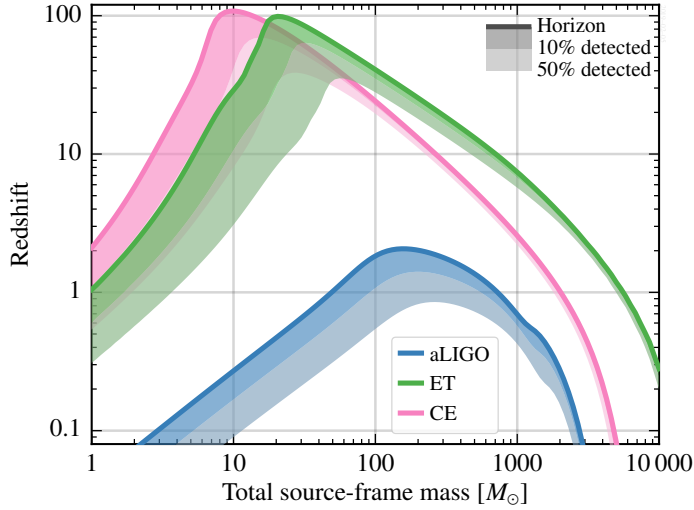


Figure 2.1: Astrophysical reach for equal-mass, nonspinning binaries for Advanced LIGO, Einstein Telescope and Cosmic Explorer (from ref. [2, 3]).

Telescope, will bring the gravitational wave astronomy revolution to a full realisation. Thanks to an order of magnitude better sensitivity and a wider accessible frequency band with respect to 2G detectors, 3G detectors will allow us to address a huge number of key issues related to astrophysics, fundamental physics and cosmology.

An example of the extraordinary potential of 3G detectors is provided by Fig. 2.1, which shows the detector reach, in term of cosmological redshift, as a function of the total mass of a coalescing binary. We see that the coalescence of compact binaries with total mass (20 – 100)  $M_{\odot}$ , as typical of BH-BH or BH-NS binaries, will be visible by ET up to redshift  $z \sim 20$  and higher, probing the dark era of the Universe preceding the birth of the first stars. (In particular, BH-BH mergers seen at such distances would necessarily have a primordial origin.) By comparison, in the catalog of detections from the O1 and O2 Advanced LIGO/Virgo runs, the farthest BH-BH event is at  $z \simeq 0.5$ , while, in the O3 run, the recently announced detection GW190521 is at  $z \simeq 0.8$ . At final target sensitivity, 2G detectors should reach  $z \simeq 1$  for BH-BH with component mass of about 30  $M_{\odot}$ . The range of BH masses accessible will also greatly increase; as we see from Fig. 2.1, ET will be able to detect BHs with masses up to several times  $10^3 M_{\odot}$ , out to  $z \sim 1 - 5$ .

For NS-NS binaries, whose total mass is around 3  $M_{\odot}$ , ET will reach  $z \simeq 2 - 3$ ; by comparison, the NS-NS binary GW170817 was at  $z \simeq 0.01$  and, at final target sensitivity, 2G detectors should reach  $z \simeq 0.2$ .

The corresponding detection rates will be impressive, of order  $10^5 - 10^6$  BH-BH and  $7 \times 10^4$  NS-NS coalescences per year for a single detector such as ET [54–56]; depending on the network of electromagnetic facilities operating at the time of 3G detectors, over a few years one might collect  $O(10^2 - 10^3)$  NS-NS GW events with observed electromagnetic counterpart [56]. The signal-to-noise ratio of many of these events will be huge, which will allow us to determine the shape of the gravitational wave with exquisite precision.

*The combination of distances and masses explored, sheer number of detections, and detections with*

*very high signal-to-noise ratio will provide a wealth of data that have the potential of triggering revolutions in astrophysics, cosmology and fundamental physics.*

Beside coalescing binary systems, ET will be able to detect several other kinds of signals, such as stochastic backgrounds of GWs, signals from isolated pulsars, or supernovae, with a sensitivity that improves by an order of magnitude compared to 2G detectors.

As we shall see, there are several spectacular goals that can only be achieved through the detection of gravitational waves with a 3G detector like ET, and other planned 3G detectors like Cosmic Explorer in the U.S. For other goals, GW detectors are complementary to facilities exploiting electromagnetic radiation or other messengers, such as neutrinos and cosmic rays. Combined observations through GWs, electromagnetic signals, neutrinos and/or cosmic rays, will give us a multi-messenger and more comprehensive picture of many energetic phenomena of the Universe. Schematically, we can identify the following main items as part of the ET science case:

- Astrophysics
  - Black hole properties: origin (stellar vs. primordial), evolution, demography.
  - Neutron star properties: interior structure (QCD at ultra-high densities, exotic states of matter), demography.
  - Multi-messenger astronomy: nucleosynthesis, physics of jets, role of neutrinos.
  - Detection of new astrophysical sources of GWs: core collapse supernovae, isolated neutron stars, stochastic background of astrophysical origin.
- Fundamental physics and cosmology
  - The nature of compact objects: near-horizon physics, tests of no-hair theorem, exotic compact objects.
  - Dark matter: primordial BHs, axion clouds, dark matter accreting on compact objects.
  - Dark energy and modifications of gravity on cosmological scales.
  - Stochastic backgrounds of cosmological origin and connections with high-energy physics (inflation, phase transitions, cosmic strings, ...)

It should be stressed, however, that many questions cross the borders between domains outlined above. For instance, understanding whether the BHs observed by GW detectors are of stellar or primordial origin obviously has an astrophysical interest, but a primordial origin would have deep consequences on our understanding of early Universe physics, inflation, etc., subjects that belong to the domain of cosmology and of fundamental physics. As another example, determining the equation of state in the core of neutron stars is of great importance both in astrophysics and for understanding the theory of strong interactions, QCD, in the regime of ultra-high density, where phase transitions can take place.

In the following sections we discuss some of the science that ET will be able to address, following [57]. We will conclude with a summary of the Key Science Objectives in Section 5, underlying in particular what science a single ET observatory can achieve. A more detailed discussion of the science of 3G detectors will be presented in [3].





## 3. Astrophysics

### 3.1 Black hole binaries

Observationally, BHs have been first identified through X-ray binaries - binary systems in which a BH accretes matter from a companion star. The remarkable GW detections of LIGO and Virgo in the O1 and O2 runs, and the first results that are being published from the O3 run, have then revealed a whole new population of stellar-mass binary BHs with much higher masses, see Fig. 3.1.

With BH-BH and BH-NS coalescence, 3G detectors will explore the Universe to extraordinary depths, providing an unobstructed view on the earliest Universe up to the dark ages, and generally with higher SNR signals compared to current EM observations from these early times.<sup>1</sup> *ET will uncover the full population of coalescing stellar and intermediate mass BHs in the Universe, over the whole epoch since the end of the cosmological dark ages.* This will allow ET to answer several key questions about the origin and evolution of BH-BH systems. In particular:

(1) The ET observations of BH-BH binaries across the whole epoch of star formation would contain evidence, accessible in no other way, of the cosmic history of stellar evolution, including the earliest populations of stars formed in the Universe. Since it is expected that compact-object formation is a metallicity-dependent process, that information will be complementary to improving electromagnetic constraints on the star-formation history of the Universe. The fact that ET will observe BH-BH mergers beyond the reionization epoch, at  $z \geq 6$ , will enable the determination of features such as the masses of the first metal-poor progenitor stars, and the relation between star metallicity and BH masses.

(2) GW observations of BH-BH binaries probe the physics of BH formation in situations which lead

---

<sup>1</sup>To understand how this is possible, it is useful to recall that a BH-BH coalescence such as the first detected event, GW150914, converted into GWs an energy of  $3M_{\odot}c^2$  in just the last few milliseconds of the coalescence. The peak luminosity of the event,  $3.6 \times 10^{56}$  erg/s, or  $200 M_{\odot}c^2/s$ , was an order of magnitude larger than the estimated combined electromagnetic luminosity of all star and galaxies in the observable Universe!

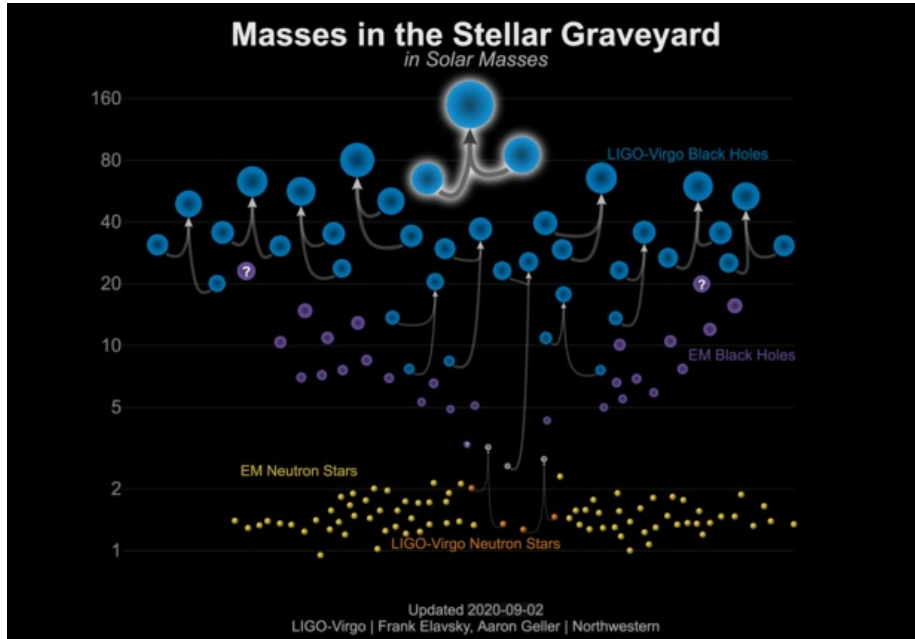


Figure 3.1: Black holes detected through electromagnetic observations (purple), black holes measured by gravitational-wave observations (blue), neutron stars measured with electromagnetic observations (yellow), and neutron stars detected through gravitational waves (orange). GW190521 is highlighted in the middle of the graphic as the merger of two black holes that produced a remnant that is the most massive black hole observed yet in gravitational waves. Image credit: LIGO-Virgo/ Northwestern U. / Frank Elavsky and Aaron Geller. Image taken from <https://www.ligo.caltech.edu/image/ligo20200902a>.

to mergers. ET will provide some events with extraordinarily well-measured properties, alongside large samples of mergers from which statistical population characteristics can be extracted. This will allow us to understand how binary evolution results in BH-BH mergers, and will give information on several aspects of the dynamics of binaries, such as the impact of the common envelope phase in the progenitor binaries, or the role of the dynamics of star clusters and galactic nuclei in producing close binaries of compact objects.

(3) Thanks to the fact that the reach of ET for BH-BH systems is well beyond the peak of the star formation at  $z \sim 2$ , by comparing the redshift dependence of the BH-BH merger rate with the cosmic star formation rate it will be possible to disentangle the contribution of BHs of stellar origin from that of possible BHs of primordial origin (whose merger rate is not expected to be correlated with the star formation density). Moreover, BH-BH systems of stellar origin are expected to form in galaxies, while primordial systems should trace the distribution of dark matter rather than that of baryons. The huge number of detections in ET will allow to perform cross-correlations between the detected GW events and large-scale structures, providing another clue to the origin of the observed BHs. *Showing that at least a fraction of the observed BHs are of primordial origin would be a discovery of fundamental importance not only in astrophysics but also from the point of view of fundamental physics.* Primordial BHs of mass around a solar mass could have formed at the QCD quark-hadron transition via gravitational collapse of large curvature fluctuations generated during the last stages of inflation [58]. This could explain not only the present abundance of dark matter but also the baryon

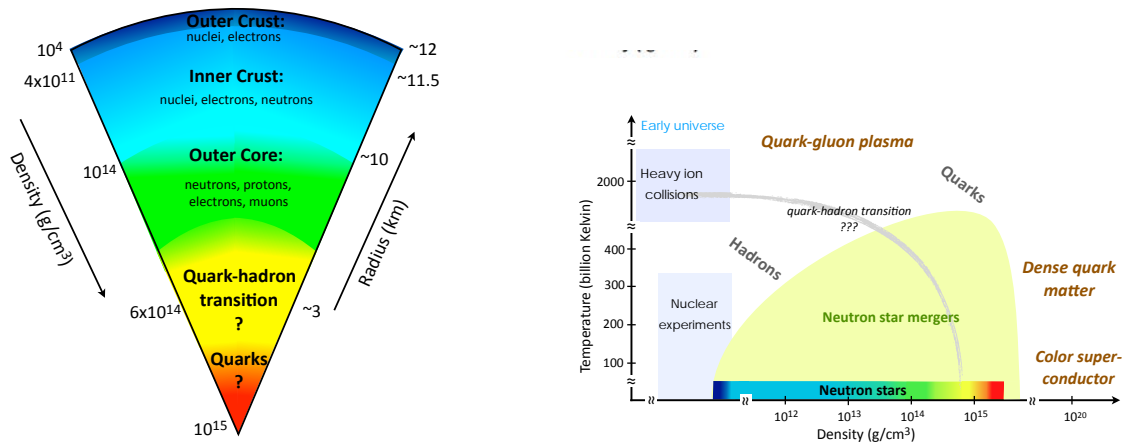


Figure 3.2: Left: Conjectured interior structure of a neutron star. Right: Matter encountered in neutron stars and binary mergers explores a large part of the QCD phase diagram in regimes that are inaccessible to terrestrial collider experiments.

asymmetry of the Universe [59]. The large number of binary BH detections with ET, as a function of mass and redshift, would also allow us to obtain detailed characterization of the population of primordial BHs, their mass and spin distributions and their formation times as a function of mass, as well as their clustering properties, as inferred from their merger rates and the induced stochastic GW background [60–62].

(4) The discovery of luminous quasars at redshift as large as  $z \sim 7$  suggests that, at  $z > 7$ , there should be a population of ‘seed’ BHs, with masses in the range  $(10^2 - 10^5)M_\odot$ , from which these supermassive BHs have grown through gas accretion. Furthermore, possible seed BHs that were in an environment such that further growth by gas accretion was suppressed could be present at smaller redshifts, with masses close to their initial values. As we see from the left panel of Fig. 2.1, ET has the sensitivity necessary to detect BH binary systems containing a BH with mass between  $O(10^2)M_\odot$  and a few times  $10^3 M_\odot$ , up to large redshifts. ET could therefore detect these seed BHs, providing crucial missing links in the formation and evolution of structures in the early Universe, and unraveling the possible connection between stellar-mass black holes and supermassive black-hole in the center of the galaxies.

### 3.2 Neutron stars

Neutron stars (NSs) are extraordinary laboratories for studying the fundamental properties of subatomic matter under conditions far from the realm accessible to experiments and first-principles theoretical calculations. In NSs, intense gravity compresses matter to several times the density of an atomic nucleus. Predicting the composition of such matter and the multi-body interactions providing sufficient pressure to prevent utter collapse to a BH requires large extrapolations from known physics and has been a longstanding scientific frontier. The left panel in Fig. 3.2 illustrates the conjectured interior structure of NSs, spanning a vast range in density. Near the surface of a NS, neutron-rich nuclei and free electrons dominate, while at higher densities towards the interior the nuclear structure

dissolves into primarily a uniform liquid of neutrons. In the cores of NSs yet more exotic states of matter may emerge, such as condensates of particles containing strange quarks. In addition, the quark substructure of the hadrons is expected to become important at densities a few times nuclear density, where states of matter comprising de-confined quarks may appear [63]. The properties and parameter space of the transition between nuclear and quark matter and the states of quark matter encountered at low temperature, in the interaction-dominated ground state of dense matter, have been key questions in subatomic physics. Neutron stars thus provide a unique window onto the behavior of QCD, the fundamental theory of strong interactions, in a regime complementary to the higher temperatures and lower baryon densities accessible in collider experiments that probe the quark-gluon plasma.

A complete understanding of the entire QCD phase diagram requires a synergy of the complementary insights gained from the terrestrial heavy-ion collision experiments and the astrophysical collisions of two NSs at close to the speed of light driven by dynamical gravity. In such NS mergers, matter encounters yet higher densities and temperatures than in individual NSs, thus providing a window onto a completely unexplored regime of subatomic physics. The right panel in Fig. 3.2 shows the regimes in the QCD phase diagram relevant to NS binaries, which occupy a large swath of unexplored parameter space and a complex nonperturbative regime between our current understanding of matter at low baryon densities from nuclear physics at low temperature and heavy-ion collisions at higher temperatures, and the extremely high-densities where quark-matter calculations are valid.

The fundamental properties of NS matter give rise to characteristic imprints in the GW signals from NS binaries or individual asymmetric NSs, making GWs unique probes of subatomic physics in unexplored regimes. A 3G GW detector with a high sensitivity and large frequency bandwidth such as ET will be critical to shed light on important fundamental physics questions, by precisely determining the properties of cold, dense matter in NSs as well as the new physics encountered during a binary NS merger.

### 3.2.1 Coalescing neutron star binaries

With 2G detectors, the first observed NS-NS coalescence GW170817 demonstrated that useful limits on the NSs' tidal deformability, a characteristic parameter that depends on the properties of matter in their interiors, could be extracted from the inspiral part of the GW signal [35]. However, despite the proximity of GW170817, the inferred constraints on the equation of state of NS matter [64] are too weak to discriminate between realistic models, nor do they offer new insights about phase transitions [65–67].

To determine in detail the nature of matter and interactions in NS interiors requires measuring tidal deformability with an order of magnitude higher accuracy. In addition, such high-fidelity measurements must be obtained for a population of NSs spanning a wide range of masses to map out the parameter dependencies and identify potential signatures of phase transitions. Both can be achieved with ET, which, as discussed in sect. 2, will detect a huge number of NS-NS coalescences, of order  $7 \times 10^4$  per year, and will observe their signal with orders of magnitudes higher accuracy. As an example, an event like the first observed coalescing NS-NS binary, GW170817, would be seen at ET with a signal-to-noise ratio larger than the one of the event actually observed in LIGO/Virgo by a factor  $O(50)$ , resulting in an overall signal-to-noise ratio as large as  $\sim 1700$ . This sensitivity could even allow us to access magnetic and rotational tidal Love numbers of the component neutron

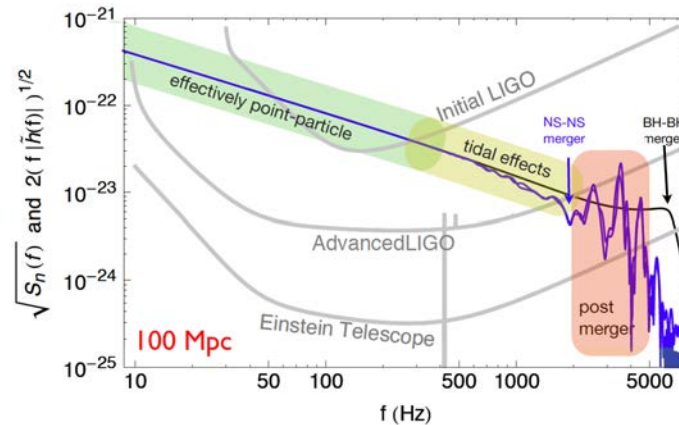


Figure 3.3: Gravitational wave signal from a NS-NS merger at a distance 100 Mpc, as it sweeps across the detector-accessible frequency range. From [4] (figure courtesy of Jocelyn Read, based on results presented in [5]).

stars [68].<sup>2</sup>

The high-accuracy measurements performed with a 3G detector will also enable us to discern subdominant signatures of matter in GWs from binary inspirals that are inaccessible with 2G instruments. Such effects encode key information on details of the fundamental physics in NS interiors that are not probed directly with the tidal deformability. For instance, detecting GW signatures from the tidal excitation of a NS’s internal oscillation modes during an inspiral, as will likely be possible with ET, would provide an unprecedented spectroscopic view of NS interiors and reveal exquisite details about the existence and nature of phase transitions to new states of matter.

A further unique capability of 3G detectors such as ET with a high sensitivity extending to frequencies in the kHz range is to open the major new scientific discovery space of matter phenomena beyond the inspiral. Witnessing the tidal disruption of a NS by a BH for a variety of systems will yield further insights into the properties of NS matter under extremes of gravity, and tracking the violent collision of two NSs and its aftermath will provide an exceptional window onto fundamental properties of matter in a completely unexplored regime, at higher temperatures and yet greater densities than encountered in individual NSs.

The outcome of a binary NS merger strongly depends on the parameters. It is either a short-lived hypermassive NS that is temporarily stabilized by rotational effects yet ultimately collapses to a BH, or a BH that forms immediately upon merger, or a temporary supra-massive NS that settled to a NS remnant. The emitted GWs are distinct for the different scenarios and contain copious information on the complex microphysics. To fully capitalize on the enormous science potential with GWs from NS binaries systems will require accurately measuring both the GWs from the inspiral that determine the progenitor properties (e.g. masses, spins, cold NS matter, orbital eccentricity) and the GW signatures of the new physics encountered at the merger and its aftermath, as 3G detectors such as ET will enable. Figure 3.3 illustrates the potential of ET for detecting these effects, compared to current 2G detectors, for a NS binary at a typical distance of 100 Mpc (see also [69]). The current 2G detectors

<sup>2</sup>The ‘Love numbers’ parametrize the axial and polar perturbations of the metric generated by a compact body, when the body is perturbed by an external gravitational field, see sect. 14.4.1 of [4].

are largely limited to observing the long inspiral, dominated by the center-of-mass dynamics of the NSs, with glimpses of the tidal effects which become important at higher frequencies, and are insensitive to the details of the merger and post-merger epochs. By contrast, a detector such as ET, besides observing the inspiral phase and the onset of tidal effects with much higher signal-to-noise ratio, will also clearly observe the final merger and post-merger signals and enable detailed insights into the fundamental properties of nuclear matter in a large swath of unexplored regimes in the QCD phase diagram.

The coalescence events of NS-NS and NS-BH systems also have key significance as the production site of elements heavier than iron in the cosmos. Heavy elements can be synthesized from the neutron-rich material expelled during the merger or tidal disruption of NSs or through winds from the remnant accretion disk. The subsequent radioactive decay of the freshly synthesized elements powers leads to an electromagnetic transient known as a kilonova. Multi-messenger observations of a large sample of NS binaries will provide the unique opportunity to study heavy element formation at its production site, to determine how the initial conditions of an astrophysical binary system map to the final nucleosynthetic yields, and the extent to which different NS binary progenitors contribute to the cosmic abundances over time.

*In summary, the greater sensitivity and larger frequency bandwidth of a detector such as ET will be critical to observe a diverse population of NS binaries, accurately measure GW signatures of matter during the inspiral, and probe details of the merger and post-merger phenomena. These measurements are essential to substantially advance frontiers of subatomic physics by determining (1) the properties of cold, dense matter in NSs, (2) the new physics encountered during a binary NS merger, at higher temperatures and more extreme densities, and (3) the formation of heavy elements in the cosmos from synergies with electromagnetic observations.*

### 3.2.2 Continuous waves from spinning neutron stars

A spinning NS, isolated or in a binary system, can also emit continuous semi-periodic GWs if asymmetric with respect to its rotational axis [4]. Such asymmetry can derive from frozen deformations produced right after its violent birth, from a strong enough inner magnetic field (provided it is not aligned with the rotation axis), from non-axisymmetric motions or density perturbations due, for instance, to Ekman flow or to the excitation of normal modes associated to the star rotation, such as the so-called r-modes, or due to thermal or composition gradients induced by matter accretion from a companion star [70].

No continuous gravitational wave signal has so far been observed by Advanced LIGO and Advanced Virgo, see e.g. [71–76] for recently obtained upper limits. The maximum degree of deformation that a NS can sustain depends on the equation of state: for standard equations of state the maximum value of the ellipticity is  $\epsilon_{max} \sim 10^{-6}$  [77], but for exotic objects, containing hyperons or quark matter, is expected to be much higher,  $\epsilon_{max} \sim 10^{-4} - 10^{-3}$  [78]. In practice, it is difficult to predict the actual deformation of a specific NS, that can depend on the star's history and could be well below the maximum sustainable value. A recent argument [79] suggests that the typical spin-down of millisecond pulsars can be explained assuming a typically ellipticity of about  $10^{-9}$ .

Figure 3.4 (which is an updated version of that shown in [80]) shows the minimum detectable ellipticity (at 90% confidence level) for currently known NSs potentially emitting in the detector band,

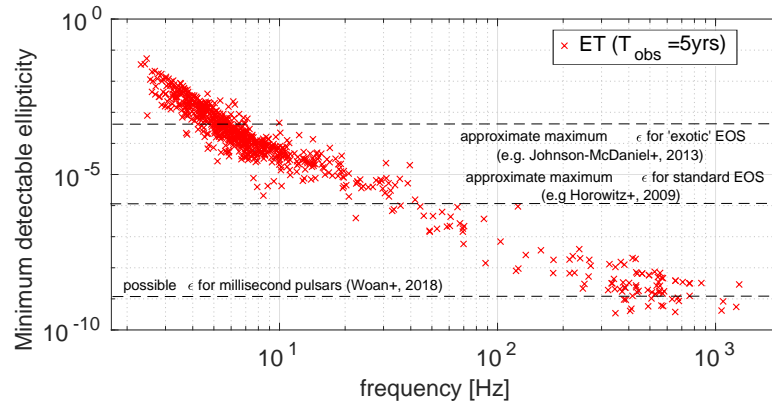


Figure 3.4: Minimum ellipticity detectable by ET at 90% confidence level in a full coherent search of continuous waves from known pulsars, assuming an observation time  $T_{\text{obs}} = 5$  yr.

assuming two proposed ET configurations and that a full coherent matched filter analysis is done over an observation time  $T_{\text{obs}} = 5$  yr; we see that ET will be sensitive to ellipticities of the order of few times  $10^{-10}$  for the nearest millisecond pulsars, and of  $\sim 10^{-6} - 10^{-7}$  for young pulsars. To produce this plot we used the minimum detectable signal strain amplitude at 90% confidence level,  $h_{\text{min}}$ , which is given -when matched filter is used- by  $h_{\text{min}}(f) \approx 10\sqrt{S_n(f)/T_{\text{obs}}}$ , where  $S_n(f)$  is the detector noise spectral density (measured in 1/Hz) at the frequency  $f$ . Hence, by exploiting the relation between the signal amplitude and the source ellipticity, at known distance and emission frequency (see eq. 5 of [81]), the minimum detectable ellipticity can be computed. *It is quite impressive to realize that detecting GWs due to an eccentricity of, say,  $\epsilon = 10^{-10}$  in a NS means that we would detect the effect due to a “mountain” on a NS, with a height of about  $10^{-10} \times 10 \text{ km} = 10^{-3} \text{ mm}$ .* Given the expected variety of ellipticities in NS (which depend also on their past history) the limits obtained from the whole Galactic population will be much more significant than current upper limits from specific pulsars.

Figure 3.5 shows the maximum distance at which a continuous wave source would be detected, by making a full coherent search over an observation time  $T_{\text{obs}} = 5$  yr, as a function of its ellipticity for different values of the signal frequency, assuming that the source spin-down is dominated by the emission of GWs. In this case by equating the signal amplitude to the minimum detectable value  $h_{\text{min}}$ , we can obtain the maximum distance as a function of the source ellipticity for any given initial value of the signal frequency. It is worth to stress that a neutron star spinning at say 50 Hz (and then emitting a continuous GW signal at 100 Hz) would be detectable in the whole Galaxy as long as its ellipticity is larger than  $10^{-7}$ . Very fast spinning and highly distorted neutron stars, such as newborn magnetars produced in core collapses or as post-merger remnants of coalescing binaries, could lead to detectable emission at even higher frequencies. In this case the signal can only be observed for a shorter time, since these objects are characterized by a very high spin-down and the signal frequency eventually leaves the detector sensitivity band within a few days. However, at birth they could have ellipticities as large as  $10^{-3}$  [82] so, even taking into account uncertainties in the data analysis due to the very large initial parameter space (initial frequency, spin-down, braking index), these objects could still be detected out to distances of tens of Mpc [83].

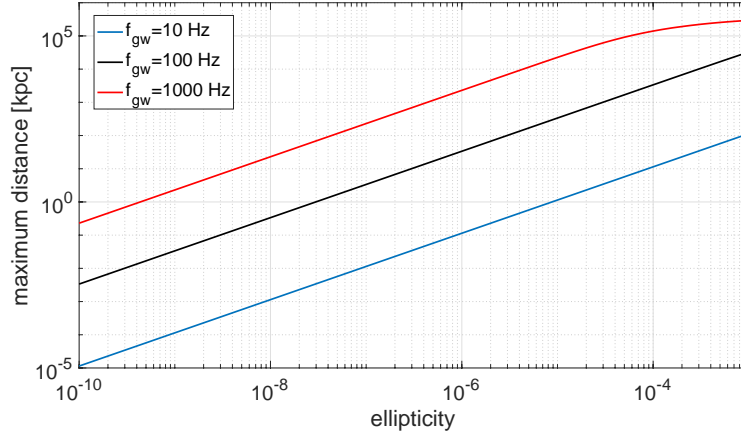


Figure 3.5: Maximum distance at which a continuous wave source would be detected in a full coherent search over  $T_{\text{obs}} = 5$  yr as a function of the source ellipticity, for three different values of the initial signal frequency, for the ET detector. Here we make the assumption that source spin-down is dominated by the emission of GWs and that matched filtering is used in the analysis.

The detection of continuous signals from spinning neutron stars will represent a complementary tool to the merger and post-merger signal for the study of the NS interior, especially if concurrent electromagnetic observations are available. It will also provide clues about NS formation and demography, their spin, thermal and possibly magnetic field evolution.

It is also important to observe that, even for a single detector such as ET, the prolonged observation of the continuous signals from a NS allows, over the time of months, to localize it with extremely good accuracy, exploiting the movement of the Earth during the observation time. The angular resolution, for a source emitting a signal at frequency  $f_{\text{gw}}$ , and observed over a timescale  $T_{\text{obs}}$ , is about  $3 \times 10^{-6} (100 \text{ Hz}/f_{\text{gw}}) (1 \text{ yr}/T_{\text{obs}})$  rad [84].

Low-Mass X-ray Binaries (LMXB) are another very interesting target for ET, under the assumption that a balance among angular momentum accreted through matter infall and the emission of GWs exists. In this scenario, by comparing the signal amplitude given in [85] to the planned ET sensitivity curve, we see that at least one LMXB, namely Sco-X1, would be detectable by ET if the unknown star rotation frequency lies in its observation band.

*In summary, the detection of continuous GWs from NS by ET would be a fundamental breakthrough, that would provide clues about the condition of formation of isolated NS, their spin, thermal evolution and magnetic field. Furthermore, detecting such a signal would again give information on the inner structure of NS and on the corresponding aspects of nuclear and particle physics, such as the existence of exotic matter in the NS core.*

### 3.2.3 Burst signals from neutron stars

Neutron stars can also emit transient bursts of GWs in association, for instance, with magnetar giant flares and pulsar glitches. Magnetars are NSs endowed with a very strong magnetic field of  $10^{14}$  G or more, and are observed as anomalous X-ray pulsars (AXP) or soft gamma-ray repeaters (SGR) [86].

SGRs are characterized by recurrent short-duration X-ray bursts and more energetic giant flares ( $10^{44} - 10^{47} \text{ erg s}^{-1}$  in  $\sim 0.1$  s), due to global rearrangement of the inner magnetic field or of the magnetosphere. These events can induce a significant structural changes in the NS, or excite polar oscillations, like the f-modes, causing an emission of GWs. The strongest pulsar glitches, like those of the Vela pulsar, are explained as due to the occasional “unpinning” of quantized superfluid vortices in the interior of the spinning-down NS, which move outward and release their angular momentum. The prediction on the emission of GWs are, however, still not robust due to the lack of a detailed knowledge of the process. Moderately optimistic models predict that these signals can be detected by ET.

### 3.3 Multi-band and multi-messenger astrophysics: synergies with other gravitational-wave detectors and electromagnetic/neutrino observatories

ET, with its triangular configuration corresponding to three nested interferometers, is designed so to have an extraordinary science output even when operated as a single GW detector. However, a further enhancement of its capabilities will take place when it operates in synergies with other observatories.

#### 3.3.1 Networks of ground-based gravitational-wave detectors

The first obvious synergy is with other GW detectors, either with a network of 2G GW detectors (LIGO Livingston, Hanford and India, Virgo, and KAGRA), or with another third-generation detector such as Cosmic Explorer (CE), currently under study in the US [87, 88] (possibly in a network configuration with one ET and two CE detectors). A first important benefit from coincident detections in multiple detectors will be the reduced impact of instrumental glitches on GW detections and analyses.<sup>3</sup> These problems affect, in particular, short duration transients lasting a few milliseconds - especially the unmodeled ones - while it will be less problematic for the signals associated to the coalescence of BHs or NSs binary systems, thanks to the relatively long duration of the signals in the sensitivity band of the detectors.

A network of detectors, compared to a single detector, will also improve significantly the accuracy in the localization of the sources. As we already mentioned, for the continuous GWs emitted by spinning NSs, a single ET detector already provides a very accurate parameter estimation - including position - thanks to the very specific modulation of the signals due to Doppler effect induced by the Earth motion. For coalescing NS-NS binaries, a single ET detector still has some localization capability. Low-mass system, such as a binary NS, can be observed for up to a few days, and also in this case, the modulation due to Earth’s rotation helps to localize the source. The average sky-localization is around  $150 \text{ deg}^2$  for a binary NS at  $z = 0.1$ , but it can become of order of just a few  $\text{deg}^2$  for the best localized sources [89, 90]. Even for BH-NS binaries, in the best cases, ET alone can provide a localization better than  $10 \text{ deg}^2$ . Poor localization will in general be available for massive BBHs; because of their higher total mass, they will stay in the detector bandwidth for a much shorter time. A network of three 3G GW detectors, in contrast, will have quite good localization accuracy for all types of binary coalescences; for example, a large fraction of NS-NS

---

<sup>3</sup>Actually, a single ET triangle might already provide a good enough background rejection through its null stream. However, this is not 100% efficient due to possible correlations between instrument noise in different ET interferometers.

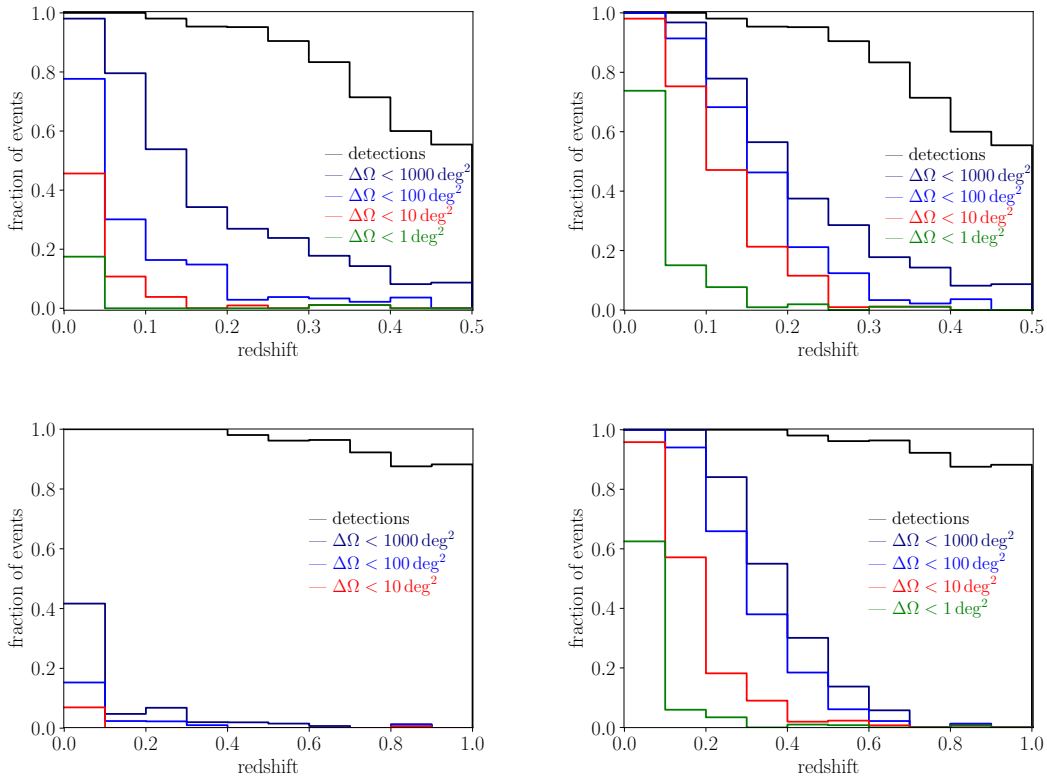


Figure 3.6: Localization errors of BNSs and BBHs per redshift bin. Top: BNS. Bottom: BBH. Left: ET alone. Right: ET together with currently foreseen future upgrades of Advanced LIGO Hanford, Livingston, India, Advanced Virgo, and KAGRA. We impose a conservative ET detection threshold SNR of 12, and for the plots in the right column that at least one 2G detector has SNR  $> 4$  to include 2G data for the sky localization. Duty cycle is taken 100% for all detectors.

binaries will have sky localization smaller than  $1 \text{ deg}^2$  up to  $z = 0.5$  [91]. In terms of science output, this means that a 3G detector network will be able to provide good localization information to electromagnetic observatories, making possible the detection of an electromagnetic counterpart. However, the detection of a kilonova associated with a NS-NS binary merger will be limited by the optical telescope capabilities, as we will discuss in more detail in Section 3.3.2. Even for the largest telescopes operating in the optical or infrared, such as the 39-m E-ELT [92], it will be difficult to observe the kilonova beyond  $z \sim 0.5$  photometrically, and beyond  $z \sim 0.3$  spectroscopically [93, 94] (see for example <http://www.mosaic-elt.eu/index.php>). Furthermore, the direct detection with these large telescopes will be possible only for arcmin-arcsec localized sources. For more distant NS-NS mergers, the electromagnetic counterpart detection would be possible through the associated emission of gamma-ray bursts. Accurate localization would be also important in order to use statistical techniques, such as those based on the probabilistic determination of the redshift of the associated galaxy [95, 96], as well as on cross-correlations between binary coalescences and large-scale structures [97, 98]. These statistical techniques will be important for the cosmological studies which will be discussed in Section 4.3.

ET is also expected to operate with a network of five 2G GW detectors: LIGO Livingston, Hanford and India, Virgo, and KAGRA. Assuming currently foreseen sensitivity increase of 2G detectors from the implementation of technology upgrades [99], the improvement of the sky localization of this network compared to ET alone is shown in Fig. 3.6. The top row is for binary NSs, while the bottom row is for binary BHs. We obtained these results from a Fisher-matrix analysis based on a time-domain simulation of the GW signals to incorporate the effect of a rotating Earth, which is fundamental to the sky-localization capability of a single ET detector. Accordingly, about 80% of BNS mergers in  $0.05 < z < 0.1$  will be localized within  $10 \text{ deg}^2$  in such a network, while ET alone achieves for a similar fraction of BNS mergers better than  $1000 \text{ deg}^2$  localization errors in the same redshift bin. Note that the 2G network has a significant impact on sky-localization of BNSs up to redshifts of 0.3. It is also remarkable that a single ET detector is able to provide good sky localization at least for a small fraction of the closest BBHs.

The different sensitivity curves planned for ET and CE imply that, from other points of view, these detectors will be complementary. For instance, as can be seen from Fig. 2.1, ET will be able to detect heavier systems, with total masses higher than  $10^3 M_{\odot}$  (thanks to its sensitivity in the low-frequency regime), while CE has a greater reach for light systems such as NS-NS binaries. The different sensitivity curves also mean that, for a given astrophysical system, the signal-to-noise ratio is accumulated differently in ET and in CE, providing complementary information.

*In summary, if ET will be included in a network of 2G and 3G ground-based detectors, the science outcome could benefit from the detector synergy and complementarity increasing the number of detections, improving the sky-localization for the electromagnetic/neutrino follow-up, and increasing the information to be extracted from the signal about source progenitors and remnant.*

### 3.3.2 Joint gravitational-wave and electromagnetic observations

The discovery and electromagnetic follow-up of GW170817 showed the enormous potential of gravitational-wave observations for multi-messenger astrophysics. The gravitational-wave observations combined with the results from the extensive multi-wavelength observational campaign (still ongoing) had a huge impact on our knowledge of the physics of compact objects, relativistic jets, nucleosynthesis, and cosmology (see e.g., [43, 44, 47, 50, 100–103]). Identifying the electromagnetic signatures of the gravitational wave sources enables to maximize the science return from a gravitational-wave detection by probing strong-field gravity, matter under extreme conditions together with the interaction of the source with its environment.

*ET will detect binary systems containing neutron stars up to redshifts corresponding to the peak of the cosmic star-formation rate. This represents a step forward for studying the formation, evolution and physics of neutron stars in connection with kilonovae and short gamma-ray bursts, along with the star formation history and the chemical evolution of the Universe. Its better sensitivity and larger sample of detections will make it possible to connect progenitor and merger remnant properties to the multi-messenger emission mechanism, and to distinguish between geometric and intrinsic properties of the source. ET will operate together with a new innovative generation of observatories covering the electromagnetic spectrum from the radio to the high-energy bands. In the following we will not discuss exhaustively all the instruments which could operate with ET, but we will consider some of the main future observatories with a large involvement of the European community.*

Sensitivity (in terms of observable distances) and sky-localization capabilities of ET will determine the observatories able to effectively operate in synergy with ET. Larger sky localization and larger distance decrease the efficiency of the electromagnetic search, due to a major difficulty to find a fainter counterpart among many contaminant transient signals and many possible host galaxies. As we already mentioned, ET as single detector can localize the majority of detectable binary neutron stars at a distance of  $\leq 200$  Mpc to within a 90% credible region of  $100 \text{ deg}^2$  [89, 90]. Operating with a network of five 2G detectors, similar localization capabilities will be possible up to about 1 Gpc. Going to larger distances, the sky-localization of ET will be larger than  $10^3 - 10^4 \text{ deg}^2$  for the majority of the sources. These localizations require instruments able to monitor quickly large parts of the sky, and follow-up observations to characterize the nature of the counterpart. The Square Kilometre Array [SKA, 104], the ULtraviolet TRansient Astronomy SATellite [ULTRASAT, 105], the Vera C. Rubin Observatory, previously named as the Large Synoptic Survey Telescope [LSST, 106], THESEUS [mission concept, 107], the Cherenkov Telescope Array [CTA, 108] will be able to observe large regions of the sky from the radio, ultraviolet, optical to the X-ray and very high energy gamma-rays, going to deeper sensitivity than current observatories; 40-meters class telescope, such as the European Extremely Large Telescope [E-ELT, 94] and satellite like the Advanced Telescope for High ENergy Astrophysics [ATHENA, 109] will be able to characterize the source in the optical and X-ray band. For specific emissions and science goals, there will be two regimes: close sources (up to 400 Mpc), where we will strongly benefit of the higher sensitivity of ET and thus, with respect to 2G detectors, we will be able to better evaluate the properties of the source progenitor, merger remnant and environment interactions in single detections; and a second regime for distant sources where we will benefit of larger samples of joint electromagnetic and gravitational wave detections.

The ET sensitivity at low frequencies enables enough signal-to-noise ratio to accumulate before the merger, providing an early detection and warning for electromagnetic/neutrino follow-up. Requiring a signal-to-noise ratio  $\geq 12$  and a sky localization smaller than  $100 \text{ deg}^2$ , ET can send an early warning alert between 1 and 20 hours before the merger (with the mean of the distribution at about 5 hours) for signals at 40 Mpc [90]. At 200 Mpc, about 30% of the detectable signals will have accumulated enough SNR for early warning between 1 to 6 hours prior to the merger. About 10% of the detectable sources within 400 Mpc can still be announced with an early warning smaller than 1 hour; this percentage drops to 3% for sources at 800 Mpc, and no detection of source at 1.6 Gpc can be announced 1 hour before from the merger. Releasing an early warning increases the chance of successfully detecting the electromagnetic counterparts, by allowing astronomers to point the telescope in the region of the signal or starting the monitoring to obtain pre-merger images, which are extremely useful to discard contaminant transient objects. This enables to detect the early electromagnetic emission, which is fundamental to understand the physics of the engine and the merger remnant.

### 3.3.3 Nucleosynthesis, nuclear physics and kilonovae

The cosmic origin of elements heavier than iron has long been a mystery. GW17017 provided the first observational test to theoretical models which predict the rapid neutron capture process (r-process) nucleosynthesis during binary neutron star mergers [see e.g., 110, 47, 111]. The thermal emission observed in the ultraviolet, optical, and near-infrared detected with GW17017 was found to be consistent with kilonova emission powered by the radioactive decay of heavy nuclei (including

lanthanides) synthesized in the merger ejected by the r-process [see e.g., 45, 46, 112]. On the basis of the merger rate estimated using the LIGO and Virgo observations and the amount of ejected mass estimated by the kilonova observations, binary neutron star mergers are now understood to be a major channel of r-process production, able to explain the heavy elements abundances in the Milky Way stellar population. However, the role of rare classes of supernovae, such as the collapsars associated with long gamma ray bursts, which are expected to be an additional significant source of r-process elements [113], is still uncertain. Also, the interpretation of the kilonova emission and spectral evolution over many days is still incomplete; the contribution of the multiple ejecta (dynamical, wind, viscous, etc.) and their properties are not fully understood, as well as what are the exact elements formed and their abundance, and what the role of the merger remnant is. Only a larger sample of kilonovae, possibly extending to larger distance, will enable us to probe the details of the kilonova emission mechanism, and the role of binary neutron star mergers in the Universe enrichment of heavy elements along the cosmic history.

When ET is expected to observe the sky, the Vera C. Rubin Observatory will operate as a wide field-of-view survey able to detect kilonova emission up to 800 Mpc. Up to the same distance, photometric and spectroscopic characterization will be possible using ground-based 30–40 m telescopes such as the Thirty Meter Telescope [TMT, 114] and E-ELT, and the James Webb Space Telescope [JWST, 115]. The binary neutron star mergers detectable in this volume are of order  $10^3$  per year. Among them, a few hundred are expected to be in the Rubin Observatory surveyed field. For the majority of these sources, the gravitational-wave localization uncertainty by ET will make it difficult to identify the optical counterpart among many optical transient contaminants. However, a significant number of joint GW/kilonova detections (of order of several tens) becomes possible considering ET operating with the second generation of detectors. *For joint gravitational-wave/kilonova detection, the precision of parameter estimation for the progenitor system (total mass, mass ratio, spin, and neutron star tidal deformability) and the detection of the signal from the merger remnant made possible by ET, represent an unprecedented opportunity to understand the physics governing the kilonova emission, and the nature and equation of state of neutron stars.*

### 3.3.4 Relativistic astrophysics and short GRBs

A single ET detector, even in the absence of good source localization, will still be able to perform joint observations with gamma-ray burst (GRB) detectors, through the observation of a temporally coincident GRB. In turn, this can allow for the measurement of the redshift of the source when the high-energy satellite is capable to precisely localize the source. Indeed, GRB satellites such as the Neil Gehrels Swift Observatory [116] regularly alert ground based spectrographs to obtain the redshifts of the host galaxies of the detected GRBs. The study in [117, 56] indicates that a few tens of short GRB per year will be detected by a GRB mission such as THESEUS in coincidence with a gravitational signal in ET. Beside the collimated prompt GRB emission, more isotropic soft X-ray emission is also expected from the GRB afterglow, and from a transient powered by the rotational energy of the merger remnant when a long-lived neutron star forms. This could possibly lead to a few hundred more coincident detections per year [117].

The discovery of the gamma-ray emission associated with GW170817 and the following afterglow observations significantly improved our knowledge of short GRB jets. Approximately two seconds after GW170817, the Fermi space telescope [118] detected a weak short-duration gamma-ray burst,

GRB170817A. Even if it showed the classical observational features that led to classify it as a short GRB, its total gamma-ray energy of about  $10^{46}$  erg was many orders of magnitude smaller than the typical energy of any GRB observed before [36, 37]. Nine and sixteen days after the GW observation of the merger, X-ray and radio emissions were also detected [41, 42]. Over longer timescale the radio, optical, and X-ray observations showed a slow achromatic flux increase until about 150 days before starting to decline [119–122]. High-resolution radio observations [44, 43] were able to constrain the source size and to show a source displacement consistent with the launch of a jet which successfully breaks through the ejecta developing an angular structure, i.e. a narrow ultra-relativistic jet surrounded by less-collimated and slower material. The structured jet was observed off-axis (i.e. the observer was misaligned with respect to the collimated ultra-relativistic jet). However, while multi-wavelength observations over two years have built a broad consensus about the interpretation of the non-thermal afterglow emission, the origin of the extremely faint prompt gamma-ray emission observed far from the jet core is still under debate; a gamma-ray emission arising from the slower part of the jet or a gamma-ray emission due to a cocoon shock breakout [see e.g., 123–127].

These results have been extraordinary. Nevertheless, only a detector such as ET will have the unprecedented capability to probe in depth short GRB jet properties, by exploring up to high redshift a large population of neutron star mergers observed perpendicular to the orbital plane (on-axis) and off-axis. Mission concepts such as THESEUS will enable the detection of about 20 on-axis short GRB/year with a localization accuracy of 1-5 arcmin up to a redshift of 5 [107, 117]. After each detection, the rapid alert system will enable to point ground-based spectrographs, such as the ones in E-ELT, and satellites such as ATHENA (at least for the ones better localized). THESEUS will give the precise position of the source, and ET and the multi-wavelength follow-up will allow us to connect detailed information of the progenitors and merger remnant properties to the jet and environment properties. *It will be possible to build a statistical sample of binary neutron star mergers able to probe the shape of the jet structure, if it is universal, and what is the typical opening angle for short GRBs. It will be possible to constrain the luminosity function of short GRBs and its relation to the jet structure and the intrinsic luminosity evolution, and to understand what is the efficiency of the jet to break through the material surrounding the NS-NS mergers. ET will be crucial to identify the nature of the binary neutron star merger remnant (black-hole, unstable or stable neutron star) and how this is connected to the short GRB central engine and afterglow properties.* Finally, large sample of GW/GRB will clarify the role of NS-BH binaries as progenitor of short GRBs.

ET will guarantee that instruments such as THESEUS, the Neil Gehrels Swift Observatory, Fermi, SVOM [128] will have a gravitational-wave detection for the majority of detected on-axis short GRBs. Over a few years, it will be possible to build a sample of several tens of joint detections with luminosity distance measured by gravitational-waves and redshift measured by ground-based telescopes, such as VLT and ELT. These detections will provide precise measurements of the Hubble constant, helping to break the degeneracies in determining other cosmological parameters obtained by CMB, SNIa and BAO surveys, and to study the nature of dark energy [56]; see section 4.3 for details.

The detection of a faint off-axis gamma-ray signal, such as the one observed by Fermi and INTEGRAL [129] for GW170817, will be difficult for present and the planned future detectors at distances larger than 100 Mpc. However, a fraction of NS-NS merger are expected to produce long-lived neutron stars. In this case, a soft X-ray transient can be powered by the new-born neutron star spin-down emission. Even if never observed so far, this emission is expected to be powerful and

nearly isotropic [130, 131]. Large field of view instruments, such as Einstein Probe [132] and the soft X-ray instrument on board of THESEUS, will allow us to detect the brighter emissions up to 1 Gpc, thereby increasing the numbers of joint GW/electromagnetic detections in high-energy to a few hundreds per year.

### 3.3.5 Core collapse supernovae

Despite the remarkable progress of the theory, the explosion mechanism of supernovae (SNe) is still an open question, and being able to measure the dynamics of matter at the onset of the explosion would bring invaluable information to the understanding of the physics of gravitational core collapse. What is fairly known since the 1970's is the role of the neutrinos in the explosion mechanism [133, 134]. During collapse, the stellar core becomes opaque to neutrinos, producing a degenerate sea of trapped neutrinos within it, which subsequently diffuses out of the core on a timescale of order tens of seconds as the nascent proto-neutron star cools and deleptonizes, eventually leading to a neutrino burst of duration of a few seconds. The three-flavor neutrino flux emanating from the proto-neutron star could power a core collapse supernova via neutrino heating on delayed timescales of order one second [135–147]. This phenomenon is central to most models today, with the exception of models of rare events involving significant rotation, which may be powered magneto-hydrodynamically and where the dynamics proceeds on shorter timescales [148–157]. Besides, the Standing Accretion Shock Instability (SASI) [158, 159] which is an instability of the supernova shock wave itself is expected, in conjunction with turbulence, to modulate the accretion flow, to excite the proto-neutron star high frequency oscillation modes as well as to generate low frequency (100 – 250 Hz) GWs [160, 156, 157]. This low frequency GW emission depends on the nuclear equation of state, with softer equations of state leading to larger SASI amplitude [156].

A general consensus from all modern numerical simulations is that the expected GW signal is weak (GW released energy of the order of  $10^{-9} M_{\odot} c^2$ ) [161]. Furthermore, the likely diversity of the GW emission mechanisms that are at play in SN explosion makes it quite difficult to use matched filtering techniques for digging the signal out of the noise, contrary to what can be done with coalescing binaries or spinning neutron stars. As a consequence, the detection of a core collapse supernova GW signal is very challenging and the discovery horizon of the current 2G detectors is limited to our galaxy [162]. The expected galactic rate of type II/Ib supernova is also rather small ( $\sim 1$  per 30 years) [163]. ET will extend the reach to our galactic neighborhood, so that the expected rate is such that, while detection is not assured, still it is a realistic possibility. The ET detection horizon for core collapse SN could be further extended using externally triggered searches which use the optical or X-ray observations of nearby SNe. As reference, a few tens of core collapse SNe per century is expected up to 5 Mpc. If the signal is likely to remain short (of the order of 1 s), it is expected to be wide band (from few Hz up to several kHz), with very different mechanisms in each frequency band. The low frequency and high frequency ET design is very well suited for detecting such kind of GW signal using promising neural network algorithms which take advantages of peculiar features of the signal [164]. Another promising signal for ET is the signal from the SN explosion remnant which is expected to be detected from several tens of Mpc if a newborn magnetar with millisecond spin and strong interior magnetic field is formed [165]. *The detection of the GWs emitted in the core collapse and post collapse would be a milestone, revealing the inner mechanisms of SN explosion and opening remarkable perspectives in multi-messenger astronomy.*

### 3.3.6 Multi-messenger astrophysics with neutrinos and cosmic rays

Shock-accelerated particles (protons and nuclei) interacting with matter and photons produce neutrinos. The astrophysical sources of gravitational-wave transient signals associated with short and long GRBs, soft gamma-ray repeaters (SGRs), and core-collapse supernovae are expected to emit neutrinos. While gravitational waves produced by the bulk motion of matter carry information on the astrophysical source dynamics, neutrinos give direct information on interactions between accelerated particles with matter and radiation surrounding the sources. GWs and neutrinos probe the innermost regions of the source typically opaque to the electromagnetic emission.

GRBs and SGRs are expected to emit high energy cosmic neutrinos (HEN) from MeV to PeV. In the GRBs, TeV-PeV HENs are expected to be produced in the baryon-loaded jets during the prompt gamma-ray emission, and PeV-EeV HENs during the afterglow phase. In SGRs, the HEN production is expected from protons accelerated by the sudden magnetic reconfiguration.

When ET will be operational, the upcoming multi-cubic-kilometer neutrino detector KM3NET, and the 10 km<sup>3</sup> facility in the Southern hemisphere IceCube-Gen2 are expected to observe the sky. The sensitivity of the neutrino detectors will make the simultaneous detection of neutrinos and GWs from on-axis short GRBs possible. The high-energy neutrinos would serve as a powerful probe of cosmic-ray acceleration in GRBs and of the physics of relativistic jets associated with NS-NS and NS-BH mergers. For long GRBs and SGRs, the joint detection is less likely and more uncertain.

Some models predict that GRBs produce Ultra-High Energy Cosmic Rays (UHECR). In the case of cosmic rays, the astrophysical source identification is complicated by the cosmic ray deflection and the time delay between the arrival of cosmic rays and photons, GW, and neutrinos imparted by magnetic fields in the galaxy hosting the source, our Galaxy, and in the intergalactic medium. In this context, ET together with gamma-ray observatories, such as Fermi [118, 166], HESS [167], MAGIC [168, 169], VERITAS [170], CTA [171] and neutrino detectors will make it possible to probe the GRB population, their progenitors, and the jet properties and composition. This will be crucial to probe the role of GRBs as possible sources of UHECRs.

Core-collapse supernovae emit low-energy neutrinos, as proved on February 23, 1987, when neutrinos with energies of a few tens of MeV emitted by the supernova SN1987A, which exploded in the nearby Large Magellanic Cloud, were recorded simultaneously by the Kamiokande-II, IMB, and Baksan detectors a few hours before its optical counterpart was discovered [172–175]. Simultaneous detection of GWs and neutrinos from the core collapse of massive stars would open remarkable perspectives in multi-messenger astronomy. They are unique probes to reveal the inner mechanisms of the explosion, the dynamics of the remnant (possibly a newborn neutron star) and the physics of the post-shock region. The current and future low-energy neutrino detectors Super-K/Hyper-K [176], DUNE [177], JUNO [178], IceCube [179], the LVD [180], SNO+ [181] and KamLAND [182] are expected to detect neutrinos from the core-collapse SNe, whose GW signal will be detectable by ET. The GW signals detected by ET from the core-collapse and its remnant (a BH or a new born magnetar) are also expected to help searching for sub-threshold neutrino events. Furthermore, a strong correlation between the GW and neutrino signals is expected as they are produced at the same interior location and powered by the downward accretion plumes associated with hydrodynamic instabilities present in the post-shock flow. These plumes and instabilities will modulate both signals [183–185]. Detecting these modulations will enable to infer the supernova triggering dynamics (e.g., the SASI).

### 3.3.7 Multi-band gravitational-wave observations with LISA

Another potentially very interesting synergy could take place with the space interferometer LISA [186], should ET be operational by the time LISA will fly (launch scheduled in 2034 with observation starting some 18 months later, for a nominal four year duration, with possible extensions), or even a few years after the end of the mission. For most sources, ground-based 3G detectors and LISA are highly complementary, because of the very different frequency range where they operate, so, both for astrophysics and for cosmology, the scientific targets of ET and of LISA are in general independent.

However, for stellar-mass BH-BH binaries, interesting synergies are possible. In particular, from the rate of BH coalescences inferred by the Advanced LIGO/Virgo O1 and O2 runs, one estimates that LISA could detect  $O(100)$  stellar-mass BH-BH binaries during their inspiral phase [186], up to  $z \approx 0.4$ . Several years later (typically, 5 to 10 yr), some of these events will cross into the ET window, where they will coalesce. For instance, the first observed GW event, GW150914, would have been in the LISA bandwidth from about 10 yr to less than 1 yr before coalescence, and could have accumulated in the LISA bandwidth a signal-to-noise ratio between three and fifteen (depending on the detector configuration), and therefore might have been detected, if at that time LISA had already been in orbit [187]. This could allow for multi-band GW observations, i.e. the observation of GW signals in widely different frequency bands.

The actual possibility of multi-band detections depends sensitively on a number of issues, in particular on the sensitivity curve assumed for LISA, especially at high frequency, on the details of the data analysis in LISA, and on the mass distribution of the component BHs in a BH-BH binary. The recent analysis in [188] finds that LISA, in a 4 yr mission, will detect  $O(80 - 90)$  stellar-mass BH-BH binaries, consistent with the earlier estimates in [187, 189].<sup>4</sup>

Multi-band observations would have many benefits: a joint LISA-ET detection would provide sky localization of the source with an error of only a few square degrees, and would make it possible to alert telescopes and look for an electromagnetic counterpart (which in principle is not expected for BH-BH coalescences, but could be present in BH-NS binaries) both in the pre-merger and post-merger phases; it would improve parameter estimation, reducing the error on the luminosity distance to the source and on the initial spins and allowing to measure with extreme precision the sky position, mass and spin of the final BH. LISA and ET observations of such events would be highly complementary; for instance LISA, by observing the long inspiral phase, will measure very accurately the masses of the initial BHs, while ET would detect the last few cycles and the merger, and would therefore measure the final masses and spin from the ringdown of the final BH. Consistency tests between the inspiral part of the waveform and the merger-ringdown part, of the type performed in [51] for the first detection GW150914, would then provide very stringent tests of General Relativity [191]. Furthermore, the early warning provided by LISA on particularly interesting events might allow real

---

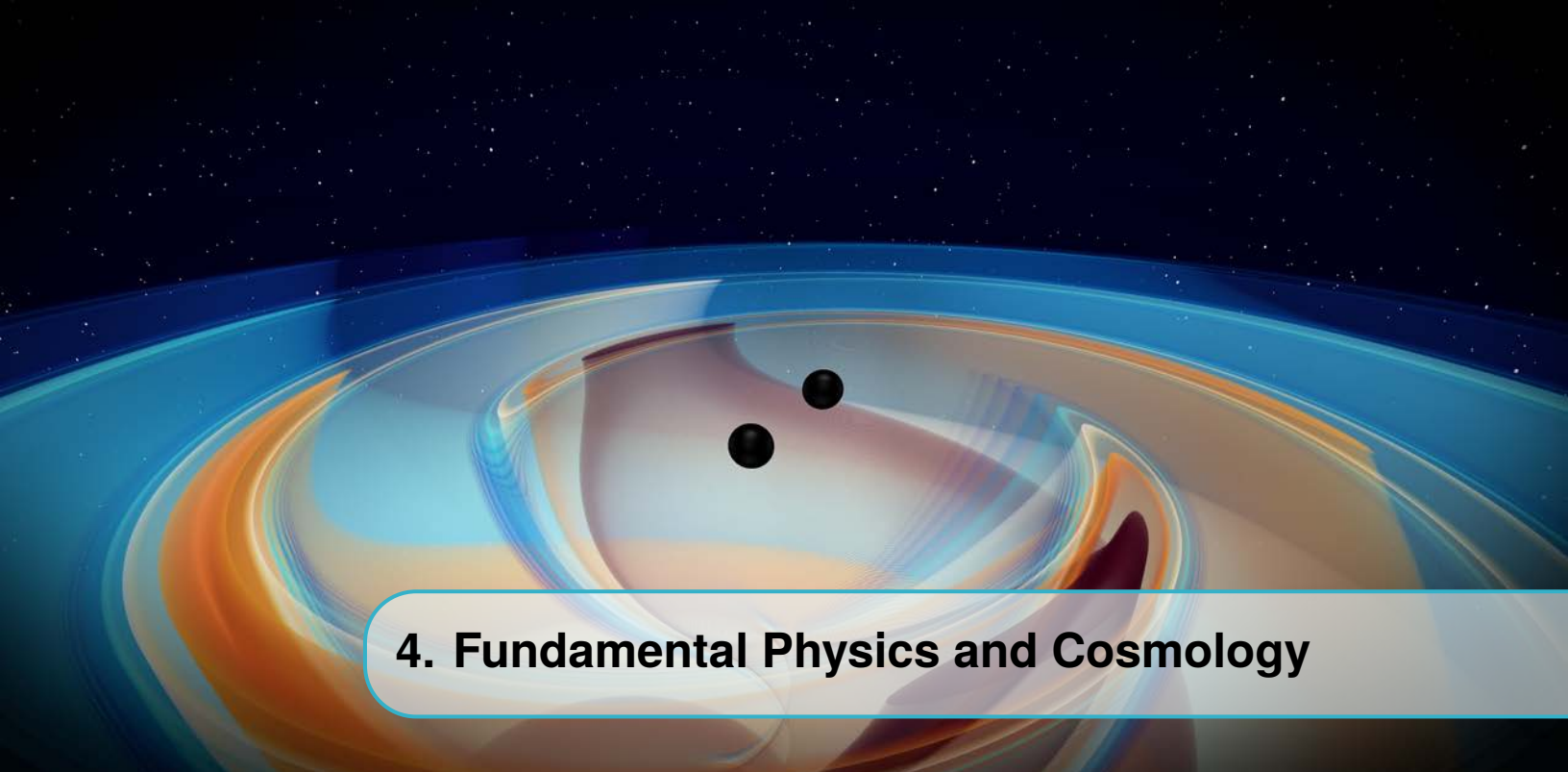
<sup>4</sup>Smaller estimates have been obtained in [190], using a pessimistic LISA sensitivity curve at high frequencies, rather than the official sensitivity curve of the LISA proposal used in [188]. This highlights the importance of the sensitivity curve at high frequencies, as well as of the other assumptions entering the estimates. Note that the analysis of [190] is restricted to binary BHs with merger times up to 100 yr. As discussed in [190], a numerous population with larger merger times could also be present. For these wide and slowly inspiraling binaries, the signal is closer to monochromatic and data analysis simplifies considerably, allowing for a lower SNR threshold. Furthermore, once detected the coalescence in ET, one could go back to archival LISA data, using a lower signal-to-noise threshold. Except for the possibility of giving a forewarning of the coalescences at ET and electromagnetic telescopes, such a search into archival LISA data would still preserve all the other advantages of multi-band detection mentioned below.

time optimization of ET to improve sensitivity to the ringdown signal [192].

The complementarity of ET and LISA observations to search for intermediate mass black-hole binaries ( $10^2 - 10^4 M_{sun}$ ) at high-redshift is a powerful tool to unveil the possible seeds forming supermassive black-hole at the center of the galaxies.

*In summary, ET represents an enormous opportunity in multi-band and multi-messenger studies. The synergies and coordination among ET, 2G and other 3G gravitational-wave detectors, and the new generation of electromagnetic and neutrino observatories will maximize the science return of each gravitational-wave detection.*

- *The inclusion of ET in a network of gravitational-wave detectors will improve the sky localization of the signal increasing the probability to detect electromagnetic counterparts;*
- *Multi-band observations with LISA will ensure to follow gravitational-wave sources, such as heavy binary black-hole systems, in different phases of their evolution, and to explore complementary mass regions for the intermediate-mass black holes probing the formation of massive and supermassive black holes;*
- *Multi-messenger studies will strongly benefit from ET's superior sensitivity, which will increase the signal-to-noise ratio for close sources and the number of detections up to high redshifts;*
- *The ET wide frequency band and sensitivity will provide unprecedented insight into the onset of tidal effects during the final inspiral phase, and into the merger and post-merger phases for close sources. This information together with the ones from the electromagnetic counterpart signals will be crucial to understand the interior structure of neutron stars, the properties of ejected mass, the physics behind kilonova emission, and in turn the NS-NS contribution to the Universe nucleosynthesis;*
- *Large samples of detections extending up to high redshift in connection with short GRBs will probe the GRB central engine, the formation, structure and properties of relativistic jets and their interaction with the environment along the cosmic history;*
- *The ET distance estimates together with the electromagnetic redshift for a large sample of GW sources will enable precise cosmology evaluating the expansion rate of the Universe and probing its geometry.*
- *ET operating together with electromagnetic and neutrino observatories will be a unique instrument to probe the physics governing the explosion of massive stars and the multi-messenger emission of nearby supernovae.*



## 4. Fundamental Physics and Cosmology

The direct detection of gravitational waves has started to give us access to the genuinely strong-field dynamics of spacetime. This is illustrated in Fig. 4.1, which shows how different kinds of observations (past, current, and future) will give us access to different regimes, in terms of spacetime curvature  $R$  and gravitational potential  $\Phi$ .<sup>1</sup>

Observations of GWs from binary BH and binary NS coalescences with Virgo and LIGO have enabled us to probe for the first time the regime where both  $R$  and  $\Phi$  are no longer small. By observing the inspiral phase we could test the predictions of GR (as encoded in the post-Newtonian coefficients) to a precision of about 10%. By observing the full inspiral-merger-ringdown process of binary black holes, we could perform a first study of the dynamics of vacuum spacetime. The observation of the binary neutron star inspiral GW170817 also gave us empirical access to the interaction of spacetime with high-density matter. Because of the large distances that GWs have to travel from source to observer, we were able to strongly constrain possible dispersion that might occur; the latter led to a bound on the mass of the graviton of  $m_g \leq 5 \times 10^{-23} \text{ eV}/c^2$ .

A 3G detector such as ET will allow us to explore the top right edge of Fig. 4.1, corresponding to strong-field dynamics at the source, with another leap in precision, compared to the current Virgo and LIGO detectors. One reason is the much larger detection rate; especially for the purposes of fundamental physics, information from multiple sources can often be combined, and the measurement accuracy on common observables tends to improve with the square root of the number of detections. For example, the post-Newtonian coefficients that govern binary inspiral will be determined with

---

<sup>1</sup>In a binary system, the gravitational potential felt by a star because of the presence of the companion is of order  $v^2/c^2$ , where  $v$  is the characteristic orbital velocity of the binary and  $c$  the speed of light; therefore, it becomes strong when the system is close to relativistic. However, for compact objects such as neutron stars, the gravitational potential generated by the star itself in its interior and close to its surface is already of order one. This can induce strong-field effects on the binary evolution even when the orbital velocity  $v \ll c$ . This can happen for instance in some scalar-tensor theories, through the phenomenon of spontaneous and induced scalarization [193, 194], as well as dynamical scalarization [195]. These effects can indeed be constrained by GW observations, see [196] for a study with 2G detectors.

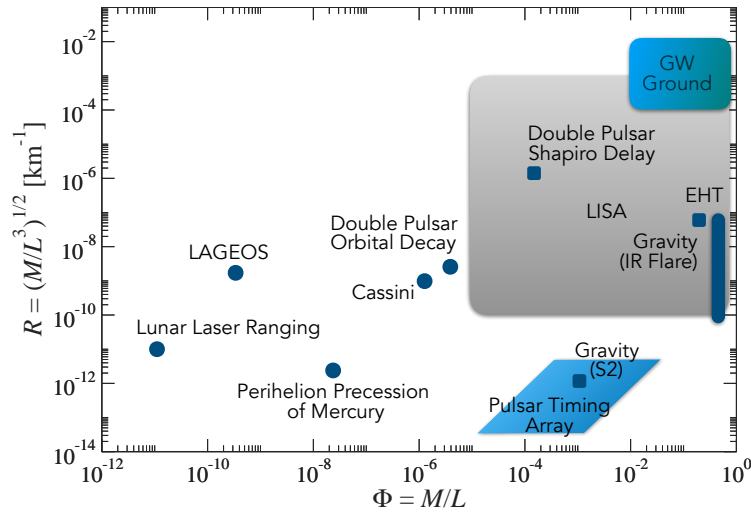


Figure 4.1: Probing gravity at all scales: illustration of the reach in spacetime curvature versus potential energy targeted by different kinds of observations.  $M$  and  $L$  are the characteristic mass and length involved in the system or process being observed. The genuinely strong-field dynamics of spacetime manifests itself in the top right of the diagram. The label EHT refers to the Event Horizon Telescope. From ref. [3, 6].

sub-percent to sub-permille accuracy. However, the fact that the same GW source will give a much stronger signal in ET will also give us access to qualitatively new effects. Below we discuss in turn the capabilities of ET in probing the properties of gravity, as well as unraveling the nature of ultra-compact objects, with potentially game-changing implications for our understanding of black holes, the make-up of dark matter, and maybe even quantum gravity itself.

At the same time, the fact that ET will be able to detect a large number of signals coming from truly cosmological distances will allow us to investigate the nature of dark energy and the possibility of modifications of GR at cosmological scales, in particular through signatures encoded in the propagation of GWs across cosmological distances, while the possible detection of stochastic backgrounds of cosmological origin would open a window on the primordial Universe at epochs corresponding to energy scales unreachable with accelerators.

## 4.1 Physics near the black hole horizon: from tests of GR to quantum gravity

### 4.1.1 Testing the GR predictions for space-time dynamics near the horizon

Black holes are one of the most extraordinary predictions of General Relativity. They are identified through their most striking property: in the case of stellar mass black holes, a mass  $O(10 - 100)M_{\odot}$  is concentrated in an extremely small volume; for instance, the Schwarzschild radius of a non-rotating BH with mass  $10M_{\odot}$  is about 30 km. However, how certain can we be that the massive compact objects that we saw merge with 2G detectors are really the standard black holes of classical General Relativity?

General Relativity gives detailed and specific predictions on the nature of BHs that a 3G detector such

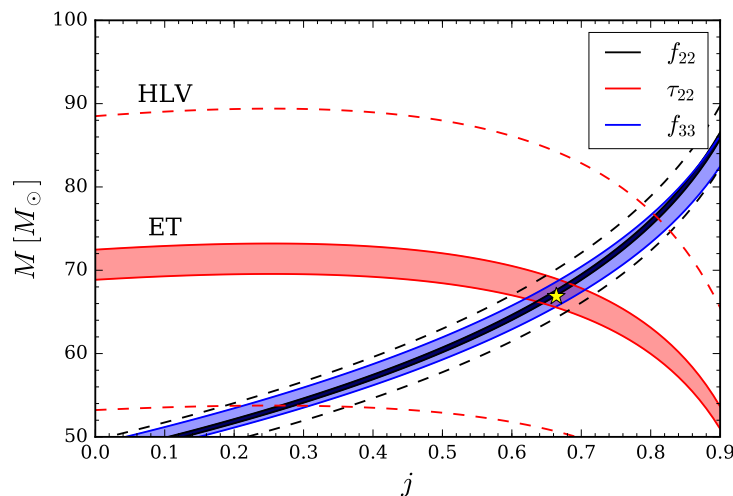


Figure 4.2: Testing the nature of black holes by using two quasi-normal modes and checking that the characteristic frequencies  $f_{22}$  and  $f_{33}$  and the damping time  $\tau_{22}$  are consistent with each other, given that for ordinary black holes these can only depend on two numbers, namely the final mass  $M$  and final spin  $j$ . The estimates are for the “ringdown” of the remnant black hole arising from a binary similar to the source of GW150914. The dashed curves marked HLV are the 95% confidence regions one would obtain from the current Virgo and LIGO detectors, while the colored bands are for ET. The star indicates the true values of  $M$  and  $j$ . Figure from ref. [3].

as ET will be able to test. The celebrated no-hair theorem of GR states that, in a stationary situation, a BH is determined by just two numbers: its mass and its spin (plus the electric charge, which however is not relevant in an astrophysical context, where it is quickly neutralized). However, when a BH is perturbed, it reacts in a very specific manner, relaxing to its stationary configuration by oscillating in a superpositions of quasi-normal modes (QNMs), which are damped by the emission of GWs.<sup>2</sup> The fact that an elastic body has normal modes is a familiar notion from elementary mechanics. It is however quite fascinating to realize that a BH, which is a pure space-time configuration, also has its quasi-normal modes. These represent pure space-time oscillations, in a regime of strong gravity, and, in a sense, describe the elasticity of space-time in a most extreme situation, in the region close to the BH horizon. The theory of BH quasi-normal modes is a classic chapter of GR (see [197, 4] for reviews), and in particular predicts the spectrum of frequencies and damping times of the quasi-normal modes as a function of the mass and spin of the BH. Highly perturbed black holes arise as the remnants of binary BH or NS mergers, and relax to the final stationary BH configuration through GW emission in the quasi-normal modes, in the so-called ‘ringdown’ phase of the coalescence, where the waveform is given by a superposition of damped sinusoids. Indeed, for the first observed BH-BH coalescence, GW150914, the final ringdown phase was visible, and was shown to be broadly consistent with the prediction of GR for the value of the parameters inferred from the inspiral part of the waveform [51].

Since the whole spectrum of frequencies and damping times of the quasi-normal modes depends only on two parameters (the mass  $M$  and the spin  $j$  of the final BH) a stringent test of GR can be

<sup>2</sup>The expression ‘quasi-normal modes’, in contrast to ‘normal modes’, emphasizes that the normal modes are unstable to GW emission.

performed if we can measure (at least) three independent quantities. Fig. 4.2 illustrates the difference in the accuracy of such a test between 2G and 3G detectors, for a single source such as GW150914 (see [198] for the 2G result). Furthermore, the accuracy of the measurement scales as  $1/\sqrt{N}$ , where  $N$  is the number of detections; as we saw, ET will detect  $N \sim O(10^5 - 10^6)$  BH binaries per year, compared to a few hundreds per year expected for 2G detectors at target sensitivity. Out of these, a large fraction will have a detectable ringdown signal. In [199], using three different population synthesis models, it was found that ET, as a single instrument, will detect between  $10^4$  and a few times  $10^5$  binary BH mergers per year in which the final ringdown phase has a signal-to-noise ratio larger than 8. If one further requires a ringdown signal sufficiently strong to be able to disentangle the fundamental  $l = m = 2$  QNM from a QNM with different  $l$  (in general, the  $l = m = 3$  mode, except in the comparable mass limit, where odd- $m$  modes are suppressed, and it becomes easier to resolve the  $l = m = 4$  mode), one finds that ET will still detect 20 – 50 events per year, with redshifts up to  $z \simeq 2$  (see Fig. 2 of [199]). For comparison, in 2G detectors the rate for resolving two different QNMs would be of order  $10^{-2}$  events per year [199]. “Black hole spectroscopy” is therefore out of reach for 2G detector, while it will be routinely performed with 3G detectors. In the comparable mass limit, where the  $l = m = 3$  mode is suppressed, another option is to make use of the fact that, for each  $(l, m)$ , there is a family of ‘overtones’ characterized by a further integer number, and it could be possible to resolve some overtones of the  $l = m = 2$  mode. As shown in [200], this requires a ringdown signal-to-noise ratio larger than  $\sim 30$ , which will be routinely achieved by ET.

One can go beyond consistency tests of GR either by working out explicit predictions for the quasi-normal mode frequencies and damping time as a function of  $(M, j)$  in specific extensions of GR, or by introducing parametrizations of deviations from the Kerr predictions (in the same spirit as the parametrization of deviations from the post-Newtonian predictions expressed by the parametrized Post-Newtonian expansion). Using the parametrization developed in [201] it is found that  $O(10)$  ringdown detections at a signal-to-noise ratio  $\sim 100$ , as can be obtained at ET, can provide significant constraints on the first ‘beyond-Kerr’ parameters.

#### 4.1.2 Exotic compact objects and signals from quantum gravity

The observation of quasi-normal modes, beside providing a spectacular test of GR in the strong-field, near-horizon regime, could also potentially lead to the discovery of different types of compact objects. Indeed, various exotic compact objects have been proposed that may act as “black hole mimickers”, such as boson stars, gravastars, stars composed of dark matter particles, etc. (see [202] for review). When such objects are part of a binary system that undergoes coalescence, they can make their presence known through various possible imprints on the GW signal emitted. Already during the inspiral phase, these objects may get tidally deformed in a way that would be impossible for a standard, classical black hole. Unlike 2G detectors, ET will for instance be able to distinguish neutron stars from boson stars even for the most compact models of the latter [203]. Another possibility is that an exotic object could be identified through an anomalous spin-induced quadrupole moment, which would again not be accessible with current detectors, but measurable with ET to the percent level [204].

If the outcome of a coalescence is different from a BH, this might leave an imprint on the ringdown phase, and could be tested by measuring quasi-normal mode frequencies and life-times, as in Fig. 4.2. For exotic compact objects where the modifications take place only at scales much shorter than the

so-called light-ring (as in the case of quantum gravity effects discussed below), the ringdown signal will be very similar to a BH, but after the ringdown has died down, exotic compact objects may continue to emit bursts of gravitational waves at regular time intervals, called *echoes* [205, 206]. The detectability of echoes has been investigated in [207, 208], showing that excluding or detecting echoes requires signal-to-noise ratios in the post-merger phase of  $O(100)$ , achievable only with 3G detectors such as ET and CE, or with LISA.

Prompted by Hawking’s information paradox, modifications of the structure of space-time at the horizon scale have been proposed, such as firewalls [209] and fuzzballs [210], for which the classical horizon is removed through macroscopic quantum effects. The absence of the horizon results in an instability, that leads to a detectable stochastic background of gravitational waves [211]. From a particle physics perspective, one is used to the fact that, at energies  $E$  much below the Planck energy scale  $M_{\text{Pl}}$ , quantum gravity effects are suppressed by powers of  $E/M_{\text{Pl}}$ , and therefore, given that the Planck scale  $M_{\text{Pl}}$  is of order  $10^{19}$  GeV, they are totally inaccessible at accelerators, even in any foreseeable future. Equivalently, at a macroscopic length-scale  $L$ , quantum gravity effects are suppressed by powers of  $l_{\text{Pl}}/L$ , where  $l_{\text{Pl}} \sim 10^{-33}$  cm is the Planck length. In contrast, near the BH horizon, where the characteristic length-scale  $L$  is given by the Schwarzschild radius  $R_S$ , effects due to quantum gravity are governed by a factor  $\log(l_{\text{Pl}}/R_S)$ , and can manifest themselves through a series of echos after the initial ringdown signal [205, 212, 213], emitted with a time delay  $\tau_{\text{echo}} \sim (R_S/c) \log(R_S/l_{\text{Pl}})$ . For instance, for a final object with mass  $M = 60M_{\odot}$ , one has  $\tau_{\text{echo}} \simeq 16\tau_{\text{BH}}$ , where  $\tau_{\text{BH}} \simeq 3$  ms is the fundamental damping time of a Schwarzschild BH with this mass. Such signals are potentially within the reach of ET. The quantization of the area of BHs, suggested by quantum gravity arguments [214, 215], might also leave an observable imprint on the waveform of a BBH coalescence [216]. This raises the tantalizing possibility of accessing quantum gravity effects at ET.

To summarize, *the transition from second generation observatories to Einstein Telescope will lead to a qualitative leap in our ability to probe both the nature of gravity in the strong field regime and the structure of compact objects, and could even lead to exploring the quantum gravity regime.*

## 4.2 The nature of dark matter

From cosmological observations we know that the elementary constituents that we observe everyday in the lab (electrons, protons, atoms, etc.) are responsible for only about 5% of the energy density of the Universe; about 25% is made of “dark matter”, i.e. matter that does not have electromagnetic interactions and whose existence is only inferred through its gravitational attraction, while the rest, about 70%, is currently attributed to “dark energy”, a form of energy that formally produces a negative pressure and therefore cannot be identified with any known or unknown type of matter. Understanding the nature of dark matter and of dark energy is one of the crucial problems in astrophysics, cosmology and fundamental physics. ET may be able to shed light on both questions. In this section we discuss the potential of ET for dark matter studies, while its potential for dark energy will be discussed in Sect. 4.3.

Observations at ET will allow us to attack the problem of the origin of dark matter from several different angles. Dark matter could be composed, at least in part, of *primordial* black holes in the

mass range  $\sim 0.1 - 100 M_{\odot}$ . As we already mentioned in Section 3.1, primordial BHs could be seeded by fluctuations generated during the last stages of inflation, which then collapsed in later epochs as a consequence of drops in the pressure of the cosmic fluid, e.g. during the QCD quark-hadron transition. Their mass distribution depends on the precise model of inflation and on the epoch when they collapsed. The large number of mergers that Einstein Telescope will see, together with its ability to access a broad range of masses, would allow us to map the black hole mass distribution and identify an excess of black holes in certain mass intervals. For black holes with masses well below a solar mass, no plausible astrophysical formation mechanism is available, so that their detection would point to the existence of primordial black holes. A unique advantage of Einstein Telescope is the possibility of observing stellar-mass black hole mergers at redshifts of  $\sim 10 - 20$ , before any stars had formed that could create black holes in the usual way; should such an event be observed then (irrespective of masses) the objects involved are bound to be of primordial origin.

If most of the dark matter occurs in the form of particles beyond the Standard Model, then also in that case gravitational wave observations can be used to search for them. Black holes could not only accrete dark matter particles, but also be subject to gravitational drag, which in a binary system would accumulate over the course of many orbits. If Einstein Telescope will be operational during the same period as LISA, joint LISA-ET observations of the same source will be of great value. In fact, LISA can constrain the parameters of the binary with great accuracy, from the long observation of the inspiral phase, and predict when these systems should coalesce in the ET band. Any deviation from GR that produces a cumulative effect over the orbits, such as gravitational drag, dipole radiation, etc., would then change the actual merger time in a potentially observable manner [217].

There is also the possibility that dark matter particles are captured in astrophysical objects and thermalize with the star [218]. The presence of a dark matter core in a neutron star might again have an imprint upon the GW signal during binary inspiral and merger. Dark matter accumulating in neutron stars and interacting through Yukawa-like interactions in the dark sector could affect the orbital dynamics of a neutron star binaries, and therefore the corresponding waveform, in a way detectable by ET [219], whose low-frequency sensitivity makes it an especially sensitive probe to dark matter mediated forces between neutron stars. In some models [220, 221], the accumulation of dark matter may lead to the formation of a black hole inside a neutron star, which then accretes the remaining neutron star matter, leading to black holes of  $(1 - 2) M_{\odot}$  that could be observed by ET.

Finally, ultralight bosons have been proposed in various extensions of the Standard Model, and also as dark matter candidates [222, 223]. If their Compton wavelength is comparable to the horizon size of a stellar or supermassive rotating black hole (*i.e.* for particle masses of  $10^{-21} - 10^{-11}$  eV), they can extract rotational kinetic energy from the black hole through “superradiance” to feed the formation of a bosonic “cloud” with mass up to  $\sim 10\%$  of the black hole [224–226]. These clouds annihilate over a much longer timescale than their formation, through the emission of nearly monochromatic gravitational waves which could be detected either directly or as a stochastic background from a large number of such objects throughout the Universe [227, 228]. Additionally, measuring the distribution of black hole masses and spins can yield an indication of the prevalence of superradiance through light scalars. Moreover, the presence of such clouds will again have an effect on binary orbital motion [229]. This way gravitational waves have the potential to provide a unique probe into an ultralight, weakly coupled regime of particle physics that can not easily be accessed in accelerator experiments.

*To summarize, ET has the potential of discovering, or ruling out, several dark-matter candidates that will be inaccessible by any other means.*

### 4.3 The nature of dark energy

ET will be an outstanding discovery machine for studying the nature of dark energy, using binary NSs and binary BHs as cosmological probes. Indeed, a remarkable feature of the GWs emitted in the coalescence of compact binaries is that their signal provides an absolute measurement of the luminosity distance to the source. The relation between the luminosity distance  $d_L$  and redshift  $z$  of the source carries crucial cosmological information and is among the main observables of modern cosmology. Explicitly, it is given by

$$d_L(z) = \frac{1+z}{H_0} \int_0^z \frac{dz'}{\sqrt{\Omega_M(1+z')^3 + \frac{\rho_{\text{DE}}(z')}{\rho_0}}}, \quad (4.3.1)$$

where  $H_0$  is the Hubble parameter,  $\rho_0$  is the closure energy density,  $\rho_{\text{DE}}$  is the dark energy density and  $\Omega_M = \rho_M(t_0)/\rho_0$  is the density of matter at the present time  $t_0$ , normalized to  $\rho_0$  (and we neglected for simplicity the contribution of radiation, which is irrelevant at the redshifts of interest for GW detectors, and a possible non-vanishing spatial curvature). In particular, in  $\Lambda$ CDM, which is the model that constitutes the current cosmological paradigm,  $\rho_{\text{DE}}(z)/\rho_0 = \Omega_\Lambda$  is a constant, related to the cosmological constant.

Observations performed with electromagnetic waves can infer the redshift of a source, through spectroscopic or photometric observations; however, obtaining the absolute distance to a source at cosmological distances is much more difficult. Ideally, this requires the existence of a “standard candle”, a class of sources whose intrinsic luminosity  $\mathcal{L}$  is known, so that, from a measurement of the energy flux  $\mathcal{F}$  received by the observer, we can reconstruct the luminosity distance  $d_L$  from  $\mathcal{F} = \mathcal{L}/(4\pi d_L^2)$ . A classic example of standard candle in cosmology is provided by type Ia supernovae: these are bright enough to be visible at cosmological distances, and, after some empirical corrections, their intrinsic luminosity can be considered as fixed; its value is then calibrated through the construction of a “cosmic distance ladder”, in which classes of sources at shorter distances are used to calibrate different sources at higher and higher distances. Indeed, type Ia Supernovae provided the first conclusive evidence for the existence of dark energy [230, 231], a discovery that was awarded with the 2011 Nobel Prize in Physics.

GW observations of compact binary coalescences completely bypass the need for empirical corrections and the uncertainties in the calibration of the cosmic distance ladder, since the observed waveform of the inspiral phase directly carries the information on the luminosity distance  $d_L$  [95]. In this context, coalescing binaries are called “standard sirens”, the GW analogue of standard candles.<sup>3</sup> By contrast, the GW signal does not carry direct information on the redshift, so the situation is reversed compared to electromagnetic observations. An ideal situation then takes place when one has a joint GW-electromagnetic detection, as was the case for the NS-NS binary GW170817. In this

<sup>3</sup>The origin of the name is related to the fact that, from several points of view, GWs are more akin to sound than to visible light. For instance, GWs are generated by bulk coherent motions of matter, and detectors do not need to point the source to detect them.

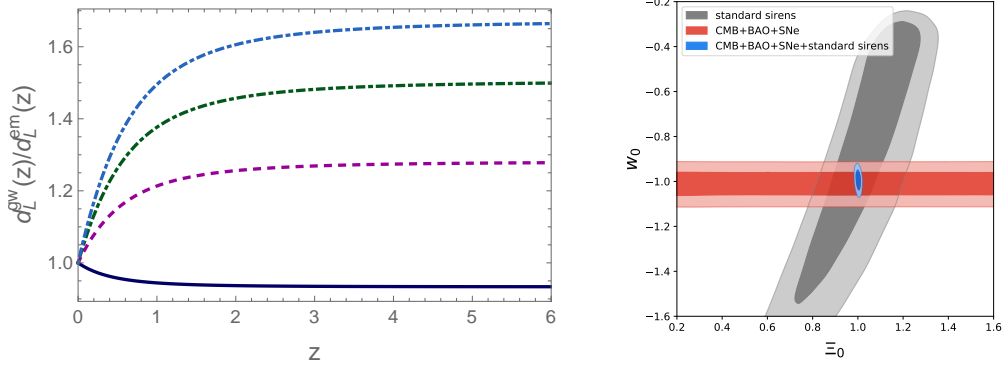


Figure 4.3: Left panel: an example of the ratio of the gravitational to electromagnetic luminosity distance in a modified gravity model, for different values of a parameter of the model. In the upper curve, at large redshift the deviations of  $d_L^{\text{GW}}(z)$  from  $d_L^{\text{EM}}(z)$  reaches 60% (from ref. [7]). Right panel: constraints on the parameters  $(\Xi_0, w_0)$  that describe a non-trivial dark energy sector. Modified GW propagation is not accessible by electromagnetic observations from CMB, Baryon Acoustic Oscillations, and Supernovae, whose contours (red) are flat along the  $\Xi_0$  direction. Standard sirens at ET (gray), combined with these electromagnetic probes allow a determination of  $\Xi_0$  to better than 1% (blue). (From ref. [8]).

case the GW signal gives  $d_L$  and the electromagnetic observation the redshift  $z$ . Even in the absence of a redshift determination from an electromagnetic counterpart, several statistical methods have been discussed in the literature and published using actual measurements by Virgo and LIGO, to extract cosmological information from purely GW observations. For instance, in a modern version of a statistical method proposed already in [95], one constructs a Bayesian likelihood by assigning probabilistically a host galaxy to the GW event, within the localization volume found by the GW detectors (see [96] for a recent discussion). After collecting a sufficient number of events, the results will converge to the actual  $d_L - z$  relation. This method has been successfully applied recently to the LIGO/Virgo data to extract the Hubble constant from the binary neutron star coalescence GW170817 without making use of its counterpart [232], and from several other coalescences [233–236]. Other techniques, applicable to NSs, exploit the narrowness of their intrinsic mass distribution [237, 238] or the effect of the equation of state in the inspiral phase [239].

In the low redshift limit  $z \ll 1$  accessible to 2G detectors, eq. (4.3.1) reduces to the Hubble law  $d_L(z) \simeq H_0^{-1}z$ . Hence the observation of standard sirens at low redshifts can provide a measurement of  $H_0$ , but is insensitive to the dark energy density  $\rho_{\text{DE}}$ , or equivalently to the dark energy equation of state  $w_{\text{DE}}$ . The possibility of measuring  $H_0$  has already been demonstrated with GW170817, from which a value  $H_0 = 70.0_{-8.0}^{+12.0} \text{ km s}^{-1} \text{ Mpc}^{-1}$  was obtained [50]. With  $O(100)$  standard sirens with counterpart, or with statistical methods, a measurement of  $H_0$  at the 1% level could already be possible with 2G detectors, so already with 2G detectors it could be possible to arbitrate the current discrepancy between the value of the Hubble parameter  $H_0$  obtained from late-Universe probes [240, 241], and the value inferred from early-Universe probes [242, 243], which has currently reached the  $5.3\sigma$  level.

For a 3G detector such as ET, given the expected huge number of detections and the very high signal-to-noise ratios of nearby events, a sub-percent level accuracy on  $H_0$  could be reached. However, a much higher potential for discovery is provided by the fact that ET will have access to standard

sirens at much larger redshifts, where effects genuinely induced by a non-trivial dark energy sector and by modifications of General Relativity on cosmological scales become accessible. First of all, away from the limit  $z \ll 1$ , the effect of the dark energy density  $\rho_{\text{DE}}(z)$  becomes visible in eq. (4.3.1), which would allow us to obtain a measurement of the dark energy equation of state from GW observations [244, 245, 8]. In fact, the situation for 3G detectors is even more interesting due to a phenomenon of modified GW propagation [246–250, 8, 251]. Indeed, a natural theoretical framework for having a dark energy sector different from a simple cosmological constant is provided by modifications of GR at the cosmological scale. In a generic modified gravity theory the cosmological evolution of the background is different from that of  $\Lambda$ CDM, and this is encoded in a non-trivial dark-energy density  $\rho_{\text{DE}}(z)$  [or, equivalently, in the dark energy equation of state  $w_{\text{DE}}(z)$ ]. On top of this, cosmological perturbations will also be different. The modification in the scalar perturbation sector will affect the predictions for the growth of structures or lensing, and are among the targets of future experiments such as Euclid, DESI or SKA. The modification in the tensor perturbation sector will instead affect the propagation of GWs over cosmological distances. In GR the GW amplitude scales as the inverse of the scale factor,  $h \propto 1/a$ , which eventually results in the fact that the signal from coalescing binaries at cosmological distances is proportional to  $1/d_L(z)$ . In modified gravity theories this behavior is changed (also in models where GWs propagate at the speed of light, and which therefore survive the limit imposed by GW170817).<sup>4</sup> As a result, the GW amplitude becomes inversely proportional to a “GW luminosity distance”, different from the standard electromagnetic one. An example of the resulting ratio of GW luminosity distance to the standard ‘electromagnetic’ luminosity distance, in a specific model of modified gravity, is shown in the left panel of Fig. 4.3. This behavior turns out to be completely generic to modified gravity models (scalar-tensor theories, nonlocal modifications of gravity, bigravity, etc.) [251]. For most models, the deviations from GR can be parametrized in terms of two parameters  $(\Xi_0, n)$  as [8]

$$\frac{d_L^{\text{GW}}(z)}{d_L^{\text{em}}(z)} = \Xi_0 + \frac{1 - \Xi_0}{(1+z)^n}, \quad (4.3.2)$$

where  $d_L^{\text{em}}$  is the standard electromagnetic luminosity distance. Measuring the modified GW propagation through its effect on the GW luminosity distance is a very powerful probe for the dark energy sector which cannot be accessed at all with electromagnetic observations. With a few hundreds standard sirens with counterpart, ET will constrain  $\Xi_0$  to below 1% (see the right panel in Fig. 4.3), a level significantly smaller than the deviation from GR foreseen by various alternative gravity theories. Indeed, the sector of tensor perturbations over a cosmological background can only be explored with GW detectors, and can lead to significant surprises. For instance, one can have a cosmological model that is observationally indistinguishable from  $\Lambda$ CDM in terms of current electromagnetic observations, but still, as shown in the left panel of Fig. 4.3, predicts a value of  $\Xi_0$  that can be as large as  $\Xi_0 \simeq 1.6$ , representing a 60% deviation from  $\Lambda$ CDM [7] (and in fact even up to 80% [252]). Such a large effect could be detectable even with just a single standard siren at ET.

To perform precision cosmography with ET it is also important to investigate the effect of cosmological perturbations on the propagation of gravitational waves. A detailed analysis of the effect of cosmological perturbations and inhomogeneities on estimates of the luminosity distance of BH or

<sup>4</sup>In GR the equation of propagation of GWs over a FRW background is given by  $\tilde{h}''_A + 2\mathcal{H}\tilde{h}'_A + k^2\tilde{h}_A = 0$ , where  $h_A$  is the GW amplitude,  $A = +, \times$  labels the polarization, and  $\mathcal{H} = a'/a$  is the Hubble parameter. In alternative theories this is modified to  $\tilde{h}''_A + 2\mathcal{H}[1 - \delta(\eta)]\tilde{h}'_A + k^2\tilde{h}_A = 0$ , where the function  $\delta$  encodes the details of the modification.

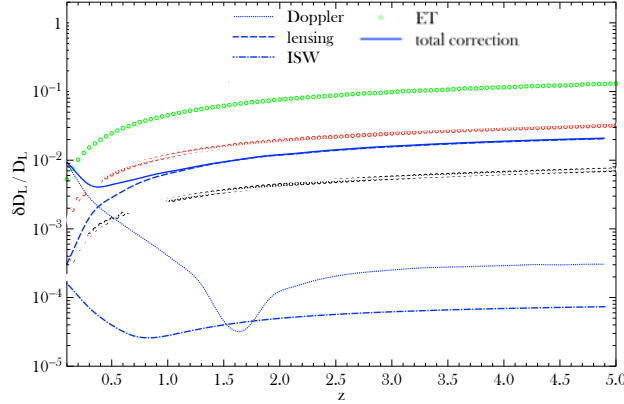


Figure 4.4: Total correction to luminosity distance estimates due to perturbations, as a function of  $z$ . The dotted, dashed and dot-dashed lines show Doppler, lensing and ISW-like contributions, respectively, while the solid line shows the total effect. The green points show the predicted precision in measurements of the luminosity distance of ET. Adapted from [9].

NS binary mergers through gravitational waves has been performed in [9], where an expression has been derived for the effect of large-scale structures on GW waveforms accounting for lensing, Sachs-Wolfe, integrated Sachs-Wolfe, time delay and volume distortion effects. In Figure 4.4 we show the correction  $\delta D_L / D_L$  to luminosity distance estimates due to perturbations, as a function of  $z$ . The dotted, dashed and dot-dashed lines show velocity, lensing and ISW-like contributions, respectively, while the solid line shows the total effect. The green points show the predicted precision in measurements of the luminosity distance, at any redshift, for the Einstein Telescope. We see that the additional uncertainty  $\delta D_L / D_L$  due to the inclusion of perturbations is below the error obtained by the sensitivity curve of ET (except at very low  $z$  where it becomes comparable) and therefore does not spoil the accuracy that can be obtained by ET.

*In summary, the sector of cosmological tensor perturbations is an unknown territory which can only be explored via GWs, and only with third-generation GW detectors such as ET, and which could offer the most powerful window for understanding the nature of dark energy and modifications of General Relativity at cosmological scales.*

#### 4.4 Toward the big bang: stochastic gravitational-wave backgrounds

The weakness of the gravitational interaction, which is responsible for the fact that GW detection is such a challenging enterprise, also implies that the observed GW signals carry uncorrupted information about their production mechanism. This is particularly significant for stochastic backgrounds of GWs of cosmological origin. For comparison, in the early Universe photons were kept in equilibrium with the primordial plasma by the electromagnetic interaction, and decoupled from it only at a redshift  $z \approx 1090$ , when the Universe already had a rather low temperature  $T \approx 0.26$  eV. The photons that we observe today from the cosmic microwave background therefore give a snapshot of the Universe at this decoupling epoch, while all information about earlier epochs was obliterated by the photon collisions with the primordial plasma. Neutrinos, which interact through weak interactions, decoupled when

the Universe had a temperature  $T \simeq 1$  MeV. By contrast, GWs were decoupled from the primordial plasma at all temperatures below the Planck scale  $\sim 10^{19}$  GeV,<sup>5</sup> corresponding to a far earlier epoch, and energies far exceeding those accessible to particle accelerators. *The detection of a stochastic background of GWs of cosmological origin would literally provide us with an uncorrupted snapshot of the earliest moments after the big bang, much earlier than those provided by the CMB, and could carry information inaccessible by any other probe.*

Stochastic GW backgrounds are characterized by the energy spectrum  $\Omega_{\text{GW}}(f)$ , which measures the GW energy density per logarithmic interval of frequency, normalized to the critical energy density for closing the Universe; by the angular spectrum, measuring the energy density at different angular scales in the sky; and by their polarization content. In order to detect a stochastic background one has to perform cross-correlation among the outputs of pairs of independent detectors, as would be possible with a single ET observatory, which is made of three non-parallel detectors.

#### 4.4.1 Cosmological backgrounds

One of the targets of ET is the detection and characterization of the stochastic GW background from astrophysical and cosmological sources. On the cosmological side, while the background generated by the amplification of quantum vacuum fluctuations due to the inflationary expansion is expected to be too low to be detected by 3G detectors, there are several other inflation-related mechanisms that can produce detectable signals [253, 254, 4]. For example, large GW amplitudes are naturally produced in inflationary models where there are secondary fields [255] (not responsible for the inflationary period) with arbitrary spin, and coupled to the inflaton either directly or only through a gravitational coupling, or in models where some symmetries are relaxed during the inflationary period [256]. On the other hand, also scenarios alternative to inflation, like e.g. pre-big-bang models inspired by string theory [257–259], predict a spectrum which grows with frequency, resulting in a potentially detectable signal in the ET bandwidth.

Such cosmological backgrounds, beside having a large spectral energy spectrum  $\Omega_{\text{GW}}(f)$ , can be characterized by peculiar features which ET will have the capability to characterize: for instance, models where the inflaton is coupled to an axion field result in a spectrum which increases with frequency (hence, is potentially visible at ET scales while still complying with CMB limits at very low frequencies, see Fig. 4.5) and is *chiral*, with an overproduction of one circular GW polarization with respect to the other. ET, using the dipolar modulation generated by the solar system motion, will be sensitive to such a feature [260], which is a clear indication of the cosmological origin of the signal. Another source of GWs is expected during the (p)reheating period of the Universe, following closely the end of inflation [261–264]. In particular, when “preheat” fields are coupled to the inflaton, these may undergo a non-perturbative excitation after inflation with the consequent generation of GWs. The amplitude of these backgrounds can be very large, and there are scenarios that can peak at frequencies in the ET range. 3G detectors will also have the ability to probe post-inflation expansion scenarios where the equation state parameter is *stiff*,  $1/3 < w \leq 1$  [265].

Different cosmological sources are expected to have different spectral shapes; however, if one is faced with a superposition of cosmological backgrounds, other observables need to be considered. With

<sup>5</sup>At least in standard four-dimensional Einstein-Hilbert gravity. The scale where gravity becomes strong can be somewhat different in string theory, and could even be significantly lowered in theories with large extra dimensions.

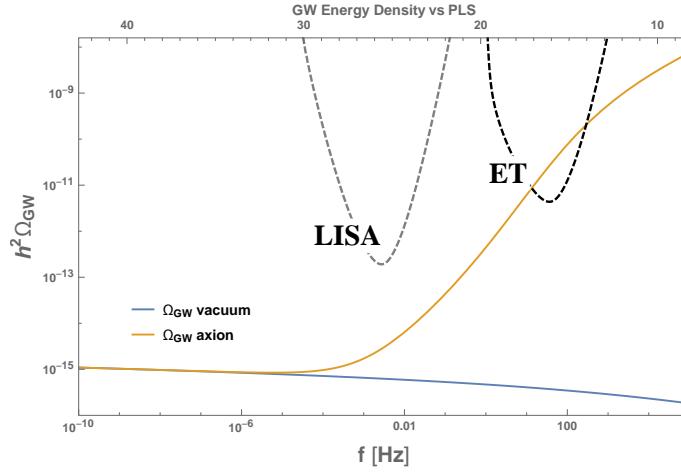


Figure 4.5: Spectrum of GWs today,  $h^2\Omega_{GW}$ , for a model of quadratic inflaton potential, with inflaton - gauge field coupling  $f = M_{Pl}/34$  vs ET and LISA Power Law Sensitivity (PLS) curves.

a network of 3G detectors the resulting angular resolution, and the possibility of cross-correlating them, would allow us to reach in the case of a detectable background the desired resolution to detect angular anisotropies in the GW energy density. At the same time, the statistical properties (and, particularly, its deviation from gaussianity) of the cosmological stochastic GW background will be another possible target for 3G detectors that will allow to distinguish a cosmological background from other stochastic signals [266].

The direct observation of a cosmological stochastic GW background with ET would also provide a unique opportunity to test General Relativity during the early Universe, through the existence of extra polarization modes of GWs. In GR, a GW has two polarization modes, while in a general metric theory of gravitation, GWs can have up to six independent polarizations. If additional polarizations would be found, it would show that the theory of gravity should be extended beyond GR, and would help to discriminate among theoretical models, depending on which polarization modes are detected.

First-order phase transitions are another potential source of a stochastic background. As the Universe expands, its temperature drops and it may undergo a series of phase transitions followed by spontaneous breaking of symmetries. If a phase transition is of first order, a stochastic GW background may be produced as true vacuum bubbles collide and convert the entire Universe to the symmetry-broken phase. In the Standard Model of particle physics, the electroweak and the QCD transitions are just cross-overs, hence any generated gravitational wave signal is not expected to be detectable. However, there are many extensions of the Standard Model (e.g., with additional scalar singlet or doublet, spontaneously broken conformal symmetry, or phase transitions in a hidden sector) which predict strong first-order phase transitions, not necessarily tied to either the electroweak or the QCD phase transition. In such models, the power of the generated gravitational wave signal depends on the energy available for conversion to shear stress, which is determined by the underlying particle physics model. Hence, a stochastic background of GWs will allow us to test particle physics models of the very early Universe, at energy scales far above those that can be reached at the Large Hadron Collider. First-order phase transitions can also lead to turbulence that may generate a stochastic background of gravitational waves.

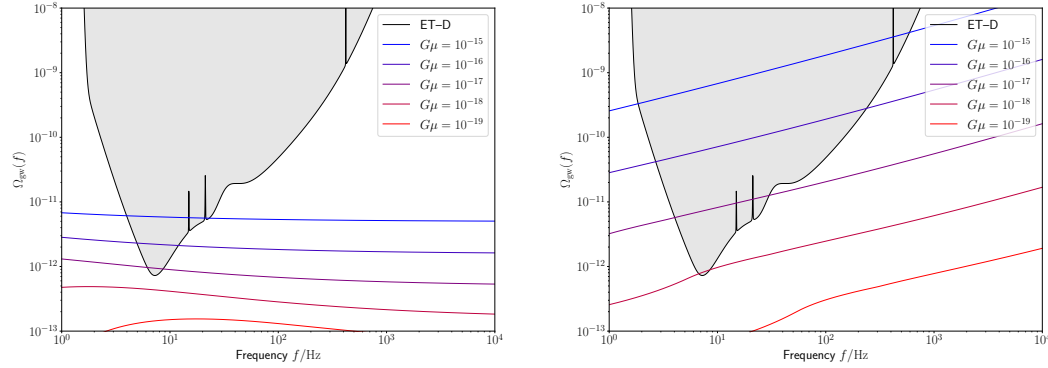


Figure 4.6: The 95% confidence detection region of ET for stochastic backgrounds assuming one year of observation time (shaded area), compared with the prediction for the stochastic GW background from cosmic strings, for two different models of the loop distribution discussed in ref. [10] (left panel) and [11] (right panel). (Figure provided by A.C. Jenkins).

Phase transitions followed by spontaneous breaking of symmetries may leave behind topological defects as relics of the previous more symmetric phase of the Universe. In the context of Grand Unified Theories, it has been shown [267] that one-dimensional defects, called cosmic strings are generically formed. Cosmic string loops oscillate periodically in time, emitting GWs, which depend on a single parameter, the string tension  $\mu$ , related to the energy scale  $\eta$  of the symmetry breaking through

$$G\mu \sim 10^{-6} \left( \frac{\eta}{10^{16} \text{ GeV}} \right)^2. \quad (4.4.1)$$

Cosmic strings may emit bursts of beamed gravitational radiation. The main sources of bursts are kinks, discontinuities on the tangent vector of a string resulting from string inter-commutations and exchange of partners, and cusps, points where the string instantaneously reaches the speed of light. Gravitational back reaction is expected to smooth out the string microstructure which implies that kinky loops become less wiggly and cusps may be the most important points for GW emission. Another possible mechanism leading to bursts of gravitational waves is kink-kink collisions, during which gravitational waves are emitted in all directions. The incoherent superposition of these bursts would generate a stationary and almost Gaussian stochastic background of gravitational waves. Occasionally there may also be sharp and high-amplitude bursts of GWs above this stochastic background. A non-detection of a stochastic background of gravitational waves imposes bounds on the cosmic string tension and therefore on particle physics models beyond the Standard Model. ET will be able to improve on 2G bounds by up to 8 orders of magnitude. As we see from Fig. 4.6, with just one year of data one can detect or exclude values of  $G\mu$  down to  $10^{-17} - 10^{-18}$ , depending on the loop distribution. Finally, within the Standard Model of particle physics, a stochastic background of GWs may be generated from a period of turbulence in the early Universe, which might arise for the evolution of primordial magnetic fields coupled to the highly conducting magnetic fields [268].

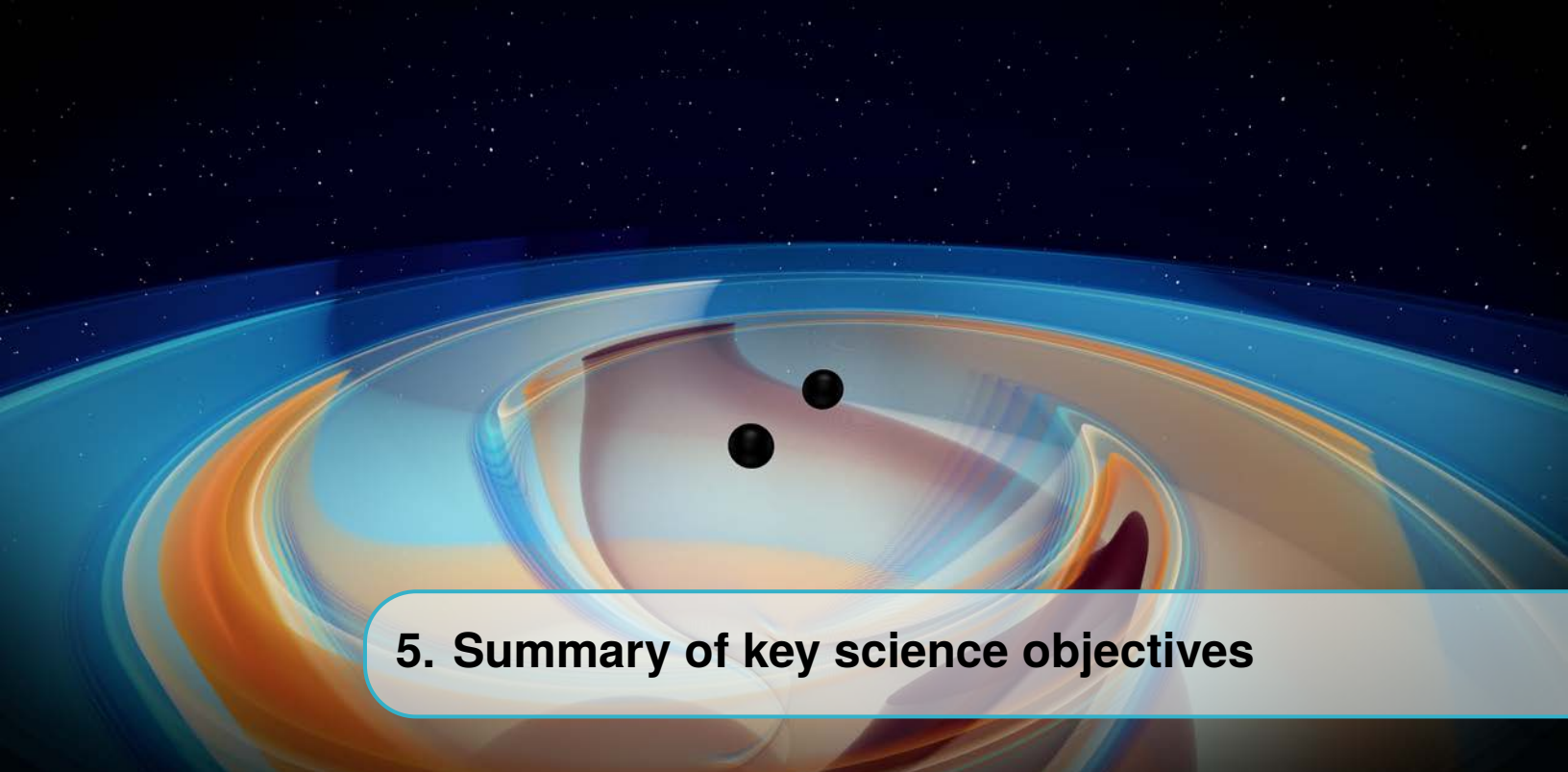
The detection of a weak cosmological background requires the removal of the astrophysical foreground, which is a formidable challenge given the high expected number of signals from coalescing binaries. A simple subtraction of estimated waveforms will be insufficient since estimated waveforms do

not perfectly match the true waveforms leaving sensitivity-limiting residuals in the data [269]. Consequently, advanced data-processing techniques need to be applied. The first method that was proposed makes it possible to project out the residuals [270]. A full Bayesian approach was suggested recently to achieve a combined estimation of the astrophysical and cosmological signals [271]. Both of these methods will push the limits of what will be computationally feasible. Therefore, the ultimate sensitivity achieved in searches of cosmological stochastic backgrounds might not only be limited by the instrument noise, but also by how effective data-analysis methods will be to understand the astrophysical foreground (which, of course, will have their own intrinsic astrophysical interest).

#### 4.4.2 Astrophysical backgrounds

In addition to the cosmological background, an astrophysical contribution will result from the superposition of a large number of unresolved sources too faint to be detected individually. Examples include short-lived burst sources, such as core collapses to neutron stars or black holes, oscillation modes of (proto)-neutron stars, or the final stage of compact binary mergers; periodic long lived sources, typically pulsars; or the early inspiral phase of compact binaries or captures by supermassive black holes, whose frequency is expected to evolve very slowly compared to the observation time [272]. The strongest astrophysical background in the frequency region of terrestrial detectors is expected to be due to the coalescence of binary black holes and binary neutron star systems. To separate the cosmological and the astrophysical backgrounds the first step will be to use any distinct spectral dependence of the average (monopole) amplitude  $\Omega_{\text{GW}}$  [273]. However, the better angular resolution of 3G detectors will most probably allow to spot the anisotropies (directionality dependence) of the astrophysical background. Such anisotropies contain information about the angular distribution of the sources and can be used as a tool for source separation as well as a tracer of astrophysical or cosmological structure. In fact the effects imprinted in the angular power spectrum of the stochastic background, due to the GW distortion by the intervening Large Scale Structure distribution, like Kaiser, Doppler and gravitational potentials effects, can be used to study the Large Scale Structure and make precision cosmology with 3G detectors [274–281]. For resolved sources, 3G detectors can join astronomy facilities to enable thousands of host galaxy identifications from BNS and NSBH mergers. As discussed in sect. 3.3.1, for the best localized sources one could reach a localization accuracy below  $1 \text{ deg}^2$  up to  $z = 0.5$ , corresponding to multipoles  $\ell \sim 100 - 1000$ . On the other hand, the resolution of 3G detectors for the anisotropies of unresolved stochastic signals will be limited by the combination of the detector response and the baseline over which the cross-correlation of individual signals is being carried out (see [282] for a methodological study referring to 2G detectors).

Finally, thanks to the better sensitivity and angular resolution of 3G detectors, also alternative scenarios of production of GWs will be tested: for instance, in U(1) extension of the Standard Model a spin-1 gauge boson, the dark photon, is predicted. If this particle is sufficiently light, it can produce an oscillating force on objects endowed with a dark charge which, on its turn, can bring to a stochastic GW signal potentially detectable by 3G detectors. Ultra-light boson clouds around spinning BH, that we already discussed in the context of continuous GW signals, can also produce a stochastic background due to the superposition of the signals produced by several decaying clouds.



## 5. Summary of key science objectives

We conclude with a summary of the key scientific questions that ET will be able to tackle, expanding on the discussion in sect. 1.2. The Science Case of ET is broad, and addresses crucial problems in astrophysics, in cosmology and in fundamental physics, as summarized below. Furthermore, we should not forget that ET will be a discovery machine: GW detection has literally opened a new window on the Universe. Thanks to third-generation detectors such as ET we will begin to look deeply through this window. This means that we will also penetrate into uncharted territories, where further surprises could (and, in fact, likely, will) await for us. A summary of the key science objectives discussed above is as follows.

- ET will detect binary black hole coalescences up to redshift  $z \sim 20$ , with a rate of order  $10^5 - 10^6$  events per year. It will therefore provide a census of the population of BHs, uncovering the full population of coalescing stellar and intermediate mass BHs in the Universe, over the whole epoch since the end of the cosmological dark ages. This will allow us answering crucial questions on the progenitors, formation, binary evolution and demographics of stellar BHs. Among the millions of events detected by ET, some will have remarkably high signal-to-noise ratio and will provide a sample of events with extraordinarily well-measured properties. This will allow us to understand how binary evolution results in BH-BH mergers, and will give information on several aspects of the dynamics of binaries. The huge number of detections will allow us to cross-correlate the distribution of GW events with large-scale cosmological structures, providing another clue to the origin of the observed BHs, and disentangling astrophysical BHs from primordial BHs that could have been produced by fluctuations in the early Universe. Showing that at least a fraction of the observed BHs are of primordial origin would be a discovery of fundamental importance, which will open a window on the very first moments of the Universe and on physics at correspondingly high energies. The astrophysical discovery potential in this direction is guaranteed. A detector network would result in further

benefits,<sup>1</sup> but even ET as a single detector is fully adequate to address these issues.

- ET will detect BH binaries over a broad mass range from sub-solar masses up to a few times  $10^3 M_\odot$ , extending in particular the upper end of the region of BH masses explored by 2G detectors, which is limited to  $O(100) M_\odot$ . ET will detect BHs of several hundreds solar masses up to redshifts of order 10 or more and BHs of several thousands solar masses up to  $z \sim 1 - 5$  (see Fig. 2.1). This opens the possibility of detecting a whole population of these intermediate mass BHs and studying the possibility that they are the seeds of the supermassive BHs in the center of galaxies. The detections could be performed by a single 3G detectors such as ET, and would complement in an ideal manner the observations expected from LISA: for masses  $M$  in the range  $(10^2 - 10^4) M_\odot$  LISA would observe the long inspiral phase, that could stay in its bandwidth for months or even years, while a 3G detector could see the final and much louder merger phase of the same events.
- ET will detect the coalescence of binary neutron stars up to  $z \simeq 2 - 3$ , with an estimated rate of about  $7 \times 10^4$  events per year. This range reaches the peak of the star formation rate and therefore covers the vast majority of NS binaries coalescing throughout the Universe. This will allow us to investigate their formation mechanisms, evolution and demographics, providing a wealth of astrophysical information. Neutron stars are also remarkable laboratory for studying the physics of strong interactions in an extreme regime of high temperatures and densities. The sensitivity of ET in the high-frequency regime will allow us to access the GW signal of the merger phase, that is inaccessible to 2G detectors and carries detailed information on the internal structure of neutron stars and on their equation of state. This will allow us to study QCD at ultra-high density, including the possibility of phase transitions in the NS core involving deconfined quarks or exotic states of matter. These detections, and a rich science output coming from them, are guaranteed. Again, these goals can be obtained even by ET as a single detector.

Depending on the network of electromagnetic observatories operating at the time, over the years ET will collect a sample of  $O(100)$  binary neutron star coalescences with observed electromagnetic counterpart. Multi-messenger observations of such a large sample of NS binaries will provide unique opportunities. The precision of parameter estimation for the progenitor system (such as masses, spins, and neutron star tidal deformability) and the merger remnant, together with the information from the ultraviolet, optical, near infrared signals, will allow us to obtain a detailed understanding of the physics governing the kilonova emission, to unveil the nuclear physics of neutron stars, and to study heavy element formation at its production site. Joint high-energy and gravitational-wave detections and their multi-wavelength follow-up up to high redshift will probe the short GRBs physics unveiling the formation, propagation and structure of relativistic jets and their interactions with the environment along the cosmic history. Such a sample of joint GW/electromagnetic detections, with luminosity distance measured by gravitational-waves and redshift measured by ground-based telescopes, will provide precise measurements of the Hubble constant, and, even more importantly, to

<sup>1</sup>As we have discussed in sect. 3.3.1, apart from reducing the false alarm rate and increasing the overall signal-to-noise ratio, a detector network is in general important for accurate source localization, which also gives the possibility of identifying an electromagnetic counterpart. For BH-BH binaries the latter point is less relevant, since BH binaries are not expected to have an electromagnetic counterpart. However, as we discussed, accurate localization could provide a characterization of the anisotropies of the binary BH population, allowing for instance studies of correlation with large-scale structure surveys.

investigate the nature of dark energy.

- ET could detect several new astrophysical sources of GWs, such as signals emitted during core collapse supernovae, continuous signals from isolated rotating NSs, and possibly burst signals from NSs. While not guaranteed, these signals would bring breakthrough information. Detecting the GWs from supernovae would elucidate the mechanisms of supernova explosions and its post-collapse phase. The detection of continuous GWs from NSs would allow us to explore the condition of formation and evolutions of isolated NS, providing information on their spin, thermal evolution and magnetic field. ET will be able to detect ‘mountains’ on the surface of a NS as small as  $10^{-3}$  mm, which in turn would again give us information on the inner structure of NS and on the corresponding aspects of nuclear and particle physics, such as the existence of exotic matter in the NS core. A single detector such as ET suffices to search for and exploit these signals. Furthermore, in the case of rotating NSs, a single detector would accurately localize the source, thanks to the Doppler effects from the Earth movement during the observation of the signal which can be continuously observed over months or year time scales.
- Among the millions of observed BH-BH and NS-NS coalescences, those with an optimal combination of masses, distance and orientation will have very high signal-to-noise ratio, and their waveform will be reconstructed by ET with exquisite precision. This will allow accurate tests of General Relativity, both in the inspiral phase, where one can test the validity of the post-Newtonian expansion of GR to sub-permille accuracy (thereby testing the non-linearities of GR), and in the merger and post-merger phase. The accurate observation of the ringdown phase of the final BH will allow the extraction of the frequencies and damping times of several of its longest-lived quasi-normal modes, allowing us to perform stringent tests of the predictions of GR in this extreme regime, literally probing the elasticity of space-time close to the BH horizon. The possibility of performing such accurate tests is guaranteed, and can be performed by ET as a single detector. These tests could also lead to surprises, such as revealing the existence of exotic compact objects, and could even carry observable imprints of quantum gravity effects. While the latter perspective is more speculative, its impact would be revolutionary.
- ET will test several dark matter candidates. If dark matter is made, at least in part, by primordial BHs in the mass range  $\sim 0.1 - 100 M_{\odot}$ , ET will be able to provide definite evidence for them. Thanks to its extraordinary reach, ET could observe BH binaries at redshift  $z \sim 10 - 20$ , before any stars had formed that could create black holes in the usual way; even a single event observed at such redshift would have necessarily a non-stellar origin. Furthermore, thanks to the extension of its frequency band toward both low and high frequencies, ET will detect BHs across a large spectrum of masses. The detection of even a single BH of sub-solar mass would again point clearly to a non-stellar origin. This topic belongs to those whose success is not guaranteed (observed BHs could, after all, have just stellar origin) but certainly belongs to the high-gain category. Showing that at least a fraction of the observed BHs are of primordial origin would be a discovery of fundamental importance not only in astrophysics but also from the point of view of fundamental physics and cosmology, providing unique information on primordial inflation and on physics at correspondingly high energies. Another dark matter candidate that will be tested by ET is an ultralight boson such as a light axion, that could form a bosonic cloud near a BH, or more generally dark matter particles that are captured by compact

objects and accumulate in the core of a NS, or that accumulate near compact objects and create a drag in the dynamics of a compact binary. ET will be able to explore these possibilities even as a single detector.

- ET will explore the nature of dark energy and the possibility of modifications of General Relativity at cosmological distances. The simultaneous measurement of the luminosity distance to the source, through GW observations, and their redshift, from an electromagnetic counterpart, provides a powerful tool of the expansion history of the Universe, and could carry very distinctive signature of modifications from GR. In particular, the propagation of GWs across cosmological distances, in theories where dark energy has a dynamical origin, is generally different from that in GR. This will allow to test the sector of tensor perturbations over a cosmological background, which is accessible only to GW experiments. Thanks to the large number of detections, ET could probe the luminosity-distance relation even using sources without electromagnetic counterpart, by using statistical techniques, but this topic would significantly benefit from the presence of a network of GW detectors leading to accurate localization of many sources (allowing for the measurement of the redshift from electromagnetic follow-up observations, as with GW170817), or from synergies with gamma-ray burst detectors. From the point of view of cosmology, ET is guaranteed to obtain important results (accurate measurement of  $H_0$ , significant limits on the equation of state of dark energy), complementary to measurements obtained with electromagnetic probes. The possibility of detecting modifications of General Relativity at cosmological scales and understanding the origin of dark energy is not guaranteed, but would be revolutionary.
- ET will search for stochastic backgrounds of GWs, which are relics of the earliest cosmological epochs. Such backgrounds, if detected, would carry information of the earliest moment of the Universe, and on physics at the corresponding high-energy scales, that would be inaccessible by electromagnetic (or neutrino) observations. ET, thanks to its design corresponding to three independent interferometers, could obtain significant limits on stochastic backgrounds already as a single detector, although a network of two well-separated 3G detectors would have a better rejection of local background noise and would allow to resolve the angular anisotropies of the background. In particular, ET can contribute to shedding light on early Universe models of inflation and is also sensitive to features that will allow to disentangle a cosmological background from an astrophysical one. It can test the post-inflationary period through GW from a (p)reheating stage after inflation and from a stiff phase of evolution. It will have enough angular resolution to distinguish galactic from extragalactic backgrounds of GW through the characterization and mapping of the angular distribution of GW anisotropies both from astrophysical and cosmological sources. Stochastic backgrounds of cosmological origin in the ET frequency window depend on physics beyond the Standard Model. Thus, the predictions are unavoidably uncertain, and the gain from a successful detection would be correspondingly high, allowing us to explore the earliest moments after the big bang.

**Part II**

**SITE, INFRASTRUCTURE AND  
INSTRUMENTATION**





## 6. Detector

This chapter will focus on the technical implementation of the detectors housed in the ET infrastructure. The strategies, designs and techniques to meet the the unprecedented sensitivity of this new observatory will be detailed.

### 6.1 Optical layout

The Einstein Telescope will consist of three nested detectors, which will be arranged in a triangular pattern as shown in figure 6.1. In contrast to the traditional L-shaped geometry of the first gravitational wave observatories this arrangement is equally sensitive for both polarisations of the gravitational wave. Additionally it shows a more isotropic antenna pattern compared to the L-shaped detectors with sky localisation possibilities. The overall frequency range covered will span from 3 Hz to several kHz.

Each individual detector in turn will comprise two interferometers, one specialised for detecting low-frequency gravitational waves and the other one for the high-frequency part of the spectrum. The sensitivity goal for each interferometer is shown in figure 1.10. Each individual interferometer has a dual-recycled Michelson topology with Fabry-Perot arm cavities. This is a mature and well tested configuration currently employed in second-generation detectors, such as the current Virgo and LIGO detectors.

This section describes the details of the ET optical layout, such as the laser beam sizes, beam shapes and distances between optical components inside the arm cavities and central interferometer including

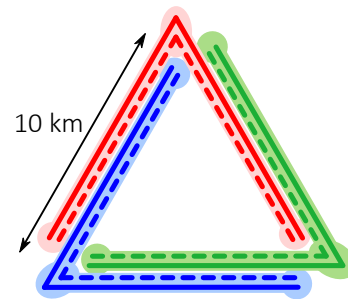


Figure 6.1: Three nested detectors in a triangular arrangement will form the final Einstein Telescope geometry.

the power and signal recycling cavities. A schematic sketch of the optical layout of all core optics of the interferometers is shown in figure 6.2.

The length of the main arm cavity is one of the most crucial parameters of the detector as it impacts the achievable sensitivity but also the construction cost. The first driver of the arm length is the science goal of ET as described in section 3.1. To detect the fusion of black holes all over the universe, numerical simulations have shown that a 10 km long arm cavity is a minimum requirement. Longer arm could always bring better sensitivity as the GW signal is accumulated over the arm length and has to be compared with the mirror local displacement noise (independent of the arm length). However it may come at the cost of a reduced bandwidth depending on the tuning of the recycling cavity.

A second, more practical argument points towards arm cavities with a maximum length of 12 km. It is a direct consequence of the diffraction of the laser beam circulating in the arms. The longer the arms, the larger the size of the laser beam on the mirror, with more light falling outside the finite size of the optics. This increase of the cavity optical loss could have a dramatic effect as it is enhanced by the cavity finesse and the recycling cavity and ultimately it is degrading the interferometer sensitivity. More specifically, the constraint comes from ET-LF as a longer wavelength means larger beams for the same cavity length and the size of the crystalline substrate is limited by industrial capabilities (which are not driven by the GW community). Currently the maximum diameter for silicon substrates is 45 cm, leading to a maximum arm length of 12 km at 1550 nm. If in the next decades, larger crystals are available, ET would still benefit from these larger cryogenic optics by using wider laser beams and hence reducing further the thermal noise level.

### 6.1.1 A xylophone design for ET

Spanning the detection band over more than three orders of magnitude in frequency, as it is expected for ET, is technically extremely challenging: different noise types dominate the various frequency bands and often show opposite responses to different tuning of the same design parameter.

In the following we provide fundamental issues of a broadband third-generation interferometer that could be resolved by using a set of xylophone detectors [283]:

- **Control Noises:** Many noise sources limiting the second generation GW detectors at the low frequency end seem to become more challenging with increased optical power: classical radiation pressure forces and torques originating from residual misalignments and beam jitter dominate the dynamics of the interferometer mirrors and hence the local and global control loops. The xylophone concept will help ET to achieve its unprecedented low-frequency sensitivity target by minimising the radiation pressure driven forces on the mirrors of the ET LF detector.
- **Shot Noise vs Radiation Pressure Noise:** Due to the fact that the shot noise contribution scales inversely with optical power, but the photon radiation pressure noise contribution on the other hand scales proportionally to the optical power, it will be hard to obtain the desired bandwidth with a single detector. Therefore, again it will be very beneficial to split ET into a low-power low-frequency and a high-power high-frequency companion.
- **High Power vs Cryogenic Temperature:** In a single broadband ET observatory the simultaneous use of high optical power (a few megawatts) to achieve the required high frequency sensitivity and test masses at cryogenic temperatures in the 10 to 20 K range in order to

Parameter	ET-HF	ET-LF
Arm length	10 km	10 km
Input power (after IMC)	500 W	3 W
Arm power	3 MW	18 kW
Temperature	290 K	10-20 K
Mirror material	fused silica	silicon
Mirror diameter / thickness	62 cm / 30 cm	45 cm/ 57 cm
Mirror masses	200 kg	211 kg
Laser wavelength	1064 nm	1550 nm
SR-phase (rad)	tuned (0.0)	detuned (0.6)
SR transmittance	10 %	20 %
Quantum noise suppression	freq. dep. squeez.	freq. dep. squeez.
Filter cavities	1×300 m	2×1.0 km
Squeezing level	10 dB (effective)	10 dB (effective)
Beam shape	TEM <sub>00</sub>	TEM <sub>00</sub>
Beam radius	12.0 cm	9 cm
Scatter loss per surface	37 ppm	37 ppm
Seismic isolation	SA, 8 m tall	mod SA, 17 m tall
Seismic (for $f > 1$ Hz)	$5 \cdot 10^{-10} \text{ m}/f^2$	$5 \cdot 10^{-10} \text{ m}/f^2$
Gravity gradient subtraction	none	factor of a few

Table 6.1: Summary of the most important parameters of the ET high and low frequency interferometers. SA = super attenuator, freq. dep. squeez. = squeezing with frequency dependent angle.

provide the required suppression of thermal noise to achieve the required low frequency sensitivity would pose a strong challenge. Even though extremely small, the residual absorption of the dielectric mirror coatings deposits heat in the mirrors which is difficult to extract, without spoiling the performance of the seismic isolation systems. The preferred solution for this problem is a xylophone design consisting of a high-frequency detector featuring high power and high temperature, and a low-frequency detector featuring low power and cryogenic temperatures.

The xylophone concept was first suggested for the Advanced LIGO project, proposing to complement the standard broadband interferometers with an interferometer optimized for lower frequency, thus enhancing the detection of high-mass binary systems [284, 285]. While a xylophone will increase the required hardware and therefore cost, this concept provides a sensitivity that would otherwise not be achievable in practice.

The baseline for ET is a 2-band xylophone detector configuration, composed of a low-frequency (ET-LF) and a high-frequency (ET-HF) interferometer. Both interferometers are Michelson interferometers featuring 10 km arm length with an opening angle of 60 degrees. Due to their similar geometry both detectors will share common tunnels. Table 6.1 gives a brief overview of the main parameters of the analysed low-frequency (ET-LF) and high-frequency (ET-HF) interferometers. Figure 6.3 shows sketches of the corresponding core interferometers and the filter cavities. The full layout of the central part of the two interferometers of a single ET detector is depicted in Figure 6.2.

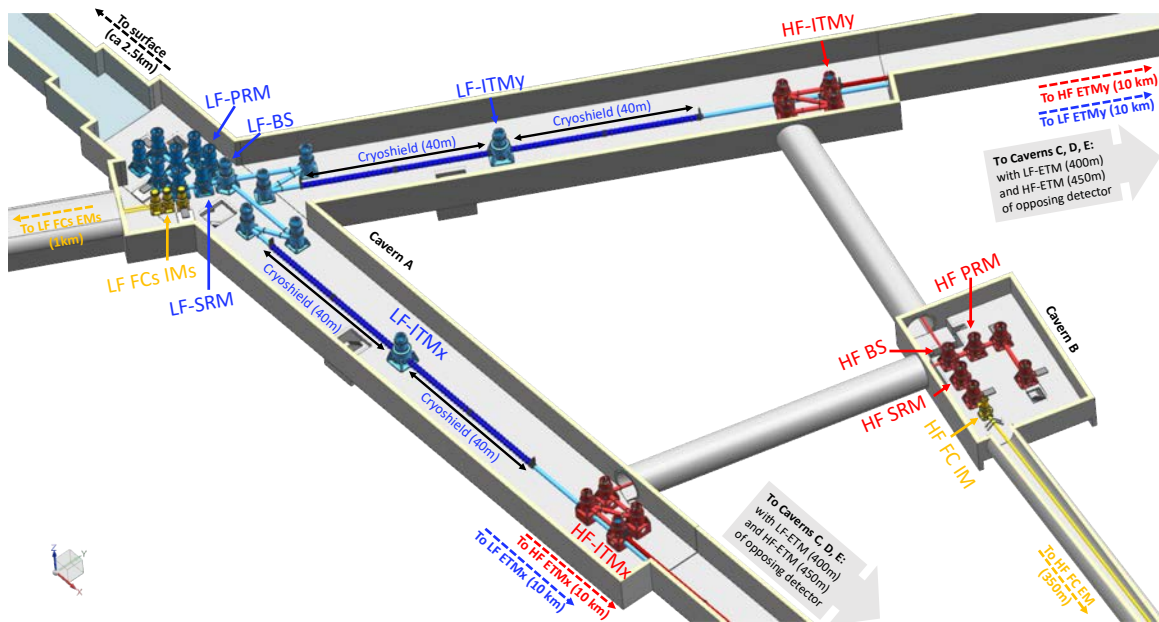


Figure 6.2: Schematic overview of the corner caverns and central interferometers of one of the three ET detectors. (Used acronyms: LF = low frequency; HF = high frequency; ITM = input mirror; ETM = end mirror; BS = beam splitter; PRM = power recycling mirror); SRM = Signal recycling; FC = filter cavity; x/y = x/y-arm).

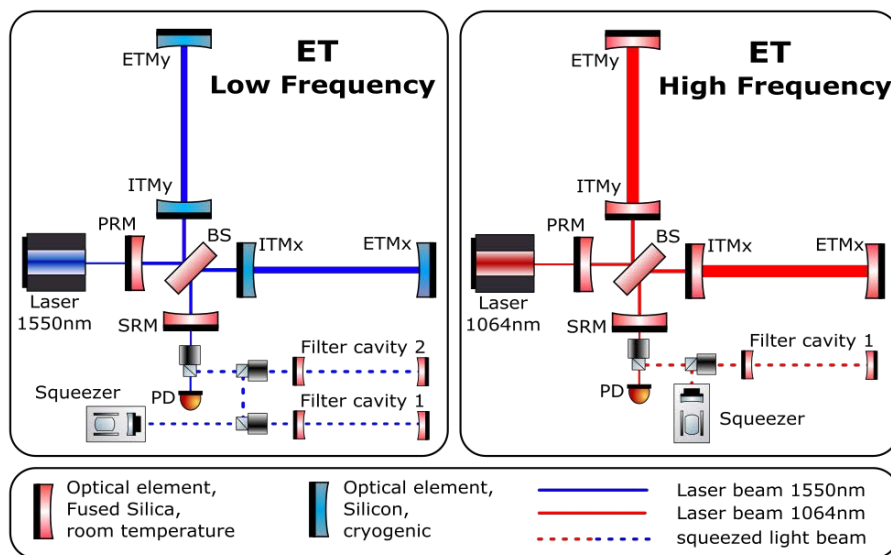


Figure 6.3: Simplified sketch of the ET low and high frequency interferometers of a single ET-detector.

### 6.1.2 Arm cavity design

The size and shape of the laser beam inside the interferometer is defined by the surface profile of the cavity mirrors; the beam sizes at the arm cavity input mirrors (ITM) and arm cavity end mirrors (ETM) as well as the position of the cavity waist are determined by only two parameters, the radii of curvature (ROC) of ITM and ETM for a fixed cavity length. Since the GW interacts with the laser light inside the two Fabry-Perot cavities of the Michelson interferometer, creating signal sidebands, the two arm cavities can be seen as the heart of the ET interferometers. The characteristics of the arm cavities have not only a high impact on the detector sensitivity and bandwidth, but also on the overall detector performance.

The choice of the beam size on the arm cavity mirrors is a trade-off process taking the following considerations into account:

- A large laser beam size on the cavity mirrors is advantageous to reduce the displacement noise induced by the various thermal noises of the mirrors.
- The upper limit for the manageable beam size is given firstly by the maximum available mirror substrate size and secondly by the closeness to the cavity instability.

A common criterion to define the beam size is to demand the optical power loss due to clipping (light being lost outside the reflective surface area) to be less than 1 ppm. This results in a scaling factor between beam and mirror radius of 2.63 (for TEM<sub>00</sub> modes), see [286].

Using the minimal beam sizes is obviously not optimal in terms of thermal noise. To reach the thermal noise induced displacement compatible with the ET-HF sensitivity, the laser beam radius on the mirror must be 12 cm which corresponds to about 62 cm substrate diameter for fused silica mirrors to have negligible clipping optical loss. For ET-LF, the diameter of the substrate is set to 45 cm for the silicon mirrors. Assuming 10 km long arm cavities, we can derive the following arm cavity characteristics.

IFO	$\lambda$	mode	mirror $\varnothing$	$R_C$	$w_0$	$z_0$	$w$	$g$ -factor
ET-HF	1064 nm	TEM <sub>00</sub>	62 cm	5070 m	1.42 cm	5000 m	12.0 cm	0.95
ET-LF	1550 nm	TEM <sub>00</sub>	45 cm	5580 m	2.9 cm	5000 m	9.0 cm	0.63

### 6.1.3 Central interferometer design

The central interferometer consists of the two recycling cavities and the central Michelson interferometer formed by the beam splitter and the arm cavity input mirrors. The design of the central interferometer is mainly determined by two constraints. First of all it should allow for the implementation of non-degenerate recycling cavities. Second, the central interferometer has to serve as mode-matching and pointing telescope for the arm cavities.

The recycling cavity design used by the current detectors can probably not be directly adapted for ET, because no beam splitter substrates of the required dimensions would be available. For example the high frequency interferometer featuring an opening angle of 60 degree would require a beam splitter with a diameter of more than 120 cm.

Therefore we plan to investigate design options making use of input mirror substrates including a focusing lens and introducing a two telescope mirrors in a z-configuration between the ITMs and the

central beam splitter, see Fig. 6.4. Please note that the arm cavity mirrors and possibly the telescope mirrors are the only full sized optical elements and that the beam splitter and recycling mirrors can be made significantly smaller.

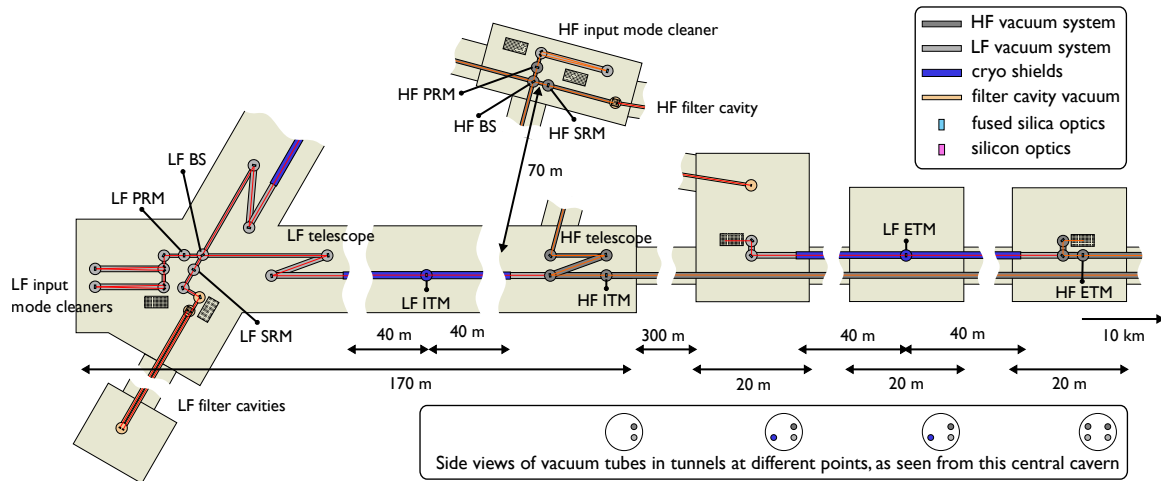


Figure 6.4: Sketch of the optical layout in one corner of the triangle of ET. One can notice in particular the geometrical design of the recycling cavities featuring folded telescopes between the beam splitter and input mirrors. The acronyms used are detailed in the text.

## 6.2 Core optics

This section focuses on the mirrors forming the arm cavities of the interferometer (ITM and ETM). Those optics, also called test masses, are the largest by dimension (with the exception of the beamsplitters) and the most critical ones whose displacement noise can directly degrade the sensitivity of the detector to the gravitational wave signals.

To ensure the best optics, the three ingredients of a mirror: substrate, polishing and coating will have to use state of the art technologies. An overview of current achievements and the core optics strategy for ET is presented in the following sections. The temperature at which the mirror is operated has a strong impact on the technological choices to be made so different materials will be used for the mirrors of the room temperature and of the cryogenic interferometers.

### 6.2.1 The substrate materials

The substrate of the large ET main optics must meet considerable requirements in terms of optical and mechanical properties, moreover it should be available in large sizes with surfaces polished to the atomic level. Due to constraints of the thermomechanical properties, only two specific materials can be considered: fused silica for room temperature interferometer and silicon for cryogenic temperatures.

### 6.2.1.1 Fused silica

Fused silica is the substrate of choice for all the current room temperature interferometers. Due to its extensive use for first and second generation gravitational wave detectors, this material has been broadly characterised at room temperature. Moreover the polishing and coating are now well mastered for this material [287].

The operating wavelength of room temperature will be 1064 nm, the same as current interferometers and well within the transparency region of fused silica. At this wavelength fused silica exhibits very low bulk optical absorption (below 1 ppm/cm) with high homogeneity of refractive index (relative optical path length  $< 0.1$  nm/cm over the central part) and very low birefringence (around 1 nm/cm [288]). The material can be isotropic in 3 dimensions which is ideal for the central beamsplitter where laser beams are crossing the substrate at different angles.

In addition to its outstanding optical properties, fused silica presents a very low Brownian thermal noise at room temperature. Additionally, there exist techniques to fabricate quasi-monolithic suspensions based on pulled fused silica fibres and silicate bonding to further reduce the suspension thermal noise. These techniques have demonstrated their reliability and performances for years in the GEO600 detector [289] and in the LIGO and Virgo detectors [290, 291].

The upgrade of Advanced Virgo, called Advanced Virgo+, will use test masses in fused silica of diameter 55 cm weighting 100 kg, an essential step towards the optics for ET-HF, which will be the same material and with a diameter of 62 cm and mass of 200 kg.

*Fused silica for large optical substrates presents the best optical and mechanical performances at room temperature and with very limited risks.*

### 6.2.1.2 Silicon

Silicon is the preferred material for the test masses for the cryogenic interferometer, ET-LF. Unlike fused silica (and sapphire), silicon is not transparent at 1064 nm and so the operating wavelength of the detector has to be shifted to 1550 nm.

Silicon has excellent mechanical and thermal properties and is easily available in relatively high quality due to the large market of the semiconductor industry. The coefficient of thermal expansion is zero at two special temperatures around 18 K and 125 K [292]. At these temperatures the contribution of thermo-elastic noise will therefore vanish. The mechanical loss of silicon has been studied by Q-factor measurements. It was experimentally shown that silicon bulk samples can reach mechanical losses as low as  $1 \times 10^{-9}$  at 10 K which is outstanding [293].

The maximum available diameter and purity of silicon depends on the fabrication process. The two main growing processes for single crystal silicon used by the semiconductor industry are the Czochralski (CZ) and the Float Zone (FZ) methods. CZ silicon is grown from a silicon melt in a silica crucible. It results in relative large samples with a reasonable purity. The most dominant impurities in undoped CZ-grown silicon are carbon (typically  $10^{-18}$  cm<sup>-3</sup>) and oxygen (typically up to  $10^{-19}$  cm<sup>-3</sup>). In contrast, FZ silicon contains the same impurities but in much smaller concentrations (up to  $10^3$  times smaller). During the FZ growth process, single or poly-crystalline silicon is remelted by means of inductive heating in vacuum or under an inert atmosphere. Impurities dissolve better in

the melt than in the solid part. The re-crystallised material has therefore a higher purity than the initial one. By slowly sweeping the melt from one end to the other it is possible to purify in steps. The mechanism of inductive heating sets limits to the current production setups and leads to smaller available samples.

Using the CZ growth technique, silicon ingots up to 45 cm of diameter can be produced however 30 cm is still the most common wafer diameter in the semiconductor industry. For FZ silicon the diameter is currently limited to 20 cm.

In the recent years, motivated by the possible use of silicon as test mass material, the optical properties of silicon have been extensively characterised. A direct link between bulk absorption at 1550 nm and the concentration of impurities was demonstrated [294]. For FZ silicon, absorption below 5 ppm/cm has been measured which is compatible with the ET-LF requirement. During the absorption studies, excess optical absorption at the surface of silicon was reported [295] which is likely linked to the polishing techniques used and not intrinsic to the material [296]. According to the latest measurement, magnetic Czochralski (mCz) growth technique would be the most suitable approach for ET as it can combine large diameter ingot (45 cm) with very low impurities, with absorption  $\sim 20$  ppm/cm achieved.

Thanks to the limited intensity of the laser beam in ET-LF, non linear effects such as two photon absorption [297] or Kerr effect are expected to be negligible in silicon.

Other characterisations done in the framework of the Einstein Telescope include the measurement of thermo-optic coefficient at low temperature [298] which is essential to derive the thermal lensing magnitude and the substrate thermo-refractive noise and also the birefringence [299] which is in the same order of magnitude as for sapphire.

To validate our choice of silicon substrates for ET-LF, we need to demonstrate optical absorption as low as a few ppm on samples with sufficient size (diameter of 45 cm). Silicon ingots made with mCz show evidence of meeting those specifications on some samples, however the repeatability has yet to be appropriately demonstrated.

### 6.2.2 Surface polishing

The polishing capability will depend on the substrate material. Polishing of fused silica is well mastered thanks to current generation of room temperature interferometers and hence presents little risks. For the Einstein Telescope, the same flatness and roughness that was achieved<sup>1</sup> for the current detectors will be enough, albeit on a larger area. Due to the heavier substrate, special handling tools will have to be manufactured. The large end mirrors of Advanced Virgo+ with a diameter of 550 mm and weighing 100 kg represent an important step towards the procurement of the ET mirrors.

Polishing of silicon does not carry any difficulties as this substrate material is commonly used for X-ray mirrors. Experiences from polishing companies indicate that silicon could be polished the same way as fused silica and similar performances on the flatness could be achieved (using also ion beam figuring to reach sub-nanometer flatness). The very low roughness is more challenging but

---

<sup>1</sup>flatness inferior to 0.5 nm RMS and roughness below 0.1 nm RMS on the central part [287].

0.2 nm RMS could be achieved and is acceptable for ET. In short, the polishing of the large silicon substrates of ET is within the reach of the current technology.

Sapphire - the backup choice for low temperature test mass - is one of the hardest known material and has always been very difficult to polish. However, as demonstrated by the KAGRA detector, the outstanding surface quality of fused silica could also be reproduced on sapphire [300] but at longer time and higher cost.

*The polishing of the large substrates of the Einstein Telescope is within the current polishing capability and as such does not pose any significant challenges.*

### 6.2.3 Other core optics

Central interferometer optics such as Power and Signal Recycling Mirrors (PRM and SRM) will be smaller in size (diameter in the order of 10 cm) and at room temperature for both interferometers. Fused silica is hence the preferred material for the substrates. The coating for 1064 nm and 1550 nm will use the same materials as for ET-HF to benefit from state of the art deposition process. The procurement of those optics does not represent any challenges.

## 6.3 Coatings

### 6.3.1 Coating procurement

Thin optical coatings, a few microns in thickness, must be applied to the surfaces of the inteferometer mirrors to make them highly reflective. Since the thermal noise from these coatings will already limit the sensitivity of current room-temperature detectors at their most sensitive frequencies [301, 302], it is essential to reduce coating thermal noise to achieve ET design sensitivity.

Highly-reflective coatings are usually composed of a stack of layers of alternating refractive index, with each layer having an optical thickness of a quarter of a wavelength. Using more layers or materials with a larger refractive index contrast results in higher reflectivity. Different layer thicknesses may be used to reduce thermo-optic noise, to optimise the coating thermal noise [303] or to provide reflectivity at more than one wavelength.

The amplitude spectral density (ASD) of coating thermal noise can be approximated by [304],

$$x(f) = \sqrt{\frac{2k_B T}{\pi^2 f} \frac{d}{w^2} \phi \left( \frac{Y_{\text{coat}}}{Y_{\text{sub}}^2} + \frac{1}{Y_{\text{coat}}} \right)} \quad (6.3.1)$$

where  $k_B$  is the Boltzmann constant,  $T$  the mirror temperature,  $f$  the frequency,  $d$  the coating thickness,  $w$  the radius of the laser beam on the coating and  $\phi$  the mechanical loss of the coating.  $Y_{\text{sub}}$  and  $Y_{\text{coat}}$  are the Young's moduli of the substrate and coating materials. This formula assumes that the bulk and shear mechanical loss angles of the coating are identical, that the mechanical loss is frequency independent and that the Poisson ratios of the coating and the substrate are zero. Further

discussion of the validity of some of these assumptions is given below. While Eqn 6.3.1 is often used to estimate thermal noise, it should be noted that the result can be as much as 30% different from the result given by the full formula which accounts for field penetration into the coating and does not neglect the Poisson ratios.

The main approaches to reducing coating thermal noise can be identified from Eqn 6.3.1:

- Reducing the loss of the coating materials (lower  $\phi$ ) e.g. by varying deposition parameters, post-deposition treatments or by developing alternative coating materials
- Reducing the required thickness of the coating (lower  $d$ ) - using materials with a large contrast in refractive index results in fewer pairs of layers being required to provide the same reflectivity.
- Reducing the mirror temperature (lower  $T$ ). While this directly reduces the thermal energy in the system, care is needed as the mechanical loss of many materials is strongly temperature dependent.
- Increasing the interferometer laser beam radius on the mirrors (larger  $w$ ). This averages thermal motion of the coating over a larger area, reducing the noise. However, the laser spot size is limited by the radius of the mirror to keep scattering / diffraction losses at the edge of the mirror to an acceptable level.

Furthermore, the lowest coating thermal noise occurs when the coating Young's modulus is matched to that of the substrate [305, 306]. Current detectors use coatings formed from alternating layers of silica ( $\text{SiO}_2$ ) and titania-doped tantala ( $\text{TiO}_2\text{-Ta}_2\text{O}_5$ ) [307–310]. The loss of these coatings has been observed to increase at cryogenic temperatures, to a peak at  $\sim 30$  K [311]. Similar loss peaks have been observed in single layers of  $\text{SiO}_2$  [312] and  $\text{TiO}_2\text{-Ta}_2\text{O}_5$  [313], with the magnitude of the loss and the temperature at which loss peaks occur being strongly dependent on post-deposition annealing temperature [314, 315]. Current coatings are therefore not suitable for use at low temperatures <sup>2</sup>.

### 6.3.2 Coating thermal noise - full treatment

Equation 6.3.1 is a useful and convenient approximation of the magnitude of coating thermal noise. However, a material can have two independent loss angles, associated with shear deformations and 'bulk' (volume change) deformations. These loss angles are assumed to be identical in Eqn 6.3.1; for many materials, this is unlikely to be a valid assumption. A more complete expression for coating thermal noise in terms of bulk and shear loss is given by Hong [317]. This treatment also shows that the thermal noise measured by an interferometer is more sensitive to the bulk loss angle than to the shear loss angle. For detailed thermal noise calculations, it is therefore important to know both the bulk and shear loss of the coating materials.

Equation 6.3.1 ignores also the effect of the penetration of the laser beam into the coating stack. In reality, the sensitivity of the interferometer to thermal motion in a particular layer is dependent on that layer's position in the coating stack [317–320]. While this usually results in a small correction of 10% or less, this effect must be taken into account when making accurate thermal noise predictions.

<sup>2</sup>One study of an ion-beam sputtered silica/tantala coating did not show evidence of a loss peak at low temperature: however, the level of loss is still higher than required for ET-LF [316]

### 6.3.3 Coating requirements

#### 6.3.3.1 ET-LF

To meet the science goals, ET-LF requires a reduction in coating displacement thermal noise by at least a factor of 10 with respect to current gravitational wave detectors. Some of this improvement can be obtained from operating at low temperature and through the use of larger laser beam spots on the mirrors. The remainder of the improvement will need to come from the coating materials themselves. The most relevant material properties are the coating mechanical loss and the coating thickness (which is determined by the combination of refractive indices of the materials used in the coating stack). However, the elastic modulus of the coating (and of the mirror substrate) also contributes to the magnitude of the coating thermal noise.

For operation at 10 K, after accounting for the effect of temperature and the use of larger beams in ET-LF, a reduction in the amplitude of coating thermal noise by a factor of 1.24 must be obtained from improved coating materials. When taking account of the substrate modulus effects, and assuming all coating properties except mechanical loss remain the same as in aLIGO, this translates to a factor of 3.8 reduction in coating loss compared to the loss of  $\text{SiO}_2/\text{TiO}_2:\text{Ta}_2\text{O}_5$  at 10 K.

#### 6.3.3.2 ET-HF

The target for ET-HF is a factor of 3.2 reduction in coating thermal noise ASD at 100 Hz compared to aLIGO design sensitivity. Accounting for the slightly larger laser beam in ET-HF, this sets a requirement of a reduction in ASD by a factor of 2.7 from the coating materials. If we assume all coating properties except the mechanical loss remain identical, then a reduction in mechanical loss by a factor of 7.1 with respect to the aLIGO coatings is required.

#### 6.3.3.3 Other requirements

In addition to meeting these thermal noise requirements, the coatings must have low optical absorption and low scattering. Low absorption is essential to minimise the heat-load on the cryogenic mirror, with a nominal target of 5 ppm absorption set. Significantly lower absorption – perhaps similar to the sub-ppm absorption of the current aLIGO and Advanced Virgo coatings – may be required to enable the design of suspension fibres which can successfully extract the laser power absorbed by the mirror while also having acceptably low thermal noise [321]. Further studies in this area are likely to be required as detailed suspension designs are developed. For ET-HF, the coating optical absorption is also critical to limit the thermal expansion of the surface of the mirrors. The same absorption limit of 0.5 ppm similar to current detectors will still hold.

Low scattering is required to minimise the optical round trip loss from the arm cavities and to prevent scattered light picking up additional phase noise (e.g. by reflection from the non-isolated beam tube) and coupling back into the interferometer beam. The target for scattering as optical loss is in the order of 10-20 ppm per mirror; point defects, for their absorption and scatter, must be strictly controlled.

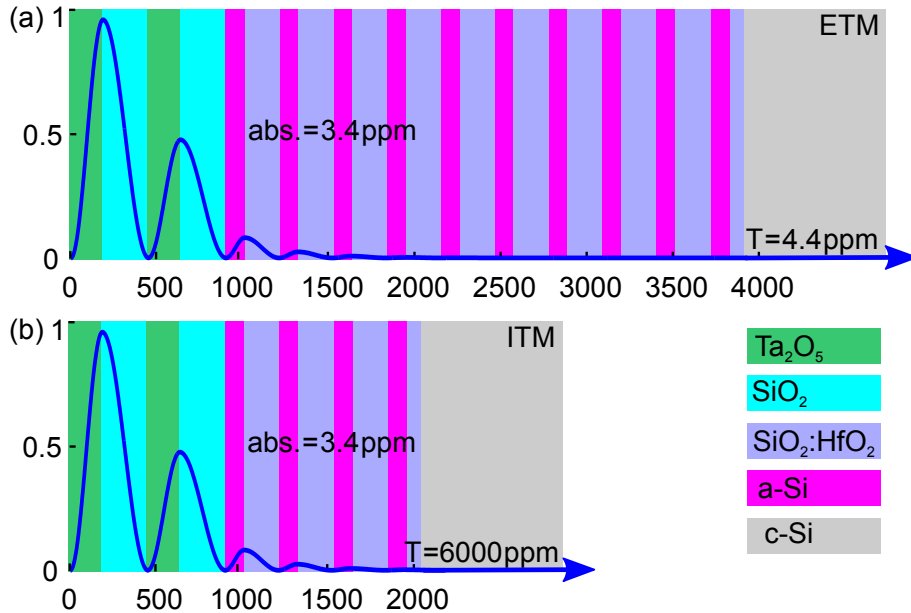


Figure 6.5: A multimaterial coatings design for (a) an ETM and (b) and ITM. This design uses an upper stack of  $\text{SiO}_2/\text{Ta}_2\text{O}_5$  on top of a  $\text{SiO}_2:\text{HfO}_2/\text{aSi}$  lower stack [12]. The blue lines show the electric field intensity as a function of depth in the coating.

### 6.3.4 Coating design solutions

#### 6.3.4.1 Multimaterial coatings

The use of so-called multimaterial coating designs has been proposed to enable the use of coating materials with higher optical absorption than can be tolerated in a traditional 2-material design [322, 323]. In a multimaterial coating, the top few coating layers are made from low-absorption materials e.g. silica/tantala. These layers reflect the majority of the incident laser power, reducing the light intensity in the coating to a level where higher-absorption materials (e.g. aSi, in combination with a low-index material) can be tolerated in the lower part of the stack. This allows the low mechanical loss of materials such as aSi to be exploited, without significantly increasing the total absorption of the coating stack.

Several possible multi-material designs have been proposed to date [12, 324–327], including one that, in principle, would meet the ET-LF coating thermal noise target for an optical absorption of 3.4 ppm [12]. This coating design relies on a level of absorption in aSi films which has been observed [327], but has not yet been demonstrated reproducibly or on the scale required for ET.

Experimental verification of the performance of prototype multimaterial coatings has been reported [328, 329] – although it should be noted that a coating meeting the thermal noise and optical requirements of ET-LF has not been tested to date.

### 6.3.4.2 Nanolayer coatings

Annealing at high temperatures is desirable to reduce the mechanical loss and optical absorption of many coatings: however, the onset of crystallisation (which results in higher mechanical loss and increased optical scattering) can limit the maximum tolerable annealing temperature. The nanolayer approach involves composing a single coating layer out of a stack of thinner layers of two materials [330, 331]. This substructure can inhibit crystallisation in the material, allowing higher annealing temperatures and lower mechanical loss to be achieved. This has been demonstrated for a high-index coating layer formed from a substructure of titania/silica nanolayers [330].

More recently, it has been shown that the cryogenic loss peaks observed in silica coatings can be eliminated by using silica nanolayers separated with titania 'blocking' layers [332]. Nanolayer coatings may therefore provide an excellent way to gain better performance from amorphous oxide materials at low temperatures. An important consideration for nanolayer coatings is to define the precision and uniformity with which each nanolayer needs to be deposited, along with consideration of diffusion between layers. Further investigations are required to validate full high-reflectivity stacks based on nanolayer structures.

### 6.3.4.3 Coating structure and mechanical loss

Significant progress has been made in predicting the cryogenic mechanical loss of coating materials computationally using molecular dynamics simulations [333–336] and to obtain agreement with trends and magnitudes of experimental loss data.

Other structural work has shown the room-temperature loss may be correlated with medium-range order in Ta<sub>2</sub>O<sub>5</sub> coatings, with more ordered structures and lower loss resulting from heat-treatment [337]. The evidence points towards the possibility that the same structural features responsible for low loss at room-temperature may be responsible for higher loss at cryogenic temperature. Raman spectroscopy studies have identified correlations between the ring structures and loss in silica coatings [338], with further recent work showing that a correlation exists between optical properties and internal friction in high-index oxide coatings [339].

Recently, evidence that specific structural units may correlate with lower loss has been found, in particular glassy structures with a high degree of corner-sharing, rather than edge or face sharing, between neighbouring tetrahedrons [340]. This allows the structures of potential coating materials - many of which are well characterised - to be examined, and promising materials exhibiting a high degree of corner sharing to be identified and further investigated.

This increased understanding of the links between atomic structure and coating loss is a highly useful tool for developing lower-loss coatings.

## 6.3.5 Possible coating materials

### 6.3.5.1 Amorphous silicon

Amorphous silicon has low mechanical loss at cryogenic temperatures [341, 342], and has a relatively high refractive index, allowing thinner coatings – with correspondingly lower thermal noise – to be made. Mechanical loss as low as  $2 \times 10^{-5}$  has been observed in aSi coatings at room temperature

and at cryogenic temperatures, and even lower loss is possible for coatings deposited at elevated temperature [343]. Elevated temperature deposition allows the aSi to form an ‘ideal glass’ structure – a low entropy amorphous state with very low loss.

While aSi is a very attractive material for thermal noise reasons, the optical absorption has historically been too high for use in gravitational wave detectors. Commercially grown ion-beam sputtered aSi coatings can have optical absorption of 1000 to 10000 ppm at 1550 nm (for a room-temperature HR stack made of aSi and SiO<sub>2</sub>) [344, 345]. Significantly lower absorption can be achieved using a commercially available ion plating technique [346], and even lower again via electron cyclotron resonance (ECR) ion-beam sputtering [345]. The absorption of aSi tends to be significantly lower – between a factor of 5 and 10 – at ~2000 nm than at 1550 nm [346]. Operating ET-LF at a wavelength close to 2000 nm may therefore be desirable to enable the use of aSi coatings for thermal noise reduction. While the absorption of the best aSi measured is still too high to allow a traditional aSi-based coating to be used, the incorporation of aSi layers into a mutimaterial coating design can allow significant thermal noise improvements while minimising the absorption contribution of the aSi layers.

aSi may also be a candidate material for a room-temperature coating. However, without further reductions in optical absorption, this is significantly more likely for a laser wavelength of 1550 nm than for 1064 nm, due to the higher optical absorption of aSi at 1064 nm. However, it is interesting to note that some thermal noise reductions may be possible using aSi in a multi-material design at 1064 nm.

### 6.3.5.2 Alternative cryogenic low-index layers

For room-temperature detectors, efforts have largely focused on improving or replacing the high-index coating layers which currently dominate the thermal noise. The current low-index material, silica, has a relatively low loss (as low as  $\sim 2 \times 10^{-5}$ ) at room temperature. However, the loss of silica films increases significantly at cryogenic temperatures [312] - with both the structure and the magnitude of the loss being strongly dependent on post-deposition heat-treatment temperature [314]. Therefore alternative low-index materials to silica will be required at for cryogenic coatings. A lower-loss low-index material is also likely to be required to achieve the required reduction in coating thermal noise at room temperature, although at the moment thermal noise remains dominated by the high index Ta<sub>2</sub>O<sub>5</sub> layers. The room-temperature loss of silica can be further reduced by annealing at higher temperatures up to 900°C [347]. In current coatings, crystallisation of the tantala layers prevents annealing above  $\sim 600^\circ\text{C}$  [347].

In order to replace SiO<sub>2</sub> layers with lower-index materials, the optical properties and the internal friction of sputtered MgF<sub>2</sub> and AlF<sub>3</sub> coatings have been characterized at room temperature [310]. Lower refractive index, higher optical absorption and internal friction have been observed. Work is ongoing to characterize the impact of annealing on absorption and internal friction, at room and low temperature, for possible implementation in future cryogenic detectors like ET-LF.

### 6.3.5.3 Silicon nitride

Silicon nitride films can have mechanical loss in the order of  $1 \times 10^{-5}$  around 10 K [348] for a film on a substrate, and less than  $1 \times 10^{-6}$  for substrate-free films [349]. The refractive index of

SiN is relatively low, making it of interest as a low-index material for use alongside aSi [350, 346]. Studies have shown that the exact composition of SiN films can strongly affect the refractive index, optical absorption and mechanical loss. Large enough refractive index variations can be obtained by changing the composition to potentially allow SiN to be used for both the high and low index coating layers. The optical absorption of SiN can be similar to the best aSi commercially available aSi films [350, 351]. A multimaterial design has been proposed to further reduce this absorption to below 5 ppm for an HR stack [326], although this design does not meet the ET-LF thermal noise requirements.

Low mechanical loss has also been demonstrated in silicon nitride at room temperature and in sputtered films [310]. Silicon nitride can withstand annealing at higher temperatures than tantala, up to 900°C [310], allowing for the possibility of high-temperature annealing to produce low loss Si<sub>3</sub>N<sub>4</sub>/SiO<sub>2</sub> based coatings.

#### 6.3.5.4 Silica-doped hafnia

HfO<sub>2</sub> coatings have been shown to have lower cryogenic mechanical loss than SiO<sub>2</sub> and Ta<sub>2</sub>O<sub>5</sub>, but the material partially crystallises on annealing, resulting in poor optical properties [352]. Doping HfO<sub>2</sub> with SiO<sub>2</sub> prevents crystallisation due to annealing, without increasing the cryogenic loss. With reasonably low optical absorption, SiO<sub>2</sub>-doped HfO<sub>2</sub> shows promise for use as a low-index coating material in combination with high-index aSi layers at cryogenic temperatures [12]. This material is not of interest for ET-HF due to a relatively high room-temperature loss [353].

#### 6.3.5.5 Alumina

Al<sub>2</sub>O<sub>3</sub> coatings can have a lower mechanical loss than SiO<sub>2</sub> at cryogenic temperatures [314]. While the refractive index is not as low as for SiO<sub>2</sub>, this material may be of interest for use as a low-index material alongside materials like aSi which has a particularly high index. There has been interesting evidence that alumina coatings deposited at elevated temperatures can have significantly lower cryogenic loss than coatings which are heat-treated after deposition.

#### 6.3.5.6 Other amorphous coatings

Improved amorphous oxides, with improvements being targeted using improved knowledge of the links between loss and structure, remain of interest for room-temperature coatings in particular. Options under investigation [310] include studies of doping/mixing to increase crystallisation temperature and enable high-temperature annealing, the formation of ideal glass states using elevated temperature deposition and identifying materials with a high degree of corner-shared structural units.

#### 6.3.5.7 Crystalline coatings

Multilayer single-crystalline coating materials can be grown epitaxially and can have very low mechanical loss. GaAs/AlGaAs crystalline coatings have been studied extensively, with a loss of  $5.4 \times 10^{-6}$  demonstrated at 20 K for substrate-free resonator [354]. Thermal noise measurements in small cavities are consistent with a coating loss of  $4 \times 10^{-5}$  at room temperature, and excellent optical absorption and scattering have been observed at wavelengths around 1550 nm and 2000 nm [355]. AlGaAs coatings are grown on GaAs substrates, and would require to be transferred and bonded to a

silica or silicon mirror - a process that needs further development for ET-sized optics. Currently the maximum available diameter of GaAs wafers is 20 cm, which is not large enough for ET mirrors. However, there is now industrial interest in the production of larger GaAs wafers, with progress towards wafer diameters up to 40 cm [356].

Recent work suggested that the bulk loss of AlGaAs may be significantly higher than the shear loss [356], however further investigation of the contribution from thermoelastic dissipation is required. Since the total coating thermal noise is more sensitive to bulk than to shear loss, or large beam sizes, further analysis and experimental results are required. It should be noted that low thermal noise has been directly measured in AlGaAs coatings on relatively small mirrors with small laser spot sizes [357]. Although further work is required, AlGaAs crystalline mirror coatings continue to hold significant promise for addressing the optical and thermal noise requirements for future gravitational wave observatories.

GaP/AlGaP crystalline coatings have also been investigated [358], with mechanical loss as low as  $2.5 \times 10^{-5}$  measured at 20 K [359]. This material is of interest as it is lattice-matched to silicon and can be grown directly onto silicon substrates, potentially removing the need for substrate transfer. Measurements of an initial highly-reflective stack showed high optical absorption of 2.3% [360]; however there may be scope to reduce this absorption e.g. reducing impurities in the coating materials. To date, the number of layers in a high-reflectivity coating is limited [359], resulting in a limited reflectivity.

For both GaAs/AlGaAs and GaP/AlGaAs coatings, the difference in refractive index between the two materials is relatively small, and so many layers are required to provide high reflectivity, reducing some of the thermal noise improvements due to the low loss.

#### 6.3.5.8 Coating deposition

The ET mirrors will be significantly larger than current gravitational detectors, thus coating uniformity over larger diameters will require development of coating deposition facilities. This development is already underway at the state-of-the-art coating facility at the Laboratoire des Matériaux Avancés in Lyon, France. Problems with point absorbers have been observed in the coatings for Advanced LIGO and Advanced Virgo: work to understand the origin of these defects and to eliminate them is a priority. Also, the occurrence of bubble-like defects limiting the annealing temperature of different coatings (high-index oxides) has been observed in multi-layer high-reflective stacks; work is currently ongoing also to understand and solve this issue.

#### 6.3.6 Coating strategy for ET

Significant progress has been made towards development of coatings suitable for use at low temperatures in ET-LF. There are several highly-promising routes to meeting the coating thermal noise and optical absorption requirements. However, further study is required of the potential trade-off between coating absorption requirements, suspension thermal noise, ultimate mirror temperature and substrate thermoelastic noise – and it seems likely that lower absorption than 5 ppm may be required.

Achieving significant reductions in coating thermal noise at room temperature may be more challenging than at low temperature. Work in this area is ongoing, both for ET and for upgrades to the aLIGO

and Advanced Virgo detectors, and there are several promising options. One limitation is that some coatings which show promise for the low-temperature detector at 1550 nm have significantly higher optical absorption at 1064 nm, the wavelength envisaged for the room-temperature detector. Detailed studies of the benefits of operating the room-temperature detector at 1550 nm may be of interest, as this may allow significant thermal noise reductions through the use of e.g. aSi-based coatings.

## 6.4 Light sources

Each of the ET interferometers will use a high power laser system with low intrinsic noise called the high power laser (HPL) in the following. Several nested stabilization control loops will be required to reduce the fluctuations of the free-running laser before the light can be injected into the main interferometer. Like in all currently operating GWDs a first ET laser stabilization layer will be installed on a seismically isolated laser table outside the vacuum system. The combined system of HPL and this stabilization layer is called the prestabilized laser (PSL) and is discussed in this section. We will start with a discussion of the PSL requirements for ET-LF and ET-HF followed by a description of the HPLs for both interferometers. The last subsection will discuss passive and active noise reduction concepts that will prepare the light for injection into the suspended input modecleaner (IMC).

### 6.4.1 Requirements

The ET-HF HPL has to operate in a single-frequency continuous-wave (cw) mode at a wavelength of 1064 nm and needs to deliver 700 W in a linear polarized fundamental spatial HG<sub>00</sub> mode. With the assumption of roughly 30% loss between the laser and the IMC output this leaves 500 W at the input of the main interferometer. The higher order mode content of this laser should be below 10% and the polarization purity at least 1/10. The ET-LF HPL needs to operate in a single-frequency continuous-wave (cw) mode at a wavelength of approximately 1550 nm with similar spatial and polarization purities as the ET-HP HPL. A laser power of 5 W is required to allow for 3 W to be injected into the main interferometer.

Both HPLs need to provide actuators with sufficient dynamic range and speed to allow for a suppression of their free running laser frequency-, power- and pointing noise and to compensate for noise introduced between the PSL interface on the laser table and the main interferometer's reference frame. The relative power noise (RPN) in the megahertz frequency range should be shot noise limited for 100 mA photo current. In addition the HPLs need to operate reliable with small drifts and only limited maintenance requirements.

A rough estimation of the ET PSL noise requirements is given here based on the present ET design. The frequency noise of the light injected into the IMC will be subject to Doppler noise between the laser table and the suspended reference frame. A frequency noise of about 10 mHz/ $\sqrt{\text{Hz}}$  should be well below this level and hence adequate as PSL requirement. Following the same line of thought the beam pointing requirement of the ET PSLs will be similar to the one of present detectors with relative lateral and angular beam fluctuations in the  $10^{-6}/\sqrt{\text{Hz}}$  range[361]. With a similar power noise coupling and a 10 fold improved sensitivity compared to the advanced GWDs the ET detectors would need a factor of ten better laser power stability of roughly  $\text{RPN} = 3 \times 10^{-10}/\sqrt{\text{Hz}}$ .

### 6.4.2 High power laser

It is likely that the 700 W laser power for ET-HF will be generated by a coherent combination of several high-power laser-amplifier stages seeded by one or more low-power low-noise laser(s). Two different concepts are currently under investigation for such master-oscillator power-amplifier (MOPA) stages at the 250 W output power level. One concept is based on mode-selectively pumped Nd:Vandate amplifiers which do not suffer from depolarization problems as Nd:YAG systems would do. A power of roughly 200 W was lately generated with a commercial neoVAN-4S-HP amplifier chain with low noise and high spatial purity [362, 363]. Investigations are underway to increase the output power of such a solid state amplifier chain to 250-300 W. As solid-state MOPA chains are more complex compared to fiber based MOPAs, solid-state MOPAs serve as fall back solutions for ET-HF HPLs and will not be further discussed in this document.

Fiber amplifiers offer a highly-efficient and compact way to amplify laser light to the kW level. The amplification of narrow linewidth single mode seed lasers is, however, limited by nonlinear effects such as stimulated Brillouin scattering (SBS). Large mode-area (LMA) fibers in combination with losses for high-order spatial modes introduced by bending of the fiber can lead to high SBS free output powers in a single spatial mode operation. Sophisticated fiber designs (photonic crystal fibers [364], photonic band gap fibers [365] and chirally-coupled-core fibers [366]) can guide a single mode with a large mode field diameter even without such bending losses. The SBS threshold can be further increased by a differential temperature induced shift of the SBS gain spectrum along the fiber and via a counter-propagating pumping scheme. Several high power fiber amplifier systems that meet the demanding ET-HF HPL noise requirements have been demonstrated up to power levels of 300 W [367–370]. A 200 W fiber laser system [371] will be installed and tested in the Advanced Virgo-gravitational wave detector in its 4th observation run. Higher power levels generated with fiber based MOPAs were reported in literature but only limited information on spatial purity and noise performance of these systems is available. Especially information on the RPN at radio frequencies is missing which is prone to increase at pump power levels well below the onset of significant SBS related power in the back-ward propagation direction [372]. Hence a conservative approach is taken for ET-HF that assumes that several fiber based MOPA systems will be coherently combined to form the ET-HF HPL. These fiber amplifier modules will each incorporate a mode-field adapter, a pump-light stripper, an active fiber and a pump-light combiner that couples the light of the fiber based pump diodes into the active LMA fiber. The amplified light will leave the fiber via a fused silica end cap to reduce the light intensity at the glass air interface and with this the risk of contamination induced damage.

Different options are under investigation for the seed laser design. A fiber-oscillator in combination with a fiber-preamplifier allows for an monolithic all fiber design that includes fiber based components such as Faraday isolators (FIs), electro-optical modulators (EOMs) and acousto-optical modulators (AOMs). All these components including the high power LMA amplifier are spliced together and form a monolithic HPL module. One disadvantage of this concept is, that modulators can only be used between the seed and the preamplifier due to limited power handling capabilities of fiber modulators.

A second concept relies on the non-planar ring-oscillator (NPRO) seed as used in all currently operating GWDs. Free space EOMs, AOMs and FIs can be used to condition the laser light before it is coupled into either a solid-state or a fiber pre-amplifier. This amplifier is either spliced or free

space coupled to the mode-field adapter of the LMA high power amplifier. A trade-off study between these two concepts will lead to the final ET-HF seed laser concept. Both seed laser concepts can provide actuators with enough range and speed for the PSL frequency stabilization. As the power noise of a MOPA system is usually dominated by the high power amplifier and as the modulation of the pump diodes of this stage offer a large actuation range, the pump current of the LMA amplifier's pump diodes will serve as the main PSL power actuator.

The coherent combination will be performed on a beam combiner (beam splitter) before the pre-modecleaner cavity (PMC, see next subsection). Both of the to-be combined beams can separately be aligned to the Eigenmode of the PMC which guarantees an optimal spatial overlap. The differential phase between the beams will be sensed at the second beam combiner port. A phase-lock control loop will feed back to either one of the seed lasers (in case different seed lasers are used) or to a piezo-controlled mirror or a fiber stretcher in one amplifier's beam path (in case of a single seed laser). Long term tests will reveal if alignment control loops are required to keep a good interference contrast at the beam combiner. First coherent combination experiments of two 40 W fiber amplifiers [373] and two 200 W fiber amplifiers [374] show promising results.

Several commercial seed lasers operating at 1550 nm and Erbium based fiber amplifiers for the same wavelength are available for use in ET-LF. The seed lasers are either based on fiber oscillators or external-cavity diode lasers to generate low noise beams with several 10 mW power. Several MOPA configurations with Er fiber amplifiers were tested at the 2 W level and show spatial purity and noise levels consistent with ET-LF requirements [375]. The amplification to the required power level of 5 W by a second Er fiber amplifier is straight forward. (Low noise fiber amplifiers with output power of more than 100 W have been demonstrated [376]). In the case of a laser diode based seed laser the pump current can be used as a fast frequency actuator with 50 kHz actuation bandwidth. The power noise can be reduced by feed-back to either the fiber amplifier's pump diodes or via an external electro-optical amplitude modulator (EOAM).

### 6.4.3 Prestabilization

Even though laser systems with very low free running power and frequency noise will be selected for ET, sophisticated nested stabilization schemes are required to achieve stability levels in the interferometers compatible with the GW sensitivity goal. A first stabilization layer, the so called prestabilization is performed on the laser table outside the vacuum system. The goal of the prestabilization system is to reduce the laser fluctuations well below the level of noise added by the Doppler and beam pointing effects due to motion of the laser table with respect to the seismically isolated interferometer frame. Power in higher order spatial modes as well as beam pointing fluctuations are reduced by passive spatial filtering with stable optical ring resonators called pre mode cleaner (PMC). In the case of ET-LF a fiber could be used as a spatial mode filter and as a transfer fiber to deliver the laser light via a seismically isolated output coupler in the interferometer reference frame. This could strongly reduce the noise introduced between the laser table and the suspended modecleaners. Further investigations will reveal if non-linear effects or added phase noise in such a fiber would prevail the benefits. In the case of ET-HF the power levels are too high for a solid-core-fiber based modecleaner such that a PMC needs to be part of the PSL. A PMC has the additional benefit, that it filters power noise at radio frequencies and that it can provide spatially stable pick-off ports for the frequency and power stabilization and potentially for phase locked loops of the squeezing or length and alignment control

subsystem.

The PSL frequency stabilization will use a rigid spacer high-finesse reference cavity which is seismically isolated inside a vacuum system. A feedback control loop with a high unity gain frequency of several hundred kHz is required to allow for high bandwidth second layer control loops. These will use the suspended modecleaner and the main interferometer as frequency references and will feed back either via a summation point into the error point of the PSL loop or to an AOM frequency shifter placed between the main laser and the rigid reference cavity.

A high unity gain frequency is also required for the PSL power stabilization control loop. This needs to reduce the RPN of the beam leaving the PMC to roughly  $10^{-8}/\sqrt{\text{Hz}}$ . As the speed of the feedback to the diode laser pump source of the HPL is limited to several 10 kHz a fast EOAM after the seed laser or the pre-amplifier will be part of this control loop. The power noise sensor for the power stabilization loop will be a high-power photodiode placed into one of the pick-off ports of the PMC. Due to pointing-to-RPN or polarization-to-RPN coupling by the suspended input modecleaner a sensor for the second layer power stabilization has to be placed after the input modecleaner close to the power recycling mirror. The second layer power stabilization loop will either feed back into the error point of the first loop or to an in-vacuum EOAM to achieve an RPN in the  $10^{-10}/\sqrt{\text{Hz}}$  range. Depending on the final RPN requirements sophisticated power noise sensing schemes based on multi-photodiode arrays[377], the optical AC coupling technique [378] or squeezed light assisted power noise sensing [379] might be required for this second loop.

The general PSL layout will be very similar for the ET-HF and ET-LF PSLs. Due to the two orders of magnitude lower power level the stabilization of the ET-LF laser might be easier as more integrated fiber components can be used. These have typically higher bandwidth and are less alignment sensitive. This small advantage might, however, be compensated by the fact that the ET-LF interferometers require stability at much lower frequencies. This is generally harder as scattered light and beam pointing coupling to the control loop's sensors is larger at low frequencies.

Prototypes for both the ET-HF and ET-LF PSLs will be set up in research labs in the near future to test the ET laser designs, the stabilization concepts and to gain insight into the longterm drift behavior of such systems.

## 6.5 Quantum noise reduction

In a laser-interferometric gravitational-wave detector, there are different types of noise sources, which are usually categorized into quantum noise sources and classical noise sources (cf. Sec. 6.1). The main difference in the detector sensitivity of different optical layout comes from the spectral distribution of the quantum noise itself, even though there could also arise differences in the susceptibility to the classical noise, due for example to different number of mirrors or geometries of the optical cavities. The particular choice of an optical layout is also defined by the choice of targeted quantum noise and the reduction techniques used.

**Quantum noise** in the interferometers originates from the fundamental quantum fluctuations of the electric field that follow the Heisenberg uncertainty relation. While the Heisenberg's uncertainty principle is known to link the incertitude in the position and the momentum of a particle, a similar relationship exists between the quantum fluctuations of the light phase and amplitude.

Quantum phase fluctuations can be viewed as a manifestation of Poissonian statistics of the photons emitted by an ideal laser and thus limit the measurement precision of any interferometric device. This uncertainty of photons arrival time at the photodiode known also as *shot noise* scales down with the increase of the number of photons used for the measurement and thus is inversely proportional to the light power interacting with the test masses of the interferometer. Amplitude fluctuations of light lead to the fluctuations of radiation pressure on the mirrors, resulting in the random displacement of the mirrors and of the arm length change that mimics the gravitational wave signal. This second component of quantum noise is known as *quantum radiation-pressure* or *quantum back-action* noise. It naturally scales up with light power and is most prominent at the low frequencies, where massive suspended mirrors have higher response to the driving force. The fact that quantum shot noise and then quantum radiation-pressure noise have an inverse dependence on power and that the underlying fluctuations of phase and amplitude are uncorrelated, gives rise to a so called standard quantum limit (SQL) [380, 381] on continuous high-precision interferometric measurements.

However the SQL is not a fundamental limitation on the achievable sensitivity of the interferometer, but rather a convenient benchmark for comparing different quantum noise mitigating schemes proposed so far for advanced gravitational-wave interferometer (see [382] and references therein). It is also a concrete example of the trade-off one has to make between high sensitivity at shot-noise-dominated high frequencies vs. the reduced back-action-noise at low frequencies (below 10 Hz) which cannot be simultaneously attained in a conventional displacement-sensitive interferometer. This obstacle can be overcome by using 2 conventional interferometers instead of one, using our xylophone configuration as described in section 6.1.1. As a short reminder, each detector in a xylophone configuration is split into two interferometers, one optimized for low frequencies, operating at low light power and the other optimized for high frequencies operating at high light power. Relevant to this section, the xylophone configuration allows the simultaneous decrease of photon shot noise and radiation pressure noise. The sensitivity of the radiation pressure noise-dominated low-frequency interferometer benefits from low light power, while the sensitivity of the shot noise-dominated high-frequency interferometer benefits from the high light power.

There is nevertheless a fundamental limit on sensitivity more stringent than the SQL [383, 384, 382]. It sets the ultimate limit on the precision attainable for a given configuration of the interferometer and goes by the name of *energetic quantum limit* [385] in GW laser interferometer or by *quantum Cramér-Rao bound* [386] in quantum metrology. In the context of laser interferometric gravitational-wave detectors, it can be expressed in terms of a power spectral density (PSD) of the Fundamental Quantum Limit (FQL) given in the interferometer noise in the units of GW strain  $h$ :

$$S_{\text{FQL}}^h(\Omega) = \frac{\hbar^2 c^2}{S_{PP}(\Omega)L^2} = \frac{4\hbar^2}{S_{\mathcal{E}\mathcal{E}}(\Omega)}. \quad (6.5.1)$$

Here  $S_{PP}$  is the single-sided PSD for the fluctuations of optical power  $P$  inside the arms and  $S_{\mathcal{E}\mathcal{E}} = 4S_{PP}L^2/c^2$  is the corresponding PSD of fluctuations of light energy stored in the arms. This means that large uncertainty in the energy of intracavity photons is necessary to probe the spacetime precisely, which is a direct upshot of the energy-time uncertainty relation.

Reaching this fundamental quantum limit in a given configuration is a non-trivial task that requires using quantum noise reduction techniques. They have different, and often very special, requirements on the optical topology. For ET, we will focus on engineering quantum correlations between the components of quantum noise with the goal of **quantum noise cancellation** or reduction.

These methods encompass a vast body of schemes, of which the most mature one is the injection of squeezed vacuum into the readout port of the interferometer first proposed by Unruh [387]. It has successfully improved the sensitivity of GEO600 [388], Virgo and LIGO [389] detectors and is now considered as an integral part of any future GW detector design. Yet the injection of squeezed vacuum alone cannot lead to the full broadband suppression of quantum noise because of the frequency dependent quantum correlations between the phase and amplitude fluctuations of the intracavity light as a result of the interaction between light and the mechanical motion of the mirrors [390]. The solution is to use frequency dependent squeezed light injection [390], **which was chosen as baseline quantum noise reduction for the initial ET configuration** and that is discussed in greater detail in Section 6.5.2.

Despite its success, squeezing injection does not allow the interferometer to reach the FQL. This calls for more sophisticated and yet experimentally unexplored quantum noise cancellation methods that rely on engineering quantum correlations between the two components of quantum noise. These techniques are known in the community as **quantum non-demolition (QND)** techniques and briefly discussed below in section 6.5.1<sup>3</sup>.

### 6.5.1 Review of quantum non-demolition topology options

The current Virgo and LIGO detectors [391, 392] are already limited by quantum noise in a major part of their detection band. Science objectives of ET (see chapter I) and other next generation instruments make it an imperative to improve low and high-frequency sensitivity by at least an order of magnitude as compared to the current detectors. This can only be achieved by using QND techniques to suppress quantum noise below the SQL.

The impressive progress in mitigation of the technical noise sources in the current interferometers as well as an extensive current R&D on reduction of thermal noise of the core optics (cf. section 6.2), on advanced seismic isolation (section 6.10) and on Newtonian noise mitigation (section 7.2.4) allows to expect that quantum noise will be the main obstacle towards reaching the design sensitivity of ET and for further progress of GW laser interferometer in general. As there are physical limitations on the mass of the mirrors and on the achievable level of light power in the arms, the significant modification of interferometer topology, optical readout and use of non-classical light sources becomes an essential for the next generation GW detectors.

There are different topology options available which can all be fitted into an L-shaped geometry [382]. A plethora of various schemes that promise significant improvement in terms of quantum noise have been developed so far, which however require significant and sometimes drastic changes to the conventional Fabry-Perot–Michelson optical scheme. Many of them have great potential in reducing the quantum noise, but there is a big disparity in terms of readiness: some are far away from being ready to be implemented into gravitational-wave detectors, others have been already demonstrated experimentally as a proof of principle or have been even already implemented into gravitational-wave detectors. The non-exhaustive list of QND options in the descending order of experimental readiness/level of R&D completeness is presented below (more detailed description can

<sup>3</sup>It should be noted that only some of these techniques satisfy a strict definition of QND measurement, however all of them allow to overcome the SQL in a broad frequency band.

be found in [382]). Only the first scheme is in the Einstein Telescope baseline; depending on future experimental validation and relevance, other schemes may be considered in future upgrades:

1. **Injection of (frequency-dependent) squeezed vacuum** in the readout port of the interferometer (see more detail in section 6.5.2) uses inherent quantum correlations in non-classical states of light to reduce quantum fluctuations in the readout quadrature of the interferometer in the shot-noise-dominated frequency range [393, 394, 389, 395]. Additional filter cavities can be used to rotate squeezing angle in an optimal frequency dependent way [390, 396, 397] to gain a broadband suppression of quantum noise. Frequency dependent squeezing compatible with current GW detectors was experimentally demonstrated in 2020 [398, 399]. This scheme will be an integral part of the Einstein Telescope and is discussed in details in the next section.
2. **Conditional frequency-dependent squeezing** [400] is a recent proposal that allows to achieve frequency dependent squeezing enhancement without filter cavities. It uses a nondegenerate two-mode squeezer<sup>4</sup> that produces entangled beams with far detuned from each other frequencies, of which one, *signal*, coincides with the pump laser frequency and another, *idler*, is shifted by several MHz, and thereby passes through the interferometer gaining only optimal frequency-dependent phase shift. Detection of the idler beam projects the signal one into an optimal frequency dependent squeezed state that gives the desired sensitivity improvement. Recent table-top experiments at ANU [401] and Hamburg [402] proved the viability of this technique, yet confirmed the penalty of twice the decoherence caused by the injection loss and the loss at the readout as compared to a single-mode squeezing-based schemes.
3. **QND speed-meter interferometers** [403–408] offer an alternative way to mitigate back-action noise in an intracavity way. This is achieved by modifying the way light passes through the interferometer so as to let it interact with the mechanical motion of the test masses two times sequentially in a coherent way, thereby making the readout signal proportional to the velocity of the mirrors and at the same time coherently subtracting a major fraction of back-action. Speed meters can be realised in various ways, either using ring arm cavities [407, 409], polarisation optics [410–414], or simply adding a long-base “sloshing” cavity to a Michelson interferometer [405, 406, 415]. Apart from Michelson interferometers, speed meters are arguably the most extensively studied and well understood interferometer topology, where the impact of real-world imperfections and asymmetries is analysed in great detail [416–418].
4. **Hybrid schemes** that seek to enhance sensitivity by coupling the interferometer light mode to a generally nonlinear quantum system. The first use of this approach was to create a so called **white-light cavity (WLC)** [419] by introducing atomic gain medium prepared in such a way to render negative dispersion for the signal sidebands in the optical cavity. In the case of the signal-recycled interferometer, the negative dispersion medium could be placed in the signal-recycling cavity, avoiding interaction of high-power carrier field with the atomic cloud. This would cancel the positive dispersion of the arm cavities and would result in a broadening of the bandwidth of the interferometer without sacrificing its peak sensitivity. The atomic medium, however, has proven to be too noisy for the purpose of GW detection, but the two new promising approaches were suggested. The first suggests to place a nonlinear (squeezer) crystal in the signal-recycling cavity [420] and the other suggests to use an unstable optomechanical filter instead [421, 422]. The main advantage of the WLC-schemes is their capacity to unlock

---

<sup>4</sup>Physically, it is the same squeezed light source that is used for frequency independent squeezing injection, but with the pump frequency detuned from the double carrier frequency by several to tens of MHz.

the kHz frequency band for detection, as it is there, where the binary neutron star merger signals mainly reside, while the conventional GW detectors' sensitivity there wanes due to finite bandwidth of the arm cavities [423].

Other uses of hybrid schemes include the **intracavity signal amplification** [424, 425] and the **coherent quantum noise cancellation (CQNC)** [426, 427] schemes. The former suggest to put the parametric optical amplifier (based on squeezer crystal) in a detuned signal recycling cavity to amplify the signal sidebands and the created optical spring, thereby enhancing the response to the GW signal. The latter one uses Kerr nonlinear system and a tailored optical coupling between the main mode and the ancilla to create a so called “negative mass” mechanical oscillator. If the mechanical susceptibility of this virtual oscillator matches the one of the test masses, the back-action noise of the two systems cancel each other completely due to the opposite sign of the effective mass. A similar effect can be reached using a spin-based negative mass oscillator as suggested in [428, 429].

### 6.5.2 Frequency dependent squeezing

Since the first implementation of the squeezing technique in a gravitational wave detector, which was realized at the GEO 600 facility in 2010 [388, 394], numerous novel schemes regarding the long term application of squeezed light have been tested and implemented. These include, for example, the generation of the squeezing phase control signals [430] and the automatic alignment of the squeezed light field with respect to the interferometer [431], as well as ultra-low noise detection electronics [432]. This led to a constant improvement of measured non-classical sensitivity enhancement [433, 434]. In 2019 an effective squeezing level of 6 dB could be measured at GEO 600, which was a world's first in a suspended gravitational wave interferometer. The Advanced Virgo and Advanced LIGO detectors have undergone upgrades that also contained the implementation of squeezed light leading to an average detected squeezing level between 2–3 dB during the third joint LIGO-Virgo observations run O3. The great potential of including the squeezed light technique in the baseline design of ET becomes evident in Fig.6.6. In order to reach the goal of an effective 10 dB quantum noise reduction, the overall optical loss for the squeezed field needs to be smaller than 10 % while the phase noise does not exceed 10 mrad in total.

The current generation of detectors achieve their exquisite sensitivity due to their kilometre-scale arm lengths, the enormous light powers circulating in the enhancement resonators (arm, power- and signal-recycling cavities), and sophisticated pendulum suspensions that isolate the test mass mirrors from the environment. When these techniques were developed, squeezing was not envisioned to become an integral part of such a system. However, the sensitivity improvements achieved already today via the injection of squeezed light (as an upgrade / add-on) are significant. For GEO 600 an effective squeezing level of 6 dB has been detected in the shot noise limited frequency band. As shown in Fig.6.6 this corresponds to 25 % optical loss with a phase jitter of the squeezing ellipse of around 30 mrad. A further reduction of optical loss and phase noise, the improvement in mode matching of the squeezed field to the interferometer signal field and mitigation of polarization mismatches will improve the effective quantum noise reduction even more in the future. During the O3 science run both Advanced LIGO detectors and the Advanced VIRGO detector have not only been limited by quantum shot noise at high frequencies but have also operated close to being limited by quantum radiation pressure noise at lower detection frequencies. As a consequence, the injected squeezing level can not be increased to improve the high frequency sensitivity without degrading the detector

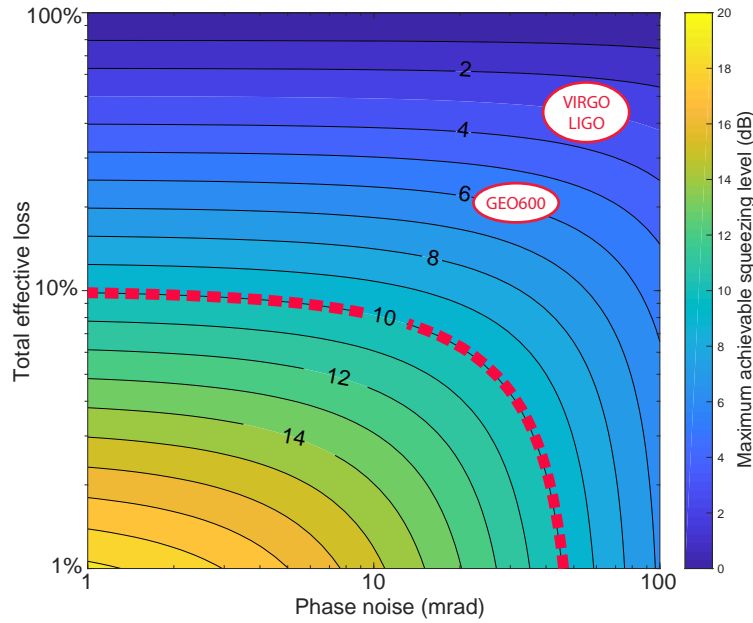


Figure 6.6: Maximum effective squeezing level as function of phase noise and optical loss. In order to reach the goal of 10 dB detected squeezing, the optical loss needs to be smaller than 10% while the phase noise must not exceed 10 mrad.

sensitivity at lower frequencies and vice versa. It was revealed by Unruh [435] and others [436, 437] that squeezed field injection with frequency dependent squeezing angle allows an overall quantum noise reduction including the radiation pressure noise thereby beating the standard quantum limit (SQL). The effect of a simultaneous suppression of quantum noise by means of a frequency dependent orientation of the squeezing ellipse (i.e. the correct squeezing phase for all detection frequencies) is illustrated in Fig. 6.7. For Advanced Virgo and Advanced LIGO, this can be realized with a detuned filter cavity and the corresponding technology is now mature and planned to be implemented before the science run O4. The ET detectors will be quantum noise limited over the entire detection band and therefore suitable filter cavities have to be implemented. For the squeezed light injection into an optical spring interferometer, an additional rotation of the squeezing ellipse is caused first by the phase-space rotation of a detuned cavity and second due to the optical spring resonance. In this case at least two filter cavities are necessary to achieve a broadband reduction of quantum noise with squeezed states of light. This is what we propose for the low-frequency ET-LF interferometer (cf. section 6.1.1). For the high-frequency ET-HF interferometer one filter cavity is enough (cf. Sec. 6.1.1 and [438]).

### 6.5.2.1 Filter cavity

The filter cavity assisted rotation of the squeezing ellipse has been experimentally demonstrated in table top experiments both at MHz [439] and kHz [397] frequencies. Recently frequency dependent squeezing with long filtering cavities has been demonstrated in the frequency band relevant to GW detectors [399, 398]. That opens the way to its implementation in the current interferometers in the coming years and both collaborations LIGO [440] and VIRGO [441] are presently working on the

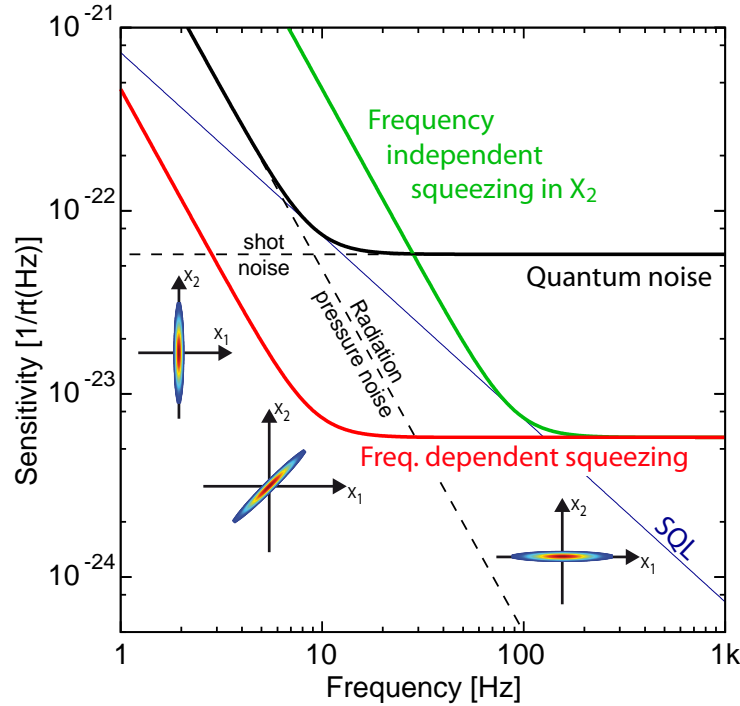


Figure 6.7: Illustration of frequency dependent and independent squeezed light injection.

development of cavities of hundreds of meter scale. The exact optimal cavity length and parameters such as finesse depend on the interferometer configuration. In this section we summarize the methods used for optimizing the filter cavities to be implemented in ET.

The use of filter cavities along the optical path of the squeezed light induces additional mechanisms and sources of squeezed light degradation which are in general frequency dependent. In optimizing the cavity design these detrimental effects must be taken into account to be mitigated:

*Filter cavity round trip loss* – The most relevant squeezing degradation mechanism comes from the filter cavity round trip losses which induce two effects: first optical loss mixes non-squeezed contributions into the squeezed vacuum state which leads to a degradation of the resulting squeezing level. Second the presence of filter cavity losses combined with the frequency dependent reflectivity mixes the two quadratures thereby corrupting squeezing with anti-squeezing. This effect cannot be compensated by a rotation of the state and therefore definitively deteriorates the actual quantum noise reduction [442]. To limit the impact of these effects the relevant parameter to be minimized is the cavity round trip loss per unit length  $l_{rt-fc}^2/L_{fc}$  [443]. Therefore in order to keep the filter cavities length to an acceptable value the round trip losses must be minimized. Round trip cavity losses ( $l_{fc-rt}^2$ ) are generally dominated by light scattering on the cavity mirror surfaces. For this reason among the possible filter cavities configurations the *linear* cavity, which minimizes the number of mirrors, is preferable [444]. Recent measurements show that 50–90 ppm can be achieved in 300 m long linear cavities [445], a similar result (<60 ppm) has been obtained for the VIRGO long arms. Moreover, in the near future a further decrease in the scattering losses is foreseen. Indeed a numerical calculation shows that with the latest mirror quality and by optimizing their diameter and radius of

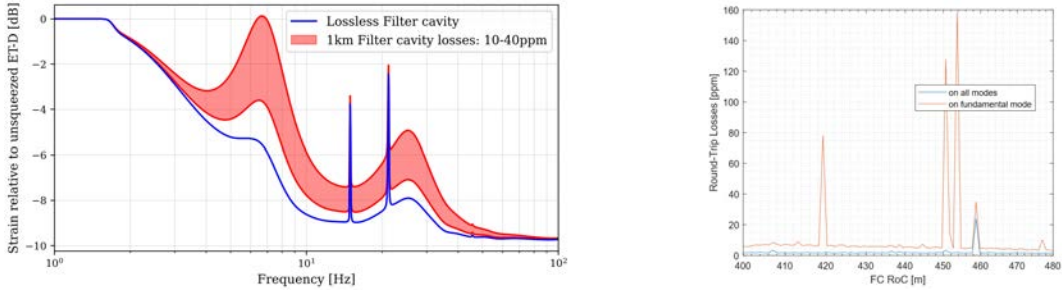


Figure 6.8: *Left*: Ratio between the ET-LF sensitivity with and without frequency dependent squeezing injection for 1 km length filter cavities. The round trip losses are assumed to range between 10 and 40 ppm (pink belt). The blue line represents the case of lossless cavities which can be approached by using longer cavities. *Right*: Expected cavity round trip losses as a function of the radius of curvature (RoC) of the mirrors for a 300 m long linear cavity, equipped with Virgo-like mirrors (left plot) 200 mm in diameter. The background value derives from the light scattered outside the cavity, while the peaks originate from scattered light that couple to the high order modes of the cavity. The calculation is based on the method used in [13].

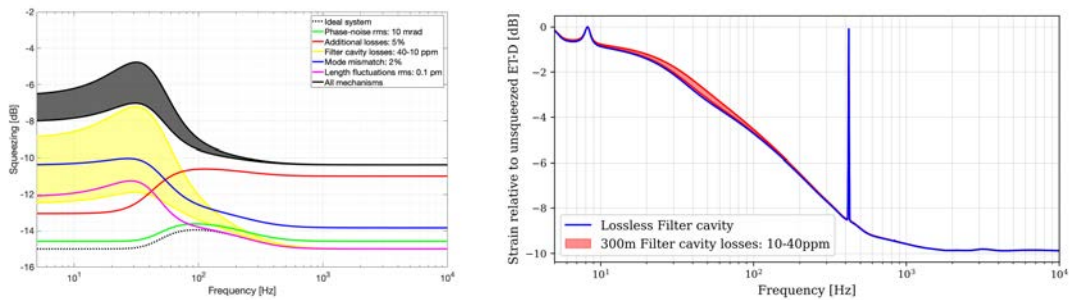


Figure 6.9: *Left*: Ratio between the quantum noise with and without squeezed light injection for a 300 meter long cavity. Several (colored curves) degradation mechanism contribute to the total squeezing degradation budget (black curve). The FC assumed round trip losses range between 40 ppm to 10 ppm (yellow belt in the plot) corresponding to different values of the total squeezing degradation budget (dark shadow in the plot). *Right*: Ratio between the ET-HF sensitivity with and without frequency dependent squeezing injection. At low frequencies the additional non-quantum noise sources make the overall sensitivity improvement lower than the corresponding quantum noise suppression (left plot). The overall sensitivity is therefore less affected by the change on the FC parameters (pink belt).

curvature, scattering losses from low spatial frequency surface error for a 300 m long cavity can be constrained to 5–10 ppm (see figure 6.8 *right*). Therefore for the early ET phase it is reasonable to assume a cavity round trip loss value of about 40 ppm which could decrease up to 10 ppm in a subsequent time.

*Mode mismatch* – A non-perfect spatial overlap (mode mismatch) between the squeezed beam and the eigenmode of the filter cavity is a source of optical loss, which is independent from the filter cavity length. The target mode matching value of ET is  $\sim 99\%$ , similar to the expected LIGO and VIRGO value once the filtering cavity is fully implemented.

*Phase noise* – The achievable sensitivity improvement by injecting squeezed light is deteriorated due to phase noise between the interferometer carrier and the squeezed field. The suspended filter cavity can produce phase noise due to residual changes of the cavity length  $\delta L_{fc}$  which generate fluctuations in the detuning frequency  $\Delta\omega_{fc}$ :

$$\delta\Delta\omega_{fc} = \omega_0 \frac{\delta L_{fc}}{L_{fc}}. \quad (6.5.2)$$

For this work we assume  $\delta L_{fc} = 0.1$  pm. which is within the reach of current technologies.

Figure 6.9-*left* shows the level of quantum noise reduction as a function of frequency when squeezed vacuum is injected in the dark port of ET-HF. The optimal cavity bandwidth  $\gamma_{fc}$  (half-width at half-maximum) and detuning  $\Delta\omega_{fc}$  are calculated analytically according to Ref. [442]. The plot shows that any reduction in the FC round trip losses or equivalently an increase in the cavity length would reduce the overall quantum noise as long as the length-independent degradation sources are negligible. Once this condition fails, a further increase in the FC length does not lead to a significant quantum noise reduction. Generally this optimization process can be stopped at shorter FC lengths since other non-quantum noise sources contribute to the total sensitivity of the interferometer and thus a strong quantum noise suppression is not required. Figure 6.9 *right*, shows how the global ET-HF sensitivity depends the value of the round trip losses or equivalently to the FC length. The dependence in the considered parameters range is quite weak and therefore for ET-HF a filter cavity longer than 300 meters is not required.

A similar optimization procedure was used for the two filter cavities required for the detuned configuration (ET-LF). In this case no analytical expression for the optimal cavities bandwidth and detuning is available. Therefore a numerical optimization of the cavities parameters around the approximated lossless solution [446] has been performed. Compared to the HF case, the optimal cavities half maximum bandwidth was considerably lower and thus cavities of several km length would be required (a narrow line cavity could also be obtained by raising the finesse but this would enhance the intracavity losses effect). Long filter cavities would greatly increase the complexity and cost of the infrastructure. Therefore for ET-LF we are considering sub-optimal 1 km long cavities as a trade-off between the need to contain costs and maximize the sensitivity. Figure 6.8 *left* shows that even in the sub-optimal case, the injection of frequency dependent squeezed vacuum in the ET-LF anti-symmetric port produces a relevant sensitivity enhancement over the whole detection band.

### 6.5.2.2 Squeezed light sources

Any optical loss between squeezing generation and detection reduces the level of measurable squeezing. Therefore, a prerequisite for the 10 dB of effective squeezing envisaged for ET, is a

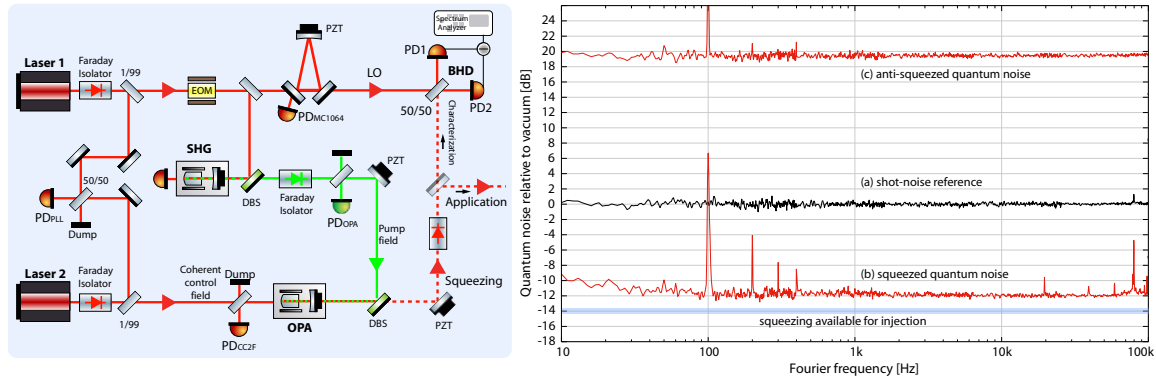


Figure 6.10: *Left:* Schematic for the generation and coherent control of squeezed vacuum states of light. Laser 1 provides the light field for homodyne detection and for frequency doubling in a second harmonic generator (SHG). The SHG provides the pump field required for the generation of squeezed vacuum states in an optical parametric amplifier (OPA) operated below threshold. The squeezed vacuum states are extracted via a dichroic beam splitter (DBS) and send towards the interferometer. Alternatively, the squeezing level can be characterized by means of a balanced homodyne detector (BHD). A Faraday isolator is implemented in the squeezing path to protect the OPA from light scattered back from the interferometer.

*Right:* Quantum noise squeezing as reported in [14]. Trace (a) represents the shot noise reference (normalized to 0 dB) measured with a homodyne detector. In reference to this trace the measured quantum noise powers for squeezing (b) and the corresponding anti-squeezing (c) are shown. Up to 12 dB squeezing and 19.6 dB anti-squeezing was observed, which is consistent with a theoretical model assuming a residual phase noise of 3.5 mrad rms and an overall optical loss of 5.3 % for the squeezed field. This includes 2.5 % optical loss due to the homodyne detection which needs to be subtracted to deduce the squeezing level available for the injection into a gravitational wave detector. This level is indicated by the blue area and corresponds to a squeezing factor of 14 dB.

squeezed light source design that can provide sufficiently strong squeezed vacuum states of light at the expected gravitational wave signal frequencies ranging from 3 Hz to several kHz.

Significant progress has been made over the last 10 years in the generation of squeezed vacuum states of light and squeeze factors beyond 10 dB are routinely produced at the two required wavelengths, 1064 nm and 1550 nm, respectively. In the same manner as today's most efficient squeezed light sources, the ET-squeezers will employ cavity-enhanced parametric down-conversion, also called optical parametric amplification, where the interaction between the fundamental and second harmonic fields via a  $\chi^{(2)}$ -process inside a non-linear crystal produces non-classical photon-pair correlations that yield a reduced noise variance in a certain field quadrature. The strongest squeezing level demonstrated to date is a squeeze factor of 15 dB below the classical shot-noise limit at the wavelength of 1064 nm, but only measured at MHz frequencies [33]. The topology of the optical parametric amplifier (OPA) used therein was a linear, standing-wave, doubly-resonant cavity with a non-linear crystal made from periodically poled potassium titanyl phosphate (PPKTP). Up to 13 dB of non-classical noise suppression was measured at a wavelength of 1550 nm [447] in a similar cavity design, but again only at MHz frequencies. By the implementation of a coherent control scheme [448] and the mitigation of parasitic interferences the frequency band of detectable squeezing can be extended from MHz down to the required GW-frequencies [449]. This has been demonstrated in tabletop experiments with various squeezed light source setups operated in-air or in-vacuum and with OPAs constructed as

bow-tie or linear resonators [448, 450, 451]. Following these developments, similar schemes were used to realize squeezing enhancement in the present large scale gravitational wave detectors.

The highest squeezing level at GW-frequencies so far was reported in 2018 [14]. Figure 6.10 summarizes the main result of this work, where squeezed light was generated in a linear, doubly-resonant OPA at a wavelength of 1064 nm. A quantum noise reduction of up to 12 dB at Fourier frequencies between 10 Hz and 100 kHz was directly measured with a diagnostic homodyne detector. The analysis revealed that the measured squeezing level corresponds to an equivalent squeezing factor of up to 14 dB available for the injection into a gravitational wave detector with only 3.5 mrad rms of phase noise attributed to the squeezed light source operated in air. The recent progress in the development of low-loss Faraday isolators [452] suggests that this squeezing factor can be even further improved in the near future. The available squeezing level and the intrinsic low phase noise are key parameters, since the obtainable effective squeezing level in the interferometer is limited by the overall amount of optical loss and phase noise as illustrated in Fig.6.6. With the demonstrated squeezing level and phase stability of the squeezed light source reported in [14] it seems feasible to realize the envisaged squeezing enhancement of 10 dB (effective) in ET-HF, which is listed as baseline parameter in Table 6.1.

For ET-LF, which will be operated at the wavelength of 1550 nm, high squeezing levels at audio-band frequencies still need to be demonstrated. The realization of a suitable squeezed light source will rely on the same building blocks as developed and demonstrated for the ET-HF squeezer technology. First experiments reporting squeezing down to kHz-frequencies at 1550 nm have already been conducted [453, 454].

Two different squeezed light sources will need to be engineered for ET for the six systems: three systems will generate squeezing at 1550 nm for the ET-LF detector and three systems operating at 1064 nm will be used for the ET-HF detectors.

## 6.6 Input and output optics

### 6.6.1 Input optics

The input optics of ET comprises the optics downstream of the lasers. The system must deliver a beam with the required power, geometrical shape, frequency and angular stability to the interferometer input.

Electro-Optic Modulators (EOM) should provide the needed RF phase or amplitude modulations (to sense longitudinal and angular degrees of freedom, see section 6.9.2.3). Two in-vacuum suspended input mode cleaners (IMC) in series will be used to geometrically clean the beam and reduce its amplitude fluctuations as well as geometrical fluctuations. The resonant IMC can also serve in the loop of laser frequency stabilization. After the IMC an intensity stabilization section will provide the signal for stabilizing the laser's relative intensity noise (RIN). An in-vacuum Faraday isolator (FI) will prevent interaction of the light reflected by the interferometer with the IMC and laser system. Finally, a mode matching telescope will provide a beam with the correct size and wave front curvature for matching it into the interferometer. Optics with super-polished surfaces will be used to lower the amplitude of scattered light. Moreover, acoustic and seismic noise can cause beam pointing noise via

components in free-space propagation (mirrors, lenses, EOM, FI, etc.). Particular effort will be given to isolate such optics from environmental noise.

The input mode cleaner provides active frequency stabilization through feedback to the laser and passive frequency noise suppression above its cavity pole frequency. The input mode cleaner also reduces the higher order modal content of the laser light, suppressing beam jitter by a factor depending on the cavity finesse. Due to the high laser power that will be stored in the IMC cavity, radiation pressure effects and absorption in the IMC cavity input and output mirrors will be the main limiting factors. The radiation pressure effects will depend on the cavity finesse chosen and can be reduced with heavy mirrors. In the linear regime, it has been shown that radiation pressure noise was not an issue for Advanced Virgo [455]. In order to avoid beam distortion induced by photothermal effects, a low-absorption fused silica grade with good homogeneity will be chosen as mirror substrate and coating absorption lower than 1 ppm will be necessary.

In order to avoid unwanted cross-coupling, light back-reflected by the interferometer should be picked up before being coupled back in the IMC cavities. The solution adopted in first and second generations of gravitational wave detectors is to install a Faraday isolator in vacuum on the beam path between the interferometer and the input mode cleaner cavity. The ET-HF Faraday isolator will have to withstand high power (1kW), provide high isolation ( $> 30\text{dB}$ ) and low residual thermal lensing (residual focal lens  $< 100\text{m}$ ), and allow high transmission ( $>95\%$ ). Developments for Advanced Virgo using TGG as magneto-optic material show promising results [456] although further developments will have to be done, in particular for withstanding the high power. For ET-LF the field of telecommunication gives several possibilities for materials that can be used in Faraday isolators. These isolators will have to be ultra-high vacuum compatible.

In ET radio-frequency (RF) modulation of the laser beam will be used in the control of the interferometer, both for longitudinal and angular controls. The beam is modulated through the use of an Electro Optical Modulator (EOM). Compared to the EOM used in 2G detectors the ET-HF EOM will have to withstand higher laser power and thermal effects might become significant and drive the choice of material. For ET-LF, as for the Faraday isolator, the experience of the telecommunication field can be used.

### 6.6.2 Output optics

Traditionally the detection systems of first and second generation gravitational wave detectors includes all optical elements downstream of the main interferometer, i.e. behind the signal recycling mirror, such as for instance the high efficiency readout photodiodes and the output mode cleaner (OMC). ET will also feature the injection of frequency dependent squeezed (FDS) light from the output port of the interferometer. The injection of frequency independent squeezing was already successfully implemented in Advanced Virgo and Advanced LIGO and FDS is planned for the upgrade phase of these detectors. ET will benefit from the expertise gained with these detectors in this area.

The design of the detection system depends on the readout scheme chosen for the extraction of the gravitational waves signal. The advanced detectors successfully use the DC readout scheme in which the local oscillator is provided by setting a small offset from the dark fringe. This is one of the options for ET. The drawback of this readout is the constraint it imposes on the laser amplitude noise as this noise couples to the GW signal through the DC offset. Another option is the so-called Balanced

Homodyne Readout (BHR) as proposed in [457]. In this scheme the interferometer is on the dark fringe and the local oscillator is provided by a pickoff beam (which can be extracted inside the PR cavity for example). The interference between this LO beam and the output beam is readout by a system of 2 photodiodes in which the amplitude noise cancels out, which is an advantage compared to the DC readout. This type of system is usually used in the characterisation of the squeezing sources and has proven to work well [450]. Another advantage of the BHR with respect to the DC readout is that it reduces the constraints on the photodiodes electronics as the amplitude of the constant voltage (due to the offset from the dark fringe present in the case of DC readout) is much reduced. BHR is one of the options for the upgrade phase of Advanced LIGO and ET could therefore benefit from the experience gained with this detector.

The goal of the OMC is to filter the imperfections of the beam profile induced by beam mismatch, misalignment or astigmatism in the interferometer. Such defects couple a fraction of the main beam into spurious geometrical modes which do not carry information on differential arm motion and increase the shot noise level. Modulation sidebands which are used for longitudinal and angular sensing in the mirror control loops should also be suppressed by the OMC in order to minimize the shot noise and also to prevent the side band power noise from spoiling the sensitivity. Two types of cavities have been developed for the actual GW detectors: a monolithic cavity made of a few centimetres long crystal as it has been designed for Advanced Virgo [458] or a ‘tombstone’ design as for Advanced LIGO [459] or GEO600 [460]. One of the limitations of the monolithic design is the risk of thermal effects which increases with the need to increase the finesse for improved filtering. However the choice of the value of the finesse is limited by the diffraction losses on the OMC mirrors. Development of a low loss and high finesse cavity are ongoing for Advanced Virgo+. One drawback of the tombstone cavity is the presence of mechanical resonances in the detection bandwidth. In both cases the cavity length noise directly affects the GW signal and will have to be carefully assessed. The experience gained with the present detectors will be very valuable in order to select the design of the ET OMCs. The readout choice will also impact the design of the OMC. In the case of BHD two OMCs (with eventually two different designs) will be needed: one to filter the main output beam (dark fringe) and one to filter the LO.

The OMC needs to be associated with several other optical components. In order to limit the amount of backscattered light a Faraday Isolator will be placed in front of the OMC. This component is also used for the squeezing injection. A telescope will be designed in order to tune with sufficient accuracy the beam matching and the beam alignment with respect to the OMC. The whole system should be seismically isolated and placed under vacuum in order to meet specifications on beam jitter. High quantum efficiency photodiodes are needed for the readout signal, including low noise electronics such that the electronic noise is typically a factor 10 below the shot noise.

## 6.7 Scattered light mitigation

Stray light in gravitational-wave interferometers is the light coming from the laser source which does not follow the intended path and recombines to the main beam. The reasons for that deviation could be many, such as scattering off non-ideal surfaces of optical elements, clipping by finite apertures, spurious reflections off anti-reflective surfaces and so on. Stray light related noise has been recognized to be an issue since the very first investigation of technical limitations in the interferometers designed

for detection of gravitational waves [461]. A tiny amount of stray light coupling with the fundamental mode after probing the vibrations of infrastructures can bury the gravitational signal. For illustration, in the case of Advanced Virgo, stray light constitutes a limitation if it recombines to the main mode with an efficiency greater than  $10^{-24}$  W/W equivalent to about five photons per second. The problem of stray light can be broken down into three different factors:

- the fraction of the beam which is scattered;
- the amplitude and frequency of the motion of the scattering element;
- the transfer function of the stray field to the anti-symmetric port of the interferometer.

The stray light contributions are in general difficult to simulate and involve non-linear effects. Nevertheless, understanding those three different factors is very useful for the mitigation of stray light.

### 6.7.1 Lessons learned

Early studies on the potential impact of stray light were performed by K. Thorne back in 1989 [462], followed soon by J.Y. Vinet, S. Braccini and V. Brisson. The main goal was to assess the impact and the possible mitigation of stray light bouncing in the long arm tubes [463, 464]. The outcomes of the studies were both the design (geometry, position, materials) of a system of baffles to be installed in the long tubes, and the adaptation of Monte Carlo methods to track photons. This latter method, however, fell short of capturing the risks of the stray light, without taking into account the coherent effects that were not easy to simulate.

This scenario changed with the development of simulation methods based on Fast-Fourier Transform applied to laser field propagation [465]. Nowadays, a paraxial direction kernel is employed to evaluate the propagation of the light in the cavities and surface maps are used to calculate the reflection of the fields on the test masses. This is combined with frequency domain simulation tools [466, 467], with capability to estimate transfer functions taking into account radiation pressure and mechanical responses in the interferometer. Low angle scatterings dominate and are originated by low spatial frequency figure errors of the mirrors and scatter from hardware surfaces close to the beam path. Wide angle contributions are due to micro-roughness and defect points in the mirrors leading to light scattered towards the surrounding structures. Other contributions include the presence of ghost beams from multiple reflections and stray light from optical benches which are difficult to simulate. These can be split into two different sources: the first one from large amplitude and slow motion (comparable or larger than the laser wavelength) of the optical benches, the second one from the small amplitude motion of optical elements (mirror mounts, sensors,...) in the detector sensitive band (3 Hz to several kHz). The first one shows up in the sensitivity as a broad band noise at low frequencies (below few tens of Hz) while the second one gives rise to resonances in all the sensitive band.

### 6.7.2 Stray light control

In LIGO and Virgo interferometers, a complex system of baffles and diaphragms are put in place with the objective to maintain the noise induced by the presence of stray light at a level of at least two orders of magnitude below the nominal sensitivity of the experiment. The design of the baffles and the materials employed to construct them are the result of detailed studies taking into account

damage thresholds, apertures, roughness and reflectivity requirements, geometry at the edges and vibrations, which vary in different parts of the interferometer. In the case of Virgo for the long arms, this translates into the need for installing hundreds of baffles distributed along the vacuum tubes, made of stainless steel with specially serrated edges to avoid coherent contributions from diffraction at the edges. Other ground-based baffles are installed in different vacuum links between interferometer towers. Most importantly, the suspension systems hosting the main test masses are equipped with stainless steel mirror polished and AR-coated baffles with the aim to suppress the dominant low angle scattering contributions. Other diaphragm baffles are installed on optical benches based on different materials including silicon carbide or diamond-like carbon and the walls of the towers hosting the large mirrors have been equipped with absorbing glass to damp stray light out of optical benches.

In the current detectors the benches are suspended to reduce the large motion coming from the ground, and put in vacuum to reduce the optics motion that can be acoustically excited. The use of super polished optics and reduced dust contamination from clean room installation and vacuum operations has also reduced the fraction of back scattered light. However, scattered light remains a significant limitation to the current detectors, and further development of techniques to reduce the scatter are a critical element of R&D to realize ET.

### 6.7.3 New and future developments for stray light reduction

Several developments and ideas have been proposed for the future detectors. These concern the monitoring of stray light, its reduction as well as the reduction of the motion of the scattering elements. Several examples are given here.

In preparation for AdV+, the Virgo Collaboration is exploring the implementation of instrumented baffles [468] surrounding the main test masses to monitor the development of the diffuse light from scattering at low angles in the interferometer. Baffles will be initially equipped with  $O(100)$  photodiodes capable to sample the scattered light at the rate of approximately 100 - 200 Hz. This opens the possibility of an active tracking of stray light contributions in critical parts of the interferometers, facilitating the alignment and commissioning tasks and providing a dynamic follow-up of mirror defects and developing higher-order modes in the cavities. The data will permit tuning the current simulations. If proven successful during AdV+ operations, instrumentation for stray light control could be extended to other parts of the interferometer relevant to wide angle scattering contributions. It is likely that active monitoring of stray light will become an integral part of ET final design in the long term.

Proposed ideas for the reduction of stray light from the optical benches are:

- coating all the aluminum optical mounts with absorbing materials such as vantablack or anoblack, in order to absorb the scattered light as soon as it leaves the optical path,
- investigate absorbing coating materials for the bench and vacuum chamber walls that are ultra high vacuum compatible and resistant to abrasion,
- systematically install diaphragms and beam dumps to absorb first order ghost beams in transmission of highly reflective optics, from reflections from anti-reflecting coatings and reflections from active absorbing materials (photodiodes, cameras).
- maintaining the beam as large as possible on all optical surfaces,

- use 3D opto-mechanical simulation to guide the placement of diaphragm and beam dumps, and to optimize the bench optical layouts.
- develop sensors with smaller back reflection, in particular quadrant photodiodes with absorbing material separating the four quadrants.

Additional design constraints will be implemented for the reduction of the motion of the scattering elements, like:

- increasing the rigidity of all optical mounts to push mechanical resonances to higher frequencies where the detectors are limited by quantum shot noise. This can be done through a combination of more massive pedestal and lowering the optical beam height.
- design mechanical mount dampers to reduce the amplitude of the motion at resonance.

Some of those ideas will be implemented and characterized in the second phase of the Advanced detectors and will serve as input for the ET design.

## 6.8 Interferometer control

To operate ET, many degrees of freedom (DOFs) need to be controlled. The most important DOFs characterise the interferometer as a whole, and can be divided into the longitudinal DOFs, which involve controlling the position of the main mirrors along the optical axis, and the angular DOFs which refer to the orientation of the main mirrors with respect to the incident beam axis. There are several more control loops, the auxiliary loops, which control e.g. the position or velocity of some part of a suspension, or the power of the laser system, but we mostly focus on longitudinal and alignment control here, since these are most critical for the overall performance of the interferometer.

Regardless of the split in longitudinal and alignment control, some links between them exist too, such as the bi-linear coupling of alignment control noise with beam spot position on test masses into the longitudinal signals. We will point these out where required.

### 6.8.1 Longitudinal control

In the steady-state operation of the interferometer, the longitudinal control maintains the longitudinal DOFs of the interferometer and optical cavities at (or sufficiently close to) their nominal operating points. Another distinctive task of longitudinal control is lock acquisition, which is the process of bringing the interferometer reliably to its steady-state operating point.

For a single Fabry-Perot cavity, consisting of two or more mirrors, the standard way to obtain an error signal for locking the cavity to resonance with the incoming laser light, is the Pound-Drever-Hall technique [469]. The technique consists of adding RF sidebands to the optical frequency of the laser using a phase modulator. Alternatively modulation can also be applied to the cavity itself, e.g. by modulating the round-trip length of the cavity by displacing a mirror. The signal in reflection of the cavity is then demodulated yielding a signal proportional to the deviation from resonance. This error signal can be used to control the length of the cavity by e.g. actuating a mirror, or to control the laser frequency. This is a very robust system while dealing with a single DOF and is applied for input mode-cleaners and output mode-cleaners of current GW interferometers, with performance compatible to the ET requirement.

A GW interferometer is more complex than a single cavity, and has more longitudinal degrees of freedom. The number of DOFs for the main interferometer is determined by the number of optical resonators that form the interferometer (plus one for controlling the interference condition of the Michelson interferometer). Typically there are more suspended mirrors than DOFs which leaves some of them uncontrolled, as for example a global translation of all mirrors or the relative position of folding mirrors within recycling cavities (the latter may be controlled for ET if required, to reduce scattered light from moving fringe patterns on folding mirrors).

The first generation interferometers, such as initial LIGO and Virgo consisted of 4 DOFs: Differential ARM length (DARM), consisting of the length difference of the two long arm cavities, Common mode ARM length (CARM), the length sum of the two long arms, the Michelson DOF (MICH) and the Power Recycling Cavity Length (PRCL). For the second generation detectors advanced LIGO, advanced Virgo and KAGRA, a fifth DOF is added: Signal Recycling Cavity Length (SRCL), which will also be the case for the ET interferometers.

Of these five DOFs, the DARM loop is of particular importance, since it directly contains the information of gravitational wave signals. This means that greatest care is taken to bring the noise performance of the corresponding readout to the most fundamental limits of the given configuration. Since this DOF is also actively controlled, the effect of the corresponding feedback loop must be taken into account to obtain a calibrated gravitational-wave signal that can be used for data analysis.

The operation of the Advanced LIGO and Advanced Virgo interferometers has demonstrated the feasibility of longitudinal control techniques for second generation detectors. In particular advanced LIGO, since operating with a signal recycling (extraction) mirror from the beginning, has demonstrated the control scheme for five longitudinal degrees of freedom, including their lock acquisition. The basic scheme is based on the Pound-Drever-Hall technique, but uses two sets of modulation frequencies simultaneously, which are designed to yield signals for all five DOFs by sensing different combinations of the sideband signals and the carrier light at different interferometer ports [470].

Ideally one would obtain one independent error signal per DOF, which is only sensitive to that DOF. In practice most signals are sensitive to more than one DOF, but to varying degrees. The situation is coped with by using multiple-input, multiple-output (MIMO) linear combinations of signals as well as gain hierarchy. Feed-forward/noise subtraction for spurious couplings is also employed as outlined below. The ET design will build on this scheme, using simulations to find optimal sets of modulation frequencies and with the best sensing location.

The operation of Advanced LIGO has shown that coupling of residual motion of the signal recycling cavity length to the main gravitational wave readout (DARM degree of freedom) is a limitation of the sensitivity at low frequencies if DC readout is used. Since this coupling is proportional to the offset chosen in the DARM DOF. In ET this limitation will be avoided with the use of balanced homodyne readout (BHR) [457], as also foreseen for the LIGO upgrade A+ currently under development. The employment of a BHR readout scheme for ET makes the optical layout a bit more complex, but the requirements seem well understood at this time. Experience at LIGO will guide the BHR design for ET.

All currently operating interferometers employ digital control loops wherever possible, for the benefit of flexibility, stability and transient noise reduction of control transfer functions. Typical sample frequencies are around 10-64 kHz, but even for faster loops digital control is now used (at Virgo the

fastest digital loop is running at 500 kHz.)

Digital demodulation is a technique that has been implemented in advanced Virgo, where optical signals are sampled with very high frequencies (several 100 MHz) in order to demodulate digitally, rather than with analog mixers [391]. Recent advances in high-speed ADCs and FPGAs allows this option. This technique maintains flexibility throughout this signal processing step, at the cost of more complex hardware and need for careful dynamic range design. The benefits probably outweigh the disadvantages, such that the application of this technology for ET seems likely. The experience gained with advanced Virgo is a strong asset.

### 6.8.2 Lock acquisition

One challenge of operating a GW interferometer is that at the operation point (steady state), several cavities need to be simultaneously resonant with picometer accuracy, while in the uncontrolled interferometer the mirrors are freely swinging by up to a micrometer per second. This already assumes that the payloads are pre-stabilized using the *local controls*, which are part of the suspension system. Since the ET interferometers have 5 DOFs, the random phase space starting point is enormous.

For systems with 3 DOFs, this problem is still manageable as demonstrated by the GEO600 lock acquisition. One can simply wait a short while until the various DOFs are close to resonance by chance, and then switch on the control loops with appropriate triggers (e.g. on some cavity power). However, already for GEO, auxiliary locking signals derived from modulation sideband power had to be used. For 4 DOFs it gets harder, but was achieved with Initial LIGO [471], in which various loops are switched on in short succession, while changing the sensing scheme on the fly. Instantaneously locking 5 DOFs at about the same time is very hard due to the enormous phase space. It had successfully been tried out at the Caltech 40 m prototype, but was ultimately judged too unreliable.

At the Virgo interferometer, the problem of locking 4 DOFs was tackled in a different way, by locking individual DOFs sequentially at different working points, before transitioning in a deterministic way to the final one in several steps. This technique is called Variable Finesse [472], since it initially locks the Michelson DOF at half-fringe, thereby making it an effective mirror with low reflectivity. In the initial state the power recycling mirror is misaligned and gets slowly aligned during the locking sequence. This technique has been perfected over the last 10 years at Virgo and works very reliably. Research is on going to extend this technique to 5 DOFs, by initially misaligning PRM and SRM mirrors, this approach could be suitable for ET, but still need to be validated by simulations.

For Advanced LIGO, as a result of the difficulty locking the 5 DOF configuration, an auxiliary laser stabilization (ALS) was developed, which can lock the arm cavities independently with a different laser [473, 474]. The technique used for aLIGO is to use an independent green laser system, which can lock the arm cavities and keep them out of resonance for the IR, while the remaining 3 central DOFs are locked in a traditional, one-shot way. Green laser light is injected from the end, and then extracted in central and interfered with the frequency doubled PSL.

Locking a dual-recycled, Fabry-Perot Michelson interferometer using arm-length stabilization has been successfully demonstrated with the Advanced LIGO interferometer [475], which is now in daily use. For the KAGRA detector a similar scheme was implemented, but with the green light injected from the central area towards the end. If this works, this would be a nice simplification of the LIGO

scheme [476]. It still employs additional hardware though, which also needs additional effort for commissioning and maintenance. If a reliable locking system can be found without using an ALS it would clearly be preferable in order to reduce the complexity of the detector.

### 6.8.3 Steady state control

Once all the degrees of freedom are controlled and moved to their final working point, all control signals are derived from error signals with the lowest available noise (the highest signal-to-noise ratio). Moreover, control loops get optimised and actuator dynamic ranges get reduced, to minimize or eliminate digital-to-analog conversion (DAC) noise. When all the low noise control loops are active, the steady state is reached, in which the most sensitive gravitational-wave measurements are possible.

In the steady state, noise of control loops should be held below the noise floor of the DARM sensing system. Noise is being introduced to the interferometer's DARM DOF (which could spoil the GW signal) by longitudinal and alignment control loops. Typically this 'control noise' is dominated by the sensing noise of the contributing loops. Control noise is very relevant for ET, where one of the biggest challenges is to move the lower frequency limit of the detection band from around 10-20 Hz (as it is in current detectors) down to 3 Hz. This is a frequency region where control noise from angular and auxiliary longitudinal DOFs typically dominates the sensitivity.

For the auxiliary longitudinal DOF's (MICH, PRCL, and SRCL) noise subtraction schemes are employed successfully for the second generation detectors, forming the model for ET. The methods can be divided in *online* and *offline* methods. Online methods work in real-time while the interferometer is operating, subtracting a sample of the auxiliary loop feedback from the DARM signal by applying it to DARM actuators with appropriate filtering. Offline methods subtract properly filtered feedback signals from auxiliary loops to DARM but only after the DARM signal has been recorded. More complex non-linear noise subtraction methods are under development, and possibly can further improve the noise subtraction performances for ET.

### 6.8.4 Alignment control

Alignment control is primarily concerned with keeping all optics aligned with respect to each other and with respect to laser beams propagating between the optics. As such, it is global in the sense that it uses interferometric information about the relative alignment of laser beam axes, predominantly obtained with differential wavefront sensing (DWS). In addition to this, alignment control is also concerned with keeping beam spots at dedicated positions (preferably close to the center) on the interferometer mirrors. This is a secondary goal, referred to as spot position control, that uses local information obtained from beam spot position sensors or from alignment (dither) modulation schemes. In the following we will be only mentioning the strategy for DWS alignment.

As for longitudinal control, alignment control for ET will be based on the successful alignment schemes existing for advanced LIGO and advanced Virgo. For differential wavefront sensing, these are based on the extended Pound-Drever-Hall scheme as devised for longitudinal control, using at least two optical modulation frequencies and several sensing ports.

However, since alignment control noise is limiting sensitivity at low frequencies in advanced LIGO and Virgo, (e.g. below about 20 Hz in LIGO during the O3 run in 2019 ), improvements will be needed for ET.

A lower alignment control noise can be achieved in two major ways, namely by

- reducing the residual alignment-relevant motion of the optics, i.e. motion without the engagement of global alignment control
- increasing the signal-to-noise ratio of the alignment (DWS) sensing signals

Advances in the sensing and control of the suspension for ET will lead to some reduction of the alignment motion of the optics. Tilt-meters can be used to break the degeneracy of tilt and acceleration sensing at low frequencies, or novel seismometer configurations (6-d seismometer) may be used to this end [477, 478]. If lower suspension (and thus mirror alignment) motion is achieved, this can be used for a reduction of alignment feedback bandwidth, thus lowering DWS control noise. For the ET-HF interferometer such potential reduction of bandwidth may be limited by the optical alignment springs (caused by radiation pressure, *i.e.*, the Sigg-Sidles instability [479]), which may require damping with DWS alignment control of sufficient bandwidth. Due to operating at lower laser power, in the ET-LF interferometer the optical alignment springs will be at lower frequencies than for ET-HF, such that a lower DWS control bandwidth may be necessary. What helps in case of ET-HF though is that the problem of alignment feedback noise is less severe in the first place. Due to the higher frequency band, the interferometer can tolerate more low-frequency control noise than the ET-LF interferometer. Here the xylophone design of ET shows another strong advantage. Furthermore, the increase of mirror masses to 200 kg for ET (about 5 times more than current detectors) helps with decreasing the alignment optical spring frequencies. There may also be alternatives to damping of alignment optical spring resonances with DWS feedback, which is to be investigated. It may be possible to damp such modes with radiation pressure of the laser light itself, applying feedback forces in a narrow frequency band. This may help to reduce control noise originating from the DWS sensors if a bandwidth reduction is possible.

It is expected that the increase in beam size in ET will make the alignment requirements more severe than for second generation interferometers. Ultimately, a detailed technical design study have to account for this, and find a suitable compromise.

Improvements in the signal-to-noise ratio of alignment sensing signals are currently more uncertain. As a benchmark, new systems would have to have sensing noise below  $10^{-15}$  rad/ $\sqrt{\text{Hz}}$ , to make substantial improvements, which needs some more R&D. The planned BHD readout will help in reducing contribution to sensing noise on wavefront-sensor signals, since it removes the first-order coupling of beam position on the wavefront sensor into the alignment signal.

Another (additional) way to reduce alignment control noise coupling to DARM is to develop (possibly non-linear) Wiener filtering, to subtract alignment feedback noise using known witness channels. Some of these implementations have successfully reduced noise at operating interferometers.

## 6.9 Calibration

Extracting new science from the observed gravitational waves recorded by the Einstein Telescope requires accurate knowledge of the amplitude and timing of the signals. With the very high SNR, up to 1000, extremely low calibration uncertainty will be mandatory for precision science.

### 6.9.1 Science-driven calibration requirements

The exact calibration requirements for the scientific objectives of 3G gravitational-wave observatories can already be estimated. There are two aspects of calibration uncertainty, the absolute uncertainty and the relative uncertainty. The first tells us how well we understand the total calibration in absolute numbers, while the latter is a frequency-dependent calibration uncertainty with respect to some fixed reference frequency. Looking for deviations from a modeled waveform template, we are mainly concerned with relative calibration uncertainty. In order to estimate distances to the sources, we are most interested in absolute calibration. In addition to the calibration error of the detector itself, the waveform models have also an uncertainty. Studies are underway to determine the exact calibration requirements integrating both detector and waveform uncertainties.

Several of the scientific targets for ET that will set our calibration requirements include BNS tidal deformation, deviations from GR, and measurements of the Hubble constant. The first two look for deviations from a modeled waveform template, while the latter is based on absolute distance measurements. With  $O(1000)$  low-redshift binary neutron-star events, the Hubble constant may be determined to a  $\sim 1\%$  level with Einstein Telescope [480]. This would require a sub-percent systematic absolute amplitude calibration. The signals with the highest SNR give the narrowest limits for GR. With a network of three 3G detectors we expect about one event per year with SNR  $\sim 1000$ . To avoid being dominated by calibration errors, we need a calibration to an amplitude of  $< 0.5\%$  and about 0.1 radian in phase integrated over 10 Hz to 400 Hz.

### 6.9.2 State of the art

Overall calibration relies on the ability to characterise the detector's control systems. The development of technologies important for calibration are discussed in the following subsections. The state of the art in calibration methods involve the use of MCMC simulation to determine unknown systematic uncertainties. The detector's control systems (sensing and actuation) have a considerable influence on the total calibration accuracy and therefore must be precisely characterized for the calibration of each gravitational wave detector. Calibration lines are applied using the detector's length actuators and/or with photon calibrators (see below) in order to compute time dependent correction factors. For Advanced LIGO, this process results in an absolute calibration uncertainty of a few percent in amplitude and a few degrees in phase across the majority of the frequency band [481].

#### 6.9.2.1 Photon calibrators

Photon calibrators provide a calibration reference starting from a traceable reference: an optical power meter. They use an amplitude modulated laser to apply a radiation pressure force to the test mass. For all interferometric gravitational-wave detectors with arm cavities, this is the current method

of choice for absolute calibration. Ultimately, the current photon calibrator implementation in second generation detectors has an absolute systematic uncertainty of 0.5%, set mainly by a combination of uncertainty in the calibration of the NIST-traceable power standard and uncertainty in position where the photon-calibrator beams and the interferometer beams impinge on the test masses [482]. The national metrology institutes are improving the primary laser power calibration standards. On request of LIGO, NIST has improved the laser power standard from 0.44% error to 0.31% and is envisioning a level of 0.05% in the next few years.

### 6.9.2.2 Newtonian calibrators

Newtonian calibrators rely on the Newtonian gravitational interaction between an interferometer test mass and a known arrangement of rapidly rotating calibration masses, with the arrangement often approximating a dipole, hexapole, or other multipole distribution [483]. These devices have absolute systematic uncertainties related to how well the geometry of the calibrator, and its distance and orientation with respect to the test mass, can be characterized. A Virgo prototype [484] has already been deployed, and an improved prototype may achieve a 1% systematic uncertainty. KAGRA is designing a dual-mass-distribution calibrator that, when combined with a photon calibrator, may achieve an absolute uncertainty of 0.17% [485]. A Newtonian calibrator prototype is also being developed for Advanced LIGO. These Newtonian calibrator technologies are still in the very early stages of development, but there is significant effort in this direction.

### 6.9.2.3 Other calibration methods

Laser frequency can also be used as a reference against which to calibrate an interferometer [486]. However further R&D is required to cut down uncertainties from current levels of about 10% (as in Advanced LIGO) to the requirements of the Einstein Telescope. It is also possible to fix certain aspects of the calibration using an astrophysical source whose properties are sufficiently well known [487]; But here also more work is needed to understand how this technique will improve the calibration for 3G detectors.

## 6.10 Seismic isolation and suspension

### 6.10.1 Seismic isolation systems

Seismic isolation systems constitute the mechanical interface between the environment and the detector core optics; they fulfill three main functions:

- to reduce seismic and vibration noise below the sensitivity requirements in the detection band;
- to reduce the broadband RMS motion of the suspension systems, and in particular the contributions from the suspension resonances and the micro-seismic peak(s);
- to provide slow large-scale position and angle control of each suspended optical element.

These functions have performance requirements that span a very large frequency range, from DC positioning for initial alignment, to day-long actuation for tides, suspension-mode damping, and isolation performance up to kHz frequencies. To meet these requirements, the seismic isolation is divided into two major components:

- a pre-isolation stage, the so-called *seismic platform*;
- a damped *suspension chain*.

The seismic platform allows large dynamic range actuation for initial alignment and compensation of tidal drifts, and provides isolation from low frequency vibrations from approximately 10 mHz up to 10 Hz. The suspension chain provides the majority of the seismic attenuation performance in the detection band, and provides mechanisms for ‘fast’ actuation for lock-acquisition and length and angle control of the interferometer.

#### 6.10.1.1 ET requirements

The extension of the detection bandwidth of the Einstein Telescope to the low-frequency region starting from 3 Hz requires improved seismic attenuation chains compared to Advanced Detectors. For this purpose, a detailed study was carried out in the framework of the 2011 ET Conceptual Design. The conclusion was that a viable solution would be a longer (17 m) version of the current Virgo SA with the same number of passive isolation stages but equally spaced.

#### 6.10.1.2 Seismic platform

The Superattenuator seismic platform consists of a massive disk, called Filter 0, supported by three legs forming an inverted pendulum with period of oscillation of tens of seconds. The inverted pendulum legs rest on a ring supported by three piezoelectric actuators for inclination control using tiltmeters laying on the ground. The platform holds several cantilever springs that isolate in the vertical direction the attenuation chain.. The Filter 0 position and yaw angle are actively controlled using accelerometers and electromagnetic actuators.

It is expected that this structure, conceived some decades ago, can be reduced in height by introducing an improved seismic platform and removing two of the SA filters. A shorter suspension, maintaining the same performance, will allow for a significant reduction in infrastructure costs. This can be achieved through a R&D program that includes the improved sensors, actuators, and signal processing power that are now available.

#### 6.10.1.3 Super-Attenuator modifications for Low-Frequency ET

In order to extend the detection bandwidth of the Einstein Telescope in the low-frequency region starting from 3 Hz, improved seismic attenuation chains are needed. For this purpose, a detailed study was carried out in the framework of the 2011 ET Conceptual Design. The conclusion was that the optimal configuration would have been a longer (17 m) equal-spaced version of the Virgo SA, that kept the number of filters unchanged.

A series of simulations of the SA horizontal transmissibility (the open-loop transfer function between mirror motion and ground motion) have been performed using the Octopus mechanical simulation software (by P. Ruggi, described in [488]). In figure 6.12 a comparison between the current SA transfer function (blue curve), based on validated mechanical parameters of the Advanced Virgo North End tower, with various longer alternative configurations is reported. Assuming the input seismic noise equals to the inertial platform sensing noise (flat  $10^{-13}$  m/ $\sqrt{\text{Hz}}$ ), a mirror displacement compatible with ET-LF design sensitivity above 1 Hz can be obtained using a 12 m tall version of the

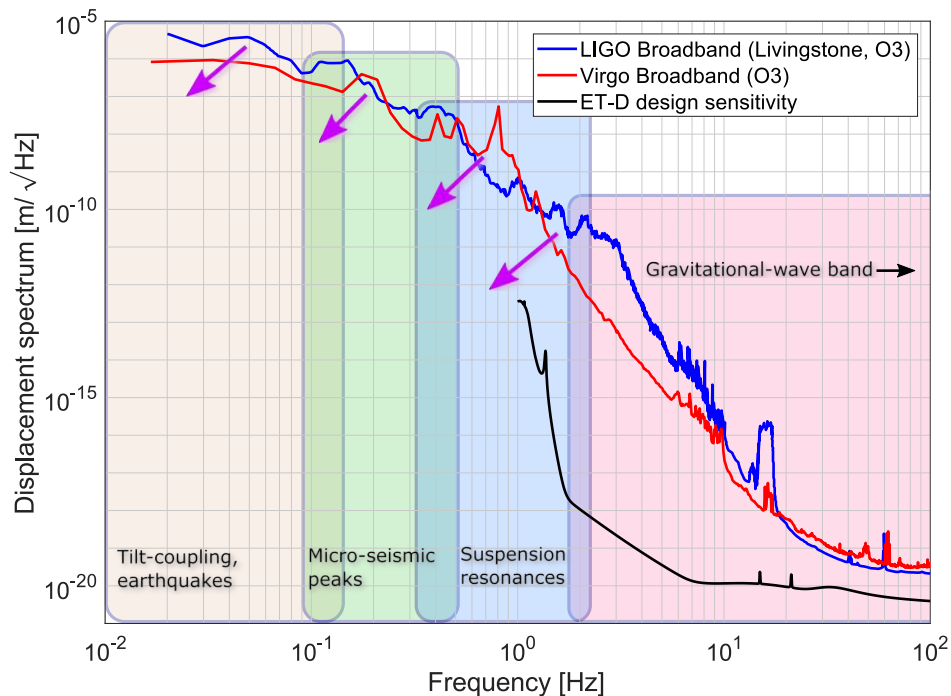


Figure 6.11: A comparison between the performance of the LIGO and Virgo instruments during the O3 observing run and the ET design sensitivity. The coloured windows show the important frequency regions, and the arrows show the regions where ET must have improved performance in order to reduce the corner-frequency of the ‘seismic wall’.

SA that is installed on a seismic platform, as shown in figure 6.13. Similar results were also shown in [489].

#### 6.10.1.4 Inter-platform motion

Experience in the LIGO and Virgo observatories has shown that large, low-frequency motion of the suspended optics relative to each other, and with respect to their environment, can result in a signal that is up-converted in frequency. This happens through scattered light that recombines with the main laser beams and interferes with a phase whose derivative depends on the relative speed. This can be observed in the gravitational-wave band [490, 491]. The problem becomes significant when the relative velocity is of the order of one radian per second of optical phase shift. Lower speeds do not cause to up-conversion.

For ET it is important to control the distances between:

- primary seismic platforms, including the power- and signal-recycling cavities;
- the interferometer optics and any location reached by a pick-off beam or ‘ghost’ reflection; and
- the seismic platforms and critical scattered light baffles.

The interferometer should be optically ‘closed’ such that no beam can reach or return from a poorly controlled surface.

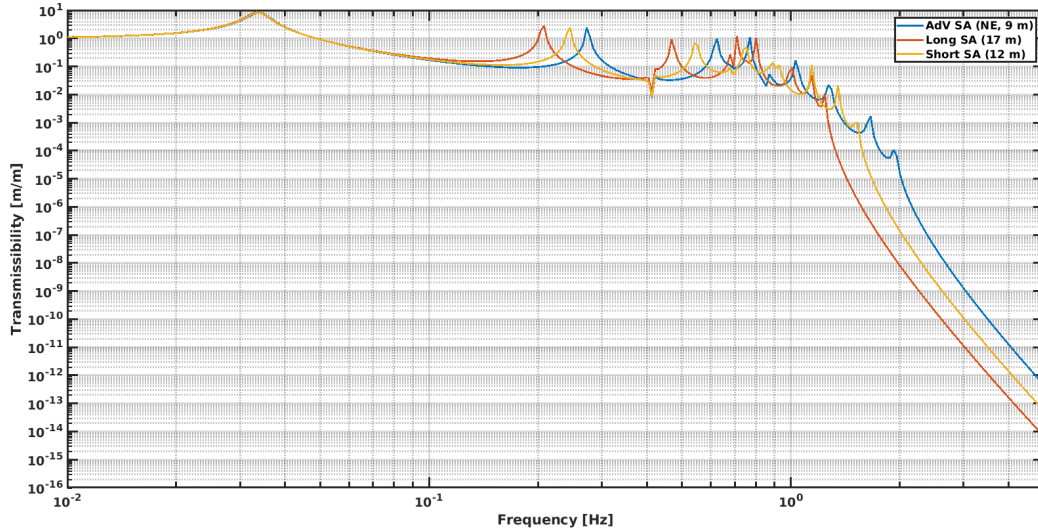


Figure 6.12: Simulation of the SA open-loop horizontal transfer function (Mirror Motion/Ground Motion), along the beam axis, in different configurations. Advanced Virgo SA (blue curve) is compared with two longer versions: 17 m (red curve) and 12 m (orange curve).

Several techniques have been applied to control relative velocities, the two most common ones are auxiliary interferometers, such as a Suspension Platform Interferometer [492], and inter-platform tracking using a combination of local sensors [493]. All current observatories use optical levers to measure the DC alignment and low-frequency motion of core optics. If these devices are mounted on seismically-isolated platforms, they will have lower noise. Comparable or improved performance can be achieved with differential interferometric sensors using either quadrant photodiodes or multiple beams.

#### 6.10.1.5 Sensor development

The seismic isolation and suspension systems of ET will require the development of new sensors not currently deployed in-vacuum at observatories. The most important classes of sensor required are:

- Inertial sensors in rotation. Actively controlling the tilt of the isolated platforms is crucial, and a suitable sensor must have self-noise of  $< 10^{-10} \text{ rad}/\sqrt{\text{Hz}}$  at 10 mHz [494, 495].
- Advanced inertial sensors in translation. Reaching a sufficiently low vibration level will require sensors with a resolution of  $\sim 10^{-13} \text{ m}/\sqrt{\text{Hz}}$  at 1 Hz.
- Precision non-contact displacement sensors for suspension damping. To actively extract energy from the suspension chain normal-modes without injecting noise, a non-contact sensor will need better resolution than the input platform motion, *i.e.*  $< 10^{-13} \text{ m}/\sqrt{\text{Hz}}$  at 1 Hz [496].
- Inter-platform sensors for displacement and rotation. There are numerous potential technologies, but the key performance metric is to have RMS noise comparable to the linewidth of the suspended cavities, *i.e.*  $\sim 10^{-10} \text{ m}/\sqrt{\text{Hz}}$  at 10 mHz.

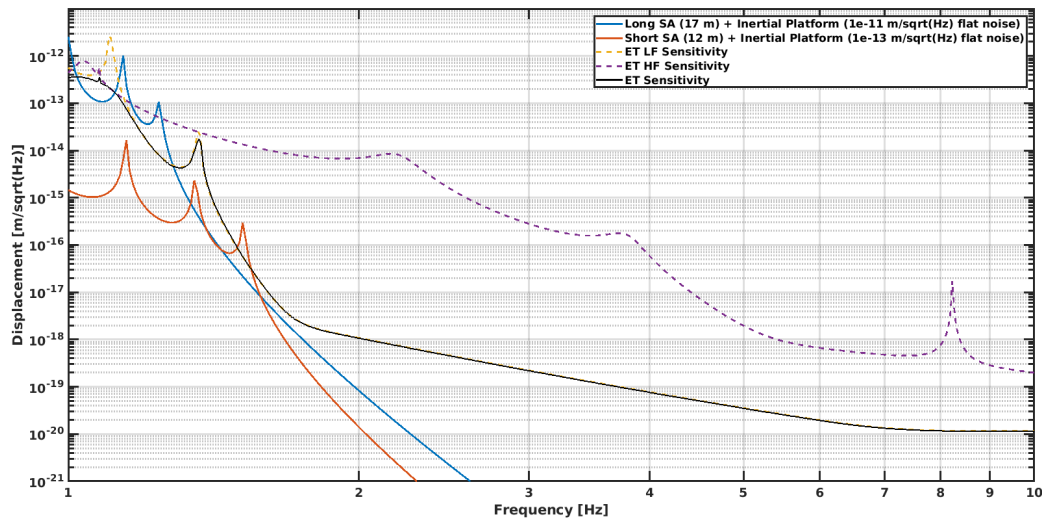


Figure 6.13: The simulated mirror displacement obtained using a 17 m-SA and 12-m SA installed on ideal sensor limited-inertial platform with different requirements (blue curve and red curve respectively) is compared with ET-LF, ET-HF, and the combined ET sensitivities (orange, magenta, and black curves respectively).

## 6.10.2 Test mass suspension systems

### 6.10.2.1 Suspension thermal noise of the mirror

As seen before, the top level requirements of a gravitational wave mirror suspension are to reduce seismic noise input from the ground and to provide a sufficiently low level of thermal noise arising from the materials used to construct the suspension. At the same time, electromagnetic/electrostatic actuators are required to steer the mirror to enable the interferometer to be aligned and locked.

The ET final stage payload will feature a design which has already been well proven in Advanced Virgo: a marionette, which supports the reaction mass and the mirror. In Advanced Virgo, position control is applied hierarchically by actuating from the super-attenuator on the marionette, and from the reaction mass on the mirror. In case of the ET payload, which is suspended via a single wire, a further reaction mass must be hosted into the cryostat to control the marionette. The benefit of this design is that it is compatible with the cryostat design described in section 6.11.1. In this section we discuss the requirements of the final stage suspension for both the Low Frequency and High frequency ET design.

Suspension thermal noise arises from mechanical dissipation in the materials adopted for the mirror suspension. This includes (i) Brownian noise which originates from surface loss in the suspension fibres and bond loss due to the attachment of the fibres to the test mass or (ii) Thermoelastic noise, which is the coupling of statistical temperature fluctuations through the thermo-mechanical properties of the suspension materials such as the thermal expansion coefficient and the Young's modulus. The suspension thermal noise can be calculated via the Fluctuation-Dissipation theorem [497], which states that above the pendulum resonance the frequency component of the displacement thermal noise  $x_{\text{susp}}(\omega)$  is given by

$$x_{\text{susp}}^2(\omega) = \frac{4k_B T \omega_0^2 \phi_{\text{total}}}{m \omega^5}, \quad (6.10.1)$$

where  $T$  is the temperature,  $m$  is the pendulum mass,  $\phi_{\text{total}}$  is the mechanical loss of the pendulum ( $\propto 1/Q$  with Quality factor  $Q$ ),  $\omega_0$  is the resonant angular frequency,  $k_B$  is Boltzmann's constant and  $\omega$  is the angular frequency. The dominant contributions arise from the horizontal pendulum resonance (under 1 Hz) and the vertical bounce mode (typically 10 Hz). At higher frequencies, the violin modes also produce narrow spikes in the detection band.

A pendulum mirror suspension stores energy both in the elastic deformation of the fibres and the gravitational potential energy. The energy stored in gravity is lossless and dominates in heavily loaded suspension fibres. This implies that the pendulum loss is lower than that of the material used for the suspension fibre which is termed *dissipation dilution*. The dilution allows the total mechanical loss ( $\phi$ ) to be diluted to  $\phi/D$ , with  $D$  being conveniently calculated from Finite Element Analysis [498]. For aLIGO and Advanced VIRGO the dilution is typically 90, showing that only 2% of energy is stored in the pendulum mode. For the vertical, or bounce, mode, the dilution is given by the cross coupling of the suspension. This enters through a term due to the curvature of the Earth, and a contribution from mechanical tolerances. This is typically at the 0.1% level.

From equation 6.10.1, it is clear that in order to provide low thermal displacement noise, a combination of a heavy mirror, low mechanical losses and temperature can be used to achieve the desired result. For the current ground-based room temperature interferometers, fused silica is the material of choice as it displays ultra-low mechanical loss at room temperature, while for the ET-LF interferometers, crystalline materials (e.g. sapphire or silicon) are favoured as they have low mechanical loss at temperatures below 150 K. These design choices, and the R&D required will be discussed in more detail in the sections below.

### 6.10.2.2 High-frequency suspension

The current room temperature interferometers (aLIGO, AdVIRGO, GEO) utilise fused silica as a material to suspend the test masses. There is over 20 years of R&D devoted towards ultra-low noise fused silica suspensions. They were initially pioneered in GEO around 1990-2000 (5.6 kg optics), upscaled for use in aLIGO and AdVIRGO (both 40 kg optics) between 2000-2012, with installation occurring from 2015 onwards. Fused silica is the material of choice as it can be pulled into long thin fibres, can be welded to form monolithic structures, has extremely low internal friction, and has a breaking strength in excess of 4 GPa.

The dominant contributions to the mechanical losses are from:

- surface losses, [499, 500] which originate from defects on the surface such as dislocations, unterminated dangling bonds and surface cracks. This is a dominant term for fibres which exhibit high surface to volume ratio;
- thermoelastic losses [501], which arise from the fact that bending a suspension fibre leads to heating/cooling via the thermal expansion coefficient. When the fibre is under tension the variation in Young's modulus with temperature leads to an additional thermoelastic contribution. For fused silica these two terms have opposite sign and the thermoelastic losses can be cancelled

in the bending region by suitable choice of the fibre geometry, a technique utilised both in aLIGO and AdVIRGO [502];

- weld losses, which arise from material which has been heated with a CO<sub>2</sub> laser [503] to fuse the silica suspension fibres to the attachment ears on the side of the test mass. This material exhibits losses which is higher than the bulk losses [504] and likely correlated with the level of thermal stress;
- bond losses, due to the attachment of fused silica ears silicate bonded to the side of the test mass. The silicate bonding process produces a strongly cross linked structure which allows glassy materials to be reproducibly attached in a mechanically and thermally stable way [505]. By careful suspension design this term can be minimised.

The ET-HF mirror mass will be increased to about 200 kg to provide lower suspension thermal noise and also a reduced radiation pressure noise. The technology of room temperature suspensions is mature, building on many years of heritage and proven technology in the field. It has already been shown that fibres of suitable geometry can be pulled and welded, and a prototype 150 kg suspension has already been demonstrated, albeit with a metal proof mass to simulate the payload.

While current ground based detectors utilise fibres stressed to 800 MPa in their thinnest section (to push violin modes above 500 Hz and the vertical bounce mode below 10 Hz), meeting the baseline thermal noise of ET-HF further requires the fibres to be lengthened to around 1 m - 1.5 m. This has the effect of lowering the vertical bounce mode (good) and the violin modes (bad). In order to push the violin modes back up above 250 Hz will require fibres to be operated at higher stress, up to 1.2 GPa. This is the baseline proposal for the US A+ upgrade to aLIGO, and thus the ET suspension can benefit from this work also. There is R&D underway on the stress corrosion of fused silica fibres which suggests that even at 1.2 GPa fibre stress, the lifetime of such fibres is greater than 1000 years [506]. Additional work has been undertaken on laser stabilisation of the fibre pulling machine which has been shown to improve the dimensional tolerance and median tensile stress of the fused silica fibres. Figure 6.14 shows the strain noise performance of an ET-HF suspension with the parameters shown in table 6.2. This comfortably meets the requirements in the high frequency range.

ET-HF Parameters			
Parameter	Value	Parameter	Value
Mass (kg)	200	Length	1.5m
Temperature (K)	300	$r_{end}, r_{middle}$ ( $\mu\text{m}$ )	762,310
$\kappa$ ( $\text{Wm}^{-1}\text{K}^{-1}$ )	1.4	$C$ ( $\text{Jkg}^{-1}\text{K}^{-1}$ )	750
$h\phi_s$ (m)	$4 \times 10^{-12}$	$\phi_{weld}$	$6 \times 10^{-6}$

Table 6.2: Proposed design parameters for the High Frequency suspension:  $r_{end}$  and  $r_{middle}$  are the radii of the fibre at end and mid sections;  $\kappa$  and  $C$  are, respectively, thermal conductivity and specific heat of fused silica at room temperature;  $h\phi_s$  is the product of the mechanical loss of the material surface,  $\phi_s$ , and the depth,  $h$ , over which surface loss mechanisms are believed to occur;  $\phi_{weld}$  is the loss angle associated with the material losses localized at the welding spots.

### 6.10.2.3 R&D required for High-Frequency suspension

While the fused silica solution is already well developed there needs to be work devoted towards the demonstration of a full scale ET-HF prototype. Key areas of future R&D include the following items:

- A full scale prototype suspension needs to be built and tested. It would be sensible to consider a staged approach, where a full scale metal system is built first, using fused silica inserts to enable the fibres to be interfaced, ultimately leading to a fully monolithic version to test the assembly/integration required. The suspension scheme proposed uses fused silica fibres with operating stresses of around 1 - 1.5 GPa, fabricated on the current fibre pulling machines that have been developed for the aLIGO/AdVIRGO instruments. The fibre ends will be thickened such that they operate at a stress of 200 MPa which is needed to null the thermoelastic contribution [502]. The fibres will be welded onto "anchors/ear" using a  $CO_2$  laser to form a system that can be integrated into the main test mass/marionette. In aLIGO, such a monolithic suspension has been shown to have extremely low mechanical losses, with quality factors for the violin modes in excess of 1 billion (a ring down of  $>5$  days at 500 Hz).
- Activities focused on further proving the long term strength of fused silica, and the techniques required to Hydroxide Catalysis Bond the ear to the test mass, will naturally follow with the development of these full scale systems. Further work to ensure that the laser stabilisation techniques provide fibres of sufficient dimensional tolerance will also be useful to verify the technology.
- The local control of test masses further plays a crucial role in gravitational wave detectors and this is an R&D activity common to both the HF and LF suspensions. The local sensors are used to damp the suspension modes to a point at which automatic error signals (e.g. wavefront sensing for angles and locking for longitudinal position) can take over. There needs to be work to ensure there are sufficiently sensitive inertial sensors available.
- Actuators also need to be developed which have sufficiently low electronic noise such that they don't spoil the noise performance of the suspension. As with aLIGO and Advanced VIRGO, a combination of electromagnetic voice-coil actuators at the marionette stage will be necessary to provide the control forces for local damping of the suspensions. For test mass actuation, an electrostatic actuation scheme could be employed, utilising high voltage actuation across the capacitance formed between the test mass and the reaction mass. R&D to ensure that excess charging is not an issue needs to be an area of further research, and the current experience of discharging schemes and measurements of charge build-up in aLIGO will be helpful.

#### 6.10.2.4 Low-Frequency suspension

In addition to providing a low seismic/thermal noise platform, the ET Low Frequency suspension also has to fulfill a second crucial duty - to extract the thermal load that is put into the optical component by the laser beam and by the thermal radiation coupled via the residual view towards the room temperature sections of the vacuum system. A 100 mW heat load on each test-mass is currently estimated, which represents a challenge for operation at cryogenic temperature. In terms of material choice fused silica is ruled out both due to its low thermal conductivity, but more seriously due to the broad dissipation peak in its mechanical loss due to its amorphous nature [507]. The materials of choice are crystalline materials which have a very high thermal conductivity at low temperatures while displaying low mechanical losses. In particular, silicon and sapphire are excellent materials in the temperature region of interest (typically below 20 K).

At low temperatures the mechanical loss of the suspension, which defines the thermal noise performance, is a key driver for the suspension design. Again heavy test masses will be utilised, with the addition of low temperature to provide enhanced thermal noise performance. At temperature

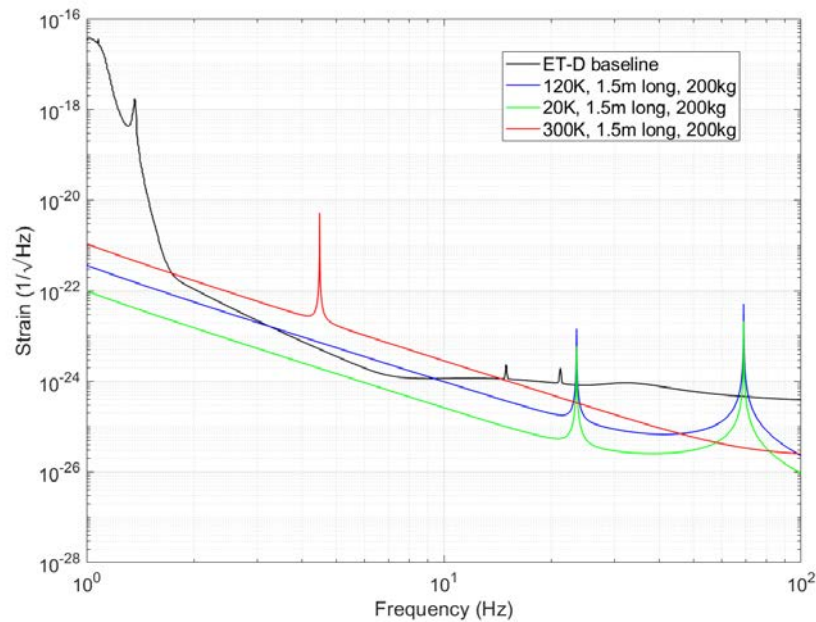


Figure 6.14: Strain sensitivity due to suspension thermal noise for the room temperature and cryogenic suspensions; red: room temperature silica, blue 120 K silicon, green 20 K silicon, black ET-D baseline

below 150 K thermoelastic noise drops away sharply, and indeed for silicon is zero around 120 K, which leaves the dominant loss mechanisms as:

- Surface loss [508] which originates from defects on the surface such as dislocations, un-terminated dangling bonds and surface cracks. Initial measurements suggest that the surface loss at low temperature could be a factor of 10x below those of fused silica at room temperature.
- Bond loss due to the attachment of anchors/ears via metallic or silicate bonding to the side of the test mass.

In common with the room temperature suspensions, techniques need to be developed to bond these crystalline materials. Significant progress has already been made particularly for sapphire and silicon, partly with the development of sapphire suspensions for KAGRA [509] [510]. There are a number of groups which have performed hydroxide-catalysis bonding of materials by growing a native oxide (e.g. wet or dry thermal oxide on silicon) or the naturally occurring oxide, and undertaking thermal cycling and mechanical loss measurements. Refs [511] and [512] have shown that these bonds can be sufficiently strong and can be cycled between room temperature and cryogenic temperature. Another technique that has been explored for KAGRA is metallic bonding with low melting point materials such as Indium and Gallium. This type of bonding has developed out of the need to replace suspension elements. While Gallium has a much lower melting point ( $\approx 30^\circ\text{C}$ ), the corrosive nature and the poisonousness of the material make handling a potential challenge. Indium on the other hand has a higher melting point ( $\approx 157^\circ\text{C}$ ) but requires the entire suspension to be warmed to this temperature to develop strong and reproducible bonds [513] [514]. KAGRA uses sapphire and has gained significant experience in suspension design, construction and commissioning.

The need for large and heavy test masses (200 kg) point to silicon as a preferred material. However, given the experience noted above with KAGRA, it would be sensible to keep a lookout for R&D that could lead to larger sapphire substrates. Silicon suspension elements are currently under investigation in the form of fibres [515] and ribbon-like structures [516]. Further R&D is focused on techniques to joint the suspension fibres to the test mass ears/anchors. For silicon and sapphire suspension elements, the challenge is to fabricate suspension elements that have tapered ends at the attachment points. This is essential to ensure that the bending energy of the suspension is maintained in the fibre rather than the anchor point, which will include the metallic or hydroxide catalysis bond. If this design is not carefully undertaken, the dissipation dilution of the suspension, and consequently the thermal noise performance, can be compromised.

Currently, there are three possible techniques under investigation for the fabrication of silicon suspension elements;

- The micro-pulling technique [515] where a thin fibre (diameter of up to a few millimetres) is drawn from a silicon melt through an extrusion. The fabricated fibres are not perfectly single crystalline - but recent work has improved the crystallinity of the fibres. Currently, these fibres are produced with a length of 30 cm for the initial investigations. In principle there is no limit for the maximum achievable length and thus this technique is promising to be used for the low temperature suspensions of ET.
- Etching suspension structures out of single crystals or wafers. This technique provides suspension elements with a rectangular cross section due to selective etching of the crystalline silicon in different directions. A number of fabrication techniques are currently under investigation including mechanical cutting, laser cutting, deep reactive ion etching and wet etching. The selective etching technique is just limited by the wafer size and in principle it is possible to create much longer elements. Current challenges are reduction in the strength of the silicon fibres due to mechanical etching, and work is underway to etch/oxidise samples to improve their strength [517].
- Similar to micro-pulling, an alternative technique is to grow a fibre from a pedestal melt; so called Laser Heated Pedestal Growth. The benefit of this technique is that it can produce extremely pure fibres with high strength, as there is no interaction with a crucible or extrusion. The downside is that the production is slow (mm/min growth rate) and requires good control of temperature and growth rate. Good quality results have previously been reported by [518] in the growth of sapphire fibres, although challenges exist with silicon as the melt changes its optical absorption strongly around the transition from solid to liquid.

Figure 6.14 shows the strain noise performance of the ET-LF suspension with the parameters shown in table 6.3. Two temperatures have been modelled; 120 K and 20 K and the respective thermal conductivity and specific heat at these temperatures are used. The code assumes a circular fibre of equivalent cross-section to a ribbon and an idealistic dilution (this would need to be properly determined for the final geometry using FEA). Since the thermal conductivity at 120 K is poor, heat extraction would be via radiative coupling.

#### 6.10.2.5 R&D required for Low-Frequency suspension

The R&D focussed on delivering a cryogenic suspension is less well developed than the room temperature suspension, and activities are needed on several fronts;

ET-LF Parameters			
Parameter	Value	Parameter	Value
Mass (kg)	200	Length	1.5m
T (K)	20,120	$r_{fibre}$ ( $\mu m$ )	2200
$\kappa$ (120 K), $\kappa$ (20 K) ( $Wm^{-1}K^{-1}$ )	690, 4900	C (120 K), C (20 K) ( $Jkg^{-1}K^{-1}$ )	328, 4
$h\phi_s$ (m)	$5 \times 10^{-13}$		

Table 6.3: Proposed design parameters for the Low-Frequency suspension:  $r_{fibre}$  is the radius of the fibre;  $\kappa$  and C are, respectively, the thermal conductivity and specific heat quoted at two possible operating temperatures;  $h\phi_s$  is the product of the mechanical loss of the material surface,  $\phi_s$ , and the depth,  $h$ , over which surface loss mechanisms are believed to occur.

- Fibre fabrication techniques to develop long thin silicon or sapphire fibres, As noted above promising fabrication strategies include micro-pulling, forming (etching or machining) from a wafer and laser heated pedestal growth. For all of the techniques a study of the resultant tensile strength, ease of fabrication, mechanical loss and thermomechanical properties needs to be undertaken to choose the optimum techniques. Research into micro-mechanical systems investigated surfaces losses in silicon (see e.g. [519–521]). However, a systematic and general modelling of surface losses has not been made and their origin is still unclear and needs to be investigated.
- The techniques necessary to joint suspension elements, while ensuring that dissipation dilution is maintained as high as possible, need to be properly explored. This could include hydroxide catalysis bonding of ears/anchors, metallic bonding and direct bonding techniques. Measurements of the thermal conductivity suggest that bonded silicon components at low temperature can be modelled as pure silicon with a thin ( $\sim 700$  nm) interfacing glass-like layer. These results suggest that hydroxide catalysis bonding can facilitate the necessary extraction of heat, deposited on the mirrors by the incident laser beam, through to the silicon suspensions elements and towards the cooled upper-stage. A further technique worth studying is direct welding of crystalline material. There has been some good success of *welding* sapphire, although this needs to be verified for silicon, and further R&D is needed here. For example, what is the thermal conductivity of a welded joint, and does the material exhibit good thermal conductivity and low mechanical loss.
- A detailed FEA model of the final stage suspension needs to be undertaken in order to estimate the effects of real fibre geometries on the dissipation dilution.
- R&D is needed in the development of elastic elements to soften the vertical bounce mode of the thick silicon or sapphire rods, connecting the test mass to the marionette (e.g. the blade springs in the case of KAGRA).
- As with the High Frequency suspension, the development of inertial sensors, with high sensitivity and large measurement band is a key point for the inertial damping to perform on the suspension system of third generation interferometric detectors. These sensors and associated actuators need to be proved for low temperature operation. There has been work proposed towards developing the monolithic folded accelerometer for cryogenic temperature [522] [523].
- Further suspension modelling needs to be undertaken to verify the operation temperature of the Low Frequency suspension. In the previous design study an operation temperature of

10 K-20 K was the operating point. As noted above this does result in challenges to extract sufficient heat through the suspension fibres. An alternative that surfaced in the last couple of years is the option of running close to 120 K where silicon exhibits a zero in its thermal expansion coefficient, making the thermoelastic noise vanish, as mentioned above. The penalty to pay is in the overall thermal noise performance which is roughly  $2.4\times$  worse.

- There is a need for prototype lower stage suspension systems similar to those developed during the fused silica development era. This includes a mix of fast turnaround tabletop systems and small scale prototypes of 10 m arm length with payload in the 1 kg to 10 kg range in the first instance.

## 6.11 Cryogenics

### 6.11.1 The ET cryostats

In order to limit the thermal noise impact on the ET sensitivity curve, it is necessary to cool at cryogenic temperature the four test masses of the LF-detector. The heat is extracted from the mirror via the suspension fibres, which are attached at the other end to the marionette. Moreover, the marionette is suspended from the super-attenuator, which attenuates the seismic noise up to a few hertz. Thus, it is extremely important at the same time (i) to preserve the mechanical isolation between the mirror and the cooling system, (ii) to guarantee an efficient thermal link between the payload and the cooling system.

The whole payload is housed in the lower part of the vacuum tower, hosting the 17 m long super-attenuator chain as shown in figure 6.15. The base of the vacuum tower is a cryostat with two thermal screens: the inner blue line schematises a surface at  $\sim 4$  K, while the outer one represents the shield at intermediate temperature ( $\sim 80$  K). The upper part and lower part of the tower are separated by a roof crossed by the Ti-6Al-4V thin rod, which holds the whole payload. The roof is robust enough to hold the suspension wires of the cryostat thermal screens surrounding the payload. In particular, the inner shield is designed to define a volume that, during the cool-down phase, may be kept at a residual pressure different from that of the upper part of the tower hosting the super-attenuator in order to improve its thermal coupling with the payload by gas conduction, if necessary. During the cool-down phase, the large valves connecting the long ultra high vacuum tube will be closed. This option would permit to faster cool down and warm up the whole payload by adding pure helium gas in this confined volume. A few mbar of helium will provide an efficient heat transfer of the payload from room to cryogenic temperature. Once the equilibrium temperature is achieved, the helium gas is pumped out before the laser light injection. This option will only be necessary, if thermal simulations yield insufficient cooling time constants for the payload due to its weak coupling with the marionette. The temperature of the marionette itself can be controlled on short time scales by appropriate cooling system design.

The base of the main tower hosting the mirror is connected to a couple of ancillary cryostats shown in figure 6.15. In the present baseline design, the far one hosts a sufficient number of pairs of pulse tube (PT) cryocoolers, which operate in phase opposition. They provide the refrigeration power to keep the mirror and the inner shields of the cryostat at cryogenic temperature. In this way, the production units of the refrigeration power are separated from the payload cryostat. A large fraction of the heat

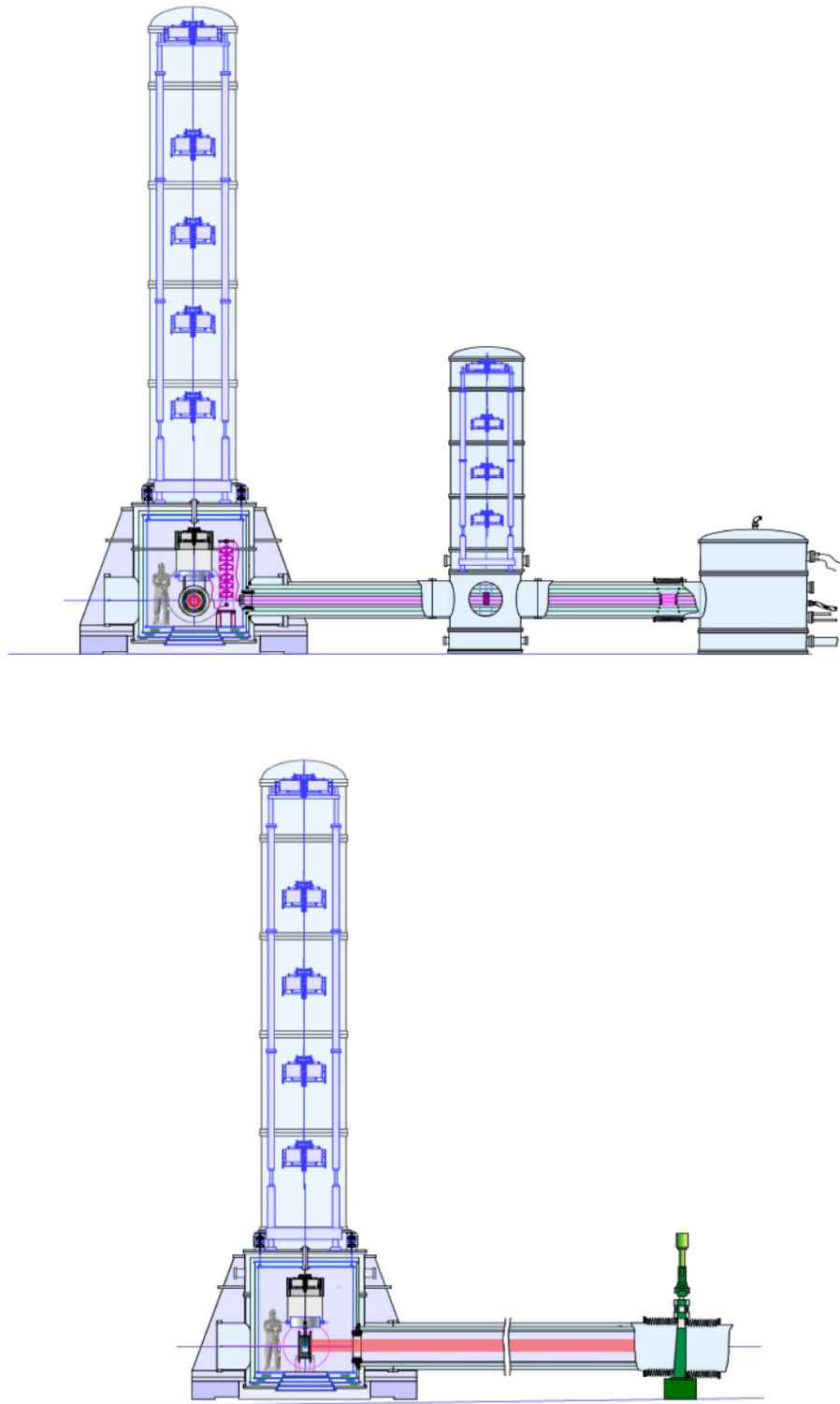


Figure 6.15: Scheme of the cryo-links and cryo-tank needed for cooling a test-mass of the LF-interferometer. Upper image: mirror frontal view. Lower image: mirror side view.

extraction path is through a pure aluminum bar, suspended in the middle of the super-attenuator hosted in the intermediate cryostat shown in the upper part of figure 6.15. This solution, where the cooling units are separated from the payload cryostat, has been adopted already in KAGRA, and has several advantages. It permits

- to decouple the vibrations generated by the refrigeration unit from the payload,
- to perform the maintenance without accessing the payload cryostat,
- to implement future more efficient and silents cooling units, based on superfluid  $^4\text{He}$

The heat extraction path of  $\sim 20$  m length connects the refrigeration units to the marionette. To reduce vibration, the aluminum bar will be connected via braids of high purity material as, for instance, electrolytic copper or grade 6 aluminum (99.9999 % purity). Both are characterized by thermal conductivity values of 2 kW/m/K in the range of 1-10 K. A braid made of 8 wires with 1 mm diameter and 20 m length can support an heat flow of 200 mW for a temperature difference of  $\sim 1$  K. The attenuation of the residual vibrations transmitted along the heat extraction path and mainly associated with the cooling system is provided by the auxiliary super-attenuator chain, hosted in the innermost volume of the main tower (attenuator chain drawn in red - upper view of figure 6.15). The soft braids are mechanically coupled to the super-attenuator filter, which has to be fully compliant with the cryogenic environment.

In order to define the cryogenic requirements, one has to estimate the cryostat thermal inputs, which depend on the cryostat dimension and the quality of the thermal insulation. Assuming that the inner vacuum chamber has to host a mirror with half a meter diameter, we derived the order of magnitude of the thermal input for a cylindrical cryostats.

Multi-layer insulation (MLI) is a standard technique used in the helium cryostats. The thermal shield is formed by highly reflective thin layers, substantially decreasing radiation heat transfer. MLI is based on layers of porous (self-vented) mylar sheets, which are aluminized on one side. The sheets are wrapped around the surface to be insulated. Unfortunately, mylar is a hygroscopic material incompatible with the UHV requirements of ET. As a consequence, one proposed solution implies to develop superinsulation sheets on a hydrophobic support and to, as much as possible, separate the chamber hosting the mirror from the insulation vacuum of the cryostat. Assuming 25 and 75 layers of self-vented aluminized mylar around the two thermal shield, the thermal input can be limited to 1 W for the 4 K shield and to around 50 W for the intermediate one. In comparison, the thermal input due to laser light absorbed by the mirror and the thermal radiation emitted by the long vacuum tube is in the range of a few tens of milliwatt. These data will be evaluated in more detail as part of the ET technical design study.

### 6.11.2 The LF-interferometer cryotrap

The main heat inputs into the cold mirror of the LF interferometer are the thermal radiation coming from the warm surface of the vacuum tube, and the heat load due to the absorption of a small fraction of the laser light into the mirror surface. The latter can be estimated considering that the laser power circulating in the optical cavity is 18 kW, and that a reference value for the absorption coefficient of the mirror optical coating at the working wavelength is around 1 ppm. This gives an approximate value of 20 mW of absorbed laser power.

In order to reduce the thermal radiation from the beam duct into the cold mirror, two strategies are viable: the reduction of the emissivity factor and the reduction of the geometric view factor, i.e. the reduction of the solid angle under which the warm surface is seen by the cold surface.

The emissivity factor is reduced by an appropriate choice of material for the wall of the tube, or through the deposition on the warm surface of a low-emissivity coating. The reduction of the geometric view factor is obtained by building in the region adjacent to the mirror cold sections of the vacuum tube (thermal shields or cryotrap), that “move away” the warm section of the tube from the mirror, and in this way reduce the solid angle, under which the warm surface is seen by the cold mirror. At the same time, the cryotrap acts as cryopumps, because the instruments hosted in the tower are not compatible with the pipe arm vacuum requirements. The temperature(s) and length(s) of these sections will be designed to fulfil both vacuum and thermal requirements. In particular, in the region immediately adjacent to the mirror, a zone colder than the mirror itself is needed to avoid the condensation of the residual gas on the surface of the mirror, that could lead to the growth of a layer of contaminants and spoil its optical characteristics.

### 6.11.3 R&D on cryogenics: lowering the temperature with Helium II

In order to increase the cooling capacity and to achieve the ultimate reduction of the thermal noise contribution, cooling of the LF-payload with superfluid  $^4\text{He}$  (He-II) is under investigation, which is produced by pumping on a normal  $^4\text{He}$  (He-I) bath. Other than in case of the cryocoolers, the cooling power is a design parameter without intrinsic limits. The second order phase transition from liquid He-I to superfluid He-II can be described by Bose-Einstein condensation, whereby  $^4\text{He}$  atoms successively condense into their ground state. This means that any thermal noise is switched off in the condensed phase.

The superfluid He-II is a quantum fluid with extremely large thermal conductivity, many orders of magnitude beyond that of solids. It conducts heat fluxes with close-to-zero gradients, which prevents any bubble formation in the liquid that otherwise might cause microphony. It is therefore possible to cool the marionette by steady-state conduction with He-II in small capillaries, i.e. without the circulation of helium, keeping the He-I/He-II-bath far away from the payload in one of the separate cryostats shown in figure 6.15. For the cool-down process, forced He-I flow can be arranged through the same capillaries.

The He-II approach has the advantage to provide more refrigeration power and to reduce the mechanical impact on the payload to the ultimate minimum. A detailed design study of this option is in progress.

## 6.12 Vacuum system

### 6.12.1 Overview and requirements

In laser interferometers for GW detection the instrument has to be kept under High-Vacuum or Ultra-High-Vacuum (HV, UHV) for several reasons:

- reduce the noise due to vacuum fluctuations along the beam path to an acceptable level;

- isolate test masses and other optical elements from acoustic noise;
- reduce test mass motion excitation due to residual gas fluctuations;
- contribute to thermal isolation of test masses and of their support structures;
- contribute the preservation of the cleanliness of optical elements.

The power spectral density of gas-induced fluctuations in the optical path length was calculated for different residual gas pressures, using conservative beam shape parameters. For the maximum acceptable residual gas pressure, a safety factor of 10 was applied with regard to the pressure at which the detector sensitivity would be limited by phase fluctuations of the residual gas at the frequency of highest sensitivity (Fig. 6.16).

The residual gas composition will be dominated by hydrogen with presence of water and other gases; we will keep the total residual pressure at about  $10^{-10}$  mbar, corresponding to a noise level below  $10^{-25}$  Hz<sup>-1/2</sup>. The vacuum system will be extremely clean from heavy organic molecules, both to limit the phase noise and to prevent pollution of the optical components. The total partial pressure of hydrocarbons (> 100 amu) shall be at the level of  $10^{-14}$  mbar.

To meet these requirements it will be necessary:

- to bake (one week in an air oven at 450 °C) the stainless steel vacuum enclosure elements (or the raw material sheets) in order to reduce the H<sub>2</sub> outgassing rate to a level of  $10^{-14}$  mbar l/cm<sup>2</sup> s
- to bake the already assembled pipes for one week at 150 °C (or possibly for longer at a lower temperature) under vacuum to remove the water molecule layers adhering to the inner pipe wall.

The ET vacuum system (Fig. 6.17) will be composed of several UHV pipes with kilometric length and several cylindrical vertical HV/UHV tanks (towers) containing the optical elements and their support structures (Fig. 6.18).

In general it is necessary to have the whole vacuum system of one interferometer constituting one single volume, without physical separations (windows) in the laser beam path. HV volumes (the towers) may contain equipment not fully compatible with UHV requirements in the long arm tubes, which are the major part of the path along which the laser beam travels. The separation between HV and UHV can be obtained by differential pumping or by cryogenic traps, stopping the migration of water and other high vapor pressure components. Large gate valves (see 6.12.5) and cryotraps (see 6.12.3) will be put at each end of the arm pipes, in order to preserve vacuum when venting a tower. For the same reason each tower will be separable from the rest of the vacuum enclosure by suitable gate valves. For baking, long term maintenance and repair work it might be useful to separate the arm tubes into smaller sections, e.g. 1 km, requiring a larger number of big gate valves. The optimal sectioning will be determined in a technical design phase. The filter cavities being less sensitive to vacuum noise require a residual pressure at the level of  $10^{-7}$  mbar. Their pipes will neither be air-baked at 450°C nor vacuum-baked at 150°C.

### 6.12.2 The arm pipes

Due to the multi interferometer/xylophone choice for ET, four beams (taking into account six interferometers) will run along each side of the triangular tunnel. Separate vacuum systems are implemented for each interferometer to avoid light scatter cross-contamination and to enable

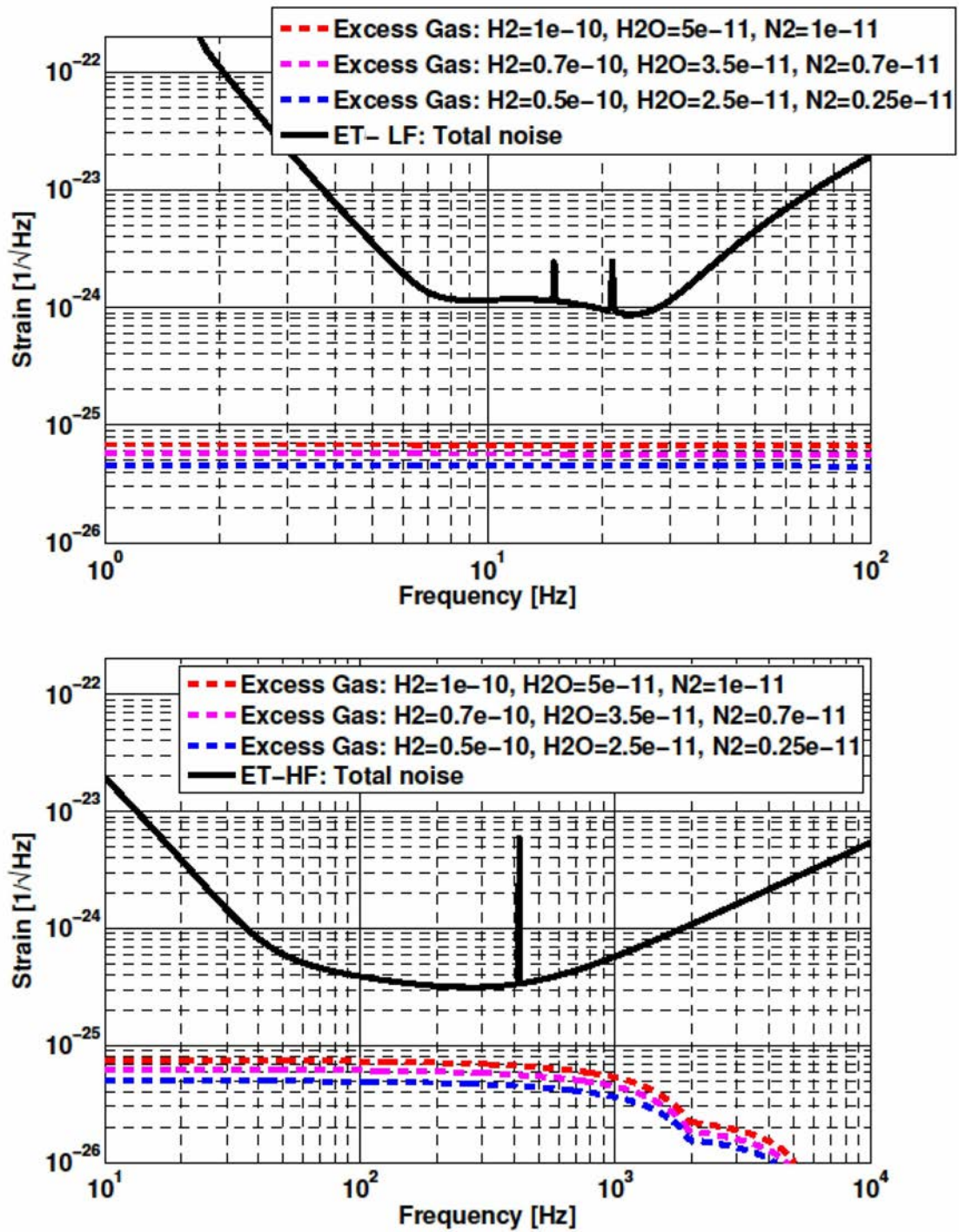


Figure 6.16: Phase noise given by the residual gases compared to the expected sensitivity, computed for the appropriate beam profile for different gas compositions. (Goal gas composition: Hydrogen [ $1 \cdot 10^{-10}$  mbar], Water [ $5 \cdot 10^{-11}$  mbar], Nitrogen [ $1 \cdot 10^{-11}$  mbar])

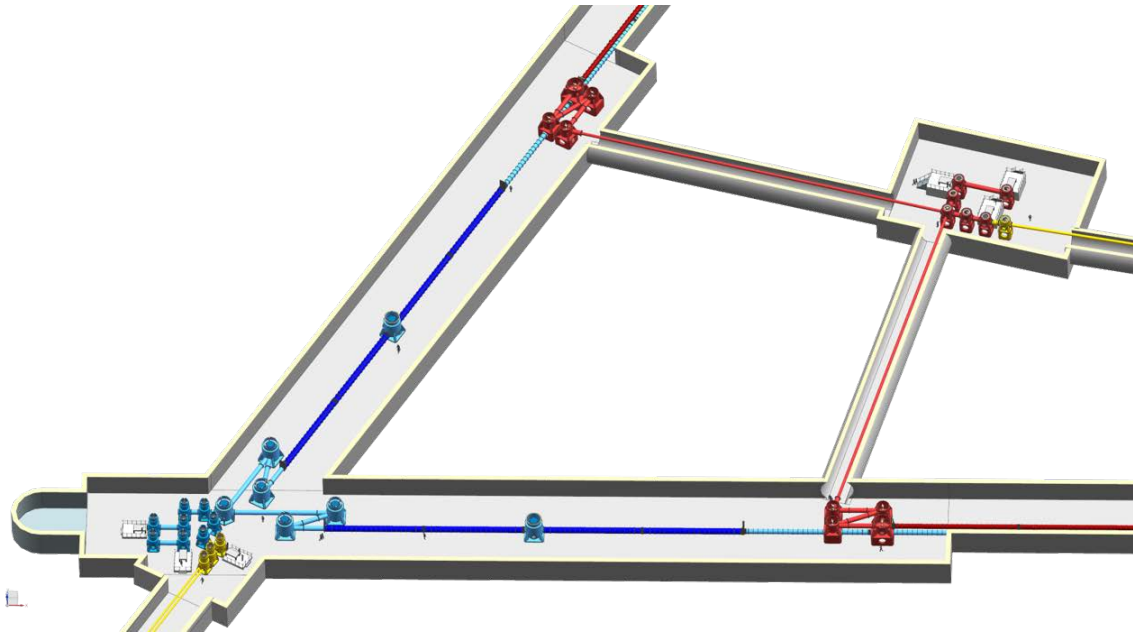


Figure 6.17: One corner of the ET vacuum system: LF detector (blue); HF detector (red); filter cavities (yellow).

independent commissioning and maintenance, as shown in Fig. 6.19. The filter cavity beam tubes will be hosted in the auxiliary tunnels for remote water drainage (see Fig. 6.20). The baseline configuration includes four pipes, one for each main beam, each having a diameter of 1 m. Both the two filter cavity beam tubes for each LF interferometer with a length of 1 km, and the single filter cavity beam tube of 300 m length for each HF interferometer will have a diameter of 500 mm.

The pipes will have stainless steel thin walls (3–4 mm thick) with external stiffening rings, one every 1–2 meters, to prevent the tubes from buckling and collapsing. Two rings will be larger, serving as attachment for the supports (see below).

20 m long pipe elements will be fabricated via industrial tools carefully calculated for large scale economy, logistics optimization and quality assurance. At one end of each element a suitable bellows will be added to accommodate thermal expansion, during bake-out (winter/summer temperature excursion are negligible under ground). At both ends 2 mm thick lips will be added, to allow UHV compatible welding of adjacent elements, without inert gas protection on the inner side of the weld. Simple supports, using steel cables and adjustable stretching screws will be sufficient, coping with the expected stability of the tunnel.

The pipes will be aligned in the tunnel using optical instruments and laser beams, since GPS will not be applicable under ground. The requested straightness error for the arms is of the order of 10 mm. Periodical surveys will be necessary every few years, in order to detect any pipe displacements due to ground movements.

Each 10 km pipe will contain a few hundreds of metallic baffles for diffused light mitigation. They shall be made out of stainless steel with a suitable conical shape and serrated inner edge (Fig. 6.21) against diffraction. The radial width of the baffles, between 50 and 100 mm, and their position will

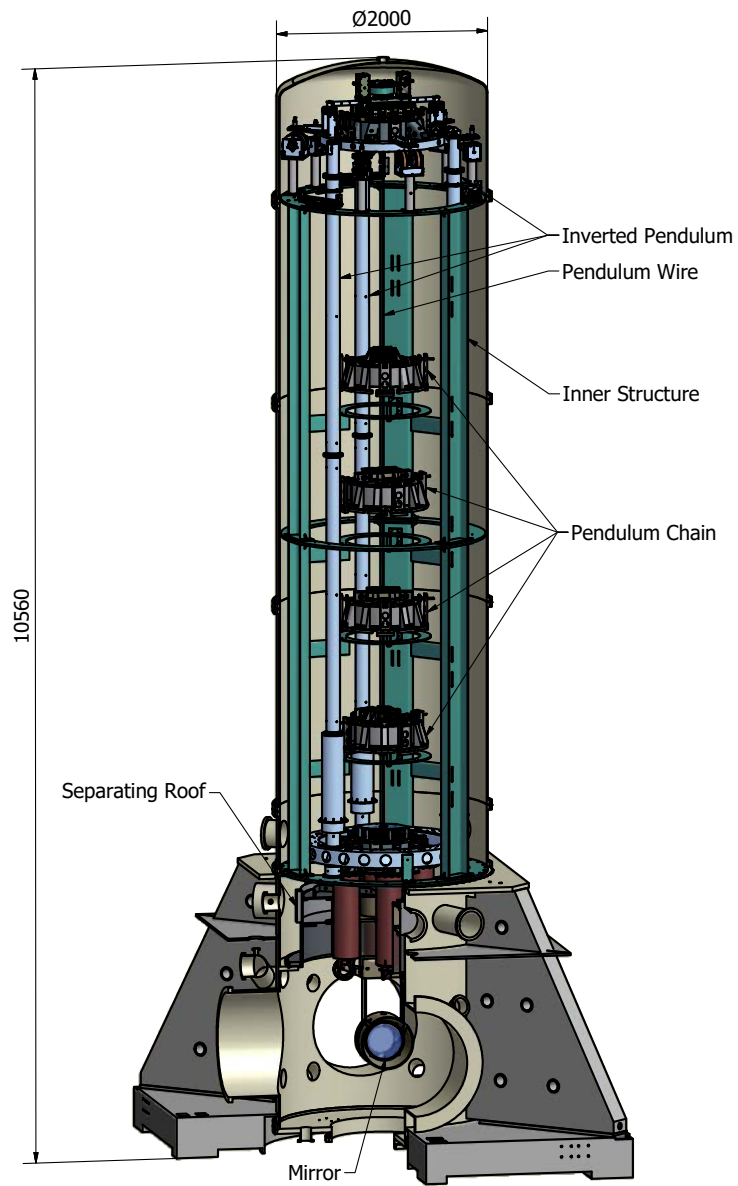


Figure 6.18: As an example the cross-section of a Virgo a mirror tower is shown.

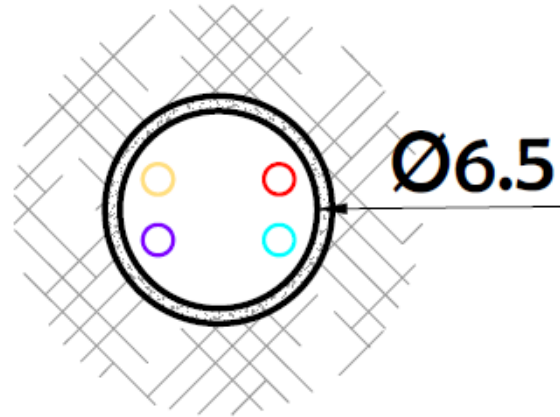


Figure 6.19: Arrangement of the vacuum pipes in the tunnel cross-section.

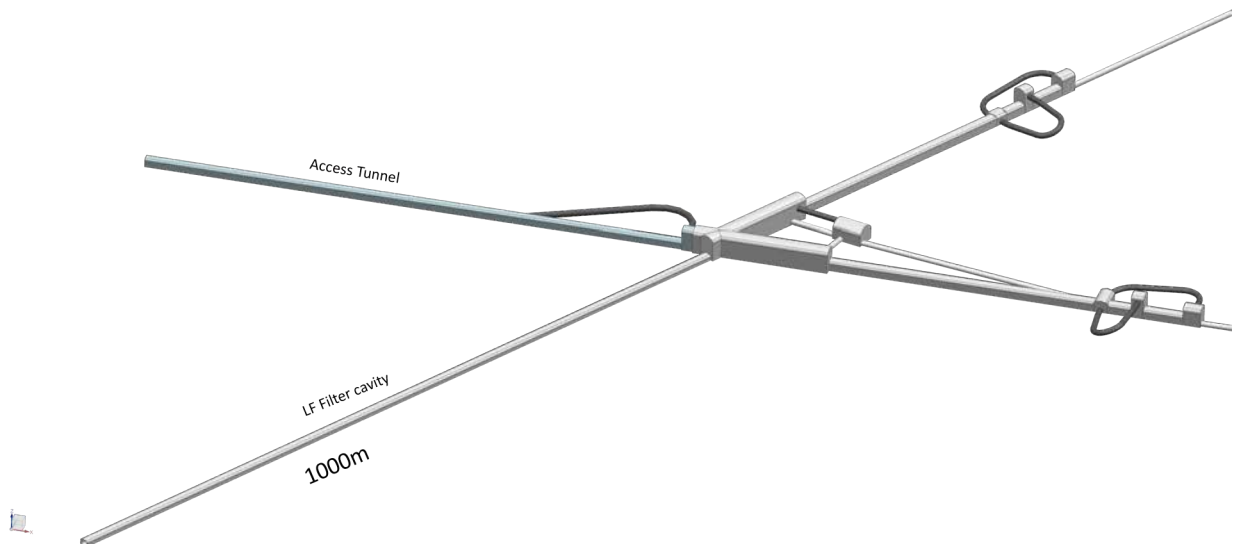


Figure 6.20: Schematic layout of the LF interferometer filter cavity auxiliary beam tube.

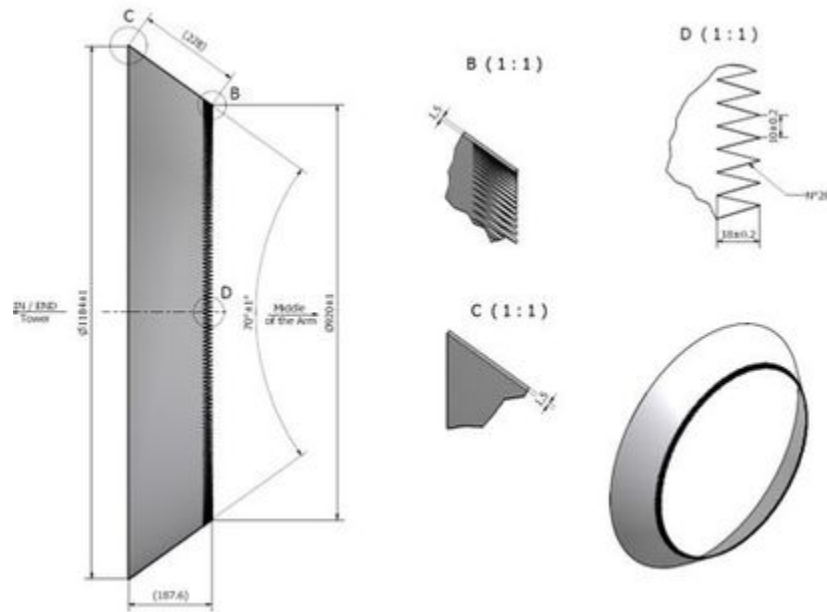


Figure 6.21: As an example the Virgo pipe conical baffles are shown.

be determined by a suitable simulation.

### 6.12.2.1 Pipe assembly

The 20 m pipe elements will be introduced into the caverns with the ends sealed by suitable end-caps and equipped with thermal insulation; each element will weight about 1.5 t. The element will be put on and bolted to a simple carriage made of two parallel 20 m long beams supported by small train wheels. In this way pipe elements can be pushed to their position one after the other by an electric tractor running on 5 km long rails reaching up to mid arm. The rails, two for each pipe, are supported by frames extending to the whole tunnel cross-section. These same frames have the function, as said before, of supporting the pipes.

Every 500 m, along the tunnel, there is an enlarged room (“pump room”, Fig. 6.22) foreseen to host pumping, bake-out and control equipment; those rooms are used also to weld the pipe elements at ease in a wide area, under a mobile clean tent. A pump room is an enlargement of the tunnel for a width of 12 m and a length of 10 m, allowing the installation of the pumps, which are held in their position by a metallic frame not shown in the figure. Three cabinets housing the electronics of the vacuum equipment are included, together with an electrical power supply for baking (60 VDC, 300 kW). A bridge crane is needed, and the room will have controlled humidity and temperature, for the longevity of the electronics.

The assembly sequence of a vacuum pipe is described below and is graphically shown in Fig. 6.23.

The first pipe element is stopped with the rear end under the tent prepared in the 9<sup>th</sup> pump room, counting from the corner cavern; when the front end of the second element is close, the sealing lids are removed, after starting appropriate clean air flows. The corresponding end lips of the

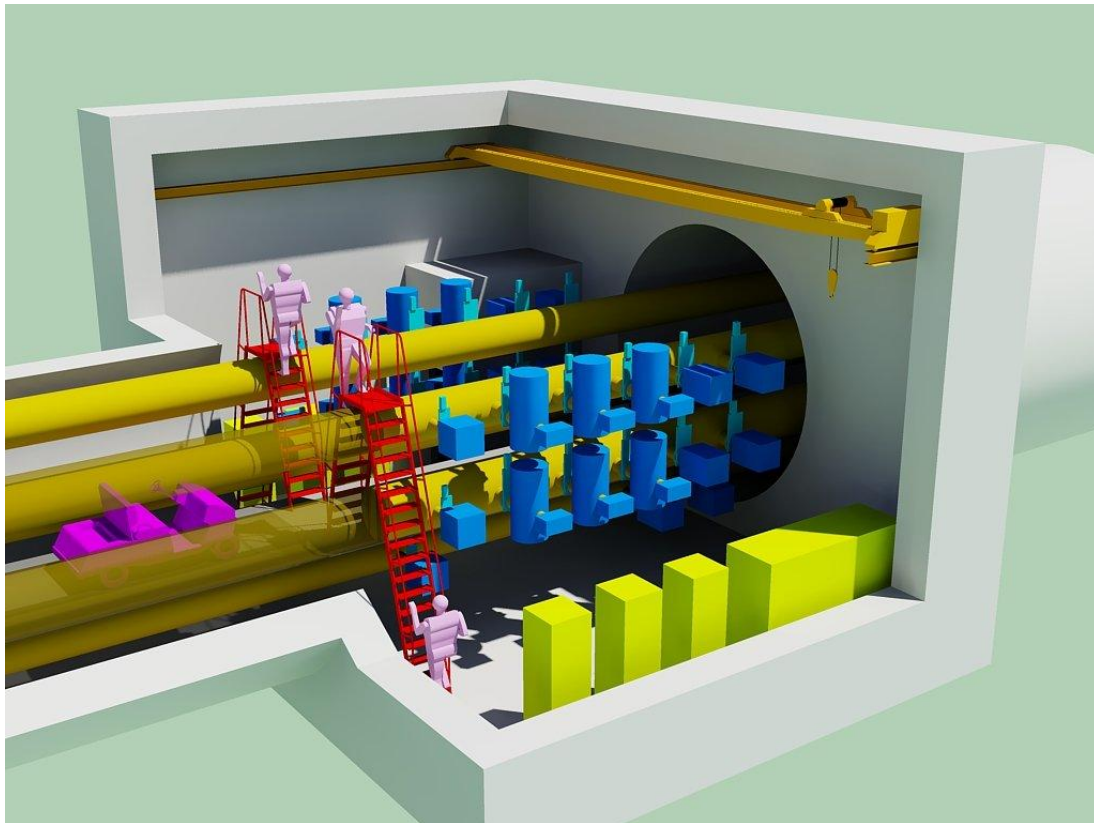


Figure 6.22: 3D view of a pumping station: the blue objects represent the pumps and sensors, the yellow ones the cabinets for pumps control and baking power supply (1 cabinet for all). A separate small room is reserved for the high voltage electrical transformer.

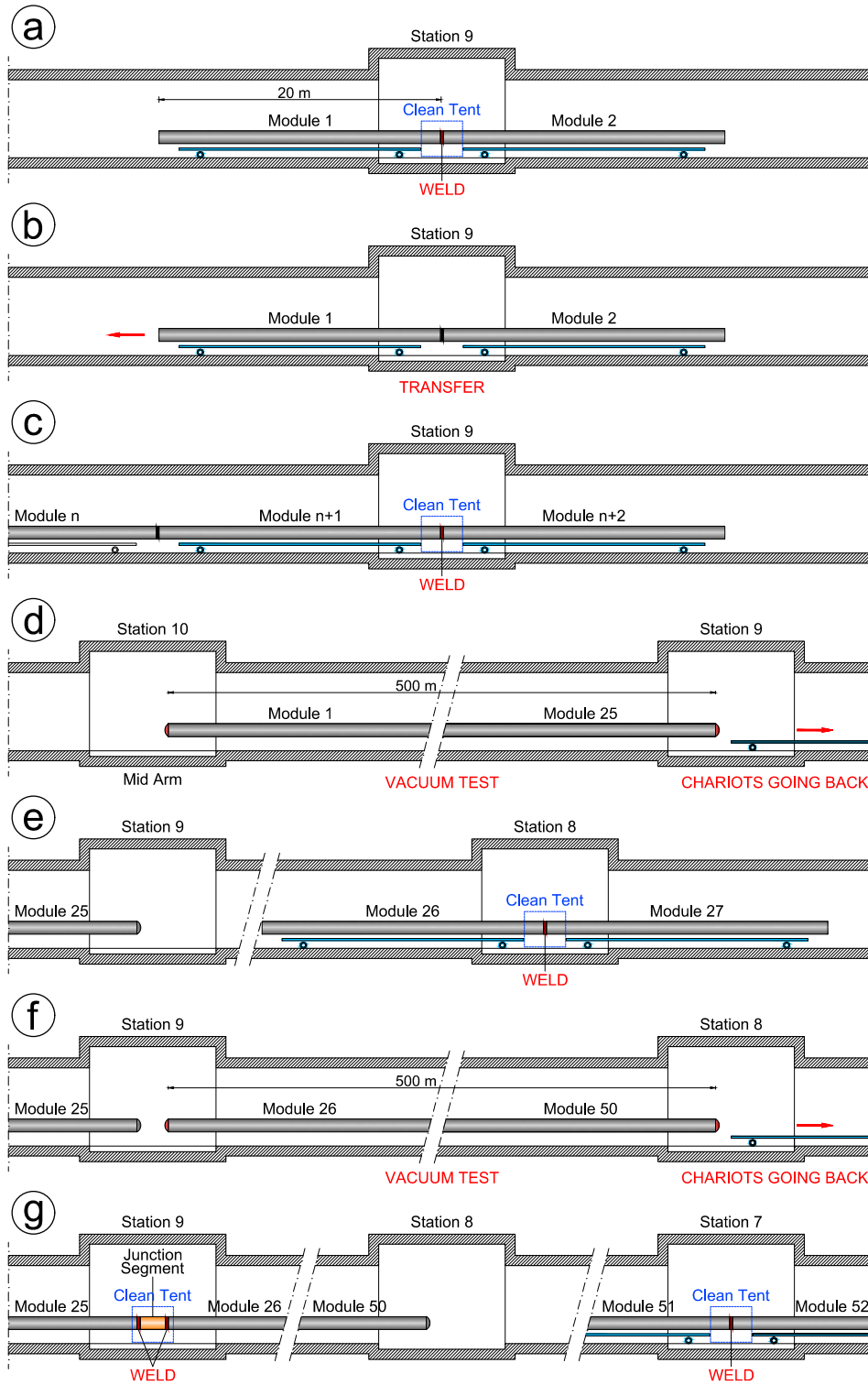


Figure 6.23: The assembly sequence of one vacuum pipe.

adjacent elements are precisely adjusted and welded. The beams of the two carriages (under or above the pipe, according to the chosen option) are rigidly bolted together, taking care of appropriate compression/extension of the bellows.

The two modules are shifted forward until the rear end of the second module is at the welding position; now the front end of the third module is adjusted and welded as before. This procedure is continued until the 25<sup>th</sup> module is welded and the 500 m long section of pipe is completed.

The 500 m long section will be then shifted by 20 m to its final position.

Every pair of upper support cables are attached to the corresponding support ring, the cables are tightened, the bolts of the pipe elements to the carriages are removed, the elements are lifted by 10 mm in 1 mm steps. The 500 m long train composed by 25 carriages is sent back to the end cavern, to start the assembly of the second 500 m pipe section. The lower support cables are attached to the pipe support rings and suitably tightened.

The ends of the assembled pipe section are closed with vacuum tight lids, the section is evacuated and tightness tests are performed. The closing lids will be strongly fastened to the tunnel wall, in order to keep the 6.4 t axial load due to atmospheric pressure.

The clean tent and the welding equipment are transferred to the next (8<sup>th</sup> from the corner cavern) pump room and the assembly of the second 500 m pipe section is started. Once completed and vacuum tested, taking advantage of the bellows and of the support cables, the front lip of the new 500 m section and the rear lip of the previous section are connected welding-in a 1 m long junction piece. These final welds are the last to be performed in that particular pump room.

The procedure continues at the same time, extending the installed pipe from mid arm to both arm ends.

Concerning the pipes arrangement in the tunnel, it is necessary to have the possibility to inspect and repair the welds between pipe elements. This could be achieved leaving a minimum clearance of about 0.5 m between the “nude” pipes and the tunnel wall (at least every 20 m). This will be just sufficient also in the case of small maintenance interventions on the tunnel wall lining.

#### 6.12.2.2 Pipe pumping system

The pipe pumping system has been conceived to be composed of standard modules, grouped together, in order to limit the number of pumping stations along the arms.

The required total residual pressure (hydrogen and other gases) of  $10^{-10}$  mbar can be obtained, after firing and bake-out, with one 5000 l/s pumping group, every 500 m, both in a 0.9 m and in a 0.7 m diameter pipe, the smaller gas load due to the smaller diameter being compensated by the reduced conductance. Below the pumping system for one single pipe is described.

Each permanent pumping group will consist of three identical modules, each made of one 2500 l/s Ti sublimation pump (TSP), connected to the pipe through a 250 mm gate valve (the Ti will be sublimated not in the tube but in a separated chamber), coupled to a 300 l/s ion pump. The former to pump active gases, the latter to pump inert gases. At such a low pressure TSPs are expected to require not more than one yearly regeneration. NEG (Non Evaporable Getter) pumps are being considered as

a possible alternative to TSPs. Some redundancy is necessary to cover the Ti pumps maintenance periods.

Besides the permanent pumping group, every pumping station will include suitable vacuum gauges and two 2000 l/s turbo, backed by a dry pump, for initial evacuation and bake-out.

The filter cavity pipes, requiring a  $10^{-7}$  mbar residual pressure, will be equipped only with the turbo/scroll groups, possibly reinforced with 77 K cryo-pumps. Ion pumps could also be taken into consideration, for their ease of operation and low noise characteristics, eventually equipped with proper shields to limit risks of charged particles emissions. To meet these specifications, a bake-out will not be necessary, hence filter pipes will not be equipped with thermal insulation.

Every 10 km pipe will have three residual gas analysers (RGA), at each end and in the middle, to monitor the vacuum quality and for easier diagnosis in case of problems.

### 6.12.2.3 Pipe bake-out system

In order to perform the 10-days bake-out under vacuum at 150°C, the pipe will be heated by electrical current flowing in its walls, closing the circuit by a suitable Al bar or cable. The use of DC will assure a uniform current and temperature distribution on the pipe walls and improve human safety. Typical arrangement of the circuit could be a series of double ring circuits with one DC source every 500 m delivering 1000 A at 60 V along 250 m in each direction. This system will deliver 200 W per meter of pipe, which has been experimentally demonstrated to be sufficient to reach 150°C, if the pipe is wrapped in a suitable 10–20 cm thick thermal insulation layer. Each DC source will consist of a transformer/rectifier supplied by medium voltage AC (15 kV). This choice is dictated to reduce the cross section of cables to distribute 2 MW along 10 km. 15 kV equipment will be confined in dedicated rooms.

In this configuration, delivering 300 W per meter of tunnel, in absence of ventilation, a very crude estimate considering a 6 m aperture tunnel, drilled in isotropic rocks – assumed  $\rho = 2500 \text{ kg/m}^3$ ,  $k = 2.0 \text{ watt/(m K)}$ ,  $C = 800 \text{ joule/(kg K)}$  – gives an increase of room and wall temperature by about +13°C after a 10 days bake-out.

These considerations, together with the specificities of the ET infrastructure (namely, underground location) suggest to investigate alternative bake-out strategies, like baking at a lower temperature for more days and improving the thermal insulation properties, in order to reduce the temperature increase of the tunnel walls. A suitable air cooling system will be designed to reduce further the ambient temperature (possibly renewing once per hour the tunnel air volume). The overall power release inside the tunnel could be reduced also performing bake-out in sequence on shorter pipe sections, separated by “pseudo-valves”, vacuum tight, but able to sustain merely null pressure difference. Furthermore, methods to deal with humidity in the tunnels and the potential problems with vacuum system lifetime will be studied in detail.

### 6.12.3 Cryotrap

HV volumes (e.g. the towers) will communicate with the UHV pipe through liquid nitrogen cryotrap, to prevent migration of water and other high vapor pressure contaminants. In order to allow the beam passage, the cryotrap will consist of a large hollow muff, containing liquid nitrogen, suspended

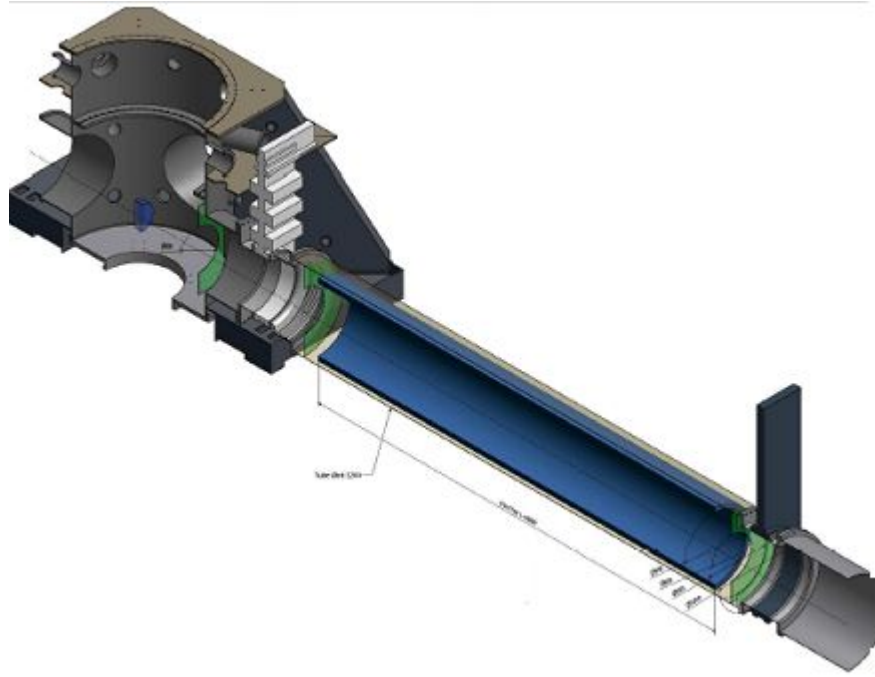


Figure 6.24: A liquid nitrogen cryotrap.

inside an increased diameter pipe section, with a design very similar to the one adopted for LIGO, Virgo and Advanced Virgo (Fig. 6.24).

The lateral surface will be thermally isolated by a few cylindrical metal screens; the heat exchange at both ends will be limited by circular baffles, leaving passage for the beam. The propagation of mechanical noise due to liquid nitrogen bubbling will be limited installing cryotrap at least 20 m away from the mirror towers.

Cryotrap will have valves at each end, in order to be confined during warming-up for regeneration (not more than once per year).

The traps will be 7–10 m long for pipes with diameters of 0.6–1.0 m. The liquid nitrogen consumption has been evaluated to be about 10 liters per hour per trap.

In correspondence of the cryogenic towers for the 10 K mirrors of the LF interferometer, the cryotrap will be much longer (50 m) and will include liquid helium sections to strongly limit the mirror heat exchange as described in the following section. We refer to the same section for a description of the supply plant for cryogenic liquids.

#### 6.12.4 Towers

The upper part of the mirror towers will have a 2–3 m diameter to contain easily the pendulum chains of superattenuators and the inverted pendulum legs; the structure will be an evolution of the Virgo towers (Fig. 6.18). The lower chamber of the towers will have a diameter up to 3 m, to contain large payloads.

The HF interferometer towers will have a large bottom lid to allow installation of payloads from a clean basement, under a filtered air shower. The height will be 10 m for the main mirrors of the warm HF interferometer. Auxiliary mirrors or benches, requiring lower isolation, will be located in shorter towers.

The towers containing the cryogenic mirrors of the LF interferometer, to achieve full seismic isolation performance down to 2 Hz, will be up to 20 m tall. In these towers, sitting on top of the HF interferometer, the payload will be installed through a lateral port. This order of superposition has been chosen to have the low power LF beam passing through the HF mirror suspensions (at room temperature) and not the high power HF beam passing through the low temperature LF mirror suspensions. The lower part of the cryogenic towers will be described in the next section.

Each cryo-tower will be coupled to an ancillary tower to support the heat extraction chain preventing seismic noise propagation.

#### 6.12.4.1 Tower pumping system

The towers will be made of two or three vacuum compartments in order to separate by differential vacuum the lower mirror chamber from the less clean suspension mechanics in the upper chamber. The horizontal separating walls will have a low conductance hole for the passage of the pendulum chain support wire.

The mirror chamber will be equipped with a permanent pumping group consisting of one 2500 l/s Ti sublimation pump coupled to a 300 l/s ion pump. In addition one 2000 l/s turbo, backed by a scroll pump, will be operated for initial evacuation.

The tower upper chamber(s) will be pumped by suitable turbo/scroll groups. An effort will be performed to build the suspension mechanics and electronics with ultra clean and low outgassing components, in order to pump permanently also the upper chamber with ion pumps.

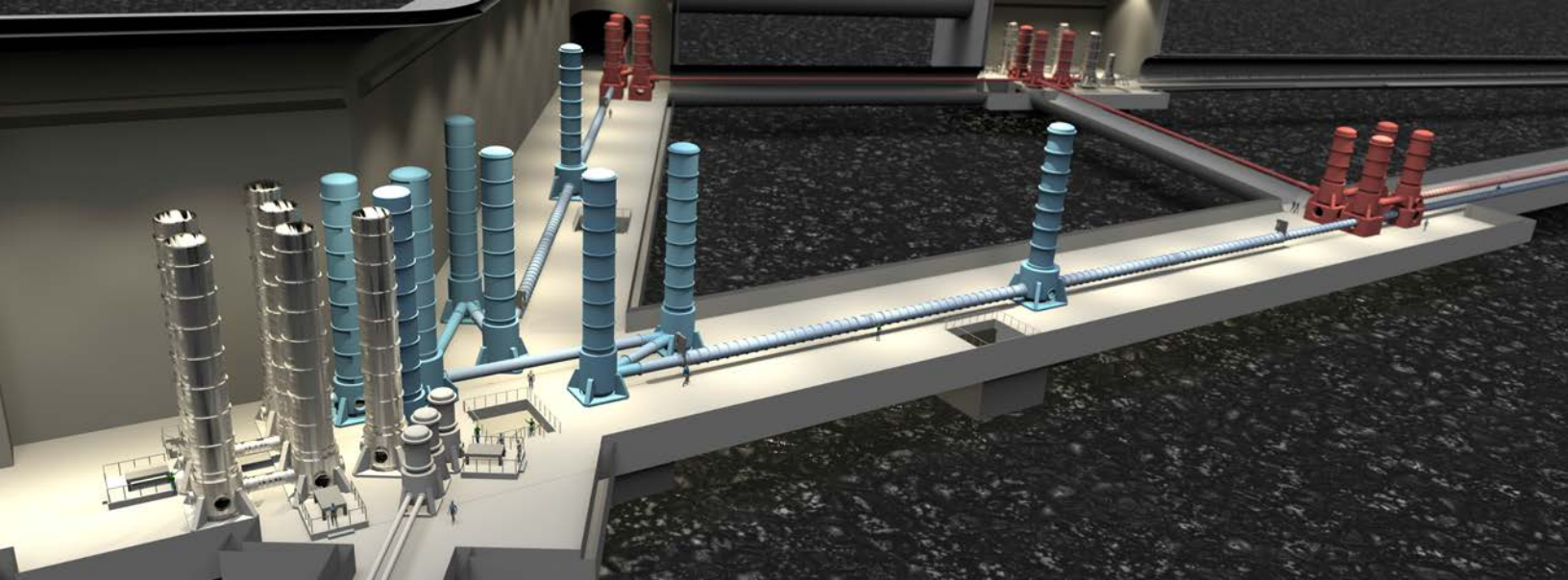
The use of large cryo-pumps is being considered to increase pumping power and to eliminate moving parts from the vicinity of mirrors.

#### 6.12.5 Valves

More than 100 UHV gate valves with large aperture, from 0.5 m up to 1 m, will be necessary. They will be all metal with only the gate gasket out of vacuum outgassed Viton.

Every tower will be separable from the rest of the vacuum system by such valves. Every cryotrap will also be separable for regeneration; the HV side will be equipped with a Viton gasket valve, while the UHV side will be equipped with a totally metallic “pseudo valve”, vacuum tight, but tolerating only a few mbar pressure difference.





## 7. Site and Infrastructure

### 7.1 Infrastructure and site requirements

#### 7.1.1 Infrastructure reference design

Interferometric gravitational-wave detectors are large and complex devices and the selection of their site is an issue of great importance. The selected site should allow the highest possible level of scientific productivity at reasonable cost of construction and operation, and making it possible to operate the infrastructure over its foreseen lifetime. Selection criteria that impact the scientific potential of the observatory have highest priority. These include natural and anthropogenic environmental noise and site geological properties that affect construction cost.

Einstein Telescope will have excellent sensitivity over a wide frequency range starting at 3 Hz up to several kHz. Within the infrasound observation bandwidth (up to 20 Hz) the scientific potential is affected directly by site location and the observatory infrastructure. Therefore, it is of paramount importance that the infrastructure reference design maximize the scientific potential of the observatory.

The local seismic activity is one of the most important site specific noise sources that can affect or degrade the interferometer performance. Mitigation of seismic displacement noise is achieved by combining careful siting with advanced suspension systems (outlined in section 6.10). A prime example of a site that exhibits extremely low seismic background noise is the site selected for the KAGRA detector in Japan. KAGRA is located in the Kamioka mine, which currently holds the Super-Kamiokande experiment and the prototype cryogenic gravitational-wave detector, CLIO. The Kamioka facility is a former zinc and gold mine and is situated 250 km west of Tokyo. Access to the underground facilities is through a well maintained horizontal road tunnel, allowing for depths down to 1000 m. The performance requirements for Einstein Telescope will surpass those of KAGRA and require that the infrastructure reference design advocates for a subterranean observatory.

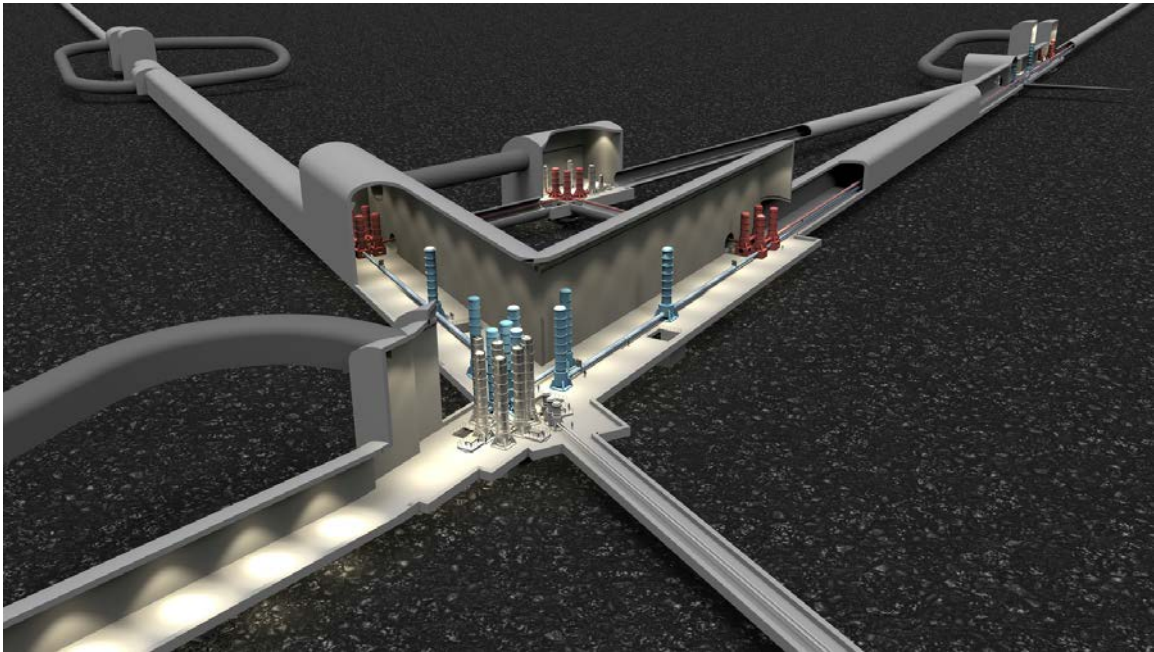


Figure 7.1: Underground infrastructure near one of the three detector vertices. The main hall hosts the majority of seismic-isolation towers, and is the cross-road between two detector arms (towards upper left and right), a tunnel for the filter cavity (towards lower right), and an access tunnel (towards lower left).

Among all sites that were studied as part of the conceptual design study of the Einstein Telescope, two candidate sites remain and are currently under investigation: a site at the Euregio Meuse-Rhine, and another site at Sardinia near the former Sos Enattos mine. The main results of these investigations will be on the site conditions such as geology, geohydrology, geotechnics, natural and man-made environment, as well as on the characterization of environmental noise of natural and anthropogenic origin.

### 7.1.2 Site conditions

In this section, we describe the site-evaluation parameters from an infrastructural and geological point of view. The content is mostly taken from a more extensive presentation of site parameters relevant to ET site selection [524]. This includes all parameters that have an impact on the excavation costs and construction timeline, detector operation, underground facility access convenience, safety of the workers in the underground environment and detector lifetime that we assume to be  $> 50$  years.

The main goal of site selection, site characterization, facility layout, and identification of applied construction methods is to find a location that allows for the construction of ET so that it can achieve its science goals and operate effectively for its proposed lifetime. The technical and cost aspects, nevertheless, can only be optimized together, as a result of a multi-component decision-making procedure, balancing among sensitivity, cost and technical risks. The most reasonable solution for the selected site, the basic design and the planned construction methods should ensure optimization both for technical readiness and the overall costs (both for construction and operation phases) of the

facility.

### 7.1.2.1 Surface

Even though ET's main infrastructure will lie underground, surface conditions are very important to the project. Parts of the infrastructure will be located at the surface, including operations buildings, underground access, a visitor center and guest houses. Seismic disturbances created by local infrastructures, e.g., traffic and industry, can interfere with the operation of the detector and produce sensitivity limitations. Interference issues between the underground and surface facilities (including the existing ones) will be carefully analysed to support the design stages. The environmental impact and the re-use or waste disposal of the material excavated to built-up the caverns and the tunnels must be carefully considered in the choice of sites and execution of the plan.

Surface site criteria that are considered most relevant for the detector construction are:

- Connection to the main and secondary road and transportation networks
- Existing utilities and technological networks in the area (power, gas, telecommunication, water supply, sewage systems, etc.)
- Presence of wells and water uptake systems
- Surface interference and land use constrains at the corner and intermediate access areas to the underground infrastructure
- Environmental policies for construction waste disposal (excavation rocks and contaminated soils), water control, natural and landscape conservation and environmental impact
- Land property status and legal issues for authorization procedures in lights of the territorial constraints.

Surface conditions for the operation of the infrastructures are identified as follows:

- Transportation and site accessibility
- Accommodation and facilities for resident staff (housing, schools, shopping, etc.)
- Accommodations for visiting staff (hotels, restaurants, etc.)
- Local technical support (qualified technicians and vendors, maintenance, fabrication, etc.)
- Existing utility networks (power, water, communication, etc.)

Additional conditions that should be considered for the sustainability of the infrastructure are:

- Natural hazards (earthquakes, floods, subsidence, landslides) and local weather trends (wind speeds, average precipitation rates, lightning rate, etc.)
- Required power supplies and related costs
- Specification and requirements for additional heating, cooling and humidity control plants for the underground caverns
- Maintenance operation requirements and related costs
- Travel time and living costs for personnel and visiting staff

### 7.1.2.2 Underground

The parameters related to the underground concern rock mechanics and groundwater. The general aim of rock-mechanical data acquisition is understanding and forecasting the real behavior of host rock mass, the variability of the parameters/processes/phenomena (as a function of rock types, weathering

level, parting, lateral and vertical position, anisotropy, etc.) in order to reduce the uncertainties of input data of static design and ensure the technical/economic optimization of the facility. Preliminary geophysical studies (mainly 2D and 3D seismic methods) must determine the positions of dislocations and faults and also the rock inhomogeneity. Some of the important geomechanical parameters and features to consider include:

- Faults and fractures
- Rock mechanical data:
  - Elastic parameters (static and dynamic Young’s modulus and Poisson’s ratio of the intact rock, and the rock mass)
  - Strength parameters (uniaxial and triaxial compressive strength, tensile strength, shear strength of intact rocks and discontinuities)
- In-situ stresses
- Rock-mass characterization
- Geomechanical hazards, e.g., squeezing, wedge failure, unravelling, face stability, swelling, subsidence, and other hazards related to the excavation method

For what concerns the Groundwater, hydrogeological data must be collected corresponding to the different lithological faces (i.e. nature of the geological formations) that can be potentially encountered. Hydraulic conductivity is the most important parameter to assess the quantity of groundwater to be potentially drained by underground galleries and cavities. As hydraulic conductivity in hardened rocks is highly dependent on the faulting, local degree of fractures, interconnectivity and apertures must be considered. Another big issue is certainly the depth-dependent values for hydraulic conductivity in a given lithology. It means that extrapolation of observed values is not easy and in situ deep borehole hydraulic tests are needed. In karstic limestones, the hydrogeological parameters are quite heterogeneous with local variation of several orders of magnitude in hydraulic conductivity added to a lack of ‘representativity’ of most of the field and borehole in situ tests and measurements. It means that the acquired values from future field tests would be processed with care and that conservative assumptions would be needed for all future hydraulic and stability calculations. The main hydrological variables and parameters to be considered are:

- Water quantity and quality variables:
  - Water pressures / piezometric heads
  - Solutes concentrations (hydrochemistry)
- Hydrogeological parameters:
  - Hydraulic conductivity
  - Porosity
  - Storativity
  - Effective drainage porosity

### 7.1.2.3 Seismicity

Seismicity plays a large role in the duty factor of large ground-based, gravitational-wave experiments [525]. Specific aspects of geology in relation to seismicity are site effects, which can vary across short distances due to local subsurface heterogeneities as identified in microzonations [526]. We can have variations of seismic amplitude at small scales due to filtering, attenuation, and amplification [527, 528]. Filtering is the frequency-dependent transmission of seismic waves, for example, through

stratified geology. Amplification under “stable conditions” is the effect of the interference of seismic waves trapped within geological bodies bounded by large seismic impedance contrasts (soft soil/bedrock, soil/free surface, etc.). The dimension of geological bodies and discontinuities to be analyzed for characterizing the relevant phenomena are of the order of the seismic wavelengths, which can range from several tens of meters to several kilometers depending on frequency and ground properties. The rate of attenuation, typically expressed as the attenuation factor  $Q$ , depends on a variety of ground properties such as the elastic properties, degree of fracturing, presence of ground water, fluid pressure and porosity.

#### 7.1.2.4 Human safety

A parameter to be considered for the safety of the workers at the detector site is the radioactivity. The primary radioactive elements in the Earth’s crust that lead to human exposure are potassium, uranium, thorium, and their radioactive decay products (e.g. radium, radon). The majority of the dose to the lung arises from exposure to the short-lived decay products of radon and its radioisotope thoron. Radon and thoron are ubiquitous in the air at ground level and are significant contributors to the average dose from natural background sources of radiation. In places with limited ventilation, the levels of these radionuclides and their decay products can accumulate to unacceptably high levels. Soils and rocks are often the main sources of radon. Certain materials can act as significant sources of indoor radon. Such materials have a combination of elevated levels of  $^{226}\text{Ra}$  (the radioactive parent of radon) and a porosity that allows the radon gas to escape. Examples are lightweight concrete with alum shale, phosphogypsum and Italian tuff. Increased demand of ventilation can interfere with the goal to achieve a low-noise infrastructure, which is why a natural environment with low radon levels is generally favorable.

Another risk element to be considered is the risk of water inrush during detector construction or operation [529]. An evaluation of the water-table size and position and rock dislocations needs to be considered in order to evaluate the risk of flooding of the underground detector facility.

#### 7.1.2.5 Lifetime

The project should foresee for the ET infrastructure a lifetime longer than 50 years (as happens for all the big infrastructures). Parameters to be considered in this respect are:

- Differential deformations within the rock mass including dislocation on active faults or subsidence across each of the 10 km arms need to be sufficiently small. Requirements need to be set across short distances (the extent of vacuum pipe modules) to limit stress on welding lips (a few mm of differential motion per 15 m segment is the limit for Virgo), and across long distances to constrain the position of the optical axis.
- Atmospheric corrosion is influenced by average and peak humidity in the caverns and tunnels, the pH of ground and condensation water, and by the presence of chemical elements (in particular chloride if stainless steel will be used for the pipes) [530]
- Microbiologically influenced corrosion [531]
- AC-induced corrosion due to nearby high voltage electric power lines [532].

## 7.2 Environmental noise

Environmental noise can limit the sensitivity of GW detectors. A series of measures is planned to mitigate the issue in ET: site selection, underground construction, noise cancellation, realization of a low-noise infrastructure, and reducing coupling to environmental fields where possible. In the following, we describe the three main environmental noises: seismic noise, magnetic noise, and Newtonian noise.

### 7.2.1 Seismic noise

Noise studies [533–535] often categorize seismic noise sources according to frequency. For the Einstein Telescope, critical frequency regions are in the range of 0.1 – 1 Hz, where the seismic noise is variable mainly due to oceanic microseisms, and 1 Hz and 10 Hz, where seismic noise is dominated by local sources including human activity. Oceanic microseisms are connected to large-scale meteorological conditions at oceans, seas or large lakes. Significant anthropogenic noise has been observed at the existing detector sites from trains, road traffic, planes, logging operations, and above all, from the detector infrastructure including pumps and ventilation systems.

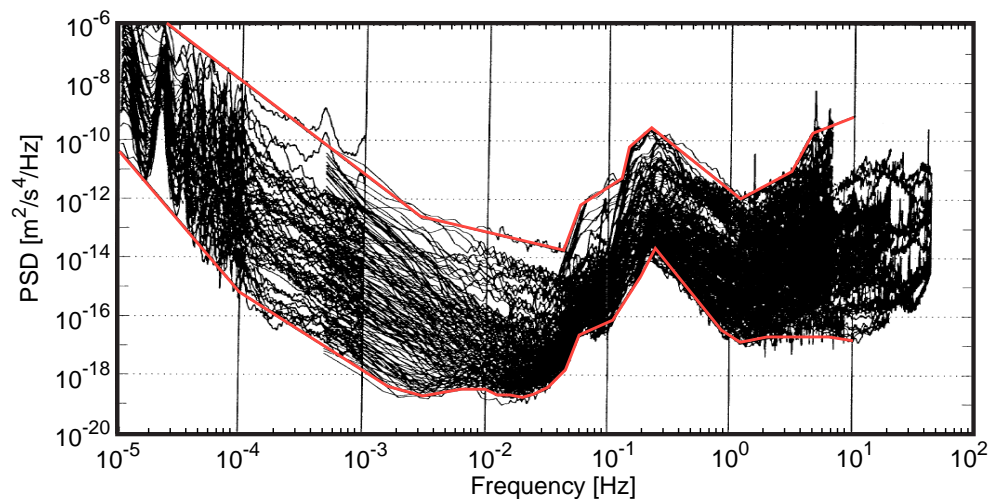


Figure 7.2: Overlay of network station spectra used in Peterson’s background noise study [15] together with straight-line segments fitted to the high-noise and low-noise envelopes of the overlay.

Seismic spectra are represented as power spectral densities (PSDs) as shown in Fig. 7.2. The largest PSD values are seen at low frequencies. Here, the surface of the Earth experiences large external forces due to the gravitational attractions of the Moon and Sun. At very low frequencies this causes the surface of the Earth to rise and fall with amplitudes of about 0.5 m with respect to the center of the Earth. This tidal motion can be seen in Fig. 7.2 at a frequency of  $2.3 \times 10^{-5}$  Hz. Since the motion occurs at very low frequency, the interferometer test masses will move *coherently* and differential test-mass motion presents no problem. Large PSD values are also observed at frequency around  $5 \times 10^{-2}$  Hz and 0.2 Hz, which correspond to oceanic microseisms, and these lead to non-coherent motions which must be suppressed through active control.

Peterson [15] catalogued acceleration noise power spectral density plots for frequencies up to 50 Hz from 75 seismic stations distributed worldwide. Several years of data were collected (about 12,000 spectra in total). From the upper and lower bound of the combined data of both surface and borehole sensors (100 - 340 m depth) Peterson derived, what is now known as, the new high/low noise model (NHNM/NLNM). The data including the upper and lower bound fit are shown in Fig. 7.2.

As explained, the NLNM is a composite of many different stations and instruments with different geology and in various geographic regions. Therefore, it is not possible to observe this spectrum at one specific location. Lowest noise in the 10 mHz to 10 Hz band is typically obtained at remote continental sites far from oceans and human activity, and with predominantly hard-rock geology. Generally, low seismic noise is also observed in boreholes and inactive mines. Highest quality surface sites as well as underground sites can have PSDs that lie only by a small factor above the NLNM.

Presently, the large interferometric detectors GEO600, LIGO, and Virgo with the exception of KAGRA are placed on the surface of the Earth and, consequently, experience relatively strong perturbations by seismic motion. Like KAGRA, ET will profit from a quieter underground environment, and its seismic attenuation system as described in section 6.10.1 will be able to suppress ground motion by many orders of magnitude down to about 2 Hz, thus opening the low-frequency window below 10 Hz to GW observations.

### 7.2.1.1 Anthropogenic seismic noise

The influence of traffic induced seismicity on GW detectors has been studied by various authors. Road noise depends on road structure and materials, traffic density and vehicle type and speed. Schofield *et al.* [536] reported that local traffic from passenger vehicles to heavy trucks induced vibrations at the LIGO Hanford, WA, site. Vibrations were measured for frequencies in the 1 – 50 Hz range, with maxima around 4 - 12 Hz. At the Virgo site, road noise was analyzed by using recordings of the seismic field at the Virgo site and correlating these recordings with measurements underneath a major high way overpass, 4 km away from the Virgo North arm terminal building [537]. Seismic noise originating from the nearby traffic was found in frequency ranges of 1 – 4 Hz, peaking at 3 Hz. Coward *et al.* [538] recorded ground vibrations near Gingin in Australia for vehicles passing the instrumentation as close as 24 m. Road noise was visible in the 5 – 30 Hz frequency band.

In addition, the infrastructure of current GW detectors is a major source of noise above about 10 Hz [539, 540]. Excess noise due to infrastructure can in principle be avoided, for example, by placing fans and pumps on dampers. Such measures are currently under investigation to lower infrastructure noise at the Virgo site. Thorne *et al.* investigated how the interferometer is affected by noise originating from humans, animals, airplanes, etc. [541]. Within the subterranean environment this extends to placement of electricity generators, pumps, and cryo-coolers to keep the facility operational. These devices will be sources of seismic noise. Nonetheless, it is of great importance to avoid excess anthropogenic noise for the 50-year lifetime of the observatory since one could otherwise spoil the advantage of underground construction.

### 7.2.1.2 Wind generated seismic noise

Wind noise has been studied by a number of authors to quantify the conversion of wind energy into ground motion [542, 543]. The presence of wind causes movement of surface objects, such as trees

or structures. It can exert turbulent pressures on topographic irregularities, and also the transport of an atmospheric pressure field with gradients by wind produces ground motion. Of particular interest for ET are the frequency characteristics of the wind noise, the wind speed threshold for it to become evident, and its persistence with depth. Most of the wind-driven sources of seismic noise predominantly produce local surface displacement and tilt. Only a fraction of this perturbation is associated with seismic waves, and the energy going into seismic waves is mostly associated with surface Rayleigh waves. Only a small fraction of wind noise propagates to below the surface. The reduction in wind noise is a prime example of seismic noise contributions that will decay with depth.

### 7.2.2 Magnetic noise

Magnetic noise would significantly limit ET's low-frequency sensitivity if it were not reduced with respect to noise levels in current GW detectors [524]. Noise cancellation might again be considered to reduce magnetic noise, and it will be important to combine it with other methods including the reduction of magnetic coupling of payloads and other relevant parts of the detector, and the reduction of magnetic fluctuations.

Electromagnetic (EM) disturbances can be produced in many ways including natural sources and self-inflicted noise from electronics [544]. The latter includes cross-coupling between electronic/magnetic components of the detector like connectors, cables, coils, and permanent magnets, transients from overhead power lines, and noise from the mains power supply (50 Hz in Europe). Natural sources include transients from lightning, but also permanent fluctuations from Schumann resonances, which are pumped by electric discharges all over the world [545, 546]. The EM fluctuations do not necessarily need to occur in the GW detection band since they can also interfere with detector control relying on signals at MHz, or non-linear couplings can produce up- and down-converted noise. Some of the EM noise can also depend on the environment, e.g., especially underground it is possible that magnetic properties of the surrounding rock lead to (de)amplification of natural field fluctuations [547], which can also change with moisture content and temperature of the rock.

It is clear that due to the large variety of sources, fluctuations should be expected to vary significantly over all time scales from very brief, strong transients, to yearly seasonal cycles of, for example, Schumann resonances and local changes in rock properties. If field fluctuations in the environment (natural or produced by the electronic infrastructure) of ET were as they are today at existing detectors, and if these fluctuations coupled as strongly with the detector output as they do in existing detectors, then ET's main environmental noise would likely be of electromagnetic origin.

Two strategies can in principle greatly reduce problems arising from EM disturbances: (1) electronics are designed to minimize EM coupling between its components and with the environment as much as possible, (2) electronics are designed to produce the weakest possible EM disturbances. If this is achieved successfully, probably as a result of a concerted effort to address the issues in the current observatories and detectors, then the remaining problem is the unavoidable coupling to natural fluctuations, for example, because of magnetic components of the actuation system. Among all sources, the Schumann resonances play an important role since they can lead to correlated noise in a global detector network [548]. It was proposed to apply noise-cancellation techniques to reduce noise from Schumann resonances [549].

The natural background of magnetic fluctuations associated with Schumann resonances is about

two orders of magnitude weaker than the actually measured magnetic fluctuations inside the Virgo buildings [550]. The coupling of these fluctuations with the detector output was measured at the Virgo [551] and LIGO [552] detectors focusing on the coupling at the payloads. Other coupling mechanisms, less well understood, might be important.

### 7.2.3 Newtonian noise

Environmental disturbances are often associated with mass-density fluctuations, which can couple through gravitational attraction with the test masses. Sources of terrestrial gravity noise, also known as Newtonian noise (NN), include seismic and atmospheric fields as well as vibrating infrastructure and moving objects [553]. As will be explained in Section 7.2.3.3, mitigation of NN is the strongest argument to construct the Einstein Telescope underground. It would be an immense, potentially impossible task to design a NN mitigation system (see Section 7.2.4) that would provide the same noise reduction at the surface. It is most difficult to model NN from the ambient seismic and atmospheric fields described in the following two sections, which have therefore enjoyed the greatest attention so far. As potentially important sources of these fields, it is important to anticipate the effect of noisy infrastructure and to present low-noise infrastructure designs. Acoustic and seismic fields at the LIGO and Virgo sites are currently dominated by infrastructure noise.

#### 7.2.3.1 Seismic gravity noise

Seismic NN is a complex composition of different effects, which means that a detailed understanding of the seismic field is required to model the seismic NN, and to predict the performance of a cancellation system if required. Seismic fields can change mass density in two ways: either they cause (de)compression of the soil and rock, or they displace interfaces between materials of different density or surfaces of materials. The two surfaces to be considered in all modeling problems are Earth's surface and the walls of underground caverns.

Seismic fields are generally a composition of several wave types including the Rayleigh waves, which are surface waves, and compressional and shear waves, which are longitudinally and transversely polarized body waves that can travel in any direction through a medium [554]. Since some of the seismic sources can be part of the detector infrastructure, one also needs to understand the properties of near fields of sources. Generally, a precise prediction of NN is only possible taking all properties of the seismic field into account including propagation directions, polarizations, location of sources, and scattering of seismic waves. Such detailed understanding can be obtained with extensive surface and underground seismometer arrays, and potentially also with a combination of limited seismic measurements and numerical simulations if detailed knowledge of geology, topography, and location of seismic sources is available.

Past observations in underground environments demonstrated that seismic fields have a high level of stationarity [555, 556], but there are only few published results to rely on, and it is conceivable that average distributions of seismic sources change over long periods of time, and even rock properties might change for example due to varying water content. Such details might become important for the design of NN cancellation systems, which is why site-characterization studies should foresee a long-term underground seismic measurement.

### 7.2.3.2 Atmospheric gravity noise

Atmospheric perturbations can produce noise in GW detectors via two main coupling mechanisms. Either they are the cause of vibrations of components of the detector, or they produce NN, which is a consequence of direct gravitational coupling between test masses and environmental disturbances. Acoustic NN can have contributions from the atmosphere, but also from the caverns that host the test masses of the Einstein Telescope [557, 553]. In the last case, infrastructure sources become relevant. Since a noise-cancellation system (see Section 7.2.3) is easier to design for cavern NN due to the absence of wind, the main challenge is to understand the atmospheric NN and to be able to predict how it is reduced by going underground.

The properties of the atmosphere give rise to many possible mechanisms to produce NN. Generally, one can associate atmospheric gravity fluctuations with fields of pressure, temperature, or humidity. It is often useful to categorize atmospheric processes according to a characteristic length scale describing the phenomena: global scale, synoptic scale (several 100 km to several 1000 km), mesoscale (several 1 km to several 100 km), and the microscale (up to several 1 km). Mostly the microscale phenomena are relevant to NN modeling in GW detectors. Mesoscale phenomena might become relevant at frequencies below a few 10 mHz, i.e., below the *Brunt-Väisälä frequency*. One source of gravity perturbations are microscale pressure fluctuations in the planetary or atmospheric boundary layer [558, 559], which is the lowest part of the atmosphere directly influenced by the surface. They can be divided into static and dynamic pressure fluctuations. Static pressure fluctuations, which include sound, are present even in the absence of wind [560], while dynamic pressure fluctuations are connected to anything that requires wind [561, 562]. There is also a connection between the two, for example, through the Lighthill process, which describes the generation of sound waves by turbulence [563, 564]. Additional structures emerge with the presence of wind such as vortices or so-called coherent structures [565].

Atmospheric gravity perturbations have been known since long to produce noise in gravimeter data [566], where they can be observed below a few mHz. Creighton published the first detailed analysis of atmospheric NN in large-scale GW detectors [567]. It includes noise models for infrasound waves, quasi-static temperature fields advected in various modes past test masses, and shockwaves. Atmospheric gravity perturbations are expected to be the dominant contribution to ambient NN below 1 Hz, and can still be significant at higher frequencies [557]. Generally, the Navier–Stokes equations need to be used to calculate density perturbations and associated gravity fluctuations [568]. Quasi-static density perturbations associated with non-uniform temperature or humidity fields can be transported past a gravity sensor and cause gravity fluctuations.

### 7.2.3.3 Considerations on detector depth

A vacuum system and sophisticated seismic isolation provide the bare minimum of decoupling between a laser-interferometric GW detector and its environment. However, a few other coupling mechanisms cannot be avoided in this way including direct gravitational coupling between environment and test masses, and stray-light noise. Stray light coupling was discussed in detail in section 6.7. Important here is that the problematic low-frequency vibrations (below a few Hz) causing most of the stray-light noise are associated with several-kilometer-long seismic waves, whose amplitudes are not significantly suppressed by going 200 m – 300 m underground as planned for the Einstein Telescope.

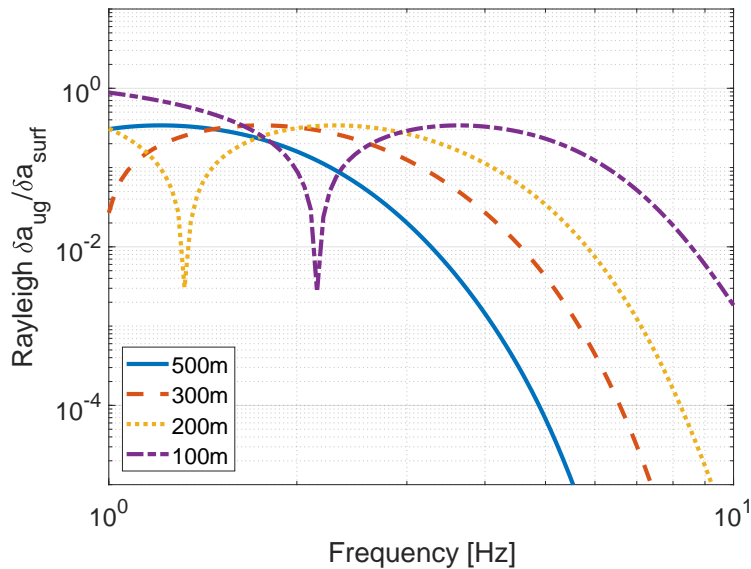


Figure 7.3: Suppression of Rayleigh-wave NN with depth. In this model, it is assumed that wave speed falls from 1.8 km/s at 1 Hz to 500 m/s at 10 Hz. These suppression curves are used in the right plot of Figure 7.4.

Going underground is beneficial for seismic isolation. Specifically, ground tilts are known to be much stronger at the surface due to the direct impact of the atmosphere [543]. The reduced tilt can make an important difference in active seismic isolation, where tilt-to-horizontal coupling in seismic sensors poses performance limitations [569, 477]. However, the implementation of tiltmeters in the active isolation systems [494] or more substantial redesigns of active seismic isolation platforms [477] are possible to mitigate the problem. Therefore, while reduced ground motion in underground environments is clearly beneficial for seismic isolation systems, it is not the most important aspect.

The most important gain of going underground is to reduce terrestrial gravity noise. Atmospheric and seismic NN can both be reduced. Predicting the reduction of surface seismic NN with depth requires the dispersion curves of surface Rayleigh waves. The slower the medium, the shorter the waves, the stronger the suppression with depth. An example of the suppression factors as a function of frequency for various depths is shown in Figure 7.3. Seismic speed is assumed to be 1.8 km/s at 1 Hz falling smoothly to 500 m/s at 10 Hz. Since the Einstein Telescope targets GW measurements down to 3 Hz, it is clear if NN needs to be reduced by an order of magnitude and more (see Figure 7.4), then a depth of 100 m would not be sufficient in this example. Also relevant, but not shown here, is the reduction of atmospheric NN. Results presented in [557] showed that atmospheric, acoustic NN is expected to be sufficiently reduced already at 100 m depth, and it is to be expected that all forms of atmospheric NN are sufficiently suppressed at such depth since the corresponding fields vary over much smaller distances compared to seismic fields, which is essential for the suppression of NN with depth.

In conclusion, the most important gain of underground construction is the reduction of NN, and seismic NN is most relevant as it requires greater depths for strong reduction. Other important criteria affected by detector depth include the detector construction cost, safety regulations, and the required performance of a NN mitigation system. To choose the optimal detector depth, one needs to weigh

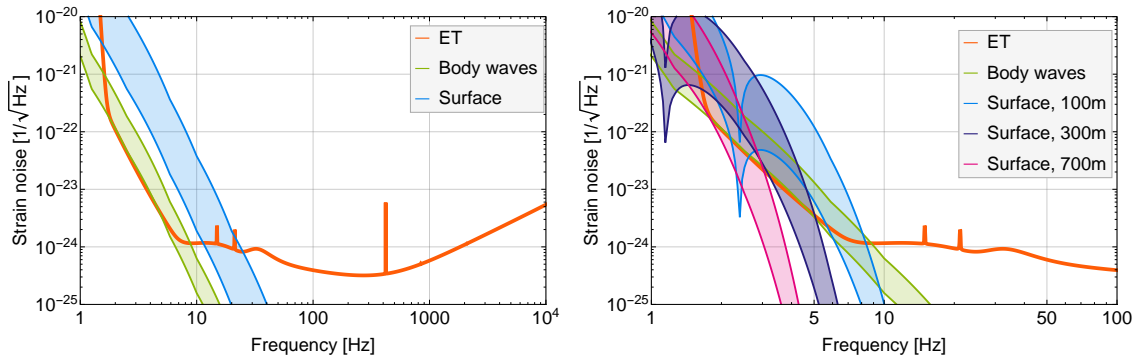


Figure 7.4: Estimates of seismic NN for ET. Left: ET constructed at the surface. Right: ET constructed underground.

the different aspects, which will generally depend on the site properties.

#### 7.2.4 Newtonian-noise cancellation

Newtonian-noise cancellation comprises techniques where auxiliary sensors are deployed to monitor sources of density perturbations, and their data are then used to produce a NN estimate that is being subtracted from the GW detector data.

As described in Section 7.1, the first step of any NN mitigation strategy is to reduce environmental disturbances. For ET, this includes site selection, underground construction, and realizing a low-noise detector infrastructure. However, only if the natural environment is among the quietest in the world, and excess anthropogenic noise can be avoided, then it might be possible to achieve the ET sensitivity target without NN cancellation. Nonetheless, without a detailed understanding of the seismic field, which is hard to obtain even with an extensive site-characterization study, NN modeling uncertainties are significant. It is therefore necessary to include NN cancellation in the R&D plans.

As shown in Figure 7.4, NN from surface waves will be strongly suppressed if the detector is constructed a few 100 m underground. However, the NN from seismic body waves cannot be avoided at any depth, and it becomes a sensitivity-limiting noise contribution below 10 Hz. Depending on the quality of the underground site, one still needs to mitigate body-wave NN by up to a factor 10. The range of body-wave NN shown in the two plots assumes that underground seismic spectra are a factor 3 to 12 above the global low-noise model [570], and an isotropic field is composed entirely of compressional waves. If it were composed entirely of shear waves, then the NN would be a factor 2 smaller. The prediction of Rayleigh NN (denoted *Surface* in the two plots) in underground detectors requires an assumption about the seismic surface spectrum, which is a factor 50 to 1000 above the global low-noise models in the two plots, but also an assumption about the dispersion curve. The slower (and therefore shorter) Rayleigh waves, the stronger is the suppression of associated NN with depth [553]. The dispersion model used for the two plots (Rayleigh wavelength plays a negligible role for NN in surface detectors) yields a Rayleigh-wave speed of 1.8 km/s at 1 Hz falling to 500 m/s at 10 Hz. There can be significant regional variations, but these values are typical. For the body-wave and Rayleigh-wave field, anisotropy can increase or decrease NN relative to the isotropic level shown in Figure 7.4.

### 7.2.4.1 Coherent noise cancellation

The basic idea for noise cancellation is to exploit correlations between NN and data from a set of auxiliary sensors. An effective technique is to use Wiener filters [571]. They are the optimal linear filters for this purpose provided that all time series are stationary, and they are effective even in the presence of non-stationary features in the data. Wiener filters can be estimated from data. It requires the calculation of correlations between all auxiliary sensors monitoring the environment, which form a correlation matrix  $\mathbf{C}_{SS}$ , and between auxiliary sensors and GW detector, which form a vector  $\vec{C}_{SN}$ . Since one is mostly interested in the frequency-domain representation of detector noise, correlations are expressed as cross-spectral densities depending on frequency  $\omega$ . The Wiener filter can then be written

$$\vec{w}(\omega) = \mathbf{C}_{SS}(\omega)^{-1} \cdot \vec{C}_{SN}(\omega) \quad (7.2.1)$$

This filter is applied to discrete Fourier transforms of data from auxiliary sensors,  $\vec{d}(\omega_i)$ , to produce an estimate  $\hat{n}(\omega_i) = \vec{w}(\omega_i)^\dagger \cdot \vec{d}(\omega_i)$  of NN, which is then subtracted from the GW detector data. In average, the relative suppression of NN by a Wiener filter is given by

$$\epsilon(\omega) = \sqrt{1 - \frac{\vec{C}_{SN}^\dagger(\omega) \cdot \mathbf{C}_{SS}(\omega)^{-1} \cdot \vec{C}_{SN}(\omega)}{C_{NN}(\omega)}}, \quad (7.2.2)$$

where  $C_{NN}(\omega)$  is the spectral density of NN in the GW detector. This expression tells us that to achieve a good subtraction efficiency, the following conditions are to be met:

- All the sensors should be coupled as much as possible to NN. In other words, the correlation  $\vec{C}_{SN}$  between sensor outputs and GW detector must be large.
- The correlations between sensors, described by the matrix  $\mathbf{C}_{SS}$ , which also include sensor noise on its diagonal, must be small.

Designing a NN cancellation system for a GW detector that is yet to be built, only the correlations among auxiliary sensors  $\mathbf{C}_{SS}$  can be measured during a site-characterization campaign. A model is required using the correlations  $\mathbf{C}_{SS}$  to obtain  $\vec{C}_{SN}$  and  $C_{NN}$  [539].

The theory of Wiener filtering does not directly address a major challenge of NN cancellation, which is the optimal placement of auxiliary sensors. This aspect is very important for the cancellation of NN from seismic and atmospheric fields. Analyses of optimal array configurations are important since, even when lacking an accurate understanding of environmental fields, optimization results provide useful estimates of the required number of auxiliary sensors, the required sensitivity of sensors, and an approximate idea of how far from the test masses sensors need to be placed. This aspect is discussed in Section 7.2.4.3.

### 7.2.4.2 Site properties relevant to Newtonian-noise cancellation

Since the Wiener filter is based on correlations in environmental fields, anything that influences these correlations affects NN cancellation. In the following, site properties relevant to seismic and atmospheric NN are briefly described.

#### Seismic fields

- **Seismic speed** Seismic correlations and correlations of seismic NN between test masses decrease with increasing distance. In frequency domain, this can be quantified in terms of a spatial correlation function  $\mathcal{F}$  that assumes its maximal value 1 when the two seismometers or test masses are sharing the same location. As a function of the separation  $L$ , one finds for isotropic Rayleigh-wave fields

$$\mathcal{F}_{\text{NN}} = J_0(2\pi L/\lambda) - J_2(2\pi L/\lambda), \quad \mathcal{F}_{\text{seis}} = J_0(2\pi L/\lambda). \quad (7.2.3)$$

As is intuitively clear, how quickly correlation decreases with increasing distance  $L$  depends on the length  $\lambda$  of a Rayleigh wave. The first zero of the seismic correlation is at a distance of about  $0.4\lambda$ . Correlations of NN between two test masses of one arm separated by several kilometers can be neglected. Due to equation (7.2.2), seismometer arrays used for NN cancellation ideally have diameters similar to the length of a Rayleigh wave.

- **Wave polarizations** Seismic-wave polarizations play a major role in NN cancellation. The two main polarizations are shear and compressional waves, and Rayleigh surface waves are a so-called inhomogeneous (amplitude decreasing exponentially with depth) extension of a superposition between these two polarizations. The composition of the seismic field in terms of wave polarizations varies between sites, and depends on local geology as well as on the type and location of seismic sources. All polarizations produce NN either through compression of the medium or by displacement of surfaces and interfaces.

If only one wave polarization is present at a time, then it is almost trivial to cancel associated NN [553, 572]. A mix of wave polarizations can however make it very difficult to cancel a significant amount of NN [572, 16]. The issue is that correlations between seismometers and test mass decrease more quickly with distance when multiple polarizations are present, which hampers efficient noise cancellation as pointed out in Section 7.2.4.1. As a consequence, a larger number of seismometers is required to be able to distinguish between polarizations and be susceptible to the correlations of each wave type.

- **Seismic sources** The distribution and type of seismic sources both influence the composition of a seismic field. Most important to know is whether seismic sources are local or distant, and whether they are underground or at the surface. Some sources might not even fall into a clear category if it is for example a surface structure anchored to a deeper part of the ground. With respect to environmental noise, it is one of the most important tasks of a site-characterization campaign to identify as many seismic sources as possible. A NN cancellation scheme can be greatly simplified or be made significantly more effective if understanding about the seismic sources is used. Furthermore, excess noise produced by the infrastructure of the Einstein Telescope will also pose additional challenges for the design of a NN cancellation system.
- **Local topography and geology** Two-point correlations of the seismic field can be affected by topography and geology. Generally, seismic-wave reflections from surfaces and interfaces cause conversions between wave polarizations. Scattering from non-planar structures can also give rise to local field components that strongly decay with distance. These local components are very similar in nature to the near-field of seismic sources. In the presence of significant geological heterogeneities or rough surface topography, it is therefore more challenging to collect all information required to design seismometer arrays for efficient NN cancellation [573]. Especially in relatively noisy environments with elevated NN where more efficient cancellation of NN might be required, site characterization should therefore assess geological properties and topography also in the context of NN cancellation.

### Atmospheric fields

Avoiding NN from the atmosphere is an important reason to construct the Einstein Telescope underground. In Section 7.2.3.2, some of the complexity of atmospheric fields and how they produce NN are described. There are serious practical challenges to design a cancellation system for atmospheric NN.

- **Wind noise** The variety of phenomena makes the monitoring of the atmosphere a challenging task. One strategy for NN cancellation would be to monitor sound, wind speed, temperature and humidity fields. Sound is typically measured with microphones. However, pressure fluctuations produced by turbulent flow in the vicinity of a microphone can mask an underlying sound signal [574]. This contribution is often called wind noise. Clever sensor design, averaging pressure signals over some baseline, or constructing wind shields can prove effective [575–577]. However, when it comes to an order of magnitude suppression of NN from sound, then even a small incoherent contribution to signals from wind noise can be detrimental. For this reason, entirely new approaches need to be considered.
- **LIDAR** LIDAR (derived from *light* and *radar*) technology has been applied to investigate microscale physics in the atmospheric boundary layer. It consists of a laser beam that scatters back from the atmosphere carrying information about the presence of certain molecules, or wind speed [578], temperature [579], etc. Volumetric observations can be performed to characterize the evolution of entire fields. It is conceivable that a LIDAR system can be developed in the foreseeable future to cancel at least modest amounts of wind-driven NN associated with temperature and humidity fields. However, atmospheric density perturbations due to sound are orders of magnitude weaker in the ET observation band, which makes it extremely challenging to develop a LIDAR to monitor sound fields.
- **Cavity atmosphere** Potentially significant NN contributions can come from the sound field inside the cavities hosting the test masses of the Einstein Telescope [557]. Due to the absence of fast air currents, wind noise in microphones located inside the cavity will be strongly reduced, and high-precision sound monitoring would be possible. At the same time, absence of fast air currents also means that all forms of cavity atmospheric NN driven by wind, i.e., associated with temperature and humidity fields, will be negligible. This means that cancellation from cavity atmospheric NN should be possible using an array of microphones.

#### 7.2.4.3 Optimized sensor arrays for seismic Newtonian-noise cancellation

Another important point to understand is how the subtraction procedure improves with the number of sensors, and how much it is sensitive to a non optimal placement of the sensors. This is important because in a practical implementation, the possibility of optimizing the placement of underground sensors will be limited.

Optimized seismometer arrays were initially studied for the cancellation of NN from Rayleigh waves [580, 553, 539], and more recently from body waves [16]. Array optimization was based on simplified models of the seismic field in all these publications, which means that the calculated array configurations are not of direct use for NN cancellation in real environments. However, the total number of seismometers and the seismometer sensitivity required to achieve a certain cancellation performance are less dependent on the model of the seismic field [539].

Accordingly, Fig. 7.5 gives an estimate of the required number of seismometers to cancel a certain

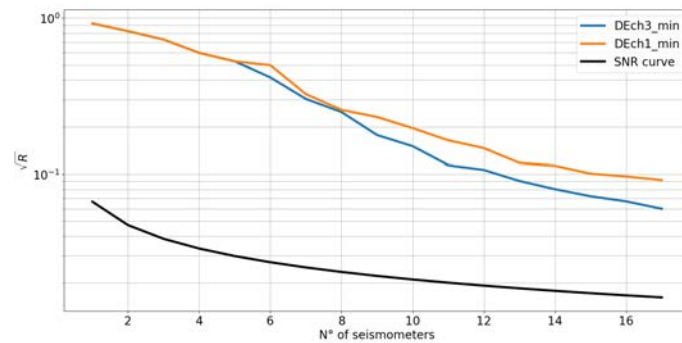


Figure 7.5: Suppression of body-wave NN as a function of number of seismometers with optimal placement. The seismometers measure seismic signals with an SNR of 15. The black curve shows the lowest possible residual determined by the seismometer SNR without considering properties of the seismic field. Plot from [16].

amount of body-wave NN provided that they assume their optimal positions. About 15 seismometers are required to achieve a factor 10 suppression. It should be emphasized that this result depends to some extent on the relative contributions of compressional waves and shear waves to the seismic field. For these results, it is assumed that compressional waves constitute 30% of the seismic power-spectral density. Fewer seismometers are required if one polarization greatly dominates over the other. These instruments need to be deployed in boreholes, and the number 15 is per test mass.

In this context, one can now address the question how accurately the seismometers need to be placed with respect to their optimal locations. While direction and vertical drilling technology has become increasingly accurate [581], significant deviations from optimal drilling are to be expected, which results in sub-optimal seismometer placements. Figure 7.6 shows the residuals that can be achieved with sub-optimal seismometer placement. To produce this plot, seismometer coordinates were shifted by a random number drawn from a Gaussian distribution of width  $\sigma$  specified in the legend relative to the length  $\lambda$  of compression waves. Assuming a compressional-wave speed of 4 km/s,  $\sigma = 0.07\lambda = 28$  m at 10 Hz. The corresponding arrays with three-axis sensors (ch3) still achieve a body-wave NN suppression by a factor 3 and better. For boreholes of a few 100 m, and drill deviation of less than 1 degree, such sensor-placement accuracy is achievable.

The remaining challenge is to have sufficient observations of the seismic field to be able to accurately calculate the optimal array configurations. In fact, incomplete knowledge of seismic correlations will likely lead to the dominant error in the seismometer placements. This error needs to be minimized by studying in detail the seismic field at the site of the Einstein Telescope also using borehole seismometer installations.

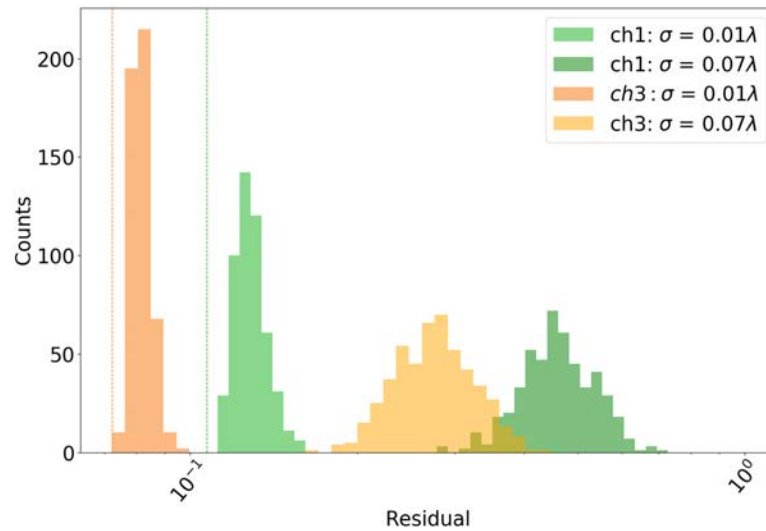


Figure 7.6: Suppression of NN from body waves with 15 single-axis (ch1) and three-axis (ch3) seismometers. Sensor locations of 500 arrays for each histogram are derived from the optimal array by adding random numbers to all optimal coordinates drawn from Gaussian distributions of width  $\sigma$ . Vertical lines mark the residual of the optimal arrays. Plot from [16].

## 7.3 Underground construction

### 7.3.1 Tunnels and caverns

The chosen detector topology for the ET wide-band gravitational wave observatory is a xylophone detection scheme containing six interferometers housed in triangular configuration. Fig. 7.1 shows a scaled impression of the underground observatory. Each xylophone detector will be centered around one of the corner stations and is composed of a high and low frequency interferometer pair.

Figure 7.7 gives a (not to scale) overview of the geometry of the infrastructure, with access tunnels and de-watering tunnels. The tunnels excavated with tunnel boring machines (TBM) have a length of ca. 9.5 km. At the corners of the triangle there is a complex of caverns and connecting tunnels as exemplified in figure 7.7 with the lengths of the various sections indicated. Figure 7.8 gives an idea of the 3D arrangement of caverns, long arm tunnels and options for access tunnels.

#### 7.3.1.1 Access to the underground infrastructure

Presently, it is not clear whether the observatory will have horizontal, inclined, or vertical access or a combination thereof. When considering sites, the manner in which access to the underground facilities is established, requires careful consideration which include in particular the geological and hydrogeological situation, environmental impact and socio-economic factors. In traditional mining, access to the underground is via a decline (ramp) or inclined vertical shaft, or adit. Shafts are considered as vertical excavations while adits are horizontal excavations into the side of a hill or mountain.

Depending on the topographic situation ramps and shafts need to be constructed with conventional

methods from the earth surface downwards. Thus, water ingress during construction poses a major risk for construction costs and time and adequate measures (e.g. systematic grouting) to counteract large inflow rates must be foreseen. An optimized design of the access tunnel alignment and measures is thus dependent on detailed hydrogeological and geological information at the corner points and can only be decided upon a robust result of the site selection procedure and detailed site investigations.

Figure 7.9 shows an impression of the observatory in case inclined ramps are employed. An inclined tunnel with a slope of ca. 10% connects a vertex cavern with the surface installations. The flexibility in the direction of the access tunnel gives flexibility of the location of the tunnel entrance within a radius of ca. 2.5 km for a depth of 250 m and an inclination of 10%. Additional shafts are foreseen at the centre of the arms (not shown). In addition, and depending on the hydrogeological and geotechnical properties of the rock mass, alternative solutions such as a combination of a vertical shaft and a horizontal access tunnel provide additional flexibility. An optimized design in terms of costs and construction time requires a detailed sub-surface site investigations program and will include existing surface infrastructure, social-economic aspects, and natural reserve areas.

Figure 7.10 sketches the scenario of a vertical access shaft close to the corner station. Vertical shafts with the potential of lowering TBMs need a diameter of >12 m.

#### 7.3.1.2 Caverns

Around each corner of the ET triangle an assembly of caverns is needed to host the various vacuum tanks containing the optics and suspensions. A perspective close-up view of those caverns and tunnels is shown in figure 7.11. For each vertex of the triangle layout, Cavern A indicates the main cavern structure of the underground laboratory and is formed by an intersection of two caverns with an identical layout at an angle of  $60^\circ$ , with lengths of about 190 m and 160 m. The smaller cavern branch (Cross-Cavern A) includes a prolongation tunnel about 1 km long, hosting the ET-LF Filter Cavity. Two identical connecting tunnels run in the prolongation of the branches of Cavern A (see figure 7.11). Each connecting tunnel in the x- and y-direction contains a series of three caverns (Cavern C,D,E) at the transition to the TBM tunnel. The three caverns have a spacing of 35 m in between them. The distance between the caverns is mainly required from an operational point of view but will be also deemed to be adequate from a geo-mechanical perspective. The Cavern B (see figure 7.14, contains the beam splitter and readout part of ET-HF and is located within the bisection line of the two branches of the “connecting tunnels”. This makes it possible to separate the vertex optics and associated vacuum tanks of ET-LF and ET-HF. Cavern B is linked to the two branches of the Cavern A (see figure 6.2) and carries an additional connection tunnel to the Cavern C.

The Cavern C (see figure 7.19) is situated about 300 m offside the Cavern B and the connection tunnel will host the filter cavity of the high frequency interferometer. The sizes and shapes of the various other caverns and the connecting tunnel are shown in figures 7.15, 7.16 and 7.22 and will be excavated by drill and blast. The current design foresees a horseshoe-shaped design of all cavern, tunnels and galleries. The shape of these caverns and tunnels might be redesigned to fit the geo-mechanical requirements (i.e. weak rock mass conditions may require a more rounded geometry of the excavations to minimize support measures).

The curved tunnels in figure 7.11 are just for construction purposes and can later also serve as safety escape routes. To the right an inclined access tunnel can be seen. The tunnel leading to the upper left of the image will have a slight downward slope, and contains vacuum tubes for the filter cavities for

creating frequency dependent squeezed light and serves for de-watering purposes. At the end of it a borehole of ca. 40 cm in diameter is considered for the actual design status for pumping out the water collected in the tunneling system.

A CAD rendering of a large vertex cavern with the tall suspension vacuum tanks, connecting vacuum tubes etc. is shown in figure 7.17. The vacuum vessels belonging to ET-LF, the cryogenic low frequency interferometer, are depicted in blue, while the room-temperature part is shown in red. Cavern heights vary between 12 m and 30 m depending on the size and height of vacuum tanks they contain. Connection tunnel sizes vary between 6x6 m and 12x12 m, depending on the number and size of vacuum tubes they contain and required space for maintenance and later upgrades.

Each of the vacuum towers is accessible from underneath such that the payload can be accessed from the bottom of the vacuum vessel, as shown in figure 7.19 and 7.14.

In the infrastructure costing in this design stage the cavern support is considered to be provided solely by a shotcrete lining. For cleanliness and dryness reasons a "house-in-house" solution is preferred for the caverns. The inner "house" is separated from the cavern walls by a gap, where water coming from the rock is collected and removed. The house in house solution would be part of subsequent laboratory installation. The required caverns to host the technical infrastructure are considered major underground excavations. Thus, one of the major objectives of the site selections procedure is identifying geological regions at the corner points with stable ground conditions to enable a cost effective construction (e.g. cavern shape) with minimal support measures and maintenance costs.

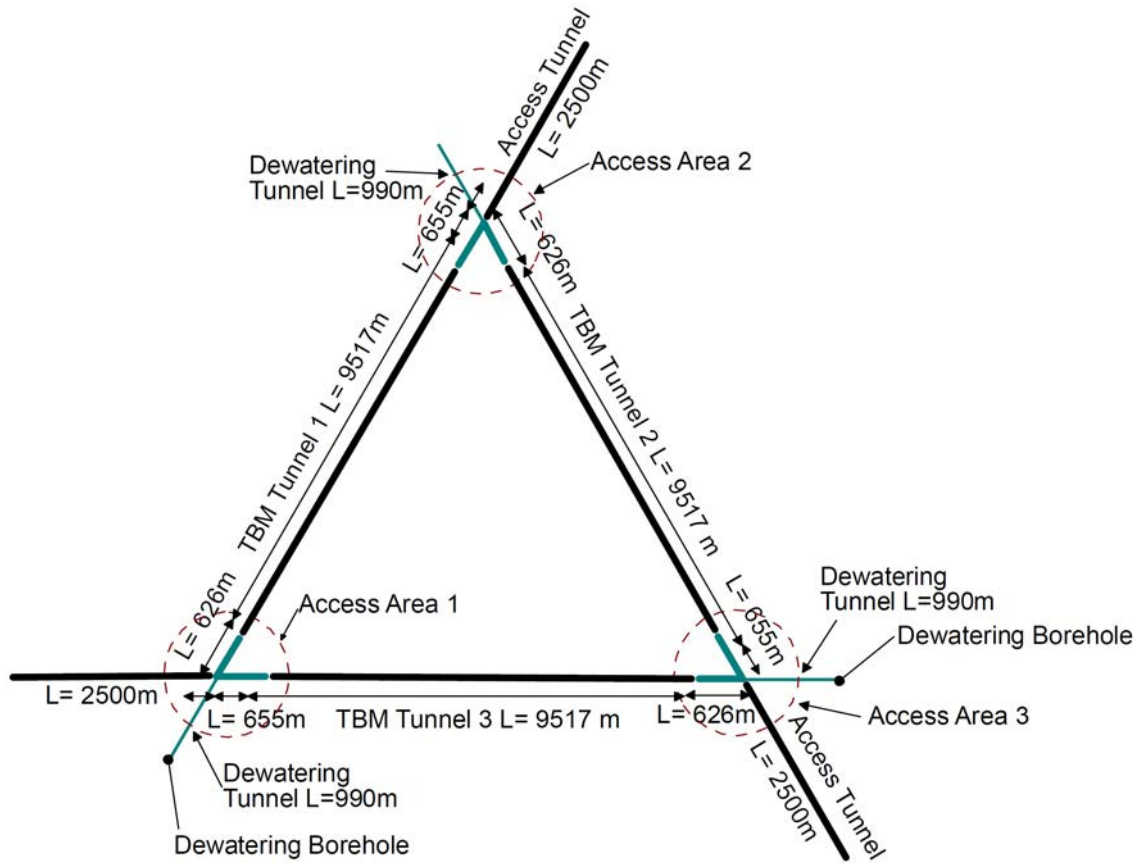


Figure 7.7: Underground infrastructure of ET. Cavern groups (shown in cyan) are connecting by the long tunnels forming the ET triangle. About 1 km long de-watering shafts also contain Filter Cavities. Each corner station is accessible by an access shaft or tunnel. The image shows the lengths of the various sections. Although accurate numeric values are shown here, the detail led length requirements need to be determined in the technical design phase. Image source Implenia.

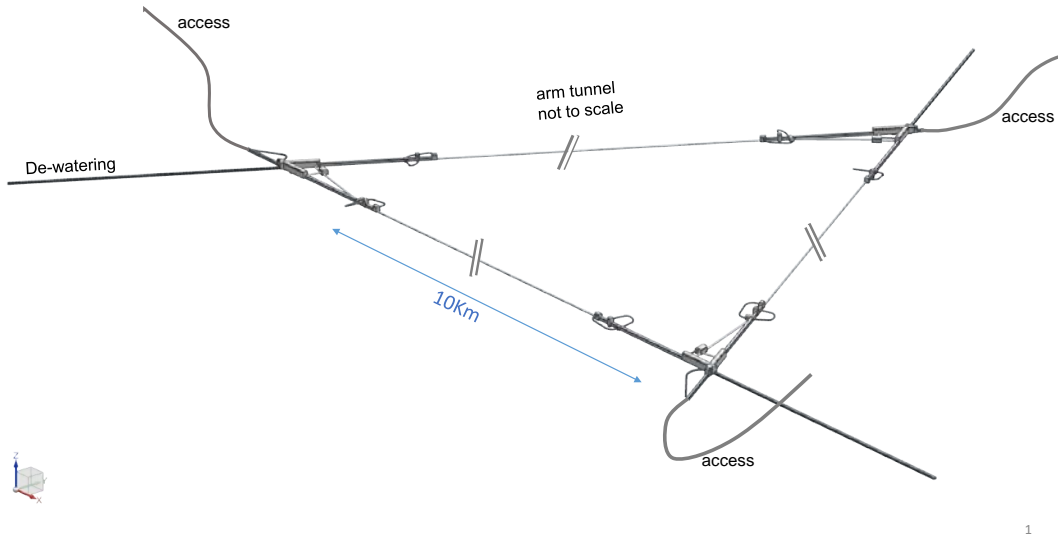


Figure 7.8: 3D impression of the overall tunnel and cavern arrangement for ET. The long tunnels are not shown to scale.

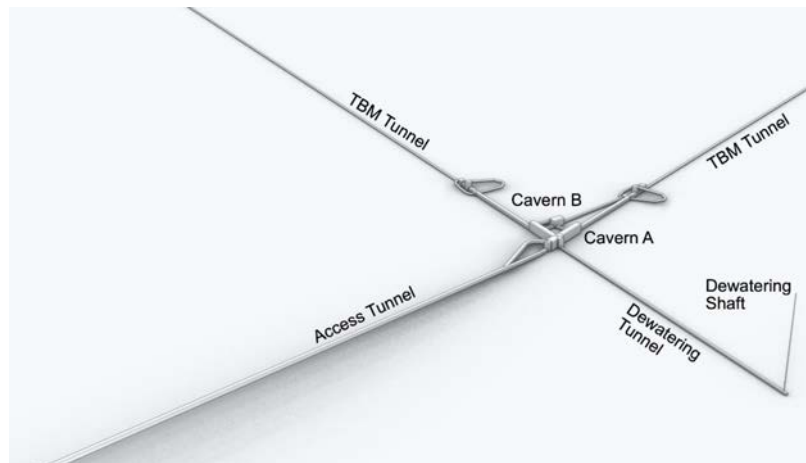


Figure 7.9: Sketch of a layout with inclined tunnels for access to the vertex stations. "TBM Tunnel" indicates the arm tunnels of the triangle, produced with a Tunnel Boring Machine.

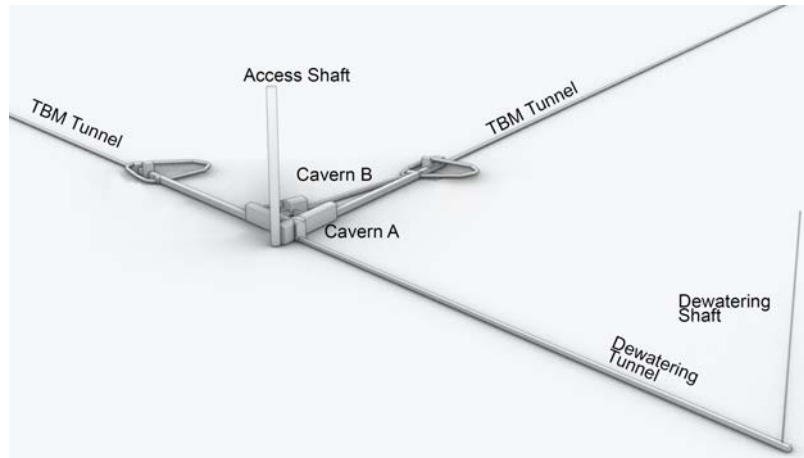


Figure 7.10: Sketch of a layout with vertical shafts for access to the vertex stations. Image source Implenia.

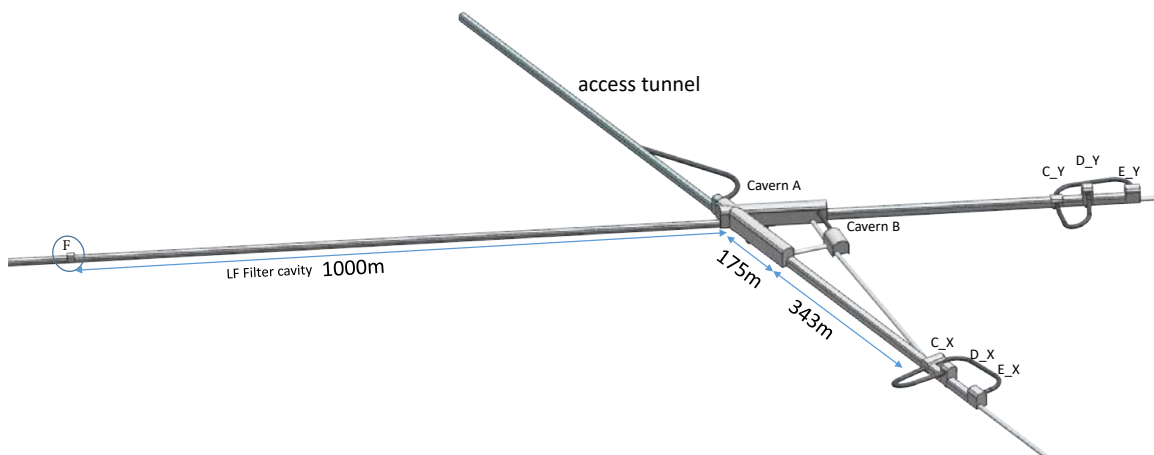


Figure 7.11: Perspective view of the underground infrastructure at the corners of the triangle. The curved tunnels connecting the caverns are for construction purposes.

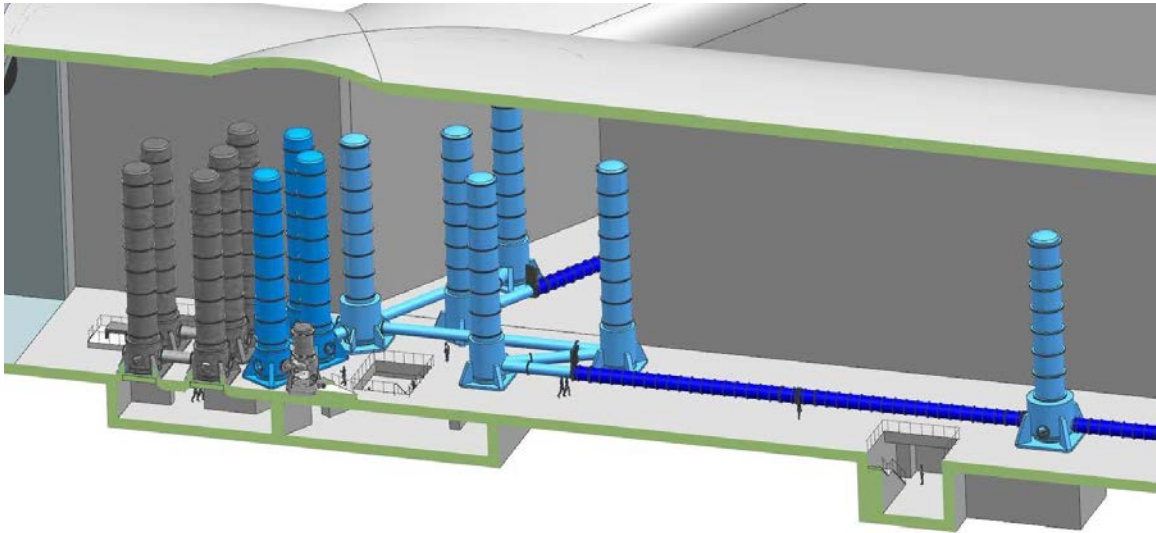


Figure 7.12: CAD rendering of a birds view of cavern A. The cut-off view shows the access basement underneath the vacuum towers and a few people for comparison in size.

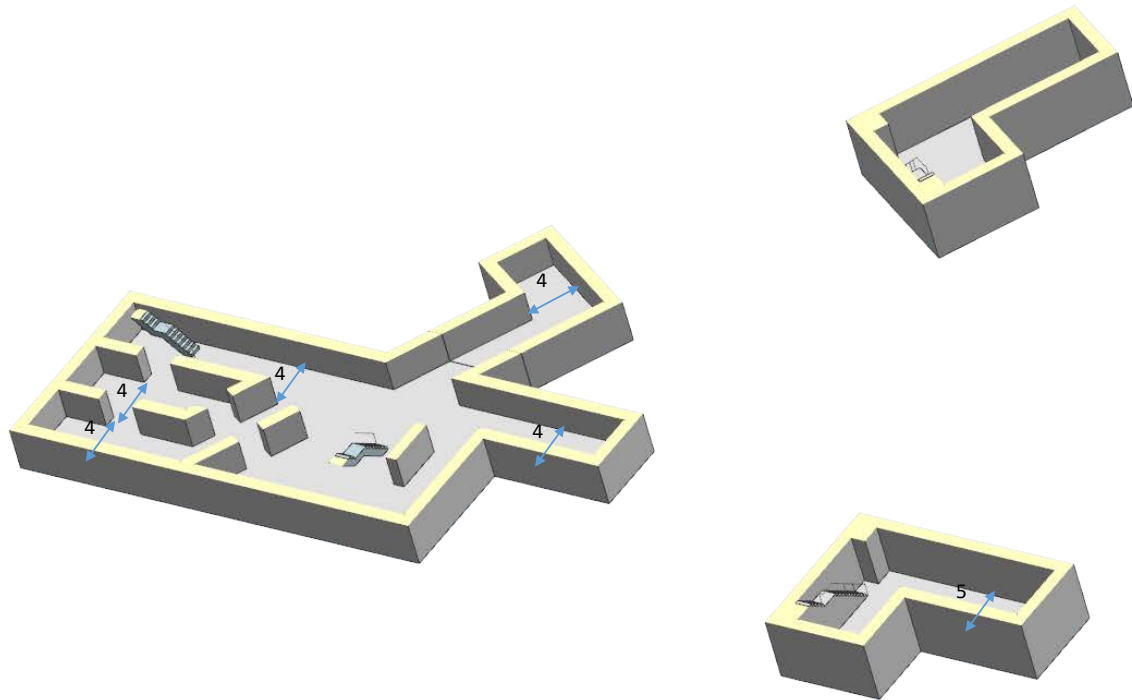


Figure 7.13: Example layout of the basement level of Cavern A with entrance rooms and reinforcement walls giving a solid support for the vacuum tank bases.

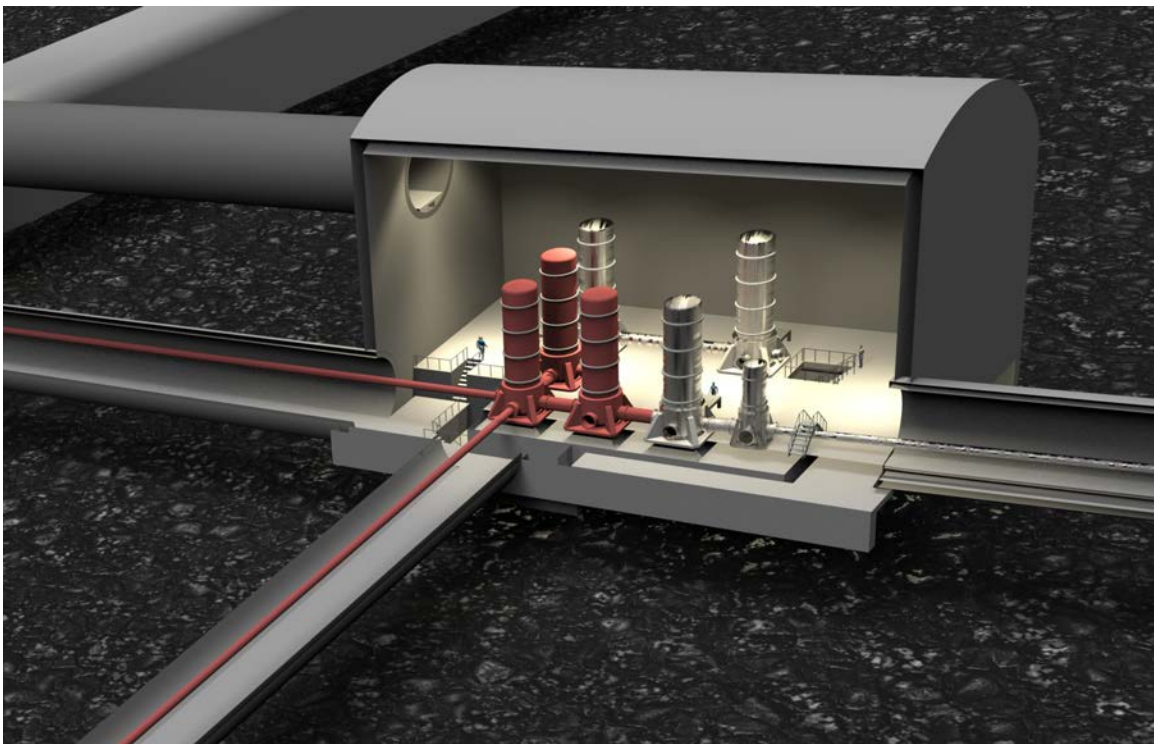


Figure 7.14: CAD rendering of a birds view of cavern B. The entrances to the basement underneath the vacuum towers and a few people for comparison in size are shown.

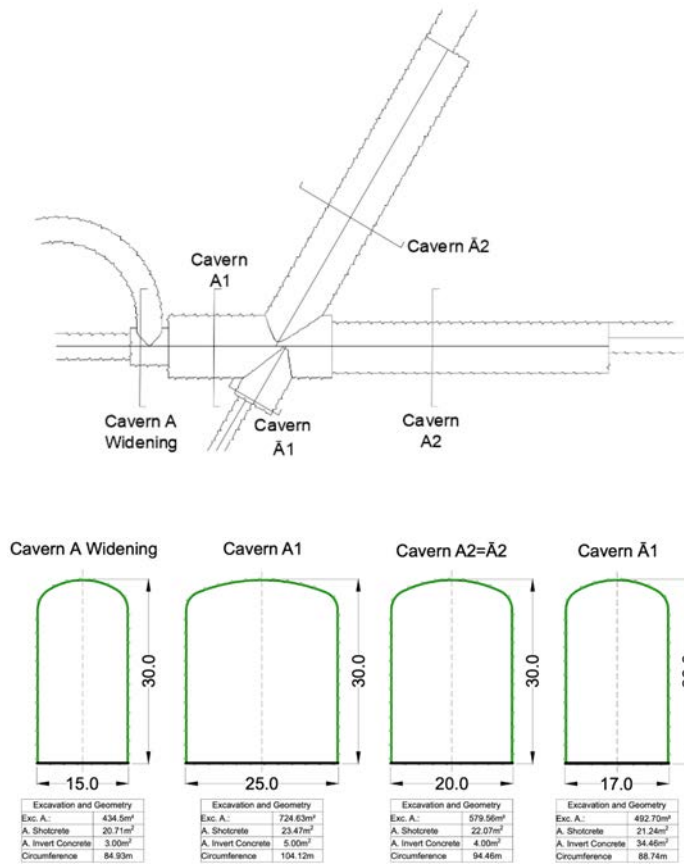


Figure 7.15: Cross section of Cavern A, image source Implenla.

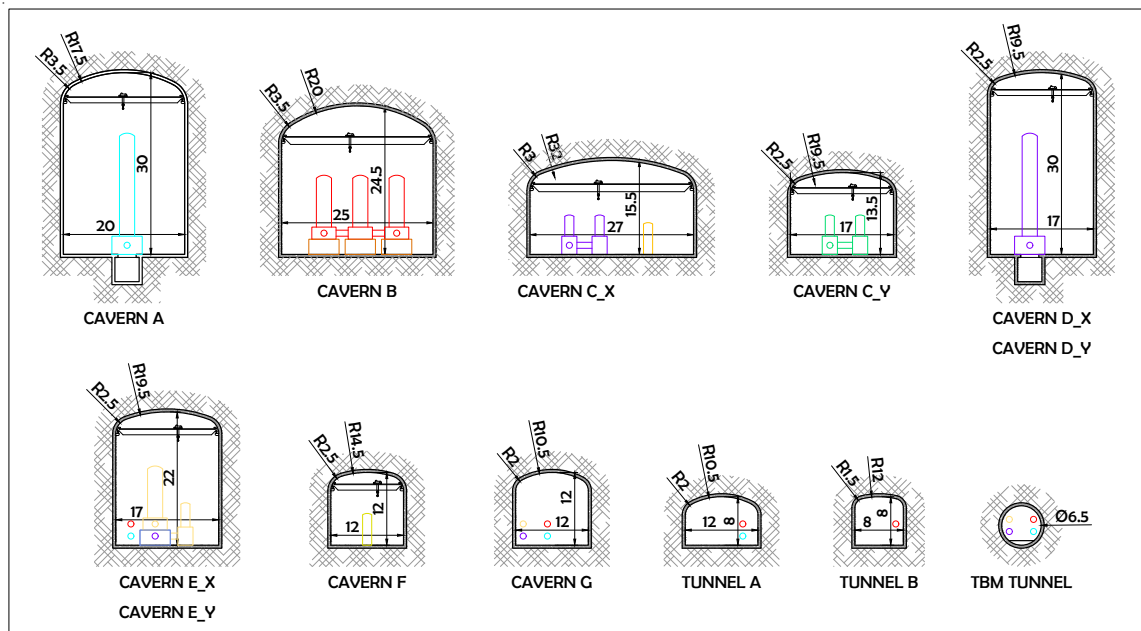


Figure 7.16: Sizes of Caverns.

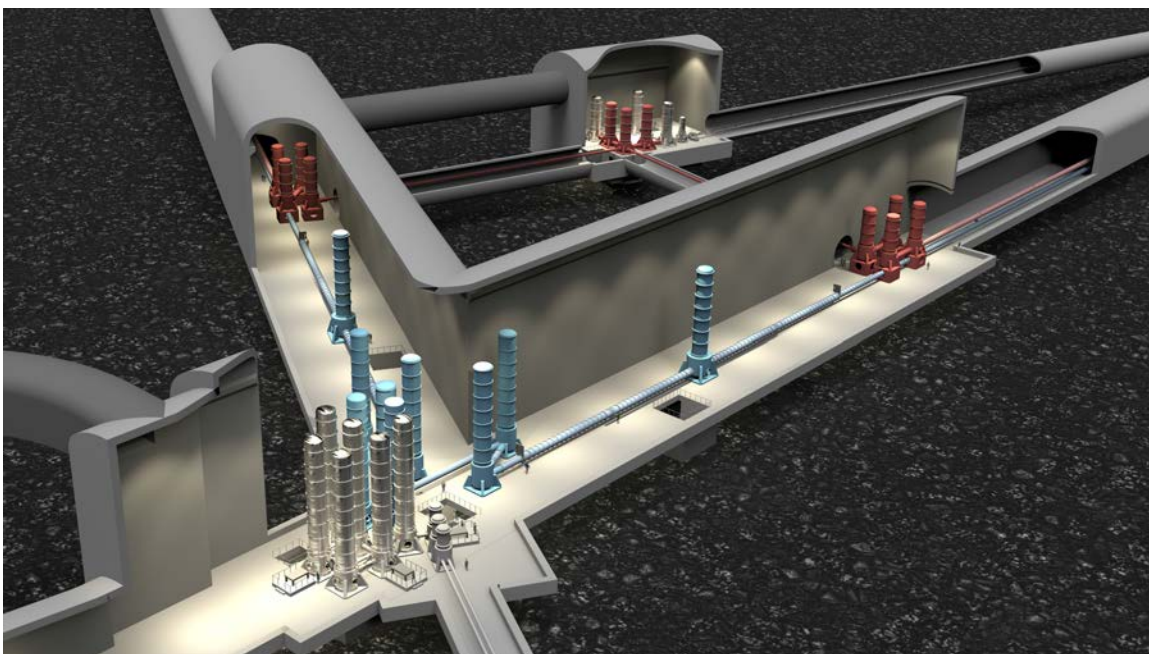


Figure 7.17: CAD rendering of the corner station with the tall suspension towers of ET-LF (blue) and ET-HF (red)

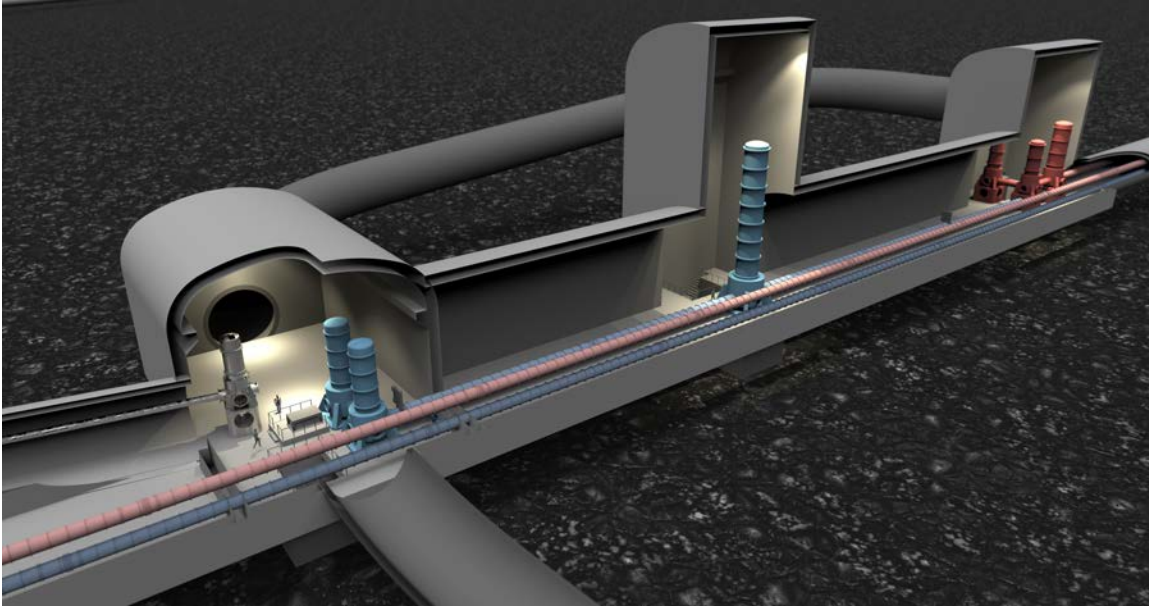


Figure 7.18: CAD rendering of the cavern assembly C-E.

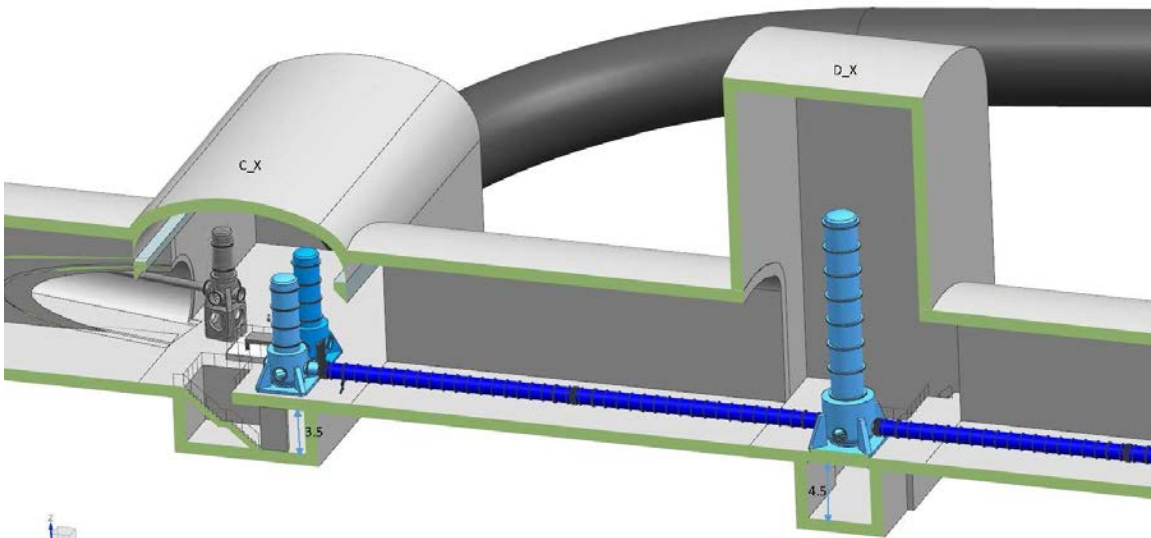


Figure 7.19: CAD rendering of the caverns C and D. The cut-off view shows the access basement underneath the vacuum towers. Cavern C also contains the vacuum tank of the ET-HF filter cavity (grey).

### 7.3.1.3 Tunnels

The corner stations of the ET triangle will be connected by tunnels of ca. 9.5 km length, see figure 7.7 accommodating four vacuum beam pipes: two for the high- and two for the low frequency interferometers (see figure 6.19). Due to the length of the tunnels, a mechanised excavation method utilising Tunnel Boring Machines (TBMs) is considered for the design stage. It is envisaged to excavate the whole length of the tunnel in one stretch without further points of intermediate access. The inner diameter will be 6.5 m, needed to host 4 vacuum pipes, which must be straight to several cm (and not follow Earth's curvature). The outer diameter could vary in a range between 7.3 m and 8.4 m depending on the type of TBM excavation (shielded or open TBM) and consequently by the lining type of the excavated tunnel (segmental pre-cast or shotcrete lining). The concept of the shielded TBM (see figure 7.20) type considers a continuous process with parallel installation of a segmental lining, which takes over the support of the rock mass. A single-layer segmental lining with all-rounded preformed elastomer gaskets would be used to control water inflow to the tunnel. The thickness of the reinforced concrete segments depends on the geotechnical conditions and may be up to 30 cm.

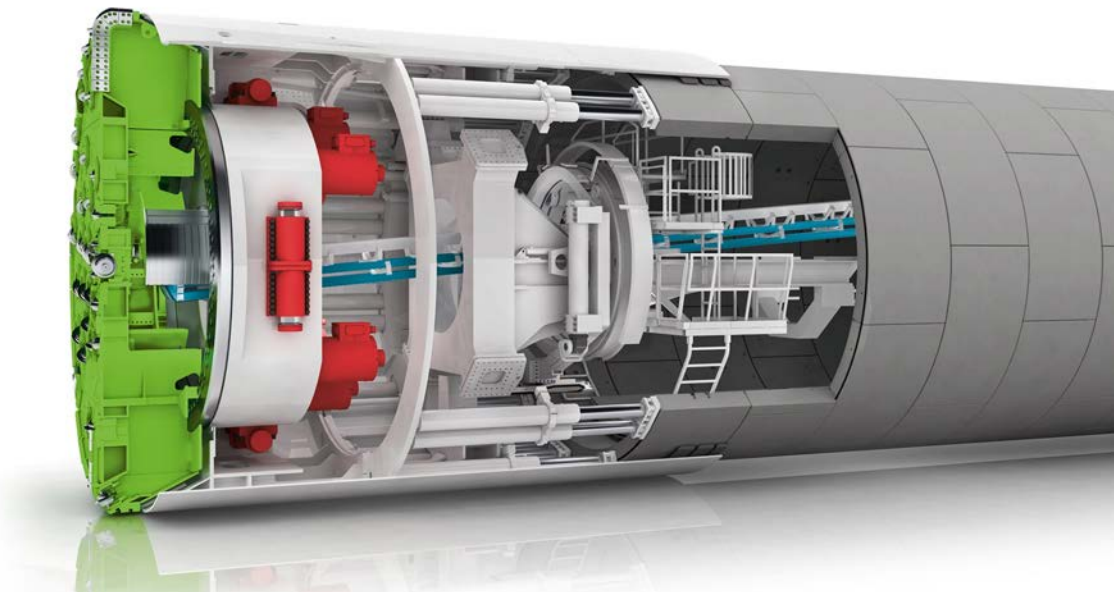


Figure 7.20: Single-shielded tunnel boring machine.

Source: <https://www.herrenknecht.com/en/products/productdetail/single-shield-tbm/>, 12.08.2020

Contrary to a shielded TBM, the open TBM (see figure 7.21) is based on applying shotcrete, steel ribs (if required) and rock bolts. As part of the excavation concept, local rock mass grouting is considered, to decrease the overall inflow of groundwater to the tunnel, since the shotcrete support is more prone to water inflow. The overall thickness of the shotcrete support layers is also of the order of 30 cm thick consisting of two layers.

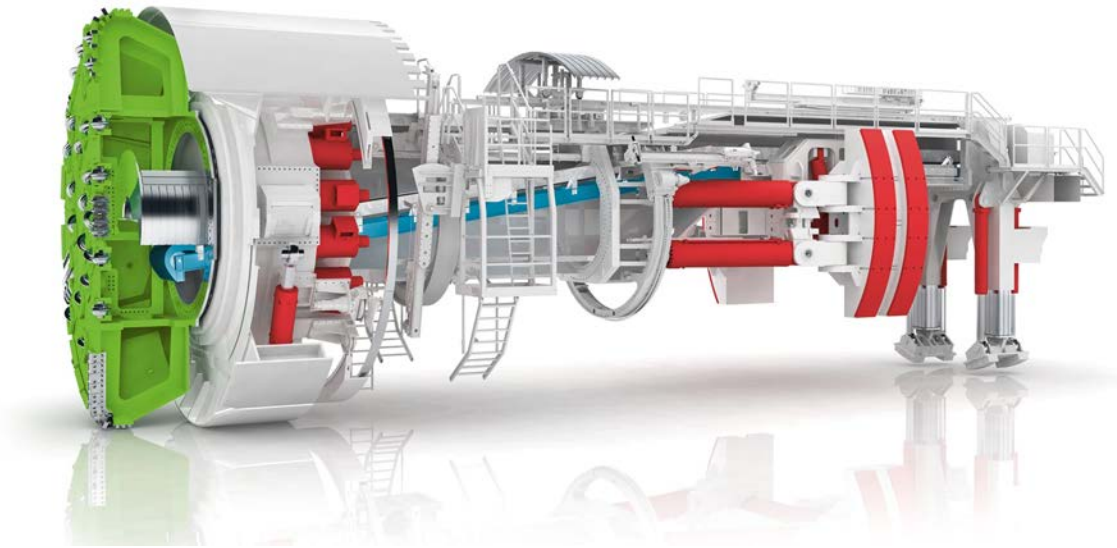


Figure 7.21: Open (Gripper) tunnel boring machine.

Source: <https://www.herrenknecht.com/en/products/productdetail/gripper-tbm/>, 12.08.2020

Regardless of the straight direction demanded for the subsequent installation of the vacuum pipes in the tunnels, the TBM excavation implies an inherent meandering of the tunnel axis as a reaction to heterogeneous geological conditions while driving. In the open TBM case part of the unavoidable meandering of the TBM can be corrected with a small excavator drum cutter (down to 10 cm) before applying the shotcrete. With segmental lining directly applied by the TBM in the boring process this is not possible and the undulation width has to be added as a margin to the tunnel radius to achieve a free inner diameter of 6.5 m around a straight line for accommodating the vacuum tubes. Furthermore the segmented lining requires an annulus gap of another 15 cm.

Tunnel construction can be done with two TBMs (one of them being refurbished after having drilled 10 km of tunnel) or with three TBMs from the beginning, resulting in an earlier completion. Depending on the number of TBMs, the lining option and vertical access shaft vs. inclined access tunnel, the construction time for tunneling varies between 5.4 years and 8.6 years and between the cheapest and the most expensive option costs vary by +/- 5% around the mean.

For removing water collected a minimal slope of the tunnels of 1/1000 is considered necessary. In a triangle with two tunnels having a slope of 1 ‰ this means that the third tunnel has to have a slope of 2 ‰. In order to minimise contributions to seismic noise the pumps needed to bring the collected water to the surface will be placed about 1 km away from the detectors at the end of de-watering tunnels, as indicated in figures 7.8 and 7.7. The anticipated cumulative inflow to the tunnel complex will be based on hydrogeological site investigations and will determine the need of local grouting operations, the capacity and dimensions of the pumps, and the dimensions of the de-watering borehole. Further, long-term drainage of the rock mass may cause surface subsidence, permanent water table changes (depending on the recharge and permeability of the overlying rock

types) and the need for an environmental friendly disposal or use. The latter issues will be addressed after the site selection procedure as part of the environmental impact report.

The main tunnels will have an inner diameter of 6.5 m. Depending on the lining concept, shotcrete vs. segmental lining, an outer tunnel diameter of 7.3 m or 8.4 m is needed. In the shotcrete lining case unavoidable undulations (assumed to be 50 cm) of the TBM around the intended straight line can be corrected

Connection tunnel sizes are given in figure 7.22. All tunnel diameters will be large enough to allow transporting equipment through them for future upgrades.

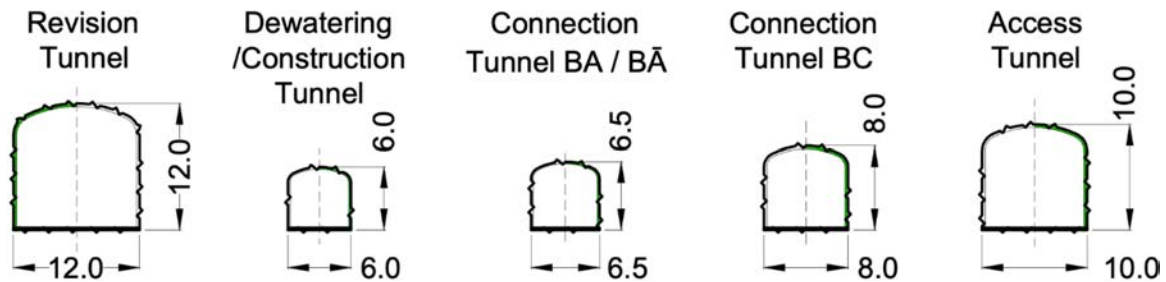


Figure 7.22: Sizes of connection tunnels. Image source Implenia.

In its final form the observatory will have more than 35 km of total tunnel length (disregarding inclined access ramps). The estimated excavation volume depends on the excavation and support methodology and ranges between 2,6 to 3,6 million m<sup>3</sup>. Detailed analysis of the usability of the excavation material as, for example, concrete aggregates are currently ongoing. It is anticipated that a part of the excavation material can be reused for construction purposes (i.e. in form of concrete aggregates). The remaining part needs to be disposed of. Disposal and transport of excavation material from the corner points to a potential disposal may pose an environmental perturbation, requires temporary infrastructure, the acceptance of the local population and has to follow regional environmental specifications and standards. Currently a variety of options are considered which include, for example, a disposal in abandoned mines using temporary railways or existing roads. Whether the excavated rock need further treatments due to chemical contamination depends on the excavation methods (i.e. explosives used for drill and blast excavations). The above topics will be addressed in the environmental impact report and require close collaboration with the local population and authorities. We anticipate that we need vacuum pumping stations along the 10 km arms spaced at intervals of ca. 500 m and gate valves at intervals of several kilometres (see section 6.12.1. Small pumping station caverns will be needed as sketched in figure 6.22. In addition, the tunnel houses the services for electricity, water, compressed air, cryogenics, safety systems and air conditioning.

During the construction of ET, the tunnel will be equipped with a system to transport sections of vacuum beam pipes to the welding and installation area. Later, this system can be converted to a personnel transport system. For safety reasons the tunnel is divided into 500 m sections that are equipped with fire retarding doors, and safety shelters. The tunnel is equipped with a safety system that allows control of the airflow in order to direct smoke in case of a fire.

During construction and operation the whole infrastructure has to be equipped with clean, conditioned air (see also section 7.1.2.4). Ventilation demands are clearly much higher during construction. A

preliminary analysis for this phase suggest a ventilation system with ca.  $20\text{ m}^3/\text{s}$  at 35 hPa with a single 1.6 m diameter ventilation tube.

During operation environmental condition will be continuously monitored and maintained at safe levels by the ventilation system. Combining the need for a minimum air exchange rate and simultaneously maintaining the quiet underground infrastructure conditions is a challenge.

Safety and health will have the highest priority during every stage of the planning, design, construction, and operation of the observatory following international safety requirements and rules. Particular attention has to be paid to key areas such as underground communication, ventilation, access, emergency egress and refuge design. During the construction of the subterranean infrastructure, the safety of both engineering and scientific personnel has to be ensured.

## 7.4 Surface facilities

The construction of the ET observatory will include a surface infrastructure formed by technical and general buildings needed for the control, maintenance and operation of the research facility.

The surface buildings will be located mainly in correspondence of the access points to the underground infrastructure and may include also intermediate stations located along the alignments of the tunnels according to the needs agreed during the final design stage for supporting safety and operational issues.

The buildings identified at this stage of the project include sheds and laboratories necessary during the construction and for the installation of instruments that is warehouses, clean rooms, mechanical and electrical workshops, control rooms, technical buildings for plants, visitor centre and access buildings to the underground labs.

A relevant issue is represented by the interference of the surface facilities with the existing transportation and technology networks. This aspect is strongly dependent on the location of the site in proximity of urbanized areas or in extra-urban areas and will be thoroughly addressed during the site proposition phase after the requirements for construction approach, power supply and water supply and drainage will be established.

### 7.4.1 Road network

A dedicated analysis will be conducted to assess the characteristics of the existing transportation network in terms of loads and geometry in order to estimate the feasibility and the required efforts for its integration or upgrading.

In relation to the needs of connecting the different surface facilities a road network will be designed within the internal area. Connection links with the existing road network will be initially setup for the construction stage (material and instrument transportation, ground movement, etc.) and then to guarantee accessibility to the site during operation.

### 7.4.2 Visitor centre

Similarly to large research infrastructures such as CERN and EGO, a visitor center is considered essential to illustrate the technological advancements setup for the built-up of the ET infrastructure and to promote the scientific innovation foreseen with the GW research field.

The center will be preferably located in proximity of one of the tunnel entrances to welcome the general public as well as groups of students and teachers. Experts and trained personnel will provide descriptive and scientific contents through a mix of multimedia tools, simulators and mockups.

The historical background leading to ET, including a focus on the way science can rapidly progress through it, will be presented adopting a modern museum approach.

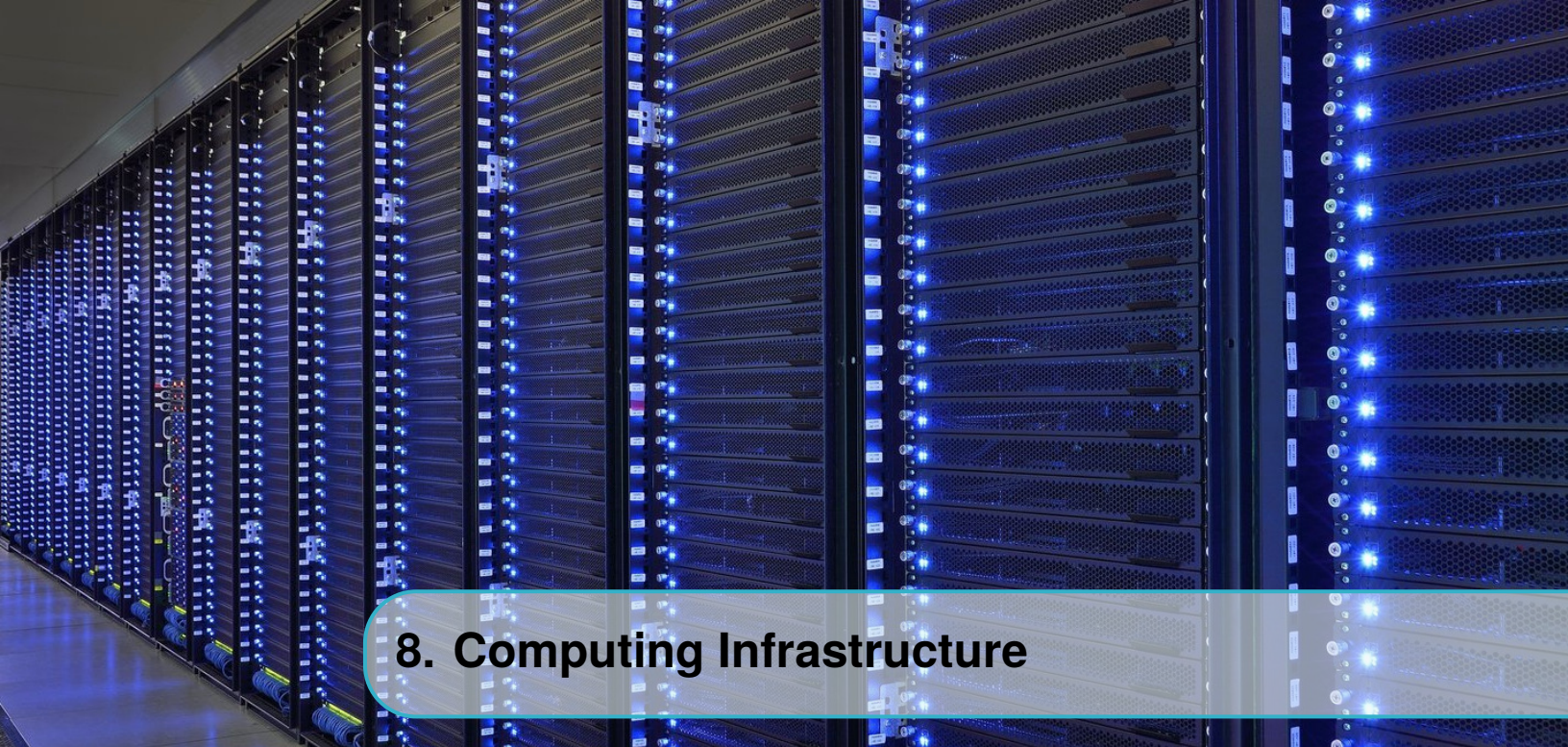
In addition to exhibition halls, the center will also host an auditorium for conferences (in person or remote), rooms for workshops and training sessions.

### 7.4.3 Environmental impact

During the preliminary design stage of the facility, major attention will be devoted to the assessment of the environmental impact in the area of interest and to the definition of mitigation actions considering the existence of landscape and urban constraints. These analyses will be supported by a team of environmental engineers and landscape architects that will share the approach with the local and national authorities.

A relevant issue for the environmental impact that also has a major impact on the feasibility and costs of the construction is the disposal of the waste and/or re-location of the excavation materials.

Different scenarios can be defined in consideration of the material typology that include, re-using, deposition or selling. It should be mentioned that a large part of the excavated material will be classified as contaminated and should be treated following the environmental regulations.



## 8. Computing Infrastructure

As with most large experiments, the scale of ET computational challenges is such that the computing infrastructure cannot be solely based on local resources. The physics community at large has a long experience in designing, building and managing global-scale computing infrastructures that can be exploited to cater to these needs. This section deals with the design of such an infrastructure dedicated to the search for GW sources with the ET, and the generation and distribution of triggers for multi-messenger astronomy. An in-depth discussion of the upcoming computing challenges for the 3G era has been done by the GWIC 3G Computing Subcommittee [582]; in the following we will focus mostly on the design of the ET computing infrastructure. As will be clear, the exact size of the computing power for ET data analysis cannot be trivially extrapolated from those of second-generation infrastructures; it is however already possible to delineate what the needs will be in terms of services.

### 8.1 Computing challenges and strategies

Even with its 6-interferometers design ET will not, even by today's standards, generate a huge data volume with respect to the 1PB of data per year produced by a 2G interferometer. For comparison, in 2018 (the final year of Run 2) the Large Hadron Collider at CERN produced 110 PB of scientific data, and is scheduled to double that figure (on average) during Run 3 (2021-2023). Even taking into account a much larger number of control channels (which however may just be stored in a circular buffer on-site and not necessarily exported for safekeeping) we should be well within the technical and funding capabilities in the ET timescale. It is the quantity of valuable scientific information hidden in the data that will grow, and with it the amount of computational power needed to extract it. Factoring in the expected technological developments in computing hardware (Moore's law is starting to fail for CPU performance, whereas its network capacity equivalent is not, see below), it turns out that data management will most likely not be an outstanding issue; computing power itself, however, will be challenging.

### 8.1.1 Data analysis challenges

As an example of the expected computational challenges, we will briefly discuss the first and possibly major one (at least with respect to the Advanced Detector era): the detection of Compact Binary Coalescences.

CBC events are currently detected by template-based matched-filtering (see, for example, the PyCBC analysis pipeline [583]). With this technique, the data time series is superimposed with templates generated by Numerical Relativity simulations, until a satisfactory match is found. Matched filtering technique essentially obtains the maximal value of the SNR corresponding to the template that best matches the signal buried in the data. It represents a grid of theoretical waveforms (templates) placed on the space of parameters, each point on the grid being associated with a specific set of parameters. The density of templates is chosen so that one loses no more than a tiny fraction of signals as a result of working with a discrete grid. The lower frequency cutoff implies a larger parameter space to explore, and the possibility to detect longer signals, possibly up to whole days. As a consequence, the template libraries to be generated and used will grow both in number (the number of templates required grows as a strong power of the lower frequency cutoff) and length of the templates. Thus, the computing power needed grows dramatically with the detector sensitivity, even if the workload is easily parallelisable<sup>1</sup>. It is unclear whether this technique will still be adequate for ET data; to mention just two examples, the longer templates are very expensive in terms of memory, and there is no experience in working with overlapping signals, which will be a distinct possibility.

After the candidate event is detected, the binary system's parameters are today extracted using Bayesian inference. This technique relies on much less parallelisable algorithms and the computing power scales linearly with the detection rate, that is expected to grow by 3 orders of magnitude with respect to 2G detectors: as a more precise example, a recent study [584] has predicted that the Einstein Telescope will detect on the order of 60,000 binary neutron star mergers per year (assuming an 80% duty cycle). If ET were to operate in coincidence with the proposed 3G GW detector Cosmic Explorer in USA the detection rate would increase by about a factor of 10, thereby meaning a binary neutron star merger observed every minute. On top of that, the run time for an event's parameter estimation varies from algorithm to algorithm and from source to source, generating latencies that may be unacceptable for the ET science goals.

Both unmodeled burst source and continuous wave searches scale essentially with the amount of data collected (i.e. with the number of interferometers and their observing time) and not with the sensitivity, so their computing requirements for 3G will not explode like the ones for CBC events. However, all-sky searches for continuous wave signals will still be limited by the available computing power.

To sum it up: even not taking into account complications such as the analysis of day-long signal candidates, for which the detector moves with respect to the source, or the more ambitious continuous wave searches, a naive extrapolation from current activities gives an increase of *at least* three orders of magnitude in computing power from 2G to 3G data.

This is out of reach, but a number of mitigation actions will be planned, exactly like what is being

---

<sup>1</sup>In computing jargon, workloads that can be trivially split into smaller tasks that are completely independent are referred to as being “embarrassingly parallel”.

done today in the HEP community for High-Luminosity LHC. These will include the exploitation of available hardware and software technologies, such as hardware accelerators or Artificial Intelligence algorithms, and intense R&D activities in the fields of search and analysis pipelines.

### 8.1.2 Low-latency infrastructure

As described in sec. 3, multi-messenger astronomy is one of the major science goals of the ET.

The cooperation between GW interferometers, land- and satellite-based EM and neutrino observatories relies on the timely and reliable distribution of candidate triggers, event information and data segments.

Triggers are generated by running search pipelines on data as they are taken; as soon as a candidate is detected, the alert needs to be distributed and the relevant information stored in a public database. With 2G infrastructures, these searches are run on-site on dedicated facilities, but this might not be possible with ET data, given both the expected data rate and the challenges described above; also the system will need to be completely automated. Thus, also low-latency searches might run on external shared facilities, as the alert generation and distribution services.

Another challenge will be to cope with so-called “negative latency alerts”. It will often be possible for the ET to identify the signal from merging binary systems, and possibly complete a rapid parameter estimation, *before* the objects merge, to allow EM observatories to point the telescopes to the right sky location on time to observe the merger, clearly a great breakthrough for multi-messenger astronomy.

The large event rate and such new challenges will call for a complex set of services: to distribute data to computing centres reliably and with very low latency, to manage the search jobs, to collect result and generate alerts, with next to null need for human supervision. Also, an integrated reliable database service will serve as a repository that contains and describes the events detected by ET and by the other GW partners.

### 8.1.3 Computing strategies

The challenges described above will call for intense R&D activities during the design and implementation phases.

Simple technological progress on CPUs will not help much, with an estimated price/performance ratio reduction of less than 15% per year [585]. In order to reconcile the huge computing power needed and the available resources, even in the long ET timescale, the community will need to work on several research lines:

- the development of novel signal detection algorithms, and the optimisation of existing ones. In-depth discussion of this topic is outside the scope of this chapter, but most of the existing code (mostly the pipelines used for offline analyses) is not optimised for performance, having been developed in an environment with little resource contention;
- the exploitation of modern hardware accelerator technologies, such as GPUs, FPGAs or whatever will be introduced on the market in the next years. Already some analysis pipelines successfully run on GPUs, but the performance improvements that are being delivered by both increased CPU parallelism and co-processors are becoming more complicated to exploit

in software, and much effort will be needed to usefully parallelise the code. Non-trivial parallelisation will also be a prerequisite for successfully exploit High-Performance Computing facilities, which will be the backbone of future Exascale infrastructures.

- the exploitation of modern software technologies, such as Artificial Intelligence, Deep Learning and more. Already several projects are exploring the use of Machine Learning algorithms for different aspects of GW data processing (see for example [586] or [587]), but much research is needed both to successfully use such technologies and to gain confidence in their application;
- finally, given the ET timescale, novel technologies such as Quantum Computing or dedicated ML processors such as the Google Tensor Processing Unit may play some role, but also this will need intense R& activities.

This will both require the planning of a series of Mock Data Challenges[582], using the version of the software, tools and e-infrastructure available at any time, and the building of a community of experts that are neither pipeline developers nor IT experts, but scientific computing professionals [588].

## 8.2 On-site computing infrastructure

As mentioned above, in this model most of the computing, both in terms of data processing and services, might run off-site on shared infrastructures. There are however at least three tasks that need to be performed on-site:

- detector and environmental control;
- data acquisition, reduction and pre-processing, to reduce the data to the size and format suitable for transfer;
- data buffering to allow for inefficiencies in shipping the data to off-site storage and processing facilities.

Except for computing power located very close to the instrumentation, acting as front-end for detector control and data acquisition, most of the needs can be catered to by a conventional Computing Centre on-site, providing storage (a size of several tens of PBs should not be an issue given the timescale) and different levels of service for computing. For example, a private Cloud infrastructure can be used to flexibly provision computing servers, probably with a Platform-as-a-Service deployment model [589].

Of course different needs may emerge in the design phase. For example, Machine Learning technologies may be used for some aspects of data preparation. ML algorithms are currently being explored for example for glitch detection; if such technologies will be used for detector control, specific computing resources such as GPU-powered farms for algorithm retraining may be needed.

## 8.3 Global computing infrastructure

Before and during the current 2G era, distributed computing activities have been mostly driven by LHC requirements, that ultimately led to the design and deployment of the Worldwide LHC Computing Grid (WLCG) infrastructure. Within the time frame of the ET initial phases, several other collaborations will reach LHC-like sizes both in data sample size and computing power requirements:

SKA and CTA, for example, but also outside of physics with, for example, the Human Brain project. Furthermore, planned High Luminosity LHC runs will increase both its data volume and computing requirements by large factors.

We therefore expect that a large scale shared European computing infrastructure will be available to meet the needs of all these collaborations; indeed, several R&D projects already exist or are being proposed to develop the tools to build such an infrastructure. We plan to use the services offered by the European Open Science Cloud as much as possible, since the ET requirements will represent only a fraction of the computing activities that will be undertaken in Europe. Given the current plans, we expect such an infrastructure to have a “Data Lake” architecture, in which storage sites with high-bandwidth connectivity feed data to large High Performance Computing (HPC) and High Throughput Computing (HTC) facilities that will provide the computing power. Also, Cloud Computing facilities should be available to deploy complex networks of interconnected services on a Platform-as-a-Service model [589], with higher-level orchestration tools to provide, for example, high-availability or scalability to deployed services.

A bird’s view of a very preliminary ET Global Computing Infrastructure is given in fig. 8.1. It is based on the current model adopted by the Virgo and LIGO collaborations, adapted to the different scale and and complexity of the ET.

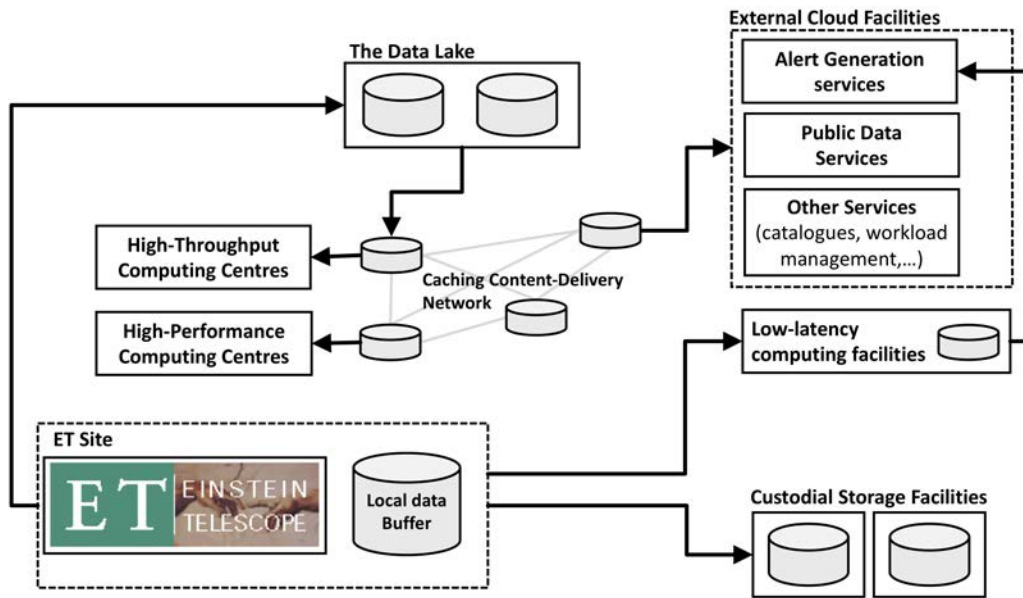


Figure 8.1: A simplified view of a preliminary Global Computing Infrastructure for the Einstein Telescope.

1. Data are collected at the ET site and stored in a local circular data buffer. The local computing infrastructure is used to pre-process and reduce the data to the format that will be used for low-latency and offline analyses;
2. Processed data to be used for low-latency searches are transferred to the low-latency search facilities, where search pipelines are automatically run;
3. in parallel, pre-processed data are shipped to the Data Lake for subsequent offline analyses.

- Depending upon the performance of the Data Lake, it may be possible also for the low-latency processing sites to exploit it, thus reducing the complexity of the system and the amount of data to be transferred;
4. again in parallel, a (somewhat reduced) version of raw data are transferred to archival sites for safekeeping; again, custodial-grade storage may be a feature of the Data Lake, further simplifying the picture;
  5. all data (raw, processed, public) is registered in a general catalogue database that functions as a single front-end both for data discovery and access;
  6. low-latency processing facilities run search pipelines and send triggers and candidate event information to the low-latency alert generation and distribution services.
  7. candidate event alerts are generated and distributed by the relevant services. Many, if not all, such services can run on Cloud facilities, for flexibility and reliability. Data segments to be distributed with the alert are not copied again but tagged in the database as “public”;
  8. offline analyses (parameter estimation, deep searches etc.) and all scientific computing (numerical relativity simulation, Machine Learning model training, etc.) are run on available HTC, HPC or even “Big Data” facilities optimised for Machine Learning, depending upon the optimal type of technology;
  9. publicly released data are not copied again, but tagged in the database and made available through public discovery and access services.

Most of the GW computing workloads are embarrassingly parallel, and so well suited to be run on conventional high-throughput distributed infrastructures, with the notable exception of the numerical relativity simulations used to prepare the template libraries. Several currently used analysis pipelines, and Deep Learning algorithm training, can profit from the use of GPUs and hardware accelerators. The exact mix of architectures needed will depend upon what will be available in ten years from now both in terms of computing technology and GW data analysis techniques.

Some of the services that will form the framework for the ET Distributed Computing Infrastructure will come from the EOSC (or its heir), or will be an evolution of existing services; anything that does not need to be run close to the experiment can and probably will be deployed on shared resources for flexibility and reliability. The level of abstraction that will be used to deploy the ET services will depend upon the maturity of the shared services provided by the shared infrastructure. For example, the Public Data distribution system may just be a part of a more general Virtual Observatory environment run by an external entity, a federated instance of a common service provided by the shared infrastructure or a separate service built by the ET community from building blocks provided by the infrastructure as microservices.

Thus, the services that will be needed to build the ET global e-Infrastructure will include:

- archival storage services, managing the storage of non-reproducible data duplicated over several data centres offering custodial-level storage facilities and providing interfaces for easy retrieval of missing data;
- data management services to timely and reliably transfer raw data from the ET local storage buffer to the relevant external data centres: custodial storage facilities, Data Lake centres, low-latency processing facilities etc. They need to provide functionalities for automatic issue detection and data loss recovery;
- network services, provided by National Research and Education Networks (NREN), and Géant,

possibly with dedicated links between the ET site and the core data centres, for stability and performance. It will be interesting to explore the possibility of having a network environment similar to the LHC Open Network Environment (LHC-ONE) [590]. This would simplify security management, performance monitoring and streamline the interfacing to the General Public Network;

- a Data Distribution infrastructure based on the concept of Data Lake (a federated set of high-performance dedicated storage sites) and a cache-based Content Delivery Network (CDN). This will probably be the architecture of choice for the future WLCG data distribution infrastructure, and is being prototyped in the context of the ESCAPE project [591]. StashCache [592], a similar existing infrastructure deployed and managed by the Open Science Grid in the US, is already being used to distribute LVC data to computing centres world-wide;
- heterogeneous, distributed HTC and HPC resources and services in a set of core data centres and a network of other resource providers, with cloud-like access and linked to the data distribution network;
- a common Authentication and Authorisation Infrastructure, based on trusted Identity Providers (IdPs) and an ET authorisation service, federated with the equivalent for existing 2G and other 3G collaborations;
- cloud resources, with Platform-as-a-Service orchestration tools, to deploy the experiment's specific services (such as the ones comprising the public alert generation system, but also higher-level ones, such as databases, data catalogues or software repositories) with high-availability and scalability features provided by the infrastructure;
- an Open Data platform for general release of public data, compliant with FAIR<sup>2</sup> principles, evolution of the existing GWOSC [594] and integrated with the Virtual Observatory platforms that will be available, such as the one being developed by the ESCAPE project.

---

<sup>2</sup>Findable, Accessible, Interoperable, Reusable. See [593]



Thanks !

With kind permission of:

Gratefully received from:

Credit to:

Very much appreciated

With the help of:

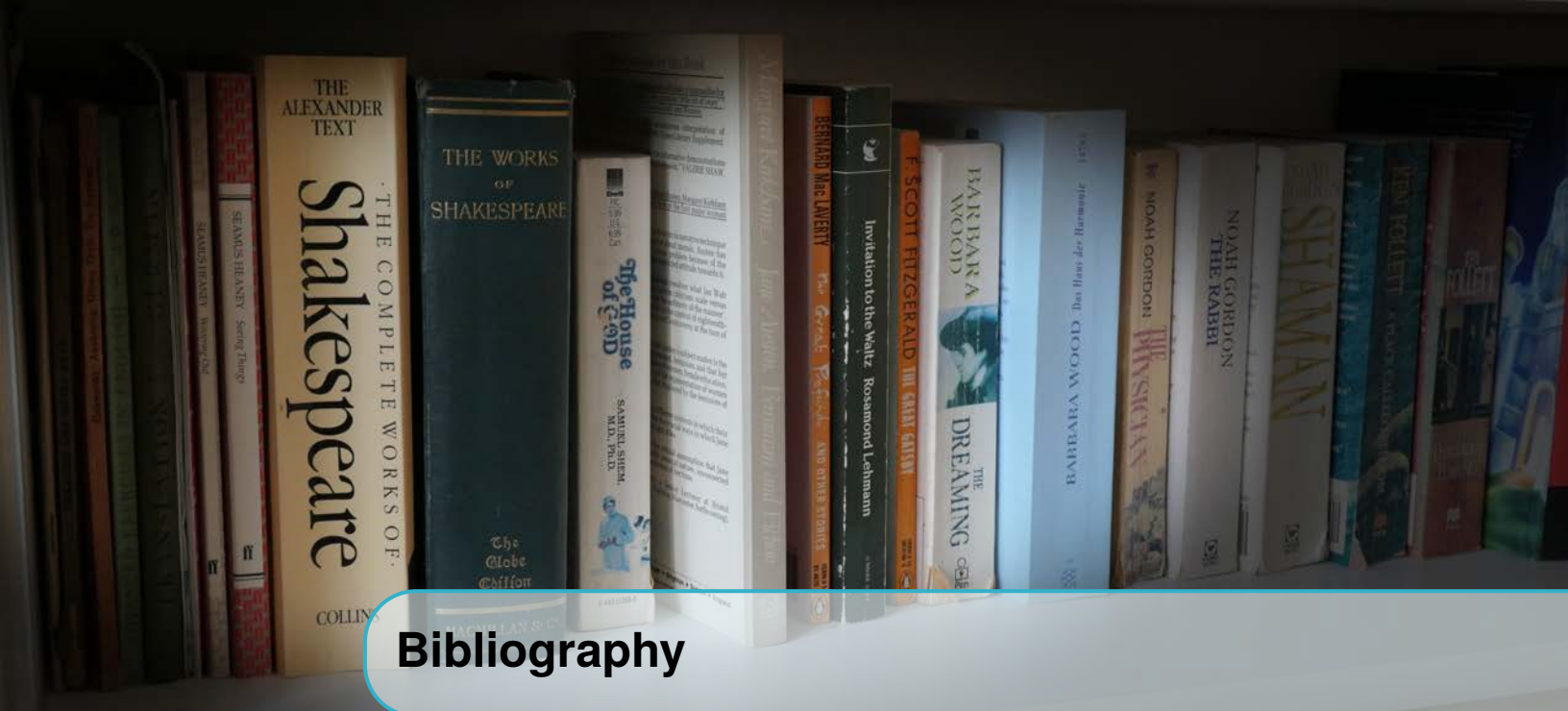
Kindly provided by:

Produced by:

## Image credits

- Cover image: Marco Kraan (Nikhef)
- Chapter headings:
  - Table of Content: Harald Lück, (Leibniz Universität Hannover and Max-Planck
  - list of figures: Elke Müller (Max-Planck Institute for Gravitational Physics)
  - list of tables: <https://pxhere.com>, creative commons license Institute for Gravitational Physics)
  - Chapter Introduction 1: Marco Kraan (Nikhef)
  - Part I Science Case Chapter
    - \* Chapter Introduction 2: Numerical Relativity Simulation: T. Dietrich (Max Planck Institute for Gravitational Physics) and the BAM collaboration
    - Scientific Visualization: T. Dietrich, S. Ossokine, H. Pfeiffer, A. Buonanno (Max Planck Institute for Gravitational Physics)
  - \* Chapter Astrophysics 3
  - \* Chapter Fundamental Physics and Cosmology 4
  - \* Chapter Summary of Key Science Objectives 5
- Part II Detector 6:
  - \* Chapter Detector 6: The Virgo Collaboration
  - \* Chapter Site and Infrastructure 7: Marco Kraan, Nikhef
  - \* Chapter Computing Infrastructure 8: AEI/Armin Okulla, s.a. <https://www.aei.mpg.de/25950/computer-clusters>
- Chapter Introduction 1:
  - \* figure 1.2
  - \* 1.1 Harald Lück (Leibniz Universität Hannover and Max-Planck Institute for Gravitational Physics)





## Bibliography

- [1] F. Sorrentino, “The advanced virgo interferometer,” in *2016 IEEE Metrology for Aerospace (MetroAeroSpace)*, pp. 251–254. 2016.
- [2] B. S. Sathyaprakash et al., “Cosmology and the Early Universe,” *arXiv* (2019) N/A, arXiv:1903.09260 [astro-ph.HE].
- [3] GWIC 3G Committee, the GWIC 3G Science Case Team, and the International 3G Science Team Consortium, “3G Science Book,” 2020.
- [4] M. Maggiore, *Gravitational Waves. Vol. 2. Astrophysics and Cosmology*. Oxford University Press, 848 p, 2018.
- [5] Jocelyn S. Read, Luca Baiotti, Jolien D. E. Creighton, and others, “Matter effects on binary neutron star waveforms,” *Phys. Rev.* **D88** (2013) 044042, arXiv:1306.4065 [gr-qc].
- [6] B. S. Sathyaprakash et al., “Extreme Gravity and Fundamental Physics,” 2019.
- [7] Enis Belgacem, Yves Dirian, Andreas Finke, Stefano Foffa, and Michele Maggiore, “Nonlocal gravity and gravitational-wave observations,” *JCAP* **1911** (2019) 022, arXiv:1907.02047 [astro-ph.CO].
- [8] E. Belgacem, Y. Dirian, S. Foffa, and M. Maggiore, “Modified gravitational-wave propagation and standard sirens,” *Phys. Rev.* **D98** (2018) 023510, arXiv:1805.08731 [gr-qc].
- [9] Daniele Bertacca, Alvise Raccanelli, Nicola Bartolo, and Sabino Matarrese, “Cosmological perturbation effects on gravitational-wave luminosity distance estimates,” *Phys. Dark Univ.* **20** (2018) 32–40, arXiv:1702.01750 [gr-qc].
- [10] Jose J. Blanco-Pillado, Ken D. Olum, and Jeremy M. Wachter, “Gravitational backreaction simulations of simple cosmic string loops,” *Phys. Rev.* **D100** no. 2, (2019) 023535, arXiv:1903.06079 [gr-qc].

- [11] Larissa Lorenz, Christophe Ringeval, and Mairi Sakellariadou, “Cosmic string loop distribution on all length scales and at any redshift,” *JCAP* **1010** (2010) 003, arXiv:1006.0931 [astro-ph.CO].
- [12] Kieran Craig, Jessica Steinlechner, Peter G. Murray, and others, “Mirror coating solution for the cryogenic einstein telescope,” *Phys. Rev. Lett.* **122** (Jun, 2019) 231102. <https://link.aps.org/doi/10.1103/PhysRevLett.122.231102>.
- [13] Eleonora Capocasa, Matteo Barsuglia, Jérôme Degallaix, and others, “Estimation of losses in a 300 m filter cavity and quantum noise reduction in the kagra gravitational-wave detector,” *Phys. Rev. D* **93** (Apr, 2016) 082004. <https://link.aps.org/doi/10.1103/PhysRevD.93.082004>.
- [14] M Mehmet and H Vahlbruch, “High-efficiency squeezed light generation for gravitational wave detectors,” *Classical and Quantum Gravity* **36** no. 1, (Dec, 2018) 015014. <https://doi.org/10.1088%2F1361-6382%2Faaaf448>.
- [15] J. Peterson, “Observations and modeling of seismic background noise.” Open-file report 93-322, 1993.
- [16] F Badaracco and J Harms, “Optimization of seismometer arrays for the cancellation of Newtonian noise from seismic body waves,” *Classical and Quantum Gravity* **36** no. 14, (Jun, 2019) 145006. <https://doi.org/10.1088%2F1361-6382%2Fab28c1>.
- [17] B. Abbott et al. (LIGO Scientific Collaboration), “LIGO: the Laser Interferometer Gravitational-Wave Observatory,” *Reports on Progress in Physics* **72** no. 7, (2009) 076901. <http://stacks.iop.org/0034-4885/72/i=7/a=076901>.
- [18] F Acernese et al., “Status of Virgo,” *Classical and Quantum Gravity* **25** no. 11, (2008) 114045 (8pp). <http://stacks.iop.org/0264-9381/25/114045>.
- [19] **VIRGO** Collaboration, F. Acernese et al., “Advanced Virgo: a second-generation interferometric gravitational wave detector,” *Class. Quant. Grav.* **32** no. 2, (2015) 024001, arXiv:1408.3978 [gr-qc].
- [20] The LIGO Scientific Collaboration, “Advanced ligo,” *Classical and Quantum Gravity* **32** no. 7, (2015) 074001. <http://stacks.iop.org/0264-9381/32/i=7/a=074001>.
- [21] B. P. Abbott et al., “Observation of Gravitational Waves from a Binary Black Hole Merger,” *Phys. Rev. Lett.* **116** no. 6, (2016) 061102, arXiv:1602.03837 [gr-qc].
- [22] Charlotte Bond, Daniel Brown, Andreas Freise, and Kenneth A. Strain, “Interferometer techniques for gravitational-wave detection,” *Living Reviews in Relativity* **19** no. 1, (Feb, 2017) 3. <https://doi.org/10.1007/s41114-016-0002-8>.
- [23] J. Mizuno, K.A. Strain, P.G. Nelson, and others, “Resonant sideband extraction: a new configuration for interferometric gravitational wave detectors,” *Physics Letters A* **175** no. 5, (1993) 273 – 276. <http://www.sciencedirect.com/science/article/pii/037596019390620F>.
- [24] Anna-Maria A. van Veggel, “Quasi-monolithic mirror suspensions in ground-based

- gravitational-wave detectors: an overview and look to the future,” *Philosophical Transactions of the Royal Society A: Mathematical, Physical and Engineering Sciences* **376** no. 2120, (2018) 20170281,  
<https://royalsocietypublishing.org/doi/pdf/10.1098/rsta.2017.0281>.  
<https://royalsocietypublishing.org/doi/abs/10.1098/rsta.2017.0281>.
- [25] B.S. Sathyaprakash and Bernard F. Schutz, “Physics, astrophysics and cosmology with gravitational waves,” 2009. <http://www.livingreviews.org/lrr-2009-2>.
- [26] G. Hammond and S. Rowan, “Thermal noise, suspensions and new materials,” in *2014 IEEE Metrology for Aerospace (MetroAeroSpace)*, pp. 515–520. May, 2014.
- [27] Lisa Barsotti, Jan Harms, and Roman Schnabel, “Squeezed vacuum states of light for gravitational wave detectors,” *Reports on Progress in Physics* **82** no. 1, (Dec, 2018) 016905.  
<https://doi.org/10.1088%2F1361-6633%2Faab906>.
- [28] Donatella Fiorucci, Jan Harms, Matteo Barsuglia, Irene Fiori, and Federico Paoletti, “Impact of infrasound atmospheric noise on gravity detectors used for astrophysical and geophysical applications,” *Phys. Rev. D* **97** (Mar, 2018) 062003.  
<https://link.aps.org/doi/10.1103/PhysRevD.97.062003>.
- [29] H. B. Callen and T. A. Welton, “Irreversibility and Generalized Noise,” *Phys. Rev.* **83** (1951) 34.
- [30] R. Kubo, “The fluctuation-dissipation theorem,” *Reports on Progress in Physics* **29** (Jan., 1966) 255–284.
- [31] William Bernard and Herbert B. Callen, “Irreversible thermodynamics of nonlinear processes and noise in driven systems,” *Rev. Mod. Phys.* **31** (Oct, 1959) 1017–1044.  
<http://link.aps.org/doi/10.1103/RevModPhys.31.1017>.
- [32] Gregory M Harry, Andri M Gretarsson, Peter R Saulson, and others, “Thermal noise in interferometric gravitational wave detectors due to dielectric optical coatings,” *Classical and Quantum Gravity* **19** no. 5, (2002) 897.
- [33] Henning Vahlbruch, Moritz Mehmet, Karsten Danzmann, and Roman Schnabel, “Detection of 15 db squeezed states of light and their application for the absolute calibration of photoelectric quantum efficiency,” *Phys. Rev. Lett.* **117** (Sep, 2016) 110801.  
<https://link.aps.org/doi/10.1103/PhysRevLett.117.110801>.
- [34] James Lough, Emil Schreiber, Fabio Bergamin, and others, “First demonstration of 6 db quantum noise reduction in a kilometer scale gravitational wave observatory,” 2020.
- [35] B. P. Abbott et al., “GW170817: Observation of Gravitational Waves from a Binary Neutron Star Inspiral,” *Phys. Rev. Lett.* **119** no. 16, (2017) 161101, arXiv:1710.05832 [gr-qc].
- [36] A. Goldstein et al., “An Ordinary Short Gamma-Ray Burst with Extraordinary Implications: Fermi-GBM Detection of GRB 170817A,” *Astrophys. J.* **848** (2017) L14, arXiv:1710.05446 [astro-ph.HE].
- [37] V. Savchenko et al., “INTEGRAL Detection of the First Prompt Gamma-Ray Signal

- Coincident with the Gravitational-wave Event GW170817,” *Astrophys. J.* **848** (2017) L15, arXiv:1710.05449 [astro-ph.HE].
- [38] B. P. Abbott et al., “Gravitational Waves and Gamma-rays from a Binary Neutron Star Merger: GW170817 and GRB 170817A,” *Astrophys. J.* **848** (2017) L13, arXiv:1710.05834 [astro-ph.HE].
- [39] B. P. Abbott et al., “Multi-messenger Observations of a Binary Neutron Star Merger,” *Astrophys. J.* **848** no. 2, (2017) L12, arXiv:1710.05833 [astro-ph.HE].
- [40] D. A. Coulter et al., “Swope Supernova Survey 2017a (SSS17a), the optical counterpart to a gravitational wave source,” *Science* **358** no. 6370, (Dec, 2017) 1556–1558, arXiv:1710.05452 [astro-ph.HE].
- [41] E. Troja et al., “The X-ray counterpart to the gravitational-wave event GW170817,” *Nature* **551** no. 7678, (Nov, 2017) 71–74, arXiv:1710.05433 [astro-ph.HE].
- [42] G. Hallinan et al., “A radio counterpart to a neutron star merger,” *Science* **358** no. 6370, (Dec, 2017) 1579–1583, arXiv:1710.05435 [astro-ph.HE].
- [43] K. P. Mooley et al., “Superluminal motion of a relativistic jet in the neutron-star merger GW170817,” *Nature* **561** no. 7723, (Sep, 2018) 355–359, arXiv:1806.09693 [astro-ph.HE].
- [44] G. Ghirlanda et al., “Compact radio emission indicates a structured jet was produced by a binary neutron star merger,” *Science* **363** no. 6430, (Mar, 2019) 968–971, arXiv:1808.00469 [astro-ph.HE].
- [45] E. Pian, P. D’Avanzo, et al., “Spectroscopic identification of r-process nucleosynthesis in a double neutron-star merger,” *Nature* **551** no. 7678, (Nov, 2017) 67–70, arXiv:1710.05858 [astro-ph.HE].
- [46] S. J. Smartt et al., “A kilonova as the electromagnetic counterpart to a gravitational-wave source,” *Nature* **551** no. 7678, (Nov, 2017) 75–79, arXiv:1710.05841 [astro-ph.HE].
- [47] Daniel Kasen, Brian Metzger, Jennifer Barnes, Eliot Quataert, and Enrico Ramirez-Ruiz, “Origin of the heavy elements in binary neutron-star mergers from a gravitational-wave event,” *Nature* **551** no. 7678, (Nov, 2017) 80–84, arXiv:1710.05463 [astro-ph.HE].
- [48] Darach Watson et al., “Identification of strontium in the merger of two neutron stars,” *Nature* **574** no. 7779, (Oct, 2019) 497–500.
- [49] B. P. Abbott et al., “GWTC-1: A Gravitational-Wave Transient Catalog of Compact Binary Mergers Observed by LIGO and Virgo during the First and Second Observing Runs,” 2018.
- [50] B. P. Abbott et al., “A gravitational-wave standard siren measurement of the Hubble constant,” *Nature* **551** no. 7678, (2017) 85–88, arXiv:1710.05835 [astro-ph.CO].
- [51] B. P. Abbott et al., “Tests of general relativity with GW150914,” *Phys. Rev. Lett.* **116** no. 22, (2016) 221101, arXiv:1602.03841 [gr-qc]. [Erratum: *Phys. Rev. Lett.* 121, no. 12, 129902 (2018)].

- 
- [52] B. P. Abbott et al., “Tests of General Relativity with GW170817,” *Phys. Rev. Lett.* **123** no. 1, (2019) 011102, arXiv:1811.00364 [gr-qc].
- [53] B. P. Abbott et al., “Tests of General Relativity with the Binary Black Hole Signals from the LIGO-Virgo Catalog GWTC-1,” 2019.
- [54] Tania Regimbau et al., “A Mock Data Challenge for the Einstein Gravitational-Wave Telescope,” *Phys. Rev.* **D86** (2012) 122001, arXiv:1201.3563 [gr-qc].
- [55] Tania Regimbau, Duncan Meacher, and Michael Coughlin, “Second Einstein Telescope mock science challenge: Detection of the gravitational-wave stochastic background from compact binary coalescences,” *Phys. Rev.* **D89** (2014) 084046, arXiv:1404.1134 [astro-ph.CO].
- [56] Enis Belgacem, Yves Dirian, Stefano Foffa, and others, “Cosmology and dark energy from joint gravitational wave-GRB observations,” *JCAP* **2019** (2020) 015, arXiv:1907.01487 [astro-ph.CO].
- [57] Michele Maggiore et al., “Science Case for the Einstein Telescope,” *JCAP* **03** (2020) 050, arXiv:1912.02622 [astro-ph.CO].
- [58] Bernard Carr, Sebastien Clesse, and Juan Garcia-Bellido, “Primordial black holes, dark matter and hot-spot electroweak baryogenesis at the quark-hadron epoch,” 2019.
- [59] Juan Garcia-Bellido, Bernard Carr, and Sebastien Clesse, “A common origin for baryons and dark matter,” 2019.
- [60] Sebastien Clesse and Juan Garcia-Bellido, “The clustering of massive Primordial Black Holes as Dark Matter: measuring their mass distribution with Advanced LIGO,” *Phys. Dark Univ.* **15** (2017) 142–147, arXiv:1603.05234 [astro-ph.CO].
- [61] Sebastien Clesse and Juan Garcia-Bellido, “Detecting the gravitational wave background from primordial black hole dark matter,” *Phys. Dark Univ.* **18** (2017) 105–114, arXiv:1610.08479 [astro-ph.CO].
- [62] Juan Garcia-Bellido, “Massive Primordial Black Holes as Dark Matter and their detection with Gravitational Waves,” *J. Phys. Conf. Ser.* **840** no. 1, (2017) 012032, arXiv:1702.08275 [astro-ph.CO].
- [63] Gordon Baym, Tetsuo Hatsuda, Toru Kojo, and others, “From hadrons to quarks in neutron stars: a review,” *Rept. Prog. Phys.* **81** no. 5, (2018) 056902, arXiv:1707.04966 [astro-ph.HE].
- [64] B. P. Abbott et al., “GW170817: Measurements of neutron star radii and equation of state,” *Phys. Rev. Lett.* **121** no. 16, (2018) 161101, arXiv:1805.11581 [gr-qc].
- [65] K. Hebeler, J. M. Lattimer, C. J. Pethick, and A. Schwenk, “Constraints on neutron star radii based on chiral effective field theory interactions,” *Phys. Rev. Lett.* **105** (2010) 161102.
- [66] S. Gandolfi, J. Carlson, and Sanjay Reddy, “The maximum mass and radius of neutron stars and the nuclear symmetry energy,” *Phys. Rev.* **C85** (2012) 032801.

- [67] Ingo Tews, Joseph Carlson, Stefano Gandolfi, and Sanjay Reddy, “Constraining the speed of sound inside neutron stars with chiral effective field theory interactions and observations,” *Astrophys. J.* **860** no. 2, (2018) 149.
- [68] Xisco Jiménez Forteza, Tiziano Abdelsalhin, Paolo Pani, and Leonardo Gualtieri, “Impact of high-order tidal terms on binary neutron-star waveforms,” *Phys. Rev.* **D98** (2018) 124014, arXiv:1807.08016 [gr-qc].
- [69] Nils Andersson, “Whispers from the edge of physics,” *J. Astrophys. Astron.* **38** (2017) 58, arXiv:1709.07215 [astro-ph.HE].
- [70] Paul D. Lasky, “Gravitational Waves from Neutron Stars: A Review,” *Publ. Astron. Soc. Austral.* **32** (2015) e034, arXiv:1508.06643 [astro-ph.HE].
- [71] B. P. Abbott et al., “Searches for Gravitational Waves from Known Pulsars at Two Harmonics in 2015-2017 LIGO Data,” *Astrophys. J.* **879** no. 1, (2019) 10, arXiv:1902.08507 [astro-ph.HE].
- [72] B. P. Abbott et al., “Narrow-band search for gravitational waves from known pulsars using the second LIGO observing run,” *Phys. Rev.* **D99** no. 12, (2019) 122002, arXiv:1902.08442 [gr-qc].
- [73] B. P. Abbott et al., “All-sky search for continuous gravitational waves from isolated neutron stars using Advanced LIGO O2 data,” *Phys. Rev.* **D100** no. 2, (2019) 024004, arXiv:1903.01901 [astro-ph.HE].
- [74] B. P. Abbott et al., “Searches for Continuous Gravitational Waves from 15 Supernova Remnants and Fomalhaut b with Advanced LIGO,” *Astrophys. J.* **875** no. 2, (2019) 122, arXiv:1812.11656 [astro-ph.HE].
- [75] Ornella J. Piccinni, Astone P., S. D’Antonio, and others, “A directed search for continuous gravitational-wave signals from the Galactic Center in Advanced LIGO second observing run,” 2019.
- [76] B. P. Abbott et al., “Search for gravitational waves from Scorpius X-1 in the second Advanced LIGO observing run with an improved hidden Markov model,” *Phys. Rev.* **D100** no. 12, (2019) 122002, arXiv:1906.12040 [gr-qc].
- [77] C. J. Horowitz and K. Kadau, “The Breaking Strain of Neutron Star Crust and Gravitational Waves,” *Phys. Rev. Lett.* **102** (2009) 191102, arXiv:0904.1986.
- [78] Nathan K. Johnson-McDaniel and Benjamin J. Owen, “Maximum elastic deformations of relativistic stars,” *Phys. Rev.* **D88** (2013) 044004, arXiv:1208.5227.
- [79] G. Woan, M. D. Pitkin, B. Haskell, D. I. Jones, and P. D. Lasky, “Evidence for a Minimum Ellipticity in Millisecond Pulsars,” *Astrophys. J.* **863** (2018) Ls40, arXiv:1806.02822 [astro-ph.HE].
- [80] M Abernathy et al., “Einstein gravitational wave Telescope: Conceptual Design Study,” 2011.
- [81] J. Abadie et al., “Beating the spin-down limit on gravitational wave emission from the Vela pulsar,” *Astrophys. J.* **737** (2011) 93, arXiv:1104.2712 [astro-ph.HE].

- 
- [82] S. Dall’Osso, L. Stella, and C. Palomba, “Neutron star bulk viscosity, spin-flip and GW emission of newly born magnetars,” *Mon. Not. Roy. Astron. Soc.* **480** no. 1, (2018) 1353–1362, arXiv:1806.11164 [astro-ph.HE].
- [83] A. Miller et al., “Method to search for long duration gravitational wave transients from isolated neutron stars using the generalized frequency-Hough transform,” *Phys. Rev.* **D98** no. 10, (2018) 102004, arXiv:1810.09784 [astro-ph.IM].
- [84] Pia Astone, Alberto Colla, Sabrina D’Antonio, Sergio Frasca, and Cristiano Palomba, “Method for all-sky searches of continuous gravitational wave signals using the frequency-Hough transform,” *Phys. Rev.* **D90** (2014) 042002, arXiv:1407.8333 [astro-ph.IM].
- [85] Lars Bildsten, “Gravitational radiation and rotation of accreting neutron stars,” *Astrophys. J.* **501** (1998) L89, arXiv:astro-ph/9804325 [astro-ph].
- [86] Robert C. Duncan and Christopher Thompson, “Formation of very strongly magnetized neutron stars - implications for gamma-ray bursts,” *Astrophys. J.* **392** (1992) L9.
- [87] Sheila Dwyer, Daniel Sigg, Stefan W. Ballmer, and others, “Gravitational wave detector with cosmological reach,” *Phys. Rev.* **D91** no. 8, (2015) 082001, arXiv:1410.0612 [astro-ph.IM].
- [88] David Reitze et al., “Cosmic Explorer: The U.S. Contribution to Gravitational-Wave Astronomy beyond LIGO,” *Bull. Am. Astron. Soc.* **51** (2019) 035, arXiv:1907.04833 [astro-ph.IM].
- [89] Wen Zhao and Linqing Wen, “Localization accuracy of compact binary coalescences detected by the third-generation gravitational-wave detectors and implication for cosmology,” *Phys. Rev.* **D97** (2018) 064031, arXiv:1710.05325 [astro-ph.CO].
- [90] Man Leong Chan, Chris Messenger, Ik Siong Heng, and Martin Hendry, “Binary neutron star mergers and third generation detectors: Localization and early warning,” *Physical Review D* **97** no. 12, (Jun, 2018) 123014, arXiv:1803.09680 [astro-ph.HE].
- [91] Evan D. Hall and Matthew Evans, “Metrics for next-generation gravitational-wave detectors,” *Class. Quant. Grav.* **36** (2019) 225002, arXiv:1902.09485 [astro-ph.IM].
- [92] Jason Spyromilio, Fernando Comerón, Sandro D’Odorico, Markus Kissler-Patig, and Roberto Gilmozzi, “Progress on the European Extremely Large Telescope,” *The Messenger* **133** (Sep, 2008) 2–8.
- [93] Ryan Chornock et al., “Multi-Messenger Astronomy with Extremely Large Telescopes,” 2019.
- [94] Y. Clénet, “ELT-CAM, the E-ELT first light imager,” in *SF2A-2013: Proceedings of the Annual meeting of the French Society of Astronomy and Astrophysics*, L. Cambresy, F. Martins, E. Nuss, and A. Palacios, eds., pp. 267–272. Nov, 2013.
- [95] Bernard F. Schutz, “Determining the Hubble Constant from Gravitational Wave Observations,” *Nature* **323** (1986) 310–311.
- [96] Walter Del Pozzo, “Inference of the cosmological parameters from gravitational waves:

- application to second generation interferometers,” *Phys. Rev.* **D86** (2012) 043011, arXiv:1108.1317 [astro-ph.CO].
- [97] Suvodip Mukherjee and Benjamin D. Wandelt, “Beyond the classical distance-redshift test: cross-correlating redshift-free standard candles and sirens with redshift surveys,” 2018.
- [98] Giulio Scelfo, Nicola Bellomo, Alvise Raccanelli, Sabino Matarrese, and Licia Verde, “GW×LSS: chasing the progenitors of merging binary black holes,” *JCAP* **1809** no. 09, (2018) 039, arXiv:1809.03528 [astro-ph.CO].
- [99] **LIGO Scientific, VIRGO, KAGRA** Collaboration, B. P. Abbott et al., “Prospects for Observing and Localizing Gravitational-Wave Transients with Advanced LIGO, Advanced Virgo and KAGRA,” *Living Rev. Rel.* **21** (2018) 3, arXiv:1304.0670 [gr-qc].
- [100] B. P. Abbott et al., “Properties of the Binary Neutron Star Merger GW170817,” *Physical Review X* **9** no. 1, (Jan, 2019) 011001, arXiv:1805.11579 [gr-qc].
- [101] David Radice and Liang Dai, “Multimessenger parameter estimation of GW170817,” *European Physical Journal A* **55** no. 4, (Apr, 2019) 50, arXiv:1810.12917 [astro-ph.HE].
- [102] Benoit Côté, Chris L. Fryer, Krzysztof Belczynski, and others, “The Origin of r-process Elements in the Milky Way,” *Astrophysical Journal* **855** no. 2, (Mar, 2018) 99, arXiv:1710.05875 [astro-ph.GA].
- [103] K. Hotokezaka, E. Nakar, O. Gottlieb, and others, “A Hubble constant measurement from superluminal motion of the jet in GW170817,” *Nature Astronomy* (Jul, 2019) 385.
- [104] C. L. Carilli and S. Rawlings, “Motivation, key science projects, standards and assumptions,” *New Astron. Rev.* **48** no. 11-12, (Dec, 2004) 979–984, arXiv:astro-ph/0409274 [astro-ph].
- [105] I. Sagiv, A. Gal-Yam, E. O. Ofek, and others, “Science with a Wide-field UV Transient Explorer,” *Astronomical Journal* **147** no. 4, (Apr., 2014) 79, arXiv:1303.6194 [astro-ph.CO].
- [106] Z. Ivezić et al., “Large Synoptic Survey Telescope: From Science Drivers To Reference Design,” *Serbian Astronomical Journal* **176** (Jun, 2008) 1–13.
- [107] **THESEUS** Collaboration, L. Amati et al., “The THESEUS space mission concept: science case, design and expected performances,” *Adv. Space Res.* **62** (2018) 191–244, arXiv:1710.04638 [astro-ph.IM].
- [108] B. S. Acharya et al., “Introducing the CTA concept,” *Astroparticle Physics* **43** (Mar, 2013) 3–18.
- [109] Kirpal Nandra, Didier Barret, Xavier Barcons, and others, “The Hot and Energetic Universe: A White Paper presenting the science theme motivating the Athena+ mission,” *arXiv e-prints* (Jun, 2013) arXiv:1306.2307, arXiv:1306.2307 [astro-ph.HE].
- [110] Brian D. Metzger, “Kilonovae,” *Living Reviews in Relativity* **20** no. 1, (May, 2017) 3, arXiv:1610.09381 [astro-ph.HE].

- 
- [111] Masaomi Tanaka, “Kilonova/Macronova Emission from Compact Binary Mergers,” *Advances in Astronomy* **2016** (Jan, 2016) 634197, arXiv:1605.07235 [astro-ph.HE].
- [112] P. A. Evans et al., “Swift and NuSTAR observations of GW170817: Detection of a blue kilonova,” *Science* **358** no. 6370, (Dec, 2017) 1565–1570, arXiv:1710.05437 [astro-ph.HE].
- [113] Daniel M. Siegel, Jennifer Barnes, and Brian D. Metzger, “Collapsars as a major source of r-process elements,” *Nature* **569** no. 7755, (May, 2019) 241–244, arXiv:1810.00098 [astro-ph.HE].
- [114] Warren Skidmore, TMT International Science Development Teams, and TMT Science Advisory Committee, “Thirty Meter Telescope Detailed Science Case: 2015,” *Research in Astronomy and Astrophysics* **15** no. 12, (Dec, 2015) 1945, arXiv:1505.01195 [astro-ph.IM].
- [115] Jonathan P. Gardner et al., “The James Webb Space Telescope,” *Space Science Reviews* **123** no. 4, (Apr, 2006) 485–606, arXiv:astro-ph/0606175 [astro-ph].
- [116] N. Gehrels et al., “The Swift Gamma-Ray Burst Mission,” *Astrophysical Journal* **611** no. 2, (Aug., 2004) 1005–1020, arXiv:astro-ph/0405233 [astro-ph].
- [117] THESEUS Collaboration, G. Stratta et al., “THESEUS: a key space mission concept for Multi-Messenger Astrophysics,” *Adv. Space Res.* **62** (2018) 662–682, arXiv:1712.08153 [astro-ph.HE].
- [118] Charles Meegan, Giselher Lichti, P. N. Bhat, and others, “The Fermi Gamma-ray Burst Monitor,” *Astrophysical Journal* **702** no. 1, (Sept., 2009) 791–804, arXiv:0908.0450 [astro-ph.IM].
- [119] G. P. Lamb et al., “The optical afterglow of GW170817 at one year post-merger,” *Astrophys. J.* **870** no. 2, (2019) L15, arXiv:1811.11491 [astro-ph.HE].
- [120] Dougal Dobie et al., “A Turnover in the Radio Light Curve of GW170817,” *Astrophysical Journal Letters* **858** no. 2, (May, 2018) L15, arXiv:1803.06853 [astro-ph.HE].
- [121] P. D’Avanzo et al., “The evolution of the X-ray afterglow emission of GW 170817/ GRB 170817A in XMM-Newton observations,” *Astronomy & Astrophysics* **613** (May, 2018) L1, arXiv:1801.06164 [astro-ph.HE].
- [122] R. Margutti et al., “The Binary Neutron Star Event LIGO/Virgo GW170817 160 Days after Merger: Synchrotron Emission across the Electromagnetic Spectrum,” *Astrophysical Journal Letters* **856** no. 1, (Mar, 2018) L18, arXiv:1801.03531 [astro-ph.HE].
- [123] Paz Beniamini, Maria Petropoulou, Rodolfo Barniol Duran, and Dimitrios Giannios, “A lesson from GW170817: most neutron star mergers result in tightly collimated successful GRB jets,” *MNRAS* **483** no. 1, (Feb, 2019) 840–851, arXiv:1808.04831 [astro-ph.HE].
- [124] O. S. Salafia, G. Ghirlanda, S. Ascenzi, and G. Ghisellini, “On-axis view of GRB 170817A,” *Astronomy & Astrophysics* **628** (Aug, 2019) A18, arXiv:1905.01190 [astro-ph.HE].

- [125] Adithan Kathirgamaraju, Rodolfo Barniol Duran, and Dimitrios Giannios, “Off-axis short GRBs from structured jets as counterparts to GW events,” *MNRAS* **473** no. 1, (Jan, 2018) L121–L125, arXiv:1708.07488 [astro-ph.HE].
- [126] Ehud Nakar, Ore Gottlieb, Tsvi Piran, Mansi. M. Kasliwal, and Gregg Hallinan, “From  $\gamma$  to Radio: The Electromagnetic Counterpart of GW170817,” *Astrophysical Journal* **867** no. 1, (Nov, 2018) 18, arXiv:1803.07595 [astro-ph.HE].
- [127] M. M. Kasliwal et al., “Illuminating gravitational waves: A concordant picture of photons from a neutron star merger,” *Science* **358** no. 6370, (Dec, 2017) 1559–1565, arXiv:1710.05436 [astro-ph.HE].
- [128] J. Wei, Cordier, et al., “The Deep and Transient Universe in the SVOM Era: New Challenges and Opportunities - Scientific prospects of the SVOM mission,” *arXiv e-prints* (Oct., 2016) arXiv:1610.06892, arXiv:1610.06892 [astro-ph.IM].
- [129] C. Winkler, T. J. L. Courvoisier, G. Di Cocco, and others, “The INTEGRAL mission,” *Astronomy & Astrophysics* **411** (Nov., 2003) L1–L6.
- [130] Brian D. Metzger and Anthony L. Piro, “Optical and X-ray emission from stable millisecond magnetars formed from the merger of binary neutron stars,” *MNRAS* **439** no. 4, (Apr, 2014) 3916–3930, arXiv:1311.1519 [astro-ph.HE].
- [131] Daniel M. Siegel and Riccardo Ciolfi, “Electromagnetic Emission from Long-lived Binary Neutron Star Merger Remnants. II. Lightcurves and Spectra,” *Astrophysical Journal* **819** no. 1, (Mar, 2016) 15, arXiv:1508.07939 [astro-ph.HE].
- [132] Weimin Yuan, Chen Zhang, Zhixing Ling, and others, “Einstein Probe: a lobster-eye telescope for monitoring the x-ray sky,” in *Space Telescopes and Instrumentation 2018: Ultraviolet to Gamma Ray*, vol. 10699 of *Society of Photo-Optical Instrumentation Engineers (SPIE) Conference Series*, p. 1069925. July, 2018.
- [133] S. A. Colgate and R. H. White, “The Hydrodynamic Behavior of Supernovae Explosions,” *Astrophysical Journal* **143** (Mar., 1966) 626.
- [134] James R. Wilson, “Coherent neutrino scattering and stellar collapse,” *Phys. Rev. Lett.* **32** (Apr, 1974) 849–852. <https://link.aps.org/doi/10.1103/PhysRevLett.32.849>.
- [135] H.-T. Janka and E. Mueller, “Neutrino heating, convection, and the mechanism of Type-II supernova explosions,” *Astronomy & Astrophysics* **306** (Feb., 1996) 167.
- [136] A. Mezzacappa, A. C. Calder, S. W. Bruenn, and others, “An Investigation of Neutrino-driven Convection and the Core Collapse Supernova Mechanism Using Multigroup Neutrino Transport,” *Astrophysical Journal* **495** (Mar., 1998) 911–926.
- [137] B. Müller, H.-T. Janka, and A. Marek, “A New Multi-dimensional General Relativistic Neutrino Hydrodynamics Code for Core-collapse Supernovae. II. Relativistic Explosion Models of Core-collapse Supernovae,” *Astrophysical Journal* **756** (Sept., 2012) 84.
- [138] B. Müller, H.-T. Janka, and A. Heger, “New Two-dimensional Models of Supernova

- 
- Explosions by the Neutrino-heating Mechanism: Evidence for Different Instability Regimes in Collapsing Stellar Cores,” *Astrophysical Journal* **761** (Dec., 2012) 72.
- [139] T. Takiwaki, K. Kotake, and Y. Suwa, “Three-dimensional Hydrodynamic Core-collapse Supernova Simulations for an 11.2 M<sub>⊙</sub> Star with Spectral Neutrino Transport,” *Astrophysical Journal* **749** (Apr., 2012) 98.
- [140] F. Hanke, B. Müller, A. Wongwathanarat, A. Marek, and H.-T. Janka, “SASI Activity in Three-dimensional Neutrino-hydrodynamics Simulations of Supernova Cores,” *Astrophysical Journal* **770** (June, 2013) 66.
- [141] J. W. Murphy, J. C. Dolence, and A. Burrows, “The Dominance of Neutrino-driven Convection in Core-collapse Supernovae,” *Astrophysical Journal* **771** (July, 2013) 52.
- [142] S. M. Couch and C. D. Ott, “Revival of the Stalled Core-collapse Supernova Shock Triggered by Precollapse Asphericity in the Progenitor Star,” *Astrophysical Journal Letters* **778** (Nov., 2013) L7.
- [143] P. Cerdá-Durán, N. DeBrye, M. A. Aloy, J. A. Font, and M. Obergaulinger, “Gravitational Wave Signatures in Black Hole Forming Core Collapse,” *Astrophysical Journal Letters* **779** (Dec., 2013) L18.
- [144] B. Müller, T. Melson, A. Heger, and H.-T. Janka, “Supernova simulations from a 3D progenitor model - Impact of perturbations and evolution of explosion properties,” *MNRAS* **472** (Nov., 2017) 491–513.
- [145] D. Radice, A. Burrows, D. Vartanyan, M. A. Skinner, and J. C. Dolence, “Electron-capture and Low-mass Iron-core-collapse Supernovae: New Neutrino-radiation-hydrodynamics Simulations,” *Astrophysical Journal* **850** (Nov., 2017) 43.
- [146] E. P. O’Connor and S. M. Couch, “Two-dimensional Core-collapse Supernova Explosions Aided by General Relativity with Multidimensional Neutrino Transport,” *Astrophysical Journal* **854** (Feb., 2018) 63.
- [147] Jade Powell and Bernhard Müller, “Gravitational Wave Emission from 3D Explosion Models of Core-Collapse Supernovae with Low and Normal Explosion Energies,” *Mon. Not. Roy. Astron. Soc.* **487** no. 1, (2019) 1178–1190, arXiv:1812.05738 [astro-ph.HE].
- [148] T. Zwerger and E. Mueller, “Dynamics and gravitational wave signature of axisymmetric rotational core collapse,” *Astronomy & Astrophysics* **320** (Apr., 1997) 209–227.
- [149] H. Dimmelmeier, J. A. Font, and E. Müller, “Gravitational Waves from Relativistic Rotational Core Collapse,” *Astrophysical Journal Letters* **560** (Oct., 2001) L163–L166.
- [150] H. Dimmelmeier, J. A. Font, and E. Müller, “Relativistic simulations of rotational core collapse II. Collapse dynamics and gravitational radiation,” *Astronomy & Astrophysics* **393** (Oct., 2002) 523–542.
- [151] H. Dimmelmeier, C. D. Ott, H.-T. Janka, A. Marek, and E. Müller, “Generic Gravitational-Wave Signals from the Collapse of Rotating Stellar Cores,” *Physical Review Letters* **98** no. 25, (June, 2007) 251101.

- [152] C. D. Ott, H. Dimmelmeier, A. Marek, and others, “3D Collapse of Rotating Stellar Iron Cores in General Relativity Including Deleptonization and a Nuclear Equation of State,” *Physical Review Letters* **98** no. 26, (June, 2007) 261101.
- [153] H. Dimmelmeier, C. D. Ott, A. Marek, and H.-T. Janka, “Gravitational wave burst signal from core collapse of rotating stars,” *Physical Review D* **78** no. 6, (Sept., 2008) 064056.
- [154] T. Kuroda, T. Takiwaki, and K. Kotake, “Gravitational wave signatures from low-mode spiral instabilities in rapidly rotating supernova cores,” *Physical Review D* **89** no. 4, (Feb., 2014) 044011.
- [155] K. N. Yakunin, A. Mezzacappa, P. Marronetti, and others, “Gravitational wave signatures of ab initio two-dimensional core collapse supernova explosion models for 12–25  $M_{\odot}$  stars,” *Physical Review D* **92** no. 8, (Oct., 2015) 084040.
- [156] T. Kuroda, K. Kotake, and T. Takiwaki, “A New Gravitational-wave Signature from Standing Accretion Shock Instability in Supernovae,” *Astrophysical Journal Letters* **829** (Sept., 2016) L14.
- [157] H. Andresen, B. Müller, E. Müller, and H.-T. Janka, “Gravitational wave signals from 3D neutrino hydrodynamics simulations of core-collapse supernovae,” *MNRAS* **468** (June, 2017) 2032–2051.
- [158] J. M. Blondin, A. Mezzacappa, and C. DeMarino, “Stability of Standing Accretion Shocks, with an Eye toward Core-Collapse Supernovae,” *Astrophysical Journal* **584** (Feb., 2003) 971–980.
- [159] T. Foglizzo, P. Galletti, L. Scheck, and H.-T. Janka, “Instability of a Stalled Accretion Shock: Evidence for the Advective-Acoustic Cycle,” *Astrophysical Journal* **654** (Jan., 2007) 1006–1021.
- [160] E. Müller, M. Rampp, R. Buras, H.-T. Janka, and D. H. Shoemaker, “Toward Gravitational Wave Signals from Realistic Core-Collapse Supernova Models,” *Astrophysical Journal* **603** (2004) 221–230.
- [161] David Radice, Viktoriya Morozova, Adam Burrows, David Vartanyan, and Hiroki Nagakura, “Characterizing the Gravitational Wave Signal from Core-Collapse Supernovae,” *Astrophys. J.* **876** no. 1, (2019) L9, arXiv:1812.07703 [astro-ph.HE].
- [162] S. E. Gossan, P. Sutton, A. Stuver, and others, “Observing gravitational waves from core-collapse supernovae in the advanced detector era,” *Physical Review D* **93** no. 4, (Feb., 2016) 042002.
- [163] Roland Diehl et al., “Radioactive Al-26 and massive stars in the galaxy,” *Nature* **439** (2006) 45–47.
- [164] P. Astone, P. Cerdá-Durán, I. Di Palma, and others, “New method to observe gravitational waves emitted by core collapse supernovae,” *Phys. Rev. D* **98** no. 12, (2018) 122002, arXiv:1812.05363 [astro-ph.IM].
- [165] S. Dall’Osso, S. N. Shore, and L. Stella, “Early evolution of newly born magnetars with a

- 
- strong toroidal field,” *MNRAS* **398** no. 4, (Oct., 2009) 1869–1885, arXiv:0811.4311 [astro-ph].
- [166] W. B. Atwood et al., “The Large Area Telescope on the Fermi Gamma-Ray Space Telescope Mission,” *Astrophysical Journal* **697** no. 2, (June, 2009) 1071–1102, arXiv:0902.1089 [astro-ph.IM].
- [167] W. Hofmann and H. E. S. S. Collaboration, “The high energy stereoscopic system (HESS) project,” in *American Institute of Physics Conference Series*, Brenda L. Dingus, Michael H. Salamon, and David B. Kieda, eds., vol. 515 of *American Institute of Physics Conference Series*, pp. 500–509. June, 2000.
- [168] J. Aleksić et al., “The major upgrade of the MAGIC telescopes, Part I: The hardware improvements and the commissioning of the system,” *Astroparticle Physics* **72** (Jan., 2016) 61–75, arXiv:1409.6073 [astro-ph.IM].
- [169] J. Aleksić et al., “The major upgrade of the MAGIC telescopes, Part II: A performance study using observations of the Crab Nebula,” *Astroparticle Physics* **72** (Jan., 2016) 76–94, arXiv:1409.5594 [astro-ph.IM].
- [170] T. C. Weekes et al., “VERITAS: the Very Energetic Radiation Imaging Telescope Array System,” *Astroparticle Physics* **17** no. 2, (May, 2002) 221–243, arXiv:astro-ph/0108478 [astro-ph].
- [171] M. Actis et al., “Design concepts for the Cherenkov Telescope Array CTA: an advanced facility for ground-based high-energy gamma-ray astronomy,” *Experimental Astronomy* **32** no. 3, (Dec., 2011) 193–316, arXiv:1008.3703 [astro-ph.IM].
- [172] K. Hirata, T. Kajita, M. Koshiba, and others, “Observation of a neutrino burst from the supernova SN1987A,” *Physical Review Letters* **58** no. 14, (Apr., 1987) 1490–1493.
- [173] K. S. Hirata, T. Kajita, M. Koshiba, and others, “Observation in the Kamiokande-II detector of the neutrino burst from supernova SN1987A,” *Physical Review D* **38** no. 2, (July, 1988) 448–458.
- [174] R. M. Bionta, G. Blewitt, C. B. Bratton, and others, “Observation of a neutrino burst in coincidence with supernova 1987A in the Large Magellanic Cloud,” *Physical Review Letters* **58** no. 14, (Apr., 1987) 1494–1496.
- [175] E. N. Alekseev, L. N. Alekseeva, V. I. Volchenko, and I. V. Krivosheina, “Possible detection of a neutrino signal on 23 February 1987 at the Baksan underground scintillation telescope of the Institute of Nuclear Research,” *Soviet Journal of Experimental and Theoretical Physics Letters* **45** (May, 1987) 589.
- [176] **Super-Kamiokande** Collaboration, K. Abe et al., “Real-Time Supernova Neutrino Burst Monitor at Super-Kamiokande,” *Astropart. Phys.* **81** (2016) 39–48, arXiv:1601.04778 [astro-ph.HE].
- [177] Artur Ankowski et al., “Supernova Physics at DUNE,” in *Supernova Physics at DUNE Blacksburg, Virginia, USA, March 11-12, 2016*. 2016. arXiv:1608.07853 [hep-ex].

- [178] Jia-Shu Lu, Jun Cao, Yu-Feng Li, and Shun Zhou, “Constraining Absolute Neutrino Masses via Detection of Galactic Supernova Neutrinos at JUNO,” *JCAP* **1505** no. 05, (2015) 044, arXiv:1412.7418 [hep-ph].
- [179] **IceCube** Collaboration, R. Abbasi et al., “IceCube Sensitivity for Low-Energy Neutrinos from Nearby Supernovae,” *Astron. Astrophys.* **535** (2011) A109, arXiv:1108.0171 [astro-ph.HE]. [Erratum: *Astron. Astrophys.*563,C1(2014)].
- [180] N. Yu. Agafonova et al., “On-line recognition of supernova neutrino bursts in the LVD detector,” *Astropart. Phys.* **28** (2008) 516–522.
- [181] **SNO+** Collaboration, S. Andringa et al., “Current Status and Future Prospects of the SNO+ Experiment,” *Adv. High Energy Phys.* **2016** (2016) 6194250, arXiv:1508.05759 [physics.ins-det].
- [182] Kazumi Tolich, “Supernova detection with KamLAND,” *Nucl. Phys. Proc. Suppl.* **221** (2011) 355.
- [183] I. Tamborra, G. Raffelt, F. Hanke, H.-T. Janka, and B. Müller, “Neutrino emission characteristics and detection opportunities based on three-dimensional supernova simulations,” *Physical Review D* **90** (2014) 045032.
- [184] B. Müller and H.-T. Janka, “A New Multi-dimensional General Relativistic Neutrino Hydrodynamics Code for Core-collapse Supernovae. IV. The Neutrino Signal,” *Astrophysical Journal* **788** (2014) 82.
- [185] Takami Kuroda, Kei Kotake, Kazuhiro Hayama, and Tomoya Takiwaki, “Correlated Signatures of Gravitational-Wave and Neutrino Emission in Three-Dimensional General-Relativistic Core-Collapse Supernova Simulations,” *Astrophys. J.* **851** no. 1, (2017) 62, arXiv:1708.05252 [astro-ph.HE].
- [186] P. Amaro-Seoane et al., “Laser Interferometer Space Antenna,” 2017.
- [187] Alberto Sesana, “Prospects for Multiband Gravitational-Wave Astronomy after GW150914,” *Phys. Rev. Lett.* **116** (2016) 231102, arXiv:1602.06951 [gr-qc].
- [188] Andrea Caputo, Laura Sberna, Alexandre Toubiana, and others, “Gravitational-wave detection and parameter estimation for accreting black-hole binaries and their electromagnetic counterpart,” 2020.
- [189] Nicola Tamanini, Antoine Klein, Camille Bonvin, Enrico Barausse, and Chiara Caprini, “The peculiar acceleration of stellar-origin black hole binaries: measurement and biases with LISA,” 2019.
- [190] Christopher J. Moore, Davide Gerosa, and Antoine Klein, “Are stellar-mass black-hole binaries too quiet for LISA?,” *Mon. Not. Roy. Astron. Soc.* **488** (2019) L94–L98, arXiv:1905.11998 [astro-ph.HE].
- [191] Salvatore Vitale, “Multiband Gravitational-Wave Astronomy: Parameter Estimation and Tests of General Relativity with Space- and Ground-Based Detectors,” *Phys. Rev. Lett.* **117** no. 5, (2016) 051102, arXiv:1605.01037 [gr-qc].

- 
- [192] Rhondale Tso, Davide Gerosa, and Yanbei Chen, “Optimizing LIGO with LISA forewarnings to improve black-hole spectroscopy,” *Phys. Rev.* **D99** (2019) 124043, arXiv:1807.00075 [gr-qc].
- [193] Thibault Damour and Gilles Esposito-Farese, “Tensor multiscalar theories of gravitation,” *Class. Quant. Grav.* **9** (1992) 2093–2176.
- [194] Thibault Damour and Gilles Esposito-Farese, “Nonperturbative strong field effects in tensor - scalar theories of gravitation,” *Phys. Rev. Lett.* **70** (1993) 2220–2223.
- [195] Enrico Barausse, Carlos Palenzuela, Marcelo Ponce, and Luis Lehner, “Neutron-star mergers in scalar-tensor theories of gravity,” *Phys. Rev.* **D87** (2013) 081506, arXiv:1212.5053 [gr-qc].
- [196] Laura Sampson, Nicols Yunes, Neil Cornish, and others, “Projected Constraints on Scalarization with Gravitational Waves from Neutron Star Binaries,” *Phys. Rev.* **D90** (2014) 124091, arXiv:1407.7038 [gr-qc].
- [197] Emanuele Berti, Vitor Cardoso, and Andrei O. Starinets, “Quasinormal modes of black holes and black branes,” *Class. Quant. Grav.* **26** (2009) 163001, arXiv:0905.2975 [gr-qc].
- [198] Richard Brito, Alessandra Buonanno, and Vivien Raymond, “Black-hole Spectroscopy by Making Full Use of Gravitational-Wave Modeling,” *Phys. Rev.* **D98** no. 8, (2018) 084038, arXiv:1805.00293 [gr-qc].
- [199] Emanuele Berti, Alberto Sesana, Enrico Barausse, Vitor Cardoso, and Krzysztof Belczynski, “Spectroscopy of Kerr black holes with Earth- and space-based interferometers,” *Phys. Rev. Lett.* **117** no. 10, (2016) 101102, arXiv:1605.09286 [gr-qc].
- [200] Swetha Bhagwat, Xisco Jimenez Forteza, Paolo Pani, and Valeria Ferrari, “Ringdown overtones, black hole spectroscopy and, no-hair theorem tests,” 2019.
- [201] Andrea Maselli, Paolo Pani, Leonardo Gualtieri, and Emanuele Berti, “Parametrized ringdown spin expansion coefficients: a data-analysis framework for black-hole spectroscopy with multiple events,” 2019.
- [202] Vitor Cardoso and Paolo Pani, “Testing the nature of dark compact objects: a status report,” *Living Rev. Rel.* **22** no. 1, (2019) 4, arXiv:1904.05363 [gr-qc].
- [203] Vitor Cardoso, Edgardo Franzin, Andrea Maselli, Paolo Pani, and Guilherme Raposo, “Testing strong-field gravity with tidal Love numbers,” *Phys. Rev.* **D95** (2017) 084014, arXiv:1701.01116 [gr-qc]. [Addendum: *Phys. Rev.* **D95**, no. 8, 089901 (2017)].
- [204] N. V. Krishnendu, K. G. Arun, and Chandra Kant Mishra, “Testing the binary black hole nature of a compact binary coalescence,” *Phys. Rev. Lett.* **119** no. 9, (2017) 091101, arXiv:1701.06318 [gr-qc].
- [205] Vitor Cardoso, Edgardo Franzin, and Paolo Pani, “Is the gravitational-wave ringdown a probe of the event horizon?,” *Phys. Rev. Lett.* **116** no. 17, (2016) 171101, arXiv:1602.07309 [gr-qc]. [Erratum: *Phys. Rev. Lett.* **117**, no. 8, 089902 (2016)].

- [206] Vitor Cardoso and Paolo Pani, “Tests for the existence of black holes through gravitational wave echoes,” *Nat. Astron.* **1** no. 9, (2017) 586–591, arXiv:1709.01525 [gr-qc].
- [207] Elisa Maggio, Adriano Testa, Swetha Bhagwat, and Paolo Pani, “Analytical model for gravitational-wave echoes from spinning remnants,” *Phys. Rev.* **D100** (2019) 064056, arXiv:1907.03091 [gr-qc].
- [208] Adriano Testa and Paolo Pani, “Analytical template for gravitational-wave echoes: signal characterization and prospects of detection with current and future interferometers,” *Phys. Rev.* **D98** (2018) 044018, arXiv:1806.04253 [gr-qc].
- [209] Ahmed Almheiri, Donald Marolf, Joseph Polchinski, and James Sully, “Black Holes: Complementarity or Firewalls?,” *JHEP* **02** (2013) 062, arXiv:1207.3123 [hep-th].
- [210] Samir D. Mathur, “The Fuzzball proposal for black holes: An Elementary review,” *Fortsch. Phys.* **53** (2005) 793–827, arXiv:hep-th/0502050 [hep-th].
- [211] Enrico Barausse, Richard Brito, Vitor Cardoso, Irina Dvorkin, and Paolo Pani, “The stochastic gravitational-wave background in the absence of horizons,” *Class. Quant. Grav.* **35** no. 20, (2018) 20LT01, arXiv:1805.08229 [gr-qc].
- [212] Vitor Cardoso, Seth Hopper, Caio F. B. Macedo, Carlos Palenzuela, and Paolo Pani, “Gravitational-wave signatures of exotic compact objects and of quantum corrections at the horizon scale,” *Phys. Rev.* **D94** no. 8, (2016) 084031, arXiv:1608.08637 [gr-qc].
- [213] Vitor Cardoso, Valentino F. Foit, and Matthew Kleban, “Gravitational wave echoes from black hole area quantization,” *JCAP* **1908** (2019) 006, arXiv:1902.10164 [hep-th].
- [214] J. D. Bekenstein, “The quantum mass spectrum of the Kerr black hole,” *Lett. Nuovo Cim.* **11** (1974) 467.
- [215] Jacob D. Bekenstein and Viatcheslav F. Mukhanov, “Spectroscopy of the quantum black hole,” *Phys. Lett. B* **360** (1995) 7–12, arXiv:gr-qc/9505012.
- [216] Ivan Agullo, Vitor Cardoso, Adrian del Rio, Michele Maggiore, and Jorge Pullin, “Gravitational-wave signatures of quantum gravity,” 2020.
- [217] Enrico Barausse, Nicolas Yunes, and Katie Chamberlain, “Theory-Agnostic Constraints on Black-Hole Dipole Radiation with Multiband Gravitational-Wave Astrophysics,” *Phys. Rev. Lett.* **116** no. 24, (2016) 241104, arXiv:1603.04075 [gr-qc].
- [218] Andrew Gould, Bruce T. Draine, Roger W. Romani, and Shmuel Nussinov, “Neutron Stars: Graveyard of Charged Dark Matter,” *Phys. Lett.* **B238** (1990) 337–343.
- [219] Stephon Alexander, Evan McDonough, Robert Sims, and Nicolas Yunes, “Hidden-Sector Modifications to Gravitational Waves From Binary Inspirals,” *Class. Quant. Grav.* **35** (2018) 235012, arXiv:1808.05286 [gr-qc].
- [220] Joseph Bramante, Tim Linden, and Yu-Dai Tsai, “Searching for dark matter with neutron star mergers and quiet kilonovae,” *Phys. Rev.* **D97** no. 5, (2018) 055016, arXiv:1706.00001 [hep-ph].

- 
- [221] Chris Kouvaris, Peter Tinyakov, and Michel H. G. Tytgat, “NonPrimordial Solar Mass Black Holes,” *Phys. Rev. Lett.* **121** no. 22, (2018) 221102, arXiv:1804.06740 [astro-ph.HE].
- [222] Rouven Essig et al., “Working Group Report: New Light Weakly Coupled Particles,” in *Proceedings, 2013 Community Summer Study on the Future of U.S. Particle Physics: Snowmass on the Mississippi (CSS2013): Minneapolis, MN, USA, July 29-August 6, 2013*. 2013. arXiv:1311.0029 [hep-ph]. <http://www.slac.stanford.edu/econf/C1307292/docs/IntensityFrontier/NewLight-17.pdf>.
- [223] Lam Hui, Jeremiah P. Ostriker, Scott Tremaine, and Edward Witten, “Ultralight scalars as cosmological dark matter,” *Phys. Rev.* **D95** no. 4, (2017) 043541, arXiv:1610.08297 [astro-ph.CO].
- [224] Asimina Arvanitaki and Sergei Dubovsky, “Exploring the String Axiverse with Precision Black Hole Physics,” *Phys. Rev.* **D83** (2011) 044026, arXiv:1004.3558 [hep-th].
- [225] Richard Brito, Vitor Cardoso, and Paolo Pani, “Black holes as particle detectors: evolution of superradiant instabilities,” *Class. Quant. Grav.* **32** no. 13, (2015) 134001, arXiv:1411.0686 [gr-qc].
- [226] William E. East and Frans Pretorius, “Superradiant Instability and Backreaction of Massive Vector Fields around Kerr Black Holes,” *Phys. Rev. Lett.* **119** no. 4, (2017) 041101, arXiv:1704.04791 [gr-qc].
- [227] Richard Brito, Shrobona Ghosh, Enrico Barausse, and others, “Gravitational wave searches for ultralight bosons with LIGO and LISA,” *Phys. Rev.* **D96** no. 6, (2017) 064050, arXiv:1706.06311 [gr-qc].
- [228] Richard Brito, Shrobona Ghosh, Enrico Barausse, and others, “Stochastic and resolvable gravitational waves from ultralight bosons,” *Phys. Rev. Lett.* **119** no. 13, (2017) 131101, arXiv:1706.05097 [gr-qc].
- [229] Daniel Baumann, Horng Sheng Chia, and Rafael A. Porto, “Probing Ultralight Bosons with Binary Black Holes,” *Phys. Rev.* **D99** no. 4, (2019) 044001, arXiv:1804.03208 [gr-qc].
- [230] **Supernova Search Team** Collaboration, A. G. Riess et al., “Observational evidence from supernovae for an accelerating universe and a cosmological constant,” *Astron.J.* **116** (1998) 1009–1038, arXiv:astro-ph/9805201 [astro-ph].
- [231] **Supernova Cosmology Project** Collaboration, S. Perlmutter et al., “Measurements of Omega and Lambda from 42 high redshift supernovae,” *Astrophys.J.* **517** (1999) 565–586, arXiv:astro-ph/9812133 [astro-ph].
- [232] M. Fishbach et al., “A Standard Siren Measurement of the Hubble Constant from GW170817 without the Electromagnetic Counterpart,” *Astrophys. J. Lett.* **871** (2019) L13, arXiv:1807.05667 [astro-ph.CO].
- [233] **LIGO Scientific, Virgo** Collaboration, B.P. Abbott et al., “A gravitational-wave measurement of the Hubble constant following the second observing run of Advanced LIGO and Virgo,” arXiv:1908.06060 [astro-ph.CO].

- [234] **DES, LIGO Scientific, Virgo** Collaboration, M. Soares-Santos et al., “First Measurement of the Hubble Constant from a Dark Standard Siren using the Dark Energy Survey Galaxies and the LIGO/Virgo Binary–Black-hole Merger GW170814,” *Astrophys. J. Lett.* **876** (2019) L7, arXiv:1901.01540 [astro-ph.CO].
- [235] A. Palmese et al., “A statistical standard siren measurement of the Hubble constant from the LIGO/Virgo gravitational wave compact object merger GW190814 and Dark Energy Survey galaxies,” arXiv:2006.14961 [astro-ph.CO].
- [236] Sergiy Vasylyev and Alex Filippenko, “A Measurement of the Hubble Constant using Gravitational Waves from the Neutron-Star Black-Hole Candidate GW190814,” arXiv:2007.11148 [astro-ph.CO].
- [237] Stephen R. Taylor, Jonathan R. Gair, and Ilya Mandel, “Hubble without the Hubble: Cosmology using advanced gravitational-wave detectors alone,” *Phys. Rev.* **D85** (2012) 023535, arXiv:1108.5161 [gr-qc].
- [238] S. R. Taylor and J. R. Gair, “Cosmology with the lights off: standard sirens in the Einstein Telescope era,” *Phys. Rev.* **D86** (2012) 023502, arXiv:1204.6739 [astro-ph.CO].
- [239] C. Messenger and J. Read, “Measuring a cosmological distance-redshift relationship using only gravitational wave observations of binary neutron star coalescences,” *Phys. Rev. Lett.* **108** (2012) 091101, arXiv:1107.5725 [gr-qc].
- [240] Adam G. Riess, Stefano Casertano, Wenlong Yuan, Lucas M. Macri, and Dan Scolnic, “Large Magellanic Cloud Cepheid Standards Provide a 1% Foundation for the Determination of the Hubble Constant and Stronger Evidence for Physics Beyond LambdaCDM,” *Astrophys. J.* **876** no. 1, (2019) 85, arXiv:1903.07603 [astro-ph.CO].
- [241] Kenneth C. Wong et al., “H0LiCOW XIII. A 2.4% measurement of  $H_0$  from lensed quasars:  $5.3\sigma$  tension between early and late-Universe probes,” 2019.
- [242] **Planck** Collaboration, N. Aghanim et al., “Planck 2018 results. VI. Cosmological parameters,” 2018.
- [243] **DES** Collaboration, T. M. C. Abbott et al., “Dark Energy Survey Year 1 Results: Constraints on Extended Cosmological Models from Galaxy Clustering and Weak Lensing,” *Phys. Rev.* **D99** (2019) 123505, arXiv:1810.02499 [astro-ph.CO].
- [244] B. S. Sathyaprakash, B. F. Schutz, and C. Van Den Broeck, “Cosmography with the Einstein Telescope,” *Class. Quant. Grav.* **27** (2010) 215006, arXiv:0906.4151 [astro-ph.CO].
- [245] W. Zhao, C. Van Den Broeck, D. Baskaran, and T. G. F. Li, “Determination of Dark Energy by the Einstein Telescope: Comparing with CMB, BAO and SNIa Observations,” *Phys. Rev.* **D83** (2011) 023005, arXiv:1009.0206 [astro-ph.CO].
- [246] I. D. Saltas, I. Sawicki, L. Amendola, and M. Kunz, “Anisotropic Stress as a Signature of Nonstandard Propagation of Gravitational Waves,” *Phys. Rev. Lett.* **113** (2014) 191101, arXiv:1406.7139 [astro-ph.CO].

- 
- [247] L. Lombriser and A. Taylor, “Breaking a Dark Degeneracy with Gravitational Waves,” *JCAP* **1603** (2016) 031, arXiv:1509.08458 [astro-ph.CO].
- [248] A. Nishizawa, “Generalized framework for testing gravity with gravitational-wave propagation. I. Formulation,” *Phys. Rev.* **D97** (2018) 104037, arXiv:1710.04825 [gr-qc].
- [249] E. Belgacem, Y. Dirian, S. Foffa, and M. Maggiore, “Gravitational-wave luminosity distance in modified gravity theories,” *Phys. Rev.* **D97** (2018) 104066, arXiv:1712.08108 [astro-ph.CO].
- [250] L. Amendola, I. Sawicki, M. Kunz, and I. D. Saltas, “Direct detection of gravitational waves can measure the time variation of the Planck mass,” *JCAP* **1808** (2018) 030, arXiv:1712.08623 [astro-ph.CO].
- [251] **LISA Cosmology Working Group** Collaboration, Enis Belgacem et al., “Testing modified gravity at cosmological distances with LISA standard sirens,” *JCAP* **1907** (2019) 024, arXiv:1906.01593 [astro-ph.CO].
- [252] Enis Belgacem, Yves Dirian, Andreas Finke, Stefano Foffa, and Michele Maggiore, “Gravity in the infrared and effective nonlocal models,” 2020.
- [253] M. Maggiore, “Gravitational wave experiments and early universe cosmology,” *Phys. Rept.* **331** (2000) 283–367, arXiv:gr-qc/9909001 [gr-qc].
- [254] Chiara Caprini and Daniel G. Figueroa, “Cosmological Backgrounds of Gravitational Waves,” *Class. Quant. Grav.* **35** no. 16, (2018) 163001, arXiv:1801.04268 [astro-ph.CO].
- [255] Jessica L. Cook and Lorenzo Sorbo, “Particle production during inflation and gravitational waves detectable by ground-based interferometers,” *Phys. Rev.* **D85** (2012) 023534, arXiv:1109.0022 [astro-ph.CO]. [Erratum: *Phys. Rev.*D86,069901(2012)].
- [256] Nicola Bartolo, Dario Cannone, Angelo Ricciardone, and Gianmassimo Tasinato, “Distinctive signatures of space-time diffeomorphism breaking in EFT of inflation,” *JCAP* **1603** no. 03, (2016) 044, arXiv:1511.07414 [astro-ph.CO].
- [257] R. Brustein, M. Gasperini, Massimo Giovannini, and G. Veneziano, “Relic gravitational waves from string cosmology,” *Phys. Lett.* **B361** (1995) 45–51, arXiv:hep-th/9507017 [hep-th].
- [258] Alessandra Buonanno, Michele Maggiore, and Carlo Ungarelli, “Spectrum of relic gravitational waves in string cosmology,” *Phys. Rev.* **D55** (1997) 3330–3336, arXiv:gr-qc/9605072 [gr-qc].
- [259] M. Gasperini and G. Veneziano, “The Pre - big bang scenario in string cosmology,” *Phys. Rept.* **373** (2003) 1–212, arXiv:hep-th/0207130 [hep-th].
- [260] Valerie Domcke, Juan Garcia-Bellido, Marco Peloso, and others, “Measuring the net circular polarization of the stochastic gravitational wave background with interferometers,” 2019.
- [261] Lev Kofman, Andrei D. Linde, and Alexei A. Starobinsky, “Reheating after inflation,” *Phys. Rev. Lett.* **73** (1994) 3195–3198, arXiv:hep-th/9405187 [hep-th].

- [262] Lev Kofman, Andrei D. Linde, and Alexei A. Starobinsky, “Towards the theory of reheating after inflation,” *Phys. Rev.* **D56** (1997) 3258–3295, arXiv:hep-ph/9704452 [hep-ph].
- [263] Patrick B. Greene and Lev Kofman, “Preheating of fermions,” *Phys. Lett.* **B448** (1999) 6–12, arXiv:hep-ph/9807339 [hep-ph].
- [264] Patrick B. Greene and Lev Kofman, “On the theory of fermionic preheating,” *Phys. Rev.* **D62** (2000) 123516, arXiv:hep-ph/0003018 [hep-ph].
- [265] Daniel G. Figueroa and Erwin H. Tanin, “Ability of LIGO and LISA to probe the equation of state of the early Universe,” *JCAP* **1908** (2019) 011, arXiv:1905.11960 [astro-ph.CO].
- [266] N. Bartolo, D. Bertacca, S. Matarrese, and others, “Anisotropies and non-Gaussianity of the Cosmological Gravitational Wave Background,” 2019.
- [267] Rachel Jeannerot, Jonathan Rocher, and Mairi Sakellariadou, “How generic is cosmic string formation in SUSY GUTs,” *Phys. Rev.* **D68** (2003) 103514, arXiv:hep-ph/0308134 [hep-ph].
- [268] Grigol Gogoberidze, Tina Kahniashvili, and Arthur Kosowsky, “The Spectrum of Gravitational Radiation from Primordial Turbulence,” *Phys. Rev.* **D76** (2007) 083002, arXiv:0705.1733 [astro-ph].
- [269] T. Regimbau, M. Evans, N. Christensen, and others, “Digging Deeper: Observing Primordial Gravitational Waves below the Binary-Black-Hole-Produced Stochastic Background,” *Phys. Rev. Lett.* **118** (Apr, 2017) 151105.  
<https://link.aps.org/doi/10.1103/PhysRevLett.118.151105>.
- [270] Curt Cutler and Jan Harms, “Big Bang Observer and the neutron-star-binary subtraction problem,” *Phys. Rev. D* **73** (Feb, 2006) 042001.  
<http://link.aps.org/doi/10.1103/PhysRevD.73.042001>.
- [271] Rory Smith and Eric Thrane, “Optimal Search for an Astrophysical Gravitational-Wave Background,” *Phys. Rev. X* **8** (Apr, 2018) 021019.  
<https://link.aps.org/doi/10.1103/PhysRevX.8.021019>.
- [272] Tania Regimbau, “The astrophysical gravitational wave stochastic background,” *Res. Astron. Astrophys.* **11** (2011) 369–390, arXiv:1101.2762 [astro-ph.CO].
- [273] Chiara Caprini, Daniel G. Figueroa, Raphael Flauger, and others, “Reconstructing the spectral shape of a stochastic gravitational wave background with LISA,” 2019.
- [274] Giulia Cusin, Cyril Pitrou, and Jean-Philippe Uzan, “Anisotropy of the astrophysical gravitational wave background: Analytic expression of the angular power spectrum and correlation with cosmological observations,” *Phys. Rev.* **D96** (2017) 103019, arXiv:1704.06184 [astro-ph.CO].
- [275] Giulia Cusin, Irina Dvorkin, Cyril Pitrou, and Jean-Philippe Uzan, “First predictions of the angular power spectrum of the astrophysical gravitational wave background,” *Phys. Rev. Lett.* **120** (2018) 231101, arXiv:1803.03236 [astro-ph.CO].

- 
- [276] Alexander C. Jenkins, Mairi Sakellariadou, Tania Regimbau, and Eric Slezak, “Anisotropies in the astrophysical gravitational-wave background: Predictions for the detection of compact binaries by LIGO and Virgo,” *Phys. Rev.* **D98** (2018) 063501, arXiv:1806.01718 [astro-ph.CO].
- [277] Alexander C. Jenkins, Richard O’Shaughnessy, Mairi Sakellariadou, and Daniel Wysocki, “Anisotropies in the astrophysical gravitational-wave background: The impact of black hole distributions,” *Phys. Rev. Lett.* **122** (2019) 111101, arXiv:1810.13435 [astro-ph.CO].
- [278] Alexander C. Jenkins, Mairi Sakellariadou, Tania Regimbau, and others, “Response to Cusin et al’s comment on arXiv:1810.13435,” 2019.
- [279] Giulia Cusin, Irina Dvorkin, Cyril Pitrou, and Jean-Philippe Uzan, “Properties of the stochastic astrophysical gravitational wave background: astrophysical sources dependencies,” *Phys. Rev.* **D100** (2019) 063004, arXiv:1904.07797 [astro-ph.CO].
- [280] Daniele Bertacca, Angelo Ricciardone, Nicola Bellomo, and others, “Projection effects on the observed angular spectrum of the astrophysical stochastic gravitational wave background,” 2019.
- [281] Guadalupe Cañas-Herrera, Omar Contigiani, and Valeri Vardanyan, “Cross-correlation of the astrophysical gravitational-wave background with galaxy clustering,” 2019.
- [282] A. I. Renzini and C. R. Contaldi, “Mapping Incoherent Gravitational Wave Backgrounds,” *Mon. Not. Roy. Astron. Soc.* **481** (2018) 4650–4661, arXiv:1806.11360 [astro-ph.IM].
- [283] S. Hild et al., “A xylophone configuration for a third-generation gravitational wave detector,” *Classical and Quantum Gravity* **27** (2010) 015003.  
<http://stacks.iop.org/0264-9381/27/015003>.
- [284] David Shoemaker, “Future limits to sensitivity.” G010026-00-G, 2001.
- [285] Gianni Conforto and Riccardo DeSalvo, “Proposal for lower frequency companions for the advanced LIGO gravitational wave interferometric detectors,” *Nuclear Instruments and Methods in Physics Research Section A: Accelerators, Spectrometers, Detectors and Associated Equipment* **518** no. 1-2, (2004) 228–232. <http://www.sciencedirect.com/science/article/B6TJM-4BT3HYH-2D/2/7b95d094bfdb00dfa6138c680dcfeb9>.  
Frontier Detectors for Frontier Physics: Proceeding.
- [286] Simon Chelkowski, Stefan Hild, and Andreas Freise, “Prospects of higher-order Laguerre-Gauss modes in future gravitational wave detectors,” *Phys. Rev. D* **79** no. 12, (Jun, 2009) 122002.
- [287] L. Pinard, C. Michel, B. Sassolas, and others, “Mirrors used in the LIGO interferometers for first detection of gravitational waves,” *Applied optics* **56** no. 4, (2017) C11–C15.
- [288] Jérôme Degallaix, Christophe Michel, Benoit Sassolas, and others, “Large and extremely low loss: the unique challenges of gravitational wave mirrors,” *J. Opt. Soc. Am. A* **36** no. 11, (2019) C85–C94.

- [289] MV Plissi, KA Strain, CI Torrie, and others, "Aspects of the suspension system for geo 600," *Review of scientific instruments* **69** no. 8, (1998) 3055–3061.
- [290] NA Robertson, G Cagnoli, DRM Crooks, and others, "Quadruple suspension design for advanced ligo," *Classical and Quantum Gravity* **19** no. 15, (2002) 4043.
- [291] M Lorenzini, Virgo Collaboration, et al., "The monolithic suspension for the virgo interferometer," *Classical and Quantum Gravity* **27** no. 8, (2010) 084021.
- [292] KG Lyon, GL Salinger, CA Swenson, and GK White, "Linear thermal expansion measurements on silicon from 6 to 340 k," *Journal of Applied Physics* **48** no. 3, (1977) 865–868.
- [293] DF McGuigan, CC Lam, RQ Gram, and others, "Measurements of the mechanical q of single-crystal silicon at low temperatures," *Journal of Low Temperature Physics* **30** no. 5, (1978) 621–629.
- [294] Jerome Degallaix, Raffaele Flaminio, Danièle Forest, and others, "Bulk optical absorption of high resistivity silicon at 1550 nm," *Optics letters* **38** no. 12, (2013) 2047–2049.
- [295] Alexander Khalaidovski, Jessica Steinlechner, and Roman Schnabel, "Indication for dominating surface absorption in crystalline silicon test masses at 1550 nm," *Classical and Quantum Gravity* **30** no. 16, (2013) 165001.
- [296] Angus S Bell, Jessica Steinlechner, Iain W Martin, and others, "Anomalous optical surface absorption in nominally pure silicon samples at 1550 nm," *Classical and Quantum Gravity* **34** no. 20, (2017) 205013.
- [297] Alan D Bristow, Nir Rotenberg, and Henry M Van Driel, "Two-photon absorption and kerr coefficients of silicon for 850–2200 nm," *Applied Physics Letters* **90** no. 19, (2007) 191104.
- [298] J Komma, C Schwarz, G Hofmann, D Heinert, and R Nawrodt, "Thermo-optic coefficient of silicon at 1550 nm and cryogenic temperatures," *Applied Physics Letters* **101** no. 4, (2012) 041905.
- [299] Christoph Krüger, Daniel Heinert, Alexander Khalaidovski, and others, "Birefringence measurements on crystalline silicon," *Classical and Quantum Gravity* **33** no. 1, (2015) 015012.
- [300] Eiichi Hirose, Dan Bajuk, GariLynn Billingsley, and others, "Sapphire mirror for the kagra gravitational wave detector," *Physical Review D* **89** no. 6, (2014) 062003.
- [301] F Acernese, M Agathos, K Agatsuma, and others, "Advanced virgo: a second-generation interferometric gravitational wave detector," *Classical and Quantum Gravity* **32** no. 2, (Dec, 2014) 024001. <https://doi.org/10.1088%2F0264-9381%2F32%2F2%2F024001>.
- [302] and J Aasi, B P Abbott, R Abbott, and others, "Advanced LIGO," *Classical and Quantum Gravity* **32** no. 7, (Mar, 2015) 074001. <https://doi.org/10.1088%2F0264-9381%2F32%2F7%2F074001>.
- [303] Akira E. Villar, Eric D. Black, Riccardo DeSalvo, and others, "Measurement of thermal noise

- in multilayer coatings with optimized layer thickness,” *Phys. Rev. D* **81** (Jun, 2010) 122001. <https://link.aps.org/doi/10.1103/PhysRevD.81.122001>.
- [304] Gregory M Harry, Andri M Gretarsson, Peter R Saulson, and others, “Thermal noise in interferometric gravitational wave detectors due to dielectric optical coatings,” *Classical and Quantum Gravity* **19** no. 5, (Feb, 2002) 897–917. <https://doi.org/10.1088/0264-9381/19/5/305>.
- [305] Gregory M Harry, Andri M Gretarsson, Peter R Saulson, and others, “Thermal noise in interferometric gravitational wave detectors due to dielectric optical coatings,” *Classical and Quantum Gravity* **19** no. 5, (Feb, 2002) 897–917. <https://doi.org/10.1088/0264-9381/19/5/305>.
- [306] Stuart Reid and Iain W Martin, “Development of mirror coatings for gravitational wave detectors,” *Coatings* **6** (Nov, 2016) 61. <https://doi.org/10.3390/coatings6040061>.
- [307] L. Pinard et al, “Mirrors used in the LIGO interferometers for first detection of gravitational waves,” *Appl. Opt.* **56** (2017) C11–C15.
- [308] R Flaminio, J Franc, C Michel, and others, “A study of coating mechanical and optical losses in view of reducing mirror thermal noise in gravitational wave detectors,” *Classical and Quantum Gravity* **27** no. 8, (2010) 084030. <http://stacks.iop.org/0264-9381/27/i=8/a=084030>.
- [309] Gregory M Harry, Matthew R Abernathy, Andres E Becerra-Toledo, and others, “Titania-doped tantala/silica coatings for gravitational-wave detection,” *Classical and Quantum Gravity* **24** no. 2, (2007) 405. <http://stacks.iop.org/0264-9381/24/i=2/a=008>.
- [310] M Granata, A Amato, L Balzarini, and others, “Amorphous optical coatings of present gravitational-wave interferometers,” *Classical and Quantum Gravity* **37** no. 9, (Apr, 2020) 095004. <https://doi.org/10.1088/0264-9381/37/9/095004>.
- [311] M. Granata, K. Craig, G. Cagnoli, and others, “Cryogenic measurements of mechanical loss of high-reflectivity coating and estimation of thermal noise,” *Opt. Lett.* **38** no. 24, (Dec, 2013) 5268–5271. <http://ol.osa.org/abstract.cfm?URI=ol-38-24-5268>.
- [312] I W Martin, R Nawrodt, K Craig, C Schwarz, et al., “Low temperature mechanical dissipation of an ion-beam sputtered silica film,” *Classical and Quantum Gravity* **31** no. 3, (2014) 035019. <http://stacks.iop.org/0264-9381/31/i=3/a=035019>.
- [313] I W Martin, E Chalkley, R Nawrodt, and others, “Comparison of the temperature dependence of the mechanical dissipation in thin films of Ta<sub>2</sub>O<sub>5</sub> and Ta<sub>2</sub>O<sub>5</sub> doped with TiO<sub>2</sub>,” *Classical and Quantum Gravity* **26** no. 15, (2009) 155012. <http://stacks.iop.org/0264-9381/26/i=15/a=155012>.
- [314] R. R. Robie, *Characterisation of the mechanical properties of thin-film mirror coating materials for use in future interferometric gravitational wave detectors*. PhD thesis, University of Glasgow, 2018.

- [315] I W Martin, R Bassiri, R Nawrodt, and others, “Effect of heat treatment on mechanical dissipation in Ta<sub>2</sub>O<sub>5</sub> coatings,” *Classical and Quantum Gravity* **27** no. 22, (2010) 225020. <http://stacks.iop.org/0264-9381/27/i=22/a=225020>.
- [316] Eiichi Hirose, Kieran Craig, Hideki Ishitsuka, and others, “Mechanical loss of a multilayer tantala/silica coating on a sapphire disk at cryogenic temperatures: Toward the KAGRA gravitational wave detector,” *Phys. Rev. D* **90** (Nov, 2014) 102004. <https://link.aps.org/doi/10.1103/PhysRevD.90.102004>.
- [317] Ting Hong, Huan Yang, Eric K. Gustafson, Rana X. Adhikari, and Yanbei Chen, “Brownian thermal noise in multilayer coated mirrors,” *Phys. Rev. D* **87** (Apr, 2013) 082001. <https://link.aps.org/doi/10.1103/PhysRevD.87.082001>.
- [318] A. Gurkovsky and S. Vyatchanin, “The thermal noise in multilayer coating,” *Phys. Lett. A* **374** (A, 2010) 3267. <https://doi.org/10.1016/j.physleta.2010.06.012>.
- [319] Michael L. Gorodetsky, “Thermal noises and noise compensation in high-reflection multilayer coating,” *Physics Letters A* **372** no. 46, (2008) 6813 – 6822. <http://www.sciencedirect.com/science/article/pii/S0375960108014692>.
- [320] N. M. Kondratiev, A. G. Gurkovsky, and M. L. Gorodetsky, “Thermal noise and coating optimization in multilayer dielectric mirrors,” *Phys. Rev. D* **84** (Jul, 2011) 022001. <https://link.aps.org/doi/10.1103/PhysRevD.84.022001>.
- [321] A V Cumming, L Cunningham, G D Hammond, and others, “Silicon mirror suspensions for gravitational wave detectors,” *Classical and Quantum Gravity* **31** no. 2, (Dec, 2013) 025017.
- [322] William Yam, Slawek Gras, and Matthew Evans, “Multimaterial coatings with reduced thermal noise,” *Phys. Rev. D* **91** (Feb, 2015) 042002. <http://link.aps.org/doi/10.1103/PhysRevD.91.042002>.
- [323] Jessica Steinlechner, Iain W. Martin, Jim Hough, and others, “Thermal noise reduction and absorption optimization via multimaterial coatings,” *Phys. Rev. D* **91** (Feb, 2015) 042001. <http://link.aps.org/doi/10.1103/PhysRevD.91.042001>.
- [324] Jessica Steinlechner, Christoph Krüger, Iain W. Martin, and others, “Optical absorption of silicon nitride membranes at 1064 nm and at 1550 nm,” *Phys. Rev. D* **96** (Jul, 2017) 022007. <https://link.aps.org/doi/10.1103/PhysRevD.96.022007>.
- [325] Peter M. Martin, ed., *Chapter 6 - Ion Plating*. William Andrew Publishing, Boston, third edition ed., 2010. <http://www.sciencedirect.com/science/article/pii/B9780815520313000065>.
- [326] Huang-Wei Pan, Ling-Chi Kuo, Lin-An Chang, and others, “Silicon nitride and silica quarter-wave stacks for low-thermal-noise mirror coatings,” *Phys. Rev. D* **98** (Nov, 2018) 102001. <https://link.aps.org/doi/10.1103/PhysRevD.98.102001>.
- [327] R. Birney, J. Steinlechner, Z. Tornasi, and others, “Amorphous silicon with extremely low absorption: Beating thermal noise in gravitational astronomy,” *Phys. Rev. Lett.* **121** (Nov, 2018) 191101. <https://link.aps.org/doi/10.1103/PhysRevLett.121.191101>.

- 
- [328] S. Gras, N. Demos, and M. Evans, “Alloys, nano-layers, and multi-material coatings.” <https://dcc.ligo.org/ligo-g1900995>, 2017.
- [329] M. Kinley-Hanlon et al., “Demonstration of multimaterial coatings for gravitational wave detectors.” <https://dcc.ligo.org/ligo-g1901633>, 2017.
- [330] Huang-Wei Pan, Shun-Jin Wang, Ling-Chi Kuo, and others, “Thickness-dependent crystallization on thermal anneal for titania/silica nm-layer composites deposited by ion beam sputter method,” *Opt. Express* **22** no. 24, (Dec, 2014) 29847–29854. <http://www.opticsexpress.org/abstract.cfm?URI=oe-22-24-29847>.
- [331] H. Sankur and W. Gunning, “Crystallization and diffusion in composite tio<sub>2</sub>-sio<sub>2</sub> thin films,” *Journal of Applied Physics* **66** no. 10, (1989) 4747–4751. <https://doi.org/10.1063/1.343784>.
- [332] Ling-Chi Kuo, Huang-Wei Pan, Chi-Li Chang, and Shiuh Chao, “Low cryogenic mechanical loss composite silica thin film for low thermal noise dielectric mirror coatings,” *Opt. Lett.* **44** no. 2, (Jan, 2019) 247–250. <http://ol.osa.org/abstract.cfm?URI=ol-44-2-247>.
- [333] Rashid Hamdan, Jonathan P. Trinastic, and H. P. Cheng, “Molecular dynamics study of the mechanical loss in amorphous pure and doped silica,” *The Journal of Chemical Physics* **141** no. 5, (2014) 054501. <https://doi.org/10.1063/1.4890958>.
- [334] Jonathan P. Trinastic, Rashid Hamdan, Chris Billman, and Hai-Ping Cheng, “Molecular dynamics modeling of mechanical loss in amorphous tantala and titania-doped tantala,” *Phys. Rev. B* **93** (Jan, 2016) 014105. <https://link.aps.org/doi/10.1103/PhysRevB.93.014105>.
- [335] Chris R. Billman, Jonathan P. Trinastic, Dustin J. Davis, Rashid Hamdan, and Hai-Ping Cheng, “Origin of the second peak in the mechanical loss function of amorphous silica,” *Phys. Rev. B* **95** (Jan, 2017) 014109. <https://link.aps.org/doi/10.1103/PhysRevB.95.014109>.
- [336] F. Puosi, F. Fidecaro, S. Capaccioli, D. Pisignano, and D. Leporini, “In silico broadband mechanical spectroscopy of amorphous tantala,” *Phys. Rev. Research* **1** (Nov, 2019) 033121. <https://link.aps.org/doi/10.1103/PhysRevResearch.1.033121>.
- [337] Martin J. Hart, Riccardo Bassiri, Konstantin B. Borisenko, and others, “Medium range structural order in amorphous tantala spatially resolved with changes to atomic structure by thermal annealing,” *Journal of Non-Crystalline Solids* **438** (2016) 10 – 17. <http://www.sciencedirect.com/science/article/pii/S0022309316300266>.
- [338] Massimo Granata, Elodie Coillet, Valérie Martinez, and others, “Correlated evolution of structure and mechanical loss of a sputtered silica film,” *Physical Review Materials* **2** no. 5, (2018) 053607.
- [339] Alex Amato, Silvana Terreni, Massimo Granata, and others, “Observation of a correlation between internal friction and urbach energy in amorphous oxides thin films,” *Scientific Reports* **10** no. 1, (2020) 1670. <https://doi.org/10.1038/s41598-020-58380-1>.
- [340] K. Prasai, J. Jiang, A. Mishkin, and others, “High precision detection of change in intermediate range order of amorphous zirconia-doped tantala thin films due to annealing,”

- Phys. Rev. Lett.* **123** (Jul, 2019) 045501.  
<https://link.aps.org/doi/10.1103/PhysRevLett.123.045501>.
- [341] Xiao Liu, B. E. White, Jr., R. O. Pohl, and others, “Amorphous solid without low energy excitations,” *Phys. Rev. Lett.* **78** (Jun, 1997) 4418–4421.  
<https://link.aps.org/doi/10.1103/PhysRevLett.78.4418>.
- [342] Peter G. Murray, Iain W. Martin, Kieran Craig, and others, “Ion-beam sputtered amorphous silicon films for cryogenic precision measurement systems,” *Phys. Rev. D* **92** (Sep, 2015) 062001. <http://link.aps.org/doi/10.1103/PhysRevD.92.062001>.
- [343] Xiao Liu, Daniel R. Queen, Thomas H. Metcalf, Julie E. Karel, and Frances Hellman, “Hydrogen-free amorphous silicon with no tunneling states,” *Phys. Rev. Lett.* **113** (Jul, 2014) 025503. <https://link.aps.org/doi/10.1103/PhysRevLett.113.025503>.
- [344] J. Steinlechner, I. W. Martin, R. Bassiri, and others, “Optical absorption of ion-beam sputtered amorphous silicon coatings,” *Phys. Rev. D* **93** (Mar, 2016) 062005.  
<http://link.aps.org/doi/10.1103/PhysRevD.93.062005>.
- [345] R. Birney, J. Steinlechner, Z. Tornasi, and others, “Amorphous silicon with extremely low absorption: Beating thermal noise in gravitational astronomy,” *Phys. Rev. Lett.* **121** (Nov, 2018) 191101. <https://link.aps.org/doi/10.1103/PhysRevLett.121.191101>.
- [346] J. Steinlechner, I. W. Martin, A. S. Bell, and others, “Silicon-based optical mirror coatings for ultrahigh precision metrology and sensing,” *Phys. Rev. Lett.* **120** (Jun, 2018) 263602.  
<https://link.aps.org/doi/10.1103/PhysRevLett.120.263602>.
- [347] Alex Amato, Gianpietro Cagnoli, Maurizio Canepa, and others, “High-reflection coatings for gravitational-wave detectors: state of the art and future developments,” *Journal of Physics: Conference Series* **957** (Feb, 2018) 012006.  
<https://doi.org/10.1088%2F1742-6596%2F957%2F1%2F012006>.
- [348] Xiao Liu, Thomas H Metcalf, Qi Wang, and Douglas M Photiadis, “Elastic properties of several silicon nitride films,” *MRS Proceedings* **989** (2007) 0989–A22–01.
- [349] D. R. Southworth, R. A. Barton, S. S. Verbridge, and others, “Stress and silicon nitride: A crack in the universal dissipation of glasses,” *Phys. Rev. Lett.* **102** (Jun, 2009) 225503.  
<https://link.aps.org/doi/10.1103/PhysRevLett.102.225503>.
- [350] H. Pan et al., “Silicon nitride films fabricated by plasma enhanced chemical vapor deposition method for coatings of the laser interferometric gravitational waves detector,” *Physical Review D* **97** (2018) 022004.
- [351] J. Steinlechner, C. Krüger, I. W. Martin, and others, “Optical absorption of silicon nitride membranes at 1064 nm and at 1550 nm,” *Phys. Rev. D* **96** (Jul, 2017) 022007.  
<https://link.aps.org/doi/10.1103/PhysRevD.96.022007>.
- [352] M R Abernathy, S Reid, E Chalkley, and others, “Cryogenic mechanical loss measurements of heat-treated hafnium dioxide,” *Classical and Quantum Gravity* **28** no. 19, (Sep, 2011) 195017.  
<https://doi.org/10.1088%2F0264-9381%2F28%2F19%2F195017>.

- 
- [353] K. Craig, *Studies of the mechanical dissipation of thin films for mirrors in interferometric gravitational wave detectors*. PhD thesis, University of Glasgow, 2015.
- [354] Garrett D. Cole, “Cavity optomechanics with low-noise crystalline mirrors,” in *Optical Trapping and Optical Micromanipulation IX*, Kishan Dholakia and Gabriel C. Spalding, eds., vol. 8458, pp. 28 – 38, International Society for Optics and Photonics. SPIE, 2012.  
<https://doi.org/10.1117/12.931226>.
- [355] Garrett D. Cole, Wei Zhang, Bryce J. Bjork, and others, “High-performance near- and mid-infrared crystalline coatings,” *Optica* **3** no. 6, (Jun, 2016) 647–656.  
<http://www.osapublishing.org/optica/abstract.cfm?URI=optica-3-6-647>.
- [356] Steven D. Penn, Maya M. Kinley-Hanlon, Ian A. O. MacMillan, and others, “Mechanical ringdown studies of large-area substrate-transferred GaAs/AlGaAs crystalline coatings,” *J. Opt. Soc. Am. B* **36** no. 4, (Apr, 2019) C15–C21.  
<http://josab.osa.org/abstract.cfm?URI=josab-36-4-C15>.
- [357] G. D. Cole, W. Zhang, M. J. Martin, J. Ye, and M. Aspelmeyer, “Tenfold reduction of brownian noise in high-reflectivity optical coatings,” *Nature Photonics* **7** no. 644, (2013) 644–650.
- [358] Angie C. Lin, Riccardo Bassiri, Kieran Craig, and others, “Epitaxial integration of monocrystalline III-V coatings on silicon for thermal noise reduction,” in *Optical Interference Coatings*, p. MA.2. Optical Society of America, 2013.  
<http://www.osapublishing.org/abstract.cfm?URI=OIC-2013-MA.2>.
- [359] A V Cumming, K Craig, I W Martin, and others, “Measurement of the mechanical loss of prototype GaP/AlGaP crystalline coatings for future gravitational wave detectors,” *Classical and Quantum Gravity* **32** no. 3, (2015) 035002.  
<http://stacks.iop.org/0264-9381/32/i=3/a=035002>.
- [360] Angie C. Lin, Riccardo Bassiri, Suraya Omar, and others, “Epitaxial growth of GaP/AlGaP mirrors on Si for low thermal noise optical coatings,” *Opt. Mater. Express* **5** no. 8, (Aug, 2015) 1890–1897.  
<http://www.osapublishing.org/ome/abstract.cfm?URI=ome-5-8-1890>.
- [361] P. Kwee, C. Bogan, K. Danzmann, and others, “Stabilized high-power laser system for the gravitational wave detector advanced LIGO,” *Opt. Express* **20** no. 10, (2012) 10617–10634.  
<http://www.opticsexpress.org/abstract.cfm?URI=oe-20-10-10617>.
- [362] Nina Bode, Fabian Meylahn, and Benno Willke, ““a 200 w laser system based on sequential Nd:YVO<sub>4</sub> laser amplifiers for second-generation gravitational wave detectors,”” 2020.
- [363] Benno Willke, “neovan-4s laser amplifier in o3 and o4,” 2019.  
<https://dcc.ligo.org/LIGO-G1900530>.
- [364] J. Limpert, O. Schmidt, J. Rothhardt, and others, “Extended single-mode photonic crystal fiber lasers,” *Opt. Express* **14** no. 7, (2006) 2715–2720.  
<http://www.opticsexpress.org/abstract.cfm?URI=oe-14-7-2715>.
- [365] Guancheng Gu, Fanting Kong, Thomas Hawkins, and others, “Ytterbium-doped large-mode-area all-solid photonic bandgap fiber lasers,” *Opt. Express* **22** no. 11, (June, 2014)

- 13962–13968.  
<https://www.osapublishing.org/oe/abstract.cfm?uri=oe-22-11-13962>.
- [366] Xiuquan Ma, Cheng Zhu, I.-Ning Hu, Alex Kaplan, and Almantas Galvanauskas, “Single-mode chirally-coupled-core fibers with larger than 50 $\mu$ m diameter cores,” *Opt. Express* **22** no. 8, (Apr., 2014) 9206–9219.  
<https://www.osapublishing.org/oe/abstract.cfm?uri=oe-22-8-9206>.
- [367] T. Theeg, H. Sayinc, J. Neumann, and D. Kracht, “All-fiber counter-propagation pumped single frequency amplifier stage with 300 w output power,” *Photonics Technology Letters, IEEE* **24** no. 20, (2012) 1864–1867.
- [368] Jian Zhao, Germain Guiraud, Christophe Pierre, and others, “High-power all-fiber ultra-low noise laser,” *Appl. Phys. B* **124** no. 6, (May, 2018) 114.  
<https://doi.org/10.1007/s00340-018-6989-7>.
- [369] Aaron Buikema, Franklin Jose, Steven J. Augst, Peter Fritschel, and Nergis Mavalvala, “Narrow-linewidth fiber amplifier for gravitational-wave detectors,” *Opt. Lett.* **44** no. 15, (Aug, 2019) 3833–3836. <http://ol.osa.org/abstract.cfm?URI=ol-44-15-3833>.
- [370] Felix Wellmann, Michael Steinke, Fabian Meylahn, and others, “High power, single-frequency, monolithic fiber amplifier for the next generation of gravitational wave detectors,” *Opt. Express* **27** no. 20, (Sept., 2019) 28523–28533.  
<https://www.osapublishing.org/oe/abstract.cfm?uri=oe-27-20-28523>.
- [371] C. Dixneuf, G. Guiraud, Y.V. Bardin, and others, “Robust all-fiber 200w single frequency laser at 1064 nm with low intensity noise,” in *2019 Conference on Lasers and Electro-Optics Europe and European Quantum Electronics Conference*, p. "cj\_p\_21". Optical Society of America, 2019. "http://www.osapublishing.org/abstract.cfm?URI=CLEO\_Europe-2019-cj\_p\_21".
- [372] Jinye Zhang and M. R. Phillips, “Modeling Intensity Noise Caused by Stimulated Brillouin Scattering in Optical Fibers,” in *Conference on Lasers and Electro-Optics/Quantum Electronics and Laser Science and Photonic Applications Systems Technologies (2005)*, paper CMH6, p. CMH6. Optical Society of America, May, 2005.  
<https://www.osapublishing.org/abstract.cfm?uri=CLEO-2005-CMH6>.
- [373] Li-Wei Wei, Frédéric Cleva, and Catherine Nary Man, “Coherently combined master oscillator fiber power amplifiers for advanced virgo,” *Opt. Lett.* **41** no. 24, (Dec, 2016) 5817–5820. <http://ol.osa.org/abstract.cfm?URI=ol-41-24-5817>.
- [374] F. Wellman, M. Steinke, F. Meylahn, and others, “Reliable high power fiber amplifiers for gravitational wave detectors,” 2020. <https://dcc.ligo.org/LIGO-G2000404>.
- [375] Fabian Meylahn and Benno Willke, “Pre-stabilized laser system at a wavelength of 1550nm for future gravitational wave detectors,” 2019. <https://dcc.ligo.org/LIGO-G1901554>.
- [376] Omar De Varona, Willy Fittkau, Phillip Booker, and others, “Single-frequency fiber amplifier at 1.5  $\mu$ m with 100w in the linearly-polarized TEM<sub>00</sub> mode for next-generation gravitational

- 
- wave detectors,” *Opt. Express* **25** no. 21, (2017) 24880–24892.  
<https://www.osapublishing.org/oe/abstract.cfm?uri=oe-25-21-24880>.
- [377] Patrick Kwee, Benno Willke, and Karsten Danzmann, “Shot-noise-limited laser power stabilization with a high-power photodiode array,” *Opt. Lett.*, *OL* **34** no. 19, (Oct., 2009) 2912–2914.  
<https://www.osapublishing.org/ol/abstract.cfm?uri=ol-34-19-2912>.
- [378] Steffen Kaufer and Benno Willke, “Optical AC coupling power stabilization at frequencies close to the gravitational wave detection band,” *Opt. Lett.* **44** no. 8, (2019) 1916–1919.  
<https://www.osapublishing.org/ol/abstract.cfm?uri=ol-44-8-1916>.
- [379] Henning Vahlbruch, Dennis Wilken, Moritz Mehmet, and Benno Willke, “Laser power stabilization beyond the shot noise limit using squeezed light,” *Physical Review Letters* **121** no. 17, (2018) 173601.  
<https://link.aps.org/doi/10.1103/PhysRevLett.121.173601>.
- [380] V. B. Braginsky, “Classical and quantum restrictions on detection of weak distributions of a macroscopic oscillator,” *Sov. Phys. JETP* **26** (1968) 831.
- [381] V. B. Braginsky and F. Ya. Khalili, “Quantum measurement,” in *Quantum measurement*, Kip S. Thorne, ed. Cambridge University Press, 1999.
- [382] Stefan L. Danilishin, Farid Ya. Khalili, and Haixing Miao, “Advanced quantum techniques for future gravitational-wave detectors,” *Living Reviews in Relativity* **22** no. 1, (Apr, 2019) 2.  
<https://doi.org/10.1007/s41114-019-0018-y>.
- [383] Haixing Miao, Rana X Adhikari, Yiqiu Ma, Belinda Pang, and Yanbei Chen, “Towards the fundamental quantum limit of linear measurements of classical signals,” *Phys. Rev. Lett.* **119** (Aug, 2017) 050801.  
<https://link.aps.org/doi/10.1103/PhysRevLett.119.050801>.
- [384] Haixing Miao and Matthew Evans, “Quantum limit for laser interferometric gravitational wave detectors from optical dissipation,” 2017. <https://dcc.ligo.org/LIGO-P1700202>.
- [385] V.B.Braginsky, M.L.Gorodetsky, F.Ya.Khalili and K.S.Thorne, “Energetic quantum limit in large-scale interferometers,” in *Gravitational waves. Third Edoardo Amaldi Conference, Pasadena, California 12-16 July*, S.Meshkov, ed., pp. 180–189. Melville NY:AIP Conf. Proc. 523, 2000.
- [386] Mankei Tsang, Howard M. Wiseman, and Carlton M. Caves, “Fundamental quantum limit to waveform estimation,” *Phys. Rev. Lett.* **106** (2011) 090401.  
<http://journals.aps.org/prl/abstract/10.1103/PhysRevLett.106.090401>.
- [387] W. G. Unruh, “Quantum nondemolition and gravity-wave detection,” *Phys. Rev. D* **19** no. 10, (May, 1979) 2888–2896.
- [388] J. Abadie, B.P. Abbott, R. Abbott, and others, “A gravitational wave observatory operating beyond the quantum shot-noise limit,” *Nature Physics* **7** no. 12, (2011) 962–965.

- [389] J. Aasi *et al.*, “Enhanced sensitivity of the ligo gravitational wave detector by using squeezed states of light,” *Nature Photonics* **7** (2013) 613–619.
- [390] H. J. Kimble, Y. Levin, A. B. Matsko, K. S. Thorne, and S. P. Vyatchanin, “Conversion of conventional gravitational-wave interferometers into quantum nondemolition interferometers by modifying their input and/or output optics,” *Phys. Rev. D* **65** no. 2, (Dec, 2001) 022002.
- [391] **VIRGO** Collaboration, F. Acernese *et al.*, “Advanced Virgo: a second-generation interferometric gravitational wave detector,” *Class. Quant. Grav.* **32** no. 2, (2014) 024001, arXiv:1408.3978 [gr-qc].
- [392] **LIGO Scientific** Collaboration, J. Aasi *et al.*, “Advanced LIGO,” *Class. Quant. Grav.* **32** (2015) 074001, arXiv:1411.4547 [gr-qc].
- [393] C.M. Caves, “Quantum-mechanical noise in an interferometer,” *Phys. Rev. D* **23** (1981) 1693–1708.
- [394] J. Abadie, B. P. Abbott, R. Abbott, and others, “A gravitational wave observatory operating beyond the quantum shot-noise limit,” *Nature Physics* **7** no. 12, (2011) 962–965. <https://doi.org/10.1038/nphys2083>.
- [395] Roman Schnabel, “Squeezed states of light and their applications in laser interferometers,” *Physics Reports* **684** (2017) 1–51. <http://www.sciencedirect.com/science/article/pii/S0370157317300595?via%3Dihub>.
- [396] T. Isogai, J. Miller, P. Kwee, L. Barsotti, and M. Evans, “Loss in long-storage-time optical cavities,” *Opt. Express* **21** no. 24, (2013) 30114–30125. <http://www.opticsexpress.org/abstract.cfm?URI=oe-21-24-30114>.
- [397] Eric Oelker, Tomoki Isogai, John Miller, and others, “Audio-Band Frequency-Dependent Squeezing for Gravitational-Wave Detectors,” *Phys. Rev. Lett.* **116** no. 4, (2016) 041102. <https://journals.aps.org/prl/abstract/10.1103/PhysRevLett.116.041102>.
- [398] L. McCuller, C. Whittle, D. Ganapathy, and others, “Frequency-dependent squeezing for advanced ligo,” *Phys. Rev. Lett.* **124** (Apr, 2020) 171102. <https://link.aps.org/doi/10.1103/PhysRevLett.124.171102>.
- [399] Yuhang Zhao, Naoki Aritomi, Eleonora Capocasa, and others, “Frequency-dependent squeezed vacuum source for broadband quantum noise reduction in advanced gravitational-wave detectors,” *Phys. Rev. Lett.* **124** (Apr, 2020) 171101. <https://link.aps.org/doi/10.1103/PhysRevLett.124.171101>.
- [400] Yiqiu Ma, Haixing Miao, Belinda Heyun Pang, and others, “Proposal for gravitational-wave detection beyond the standard quantum limit through EPR entanglement,” *Nature Physics* **13** no. 8, (Aug, 2017) 776–780.
- [401] Min Jet Yap, Paul Altin, Terry G. McRae, and others, “Generation and control of frequency dependent squeezing via EPR entanglement,” *arXiv e-prints* (Aug, 2019) arXiv:1908.08685, arXiv:1908.08685 [quant-ph].
- [402] Jan Südbeck, Sebastian Steinlechner, Mikhail Korobko, and Roman Schnabel, “Demonstration

- 
- of interferometer enhancement through EPR entanglement,” *arXiv e-prints* (Aug, 2019) arXiv:1908.09602, arXiv:1908.09602 [quant-ph].
- [403] Vladimir B. Braginsky, Mikhail L. Gorodetsky, Farid Ya. Khalili, and Kip S. Thorne, “Dual-resonator speed meter for a free test mass,” *Phys. Rev. D* **61** (2000) 044002.
- [404] F.Ya Khalili, “Quantum speedmeter and laser interferometric gravitational-wave antennae,” 2002.
- [405] Patricia Purdue, “Analysis of a quantum nondemolition speed-meter interferometer,” *Phys. Rev. D* **66** (2002) 022001.
- [406] P. Purdue, “Analysis of a quantum nondemolition speed-meter interferometer,” *Phys. Rev. D* **66** (2002) 022001.
- [407] Y. Chen, “Sagnac interferometer as a speed-meter-type, quantum-nondemolition gravitational-wave detector,” *Phys. Rev. D* **67** (2003) 122004.
- [408] S. L. Danilishin, “Sensitivity limitations in optical speed meter topology of gravitational-wave antennas,” *Phys. Rev. D* **69** (2004) 102003, arXiv:gr-qc/0312016.
- [409] C. Gräf, B. W. Barr, A. S. Bell, and others, “Design of a speed meter interferometer proof-of-principle experiment,” *Classical and Quantum Gravity* **31** no. 21, (Nov., 2014) 215009, arXiv:1405.2783 [gr-qc].
- [410] S. L. Danilishin, “Sensitivity limitations in optical speed meter topology of gravitational-wave antennas,” *Phys. Rev. D* **69** (2004) 102003.
- [411] Mengyao Wang, Charlotte Bond, Daniel Brown, and others, “Realistic polarizing Sagnac topology with DC readout for the Einstein Telescope,” *Phys. Rev. D* **87** (May, 2013) 096008. <http://link.aps.org/doi/10.1103/PhysRevD.87.096008>.
- [412] Andrew R. Wade, Kirk McKenzie, Yanbei Chen, and others, “Polarization speed meter for gravitational-wave detection,” *Phys. Rev. D* **86** (Sep, 2012) 062001. <http://link.aps.org/doi/10.1103/PhysRevD.86.062001>.
- [413] S. L. Danilishin, E. Knyazev, N. V. Voronchev, and others, “A new quantum speed-meter interferometer: Measuring speed to search for intermediate mass black holes,” *Light: Science & Applications* **7** (2018) 11, arXiv:1702.01029 [gr-qc]. <https://www.nature.com/articles/s41377-018-0004-2>.
- [414] E. Knyazev, S. Danilishin, S. Hild, and F.Ya. Khalili, “Speedmeter scheme for gravitational-wave detectors based on epr quantum entanglement,” *Physics Letters A* **382** (2018) 2219–2225. <http://www.sciencedirect.com/science/article/pii/S0375960117302888>.
- [415] Andreas Freise, Haixing Miao, and Daniel D. Brown, “Simplified optical configuration for sloshing speedmeter enhanced gravitational wave detector,” *arXiv e-prints* (Sep, 2019) arXiv:1909.04185, arXiv:1909.04185 [gr-qc].
- [416] S. L. Danilishin, C. Gräf, S. S. Leavey, and others, “Quantum noise of non-ideal Sagnac speed

- meter interferometer with asymmetries,” *New Journal of Physics* **17** no. 4, (Apr., 2015) 043031, arXiv:1412.0931 [quant-ph].
- [417] T Zhang, E Knyazev, S Steinlechner, and others, “Quantum noise cancellation in asymmetric speed metres with balanced homodyne readout,” *New Journal of Physics* **20** no. 10, (2018) 103040. <http://stacks.iop.org/1367-2630/20/i=10/a=103040>.
- [418] Teng Zhang, Stefan L. Danilishin, Sebastian Steinlechner, and others, “Effects of static and dynamic higher-order optical modes in balanced homodyne readout for future gravitational waves detectors,” *Phys. Rev. D* **95** (Mar, 2017) 062001. <http://link.aps.org/doi/10.1103/PhysRevD.95.062001>.
- [419] A Wicht, K Danzmann, M Fleischhauer, and others, “White-light cavities, atomic phase coherence, and gravitational wave detectors,” *Optics Communications* **134** (1997) 431. <http://www.sciencedirect.com/science/article/pii/S0030401896005792>.
- [420] M. Korobko, L. Kleybolte, S. Ast, and others, “Beating the Standard Sensitivity-Bandwidth Limit of Cavity-Enhanced Interferometers with Internal Squeezed-Light Generation,” *Physical Review Letters* **118** no. 14, (Apr, 2017) 143601. <http://link.aps.org/doi/10.1103/PhysRevLett.118.143601>.
- [421] Haixing Miao, Yiqiu Ma, Chunnong Zhao, and Yanbei Chen, “Enhancing the Bandwidth of Gravitational-Wave Detectors with Unstable Optomechanical Filters,” *Phys. Rev. Lett.* **115** no. 21, (Nov, 2015) 211104. <https://link.aps.org/doi/10.1103/PhysRevLett.115.211104>.
- [422] V. Peano, H. G L Schwefel, Ch Marquardt, and F. Marquardt, “Intracavity Squeezing Can Enhance Quantum-Limited Optomechanical Position Detection through Deamplification,” *Phys. Rev. Lett.* **115** no. 24, (2015) 243603. <http://journals.aps.org/prl/abstract/10.1103/PhysRevLett.115.243603>.
- [423] Haixing Miao, Huan Yang, and Denis Martynov, “Towards the design of gravitational-wave detectors for probing neutron-star physics,” *Phys. Rev. D* **98** (Aug, 2018) 044044. <https://link.aps.org/doi/10.1103/PhysRevD.98.044044>.
- [424] K. Somiya, Y. Kataoka, J. Kato, N. Saito, and K. Yano, “Parametric signal amplification to create a stiff optical bar,” *Physics Letters A* **380** no. 4, (2016) 521 – 524. <http://www.sciencedirect.com/science/article/pii/S0375960115009883>.
- [425] Mikhail Korobko, F.Ya. Khalili, and Roman Schnabel, “Engineering the optical spring via intra-cavity optical-parametric amplification,” *Physics Letters A* **382** no. 33, (2018) 2238 – 2244. <http://www.sciencedirect.com/science/article/pii/S0375960117303146>.  
Special Issue in memory of Professor V.B. Braginsky.
- [426] Mankei Tsang and Carlton M. Caves, “Coherent quantum-noise cancellation for optomechanical sensors,” *Phys. Rev. Lett.* **105** (Sep, 2010) 123601. <https://link.aps.org/doi/10.1103/PhysRevLett.105.123601>.
- [427] Maximilian H. Wimmer, Daniel Steinmeyer, Klemens Hammerer, and Michèle Heurs,

- “Coherent cancellation of backaction noise in optomechanical force measurements,” *Phys. Rev. A* **89** (May, 2014) 053836.  
<https://link.aps.org/doi/10.1103/PhysRevA.89.053836>.
- [428] F.Ya Khalili and E.S. Polzik, “Overcoming the sql in gravitational wave detectors using spin systems with negative effective mass,” 2017.
- [429] Christoffer B. Møller, Rodrigo A. Thomas, Georgios Vasilakis, and others, “Quantum back-action-evading measurement of motion in a negative mass reference frame,” *Nature* **547** no. 7662, (Jul, 2017) 191–195.
- [430] K. L. Dooley, E. Schreiber, H. Vahlbruch, and others, “Phase control of squeezed vacuum states of light in gravitational wave detectors,” *Opt. Express* **23** no. 7, (Apr, 2015) 8235–8245.  
<http://www.opticsexpress.org/abstract.cfm?URI=oe-23-7-8235>.
- [431] E. Schreiber, K. L. Dooley, H. Vahlbruch, and others, “Alignment sensing and control for squeezed vacuum states of light,” *Opt. Express* **24** no. 1, (Jan, 2016) 146–152.  
<http://www.opticsexpress.org/abstract.cfm?URI=oe-24-1-146>.
- [432] Hartmut Grote, Michael Weinert, Rana Adhikari, and others, “High power and ultra-low-noise photodetector for squeezed-light enhanced gravitational wave detectors,” *Optics express* **24** (09, 2016) 20107–20118.
- [433] H. Grote, K. Danzmann, K. L. Dooley, and others, “First long-term application of squeezed states of light in a gravitational-wave observatory,” *Phys. Rev. Lett.* **110** (May, 2013) 181101.  
<https://link.aps.org/doi/10.1103/PhysRevLett.110.181101>.
- [434] K L Dooley, J R Leong, T Adams, and others, “GEO 600 and the GEO-HF upgrade program: successes and challenges,” *Classical and Quantum Gravity* **33** no. 7, (Mar, 2016) 075009.  
<https://doi.org/10.1088%2F0264-9381%2F33%2F7%2F075009>.
- [435] W. G. Unruh, “Quantum optics, experimental gravitation and measurement theory,” in *Quantum Optics, Experimental Gravitation and Measurement Theory*, P. Meystre and M. O. Scully, eds., ch. 6, p. 647. Plenum, New York, 1982.
- [436] Horace P. Yuen, “Contractive states and the standard quantum limit for monitoring free-mass positions,” *Phys. Rev. Lett.* **51** no. 9, (Aug, 1983) 719–722.
- [437] A. F. Pace, M. J. Collett, and D. F. Walls, “Quantum limits in interferometric detection of gravitational radiation,” *Phys. Rev. A* **47** no. 4, (Apr, 1993) 3173–3189.
- [438] S Hild et al., “Sensitivity studies for third-generation gravitational wave observatories,” *Classical and Quantum Gravity* **28** no. 9, (2011) 094013.  
<http://stacks.iop.org/0264-9381/28/i=9/a=094013>.
- [439] Simon Chelkowski, Henning Vahlbruch, Boris Hage, and others, “Experimental characterization of frequency-dependent squeezed light,” *Phys. Rev. A* **71** (Jan, 2005) 013806.  
<https://link.aps.org/doi/10.1103/PhysRevA.71.013806>.
- [440] L McCuller, “A+,” 2019.  
<https://agenda.infn.it/event/15928/timetable/?view=standard>.

- [441] J. Degallaix, “Adv+,” 2019.  
<https://agenda.infn.it/event/15928/timetable/?view=standard>.
- [442] P. Kwee, J. Miller, T. Isogai, L. Barsotti, and M. Evans, “Decoherence and degradation of squeezed states in quantum filter cavities,” *Phys. Rev. D* **90** (Sep, 2014) 062006.  
<https://link.aps.org/doi/10.1103/PhysRevD.90.062006>.
- [443] F. Ya. Khalili, “Optimal configurations of filter cavity in future gravitational-wave detectors,” *Phys. Rev. D* **81** (Jun, 2010) 122002.  
<https://link.aps.org/doi/10.1103/PhysRevD.81.122002>.
- [444] M. Evans, L. Barsotti, P. Kwee, J. Harms, and H. Miao, “Realistic filter cavities for advanced gravitational wave detectors,” *Phys. Rev. D* **88** (Jul, 2013) 022002.  
<https://link.aps.org/doi/10.1103/PhysRevD.88.022002>.
- [445] Eleonora Capocasa, Yuefan Guo, Marc Eisenmann, and others, “Measurement of optical losses in a high-finesse 300 m filter cavity for broadband quantum noise reduction in gravitational-wave detectors,” *Phys. Rev. D* **98** (Jul, 2018) 022010.  
<https://link.aps.org/doi/10.1103/PhysRevD.98.022010>.
- [446] Philip Jones, Teng Zhang, Haixing Miao, and Andreas Freise, “Implications of the quantum noise target for the einstein telescope infrastructure design,” *Phys. Rev. D* **101** (Apr, 2020) 082002. <https://link.aps.org/doi/10.1103/PhysRevD.101.082002>.
- [447] Axel Schönbeck, Fabian Thies, and Roman Schnabel, “13&#x2009;&#x2009;db squeezed vacuum states at 1550&#x2009;&#x2009;nm from 12&#x2009;&#x2009;mw external pump power at 775&#x2009;&#x2009;nm,” *Opt. Lett.* **43** no. 1, (Jan, 2018) 110–113.  
<http://ol.osa.org/abstract.cfm?URI=ol-43-1-110>.
- [448] Henning Vahlbruch, Simon Chelkowski, Boris Hage, and others, “Coherent control of vacuum squeezing in the gravitational-wave detection band,” *Phys. Rev. Lett.* **97** (Jul, 2006) 011101.  
<https://link.aps.org/doi/10.1103/PhysRevLett.97.011101>.
- [449] H Vahlbruch, S Chelkowski, K Danzmann, and R Schnabel, “Quantum engineering of squeezed states for quantum communication and metrology,” *New Journal of Physics* **9** no. 10, (Oct, 2007) 371–371. <https://doi.org/10.1088%2F1367-2630%2F9%2F10%2F371>.
- [450] M S Stefszky, C M Mow-Lowry, S S Y Chua, and others, “Balanced homodyne detection of optical quantum states at audio-band frequencies and below,” *Classical and Quantum Gravity* **29** no. 14, (Jun, 2012) 145015.  
<https://doi.org/10.1088%2F0264-9381%2F29%2F14%2F145015>.
- [451] A. R. Wade, G. L. Mansell, T. G. McRae, and others, “Optomechanical design and construction of a vacuum-compatible optical parametric oscillator for generation of squeezed light,” *Review of Scientific Instruments* **87** no. 6, (2016) 063104,  
<https://doi.org/10.1063/1.4953326>. <https://doi.org/10.1063/1.4953326>.
- [452] Eric Genin, Maddalena Mantovani, Gabriel Pillant, and others, “Vacuum-compatible low-loss faraday isolator for efficient squeezed-light injection in laser-interferometer-based gravitational-wave detectors,” *Appl. Opt.* **57** no. 32, (2018) 9705–9713.

- 
- [453] Moritz Mehmet, Stefan Ast, Tobias Eberle, and others, “Squeezed light at 1550 nm with a quantum noise reduction of 12.3 db,” *Opt. Express* **19** no. 25, (Dec, 2011) 25763–25772. <http://www.opticsexpress.org/abstract.cfm?URI=oe-19-25-25763>.
- [454] Axel Schönbeck, *Compact squeezed-light source at 1550 nm*. PhD thesis, Universität Hamburg, 2018.
- [455] B. Canuel, R. Day, E. Genin, and others, “Adv inj: Preliminary design study.” <https://tds.virgo-gw.eu/?content=3&r=6614>. Internal Virgo Note (VIR-0023A-09).
- [456] Oleg V. Palashov, Dmitry S. Zheleznov, Alexander V. Voitovich, and others, “High-vacuum-compatible high-power faraday isolators for gravitational-wave interferometers,” *J. Opt. Soc. Am. B* **29** no. 7, (Jul, 2012) 1784–1792. <http://josab.osa.org/abstract.cfm?URI=josab-29-7-1784>.
- [457] Peter Fritschel, Matthew Evans, and Valery Frolov, “Balanced homodyne readout for quantum limited gravitational wave detectors,” *Opt. Express* **22** no. 4, (Feb, 2014) 4224–4234. <http://www.opticsexpress.org/abstract.cfm?URI=oe-22-4-4224>.
- [458] R. Gouaty, G. L. Corre, B. Mours, L. Rolland, and E. Tournefier, “Advanced virgo output mode cleaner: revision of the specifications.” <https://tds.virgo-gw.eu/?content=3&r=8319>. Internal Virgo Note (VIR-0020A-11).
- [459] Koji Arai, Sam Barnum, Peter Fritschel, Jeffrey Lewis, and Sam Waldman, “The final design for the advanced ligo output mode cleaner (omc),” 2010. <https://dcc.ligo.org/T1000276>.
- [460] M Prijatelj, H Grote, J Degallaix, and others, “Control and automatic alignment of the output mode cleaner of GEO 600,” *Journal of Physics: Conference Series* **228** (May, 2010) 012014. <https://doi.org/10.1088%2F1742-6596%2F228%2F1%2F012014>.
- [461] H Billing, K Maischberger, A Rudiger, and others, “An argon laser interferometer for the detection of gravitational radiation,” *Journal of Physics E: Scientific Instruments* **12** no. 11, (Nov, 1979) 1043–1050. <https://doi.org/10.1088%2F0022-3735%2F12%2F11%2F010>.
- [462] K. S. Thorne, “Output mode cleaner design.” <https://dcc.ligo.org/ligo-t890017/public>, 1989. <https://dcc.ligo.org/LIGO-T890017/public>.
- [463] J-Y. Vinet, V. Brisson, and S. Braccini, “Scattered light noise in gravitational wave interferometric detectors: Coherent effects,” *Phys.Rev.* **D 54** (1996) 1276.
- [464] J-Y. Vinet, V. Brisson, S. Braccini, and others, “Scattered light noise in gravitational interferometric detectors: A statistical approach,” *Phys.Rev.* **D 56** (1997) 6085.
- [465] Jean-Yves Vinet, Patrice Hello, Catherine N. Man, and Alain Brillet, “A high accuracy method for the simulation of non-ideal optical cavities,” *J. Phys. I France* **2** no. 7, (1992) 1287–1303. <https://doi.org/10.1051/jp1:1992211>.
- [466] “Finesse (2015).” <http://www.gwoptics.org/finesse/>. <http://www.gwoptics.org/finesse/>.
- [467] “Optickle (2015).” <https://github.com/optickle>. <https://github.com/Optickle>.

- [468] M. Martinez, "'instrumented baffles for virgo'." LIGO-G2000385 (2020).
- [469] R. W. P. Drever, J. L. Hall, F. V. Kowalski, and others, "Laser phase and frequency stabilization using an optical resonator," *Applied Physics B* **31** no. 2, (Jun, 1983) 97–105. <https://doi.org/10.1007/BF00702605>.
- [470] Kenneth A. Strain, Guido Müller, Tom Delker, and others, "Sensing and control in dual-recycling laser interferometer gravitational-wave detectors," *Appl. Opt.* **42** no. 7, (Mar, 2003) 1244–1256. <http://ao.osa.org/abstract.cfm?URI=ao-42-7-1244>.
- [471] M. Evans, N. Mavalvala, P. Fritschel, and others, "Lock acquisition of a gravitational-wave interferometer," *Opt. Lett.* **27** no. 8, (Apr, 2002) 598–600. <http://ol.osa.org/abstract.cfm?URI=ol-27-8-598>.
- [472] F Acernese, P Amico, M Al-Shourbagy, and others, "The variable finesse locking technique," *Classical and Quantum Gravity* **23** no. 8, (Mar, 2006) S85–S89. <https://doi.org/10.1088%2F0264-9381%2F23%2F8%2Fs12>.
- [473] Adam J. Mullavey, Bram J. J. Slagmolen, John Miller, and others, "Arm-length stabilisation for interferometric gravitational-wave detectors using frequency-doubled auxiliary lasers," *Opt. Express* **20** no. 1, (Jan, 2012) 81–89. <http://www.opticsexpress.org/abstract.cfm?URI=oe-20-1-81>.
- [474] Kiwamu Izumi, Koji Arai, Bryan Barr, and others, "Multicolor cavity metrology," *J. Opt. Soc. Am. A* **29** no. 10, (Oct, 2012) 2092–2103. <http://josaa.osa.org/abstract.cfm?URI=josaa-29-10-2092>.
- [475] A Staley, D Martynov, R Abbott, and others, "Achieving resonance in the advanced LIGO gravitational-wave interferometer," *Classical and Quantum Gravity* **31** no. 24, (Nov, 2014) 245010. <https://doi.org/10.1088%2F0264-9381%2F31%2F24%2F245010>.
- [476] T. Akutsu, M. Ando, K. Arai, and others, "An arm length stabilization system with vertex injection of auxiliary lasers: a new scheme scalable to longer-baseline gravitational wave detectors," 2019.
- [477] C M Mow-Lowry and D Martynov, "A 6d interferometric inertial isolation system," *Classical and Quantum Gravity* **36** no. 24, (2019) 245006. <https://doi.org/10.1088%2F1361-6382%2Fab4e01>.
- [478] Hang Yu, Denis Martynov, Salvatore Vitale, and others, "Prospects for detecting gravitational waves at 5 hz with ground-based detectors," *Phys. Rev. Lett.* **120** (Apr, 2018) 141102. <https://link.aps.org/doi/10.1103/PhysRevLett.120.141102>.
- [479] John A Sidles and Daniel Sigg, "Optical torques in suspended fabry–perot interferometers," *Physics Letters A* **354** no. 3, (2006) 167–172.
- [480] Rong-Gen Cai and Tao Yang, "Estimating cosmological parameters by the simulated data of gravitational waves from the einstein telescope," *Physical Review D* **95** no. 4, (2017) 044024.
- [481] Ling Sun, Evan Goetz, Jeffrey S Kissel, and others, "Characterization of systematic error in advanced ligo calibration," 2020.

- 
- [482] S Karki, D Tuyenbayev, S Kandhasamy, and others, “The advanced ligo photon calibrators,” *Review of Scientific Instruments* **87** no. 11, (2016) 114503.
- [483] L Matone, P Raffai, S Márka, and others, “Benefits of artificially generated gravity gradients for interferometric gravitational-wave detectors,” *Classical and Quantum Gravity* **24** no. 9, (2007) 2217.
- [484] D Estevez, B Lieunard, F Marion, and others, “First tests of a newtonian calibrator on an interferometric gravitational wave detector,” *Classical and Quantum Gravity* **35** no. 23, (2018) 235009.
- [485] Yuki Inoue, Sadakazu Haino, Nobuyuki Kanda, and others, “Improving the absolute accuracy of the gravitational wave detectors by combining the photon pressure and gravity field calibrators,” *Physical Review D* **98** no. 2, (2018) 022005.
- [486] Benjamin P Abbott, R Abbott, TD Abbott, and others, “Calibration of the advanced ligo detectors for the discovery of the binary black-hole merger gw150914,” *Physical Review D* **95** no. 6, (2017) 062003.
- [487] Matthew Pitkin, Christopher Messenger, and Liam Wright, “Astrophysical calibration of gravitational-wave detectors,” *Physical Review D* **93** no. 6, (2016) 062002.
- [488] Lucia Trozzo, *Low Frequency Optimization and Performance of Advanced Virgo Seismic Isolation System*. PhD thesis, University of Siena, 2018.
- [489] Giovanni Losurdo and Paolo Ruggi, “Some thoughts on the seismic isolation for ET,” 2019. [https://agenda.infn.it/event/15928/contributions/89742/attachments/63360/76274/GWADW\\_Elba\\_190522\\_Losurdo.pdf](https://agenda.infn.it/event/15928/contributions/89742/attachments/63360/76274/GWADW_Elba_190522_Losurdo.pdf).
- [490] T Accadia et al., “Noise from scattered light in virgo's second science run data,” *Classical and Quantum Gravity* **27** no. 19, (2010) 194011. <https://doi.org/10.1088/0264-9381/27/19/194011>.
- [491] Denis V. Martynov, *Lock Acquisition and Sensitivity Analysis of Advanced LIGO Interferometers*. PhD thesis, California Institute of Technology, 2015. <https://resolver.caltech.edu/CaltechTHESIS:05282015-142013480>.
- [492] Sina M. Köhlenbeck, *Towards the SQL interferometer : length stabilization at the AEI 10 m-prototype*. PhD thesis, Gottfried Wilhelm Leibniz Universität, Hannover, 2018. <https://doi.org/10.15488/3567>.
- [493] E. Majorana, “Ruggi’s global inverted pendulum control,” 2017. <https://dcc.ligo.org/public/0141/G1700891/001/GIPC.pdf>.
- [494] Krishna Venkateswara, Charles A. Hagedorn, Matthew D. Turner, Trevor Arp, and Jens H. Gundlach, “A high-precision mechanical absolute-rotation sensor,” *Review of Scientific Instruments* **85** no. 1, (2014) 015005, <https://doi.org/10.1063/1.4862816>. <https://doi.org/10.1063/1.4862816>.
- [495] N. Azaryan, J. Budagov, V. Glagolev, and others, “Professional Precision Laser Inclinometer: the Noises Origin and Signal Processing,” *Phys. Part. Nucl. Lett.* **16** no. 3, (2019) 264–276.

- [496] S. J. Cooper, C. J. Collins, A. C. Green, and others, “A compact, large-range interferometer for precision measurement and inertial sensing,” *Class. Quantum Grav.* **35** no. 9, (Mar, 2018) 095007. <https://doi.org/10.1088%2F1361-6382%2Faab2e9>.
- [497] H. B. Callen and T. A. Welton, “Irreversibility and generalized noise,” *Phys. Rev. B* **83** (1951) 34–40.
- [498] A. V. Cumming et al., “Finite element modelling of the mechanical loss of silica suspension fibres for advanced gravitational wave detectors,” *Class. Quant. Grav.* **26** no. 21, (2009) 215012.
- [499] A. Gretarsson and G. M. Harry, “Dissipation of mechanical energy in fused silica fibers,” *Rev. of Sci. Instr.* **70** no. 10, (1999) 4081–4087.
- [500] S. D. Penn et al., “Frequency and surface dependence of the mechanical loss in fused silica,” *Phys. Lett. A* **352** (2006) 3–6.
- [501] G. Cagnoli and P. Willems, “Effects of nonlinear thermoelastic damping in highly stressed fibres,” *Phys. Rev. B* **65** (2002) 174111.
- [502] C. Bell et al., “Experimental results for nulling the effective thermal expansion coefficient of fused silica fibres under a static stress,” *Class. Quantum Grav.* **31** (2013) 065010.
- [503] A. V. Cumming et al., “Design and development of the advanced ligo monolithic fused silica suspension,” *Class. Quantum Grav.* **29** no. 3, (2012) 035003.
- [504] A. Heptonstall et al., “Investigation of mechanical dissipation in co2 laser-drawn fused silica fibres and welds,” *Class. Quantum Grav.* **27** (2010) 035013.
- [505] S. Rowan and S. M. Twyford, “Mechanical losses associated with the technique of hydroxide-catalysis bonding of fused silica,” *Phys. Lett. A* **246** (1998) 471–478.
- [506] Kyung-Ha Lee, Giles Hammond, James Hough, and others, “Improved fused silica fibres for the advanced LIGO monolithic suspensions,” *Classical and Quantum Gravity* **36** no. 18, (Aug, 2019) 185018. <https://doi.org/10.1088%2F1361-6382%2Fab28bd>.
- [507] D. F. McGuigan et al., “Measurements of the mechanical Q of single-crystal silicon at low temperatures,” *Journal of Low Temperature Physics* **30** (1978) 621–629. <http://dx.doi.org/10.1007/BF00116202>. 10.1007/BF00116202.
- [508] R Nawrodt, C Schwarz, S Kroker, and others, “Investigation of mechanical losses of thin silicon flexures at low temperatures,” *Classical and Quantum Gravity* **30** no. 11, (May, 2013) 115008. <https://doi.org/10.1088%2F0264-9381%2F30%2F11%2F115008>.
- [509] A Khalaidovski, G Hofmann, D Chen, and others, “Evaluation of heat extraction through sapphire fibers for the GW observatory KAGRA,” *Classical and Quantum Gravity* **31** no. 10, (Apr, 2014) 105004. <https://doi.org/10.1088%2F0264-9381%2F31%2F10%2F105004>.
- [510] R Kumar, D Chen, A Hagiwara, and others, “Status of the cryogenic payload system for the KAGRA detector,” *Journal of Physics: Conference Series* **716** (May, 2016) 012017. <https://doi.org/10.1088%2F1742-6596%2F716%2F1%2F012017>.

- 
- [511] Margot Phelps, Mariela Masso Reid, Rebecca Douglas, and others, “Strength of hydroxide catalysis bonds between sapphire, silicon, and fused silica as a function of time,” *Phys. Rev. D* **98** (Dec, 2018) 122003. <https://link.aps.org/doi/10.1103/PhysRevD.98.122003>.
- [512] K. Haughian, D. Chen, L. Cunningham, and others, “Mechanical loss of a hydroxide catalysis bond between sapphire substrates and its effect on the sensitivity of future gravitational wave detectors,” *Phys. Rev. D* **94** (Oct, 2016) 082003. <https://link.aps.org/doi/10.1103/PhysRevD.94.082003>.
- [513] G Hofmann, D Chen, G Bergmann, and others, “Indium joints for cryogenic gravitational wave detectors,” *Classical and Quantum Gravity* **32** no. 24, (Dec, 2015) 245013. <https://doi.org/10.1088%2F0264-9381%2F32%2F24%2F245013>.
- [514] M.H. Phelps, *Hydroxide Catalysis and Indium Bonding Research for the Design of Ground-based Gravitational Wave Detectors*. University of Glasgow, 2018. <https://books.google.de/books?id=4WUFvgEACAAJ>.
- [515] M. Alshourbagy et al., “First characterization of silicon crystalline fibers produced with the  $\mu$ -pulling technique for future gravitational wave detectors,” *Rev. Sci. Instrum.* **77** (Apr, 2006) 044502.
- [516] S. Reid, G. Cagnoli, D.R.M. Crooks, and others, “Mechanical dissipation in silicon flexures,” *Physics Letters A* **351** no. 4-5, (2006) 205 – 211.
- [517] A V Cumming, L Cunningham, G D Hammond, and others, “Silicon mirror suspensions for gravitational wave detectors,” *Classical and Quantum Gravity* **31** no. 2, (Dec, 2013) 025017. <https://doi.org/10.1088%2F0264-9381%2F31%2F2%2F025017>.
- [518] M.M Fejer, J. L. Nightingale, G. A. Magel, and R. L. Byer, “Laser-heated miniature pedestal growth apparatus for single-crystal optical fiber,” *Review of Scientific Instruments* **55** (1984) 1791.
- [519] J. Yang, T. Ono, and M. Esashi, “Surface effects and high quality factors in ultrathin single-crystal silicon cantilevers,” *Appl. Phys. Lett.* **77** (2000) 3860–3862.
- [520] K. Y. Yasumura, T. D. Stowe, E. M. Chow, and others, “Quality Factors in Micron- and Submicron-Thick Cantilevers,” *J. of Microelectromechanical Systems* **9** (2000) 117–125.
- [521] J. Yang, T. One, and M. Esashi, “Energy Dissipation in Submicrometer Thick Single-Crystal Silicon Cantilevers,” *J. of Microelectromechanical Systems* **11** (2002) 775–783.
- [522] A Bertolini et al., “Monolithic folded pendulum accelerometers for seismic monitoring and active isolation systems,” *IEEE Trans. Geoscience and Remote Sensing* **44** (2006) 273.
- [523] J van Heijningen, “Turn up the bass,” 2018.
- [524] Florian Amann, Fabio Bonsignorio, Tomasz Bulik, and others, “Site-selection criteria for the einstein telescope,” *Review of Scientific Instruments* **91** no. 9, (2020) 094504, <https://doi.org/10.1063/5.0018414>. <https://doi.org/10.1063/5.0018414>.
- [525] N Mukund, B O’Reilly, S Somala, and S Mitra, “Effect of induced seismicity on advanced

- gravitational wave interferometers,” *Classical and Quantum Gravity* **36** no. 10, (Apr, 2019) 10LT01. <https://doi.org/10.1088%2F1361-6382%2Fab1360>.
- [526] G. Milana, R. M. Azzara, E. Bertrand, and others, “The contribution of seismic data in microzonation studies for downtown L’Aquila,” *Bulletin of Earthquake Engineering* **9** no. 3, (Jun, 2011) 741–759. <https://doi.org/10.1007/s10518-011-9246-6>.
- [527] J.F. Semblat, M. Kham, E. Parara, and others, “Seismic wave amplification: Basin geometry vs soil layering,” *Soil Dynamics and Earthquake Engineering* **25** no. 7, (2005) 529 – 538. <http://www.sciencedirect.com/science/article/pii/S0267726105000436>. 11th International Conference on Soil Dynamics and Earthquake Engineering (ICSDEE): Part 1.
- [528] John Douglas, Pierre Gehl, Luis Fabian Bonilla, and others, “Making the Most of Available Site Information for Empirical Ground-Motion Prediction,” *Bulletin of the Seismological Society of America* **99** no. 3, (06, 2009) 1502–1520, <https://pubs.geoscienceworld.org/bssa/article-pdf/99/3/1502/3670503/1502.pdf>. <https://doi.org/10.1785/0120080075>.
- [529] Massimo Coli and Alice Pinzani, “Tunnelling and Hydrogeological Issues: A Short Review of the Current State of the Art,” *Rock Mechanics and Rock Engineering* **47** no. 3, (May, 2014) 839–851. <https://doi.org/10.1007/s00603-012-0319-x>.
- [530] Chunlin Li and Kent Lindblad, “Corrosivity classification of the underground environment,” in *Rock support and reinforcement practice in mining : proceedings of the international symposium on ground support, Kalgoorlie, Western Australia, 15-17 March, 1999*, pp. 69–75. Balkema Publishers, A.A. / Taylor & Francis The Netherlands, 1999. <http://urn.kb.se/resolve?urn=urn:nbn:se:ltu:diva-27070>. Godkänd; 1999; 20090408 (andbra).
- [531] Z. Lewandowski and H. Beyenal, *Mechanisms of Microbially Influenced Corrosion*, pp. 35–64. Springer Berlin Heidelberg, Berlin, Heidelberg, 2009. [https://doi.org/10.1007/978-3-540-69796-1\\_3](https://doi.org/10.1007/978-3-540-69796-1_3).
- [532] B. Tribollet and M. Meyer, “2 - ac-induced corrosion of underground pipelines,” in *Underground Pipeline Corrosion*, Mark E. Orazem, ed., pp. 35 – 61. Woodhead Publishing, 2014. <http://www.sciencedirect.com/science/article/pii/B9780857095091500023>.
- [533] B. Gutenberg, “Microseisms,” *Advances in Geophysics* **5** (1958) 53–92.
- [534] M.W. Asten, “Arrays estimators and the use of microseisms for reconnaissance of sedimentary basins,” *Bulletin of the Seismological Society of America* **68** (2002) 1623 – 1636.
- [535] L. Peck, “Overview of Seismic Noise and its relevance to Personnel detections.” Erdc/crrel tr-08-5, us army corps of engineers, April, 2008. Engineer Research and Development Center.
- [536] R. Schofield, M. Ito, E. Mauceli, and others, “Source and propagation of the predominant 1-50 hz seismic signal from off-site at ligo-hanford,” 2000. <https://dcc.ligo.org/LIGO-G000262/public>.

- 
- [537] I. Fiori, L. Holloway, and F. Paoletti, “Studies of the 1 - 4 hz seism.” Internal Virgo Note (VIR-NOT-FIR-1390-251).
- [538] D. Coward, D. Blair, R. Burman, , and C. Zhao., “Vehicle-induced seismic effects at a gravitational wave observatory,” *Review of Scientific Instruments* **74** (2003) 4846 – 4854.
- [539] M Coughlin, N Mukund, J Harms, and others, “Towards a first design of a Newtonian-noise cancellation system for Advanced LIGO,” *Classical and Quantum Gravity* **33** no. 24, (2016) 244001. <http://stacks.iop.org/0264-9381/33/i=24/a=244001>.
- [540] M. W. Coughlin, J. Harms, J. Driggers, and others, “Implications of Dedicated Seismometer Measurements on Newtonian-Noise Cancellation for Advanced LIGO,” *Phys. Rev. Lett.* **121** (Nov, 2018) 221104. <https://link.aps.org/doi/10.1103/PhysRevLett.121.221104>.
- [541] Kip S. Thorne and Carolee J. Winstein, “Human gravity-gradient noise in interferometric gravitational-wave detectors,” *Phys. Rev. D* **60** no. 8, (Sep, 1999) 082001.
- [542] M.M. Withers, R.C. Aster, C.J. Young, and E.P. Chael, “High-frequency analysis of seismic background noise as a function of wind speed and shallow depth,” *Bulletin of the Seismological Society of America* **86** no. 5, (1996) 1507–1515.
- [543] Silvio De Angelis and Paul Bodin, “Watching the Wind: Seismic Data Contamination at Long Periods due to Atmospheric Pressure-Field-Induced Tilting,” *Bulletin of the Seismological Society of America* **102** no. 3, (2012) 1255–1265. <https://doi.org/10.1785/0120110186>.
- [544] A Effler, R M S Schofield, V V Frolov, and others, “Environmental influences on the LIGO gravitational wave detectors during the 6th science run,” *Classical and Quantum Gravity* **32** no. 3, (Jan, 2015) 035017. <https://doi.org/10.1088/0264-9381/32/3/035017>.
- [545] Michael W Coughlin, Nelson L Christensen, Rosario De Rosa, and others, “Subtraction of correlated noise in global networks of gravitational-wave interferometers,” *Classical and Quantum Gravity* **33** no. 22, (Oct, 2016) 224003. <https://doi.org/10.1088/0264-9381/33/22/224003>.
- [546] Izabela Kowalska-Leszczynska, Marie-Anne Bizouard, Tomasz Bulik, and others, “Globally coherent short duration magnetic field transients and their effect on ground based gravitational-wave detectors,” *Classical and Quantum Gravity* **34** no. 7, (Mar, 2017) 074002. <https://doi.org/10.1088/1361-6382/aa60eb>.
- [547] S. Atsuta, T. Ogawa, S. Yamaguchi, and others, “Measurement of schumann resonance at kamioka,” *Journal of Physics: Conference Series* **716** (May, 2016) 012020. <https://doi.org/10.1088/1742-6596/716/1/012020>.
- [548] E. Thrane, N. Christensen, and R. M. S. Schofield, “Correlated magnetic noise in global networks of gravitational-wave detectors: Observations and implications,” *Phys. Rev. D* **87** (Jun, 2013) 123009. <https://link.aps.org/doi/10.1103/PhysRevD.87.123009>.

- [549] Michael W. Coughlin, Alessio Cirone, Patrick Meyers, and others, “Measurement and subtraction of schumann resonances at gravitational-wave interferometers,” *Phys. Rev. D* **97** (May, 2018) 102007. <https://link.aps.org/doi/10.1103/PhysRevD.97.102007>.
- [550] A. Cirone, A. Chincarini, M. Neri, and others, “Magnetic coupling to the advanced Virgo payloads and its impact on the low frequency sensitivity,” *Review of Scientific Instruments* **89** no. 11, (2018) 114501, <https://doi.org/10.1063/1.5045397>.  
<https://doi.org/10.1063/1.5045397>.
- [551] A Cirone, I Fiori, F Paoletti, and others, “Investigation of magnetic noise in Advanced Virgo,” *Classical and Quantum Gravity* **36** no. 22, (Oct, 2019) 225004.  
<https://doi.org/10.1088/1361-6382/ab4974>.
- [552] LIGO Scientific Collaboration, “Characterization of transient noise in Advanced LIGO relevant to gravitational wave signal GW150914,” *Classical and Quantum Gravity* **33** no. 13, (Jun, 2016) 134001. <https://doi.org/10.1088/0264-9381/33/13/134001>.
- [553] Jan Harms, “Terrestrial gravity fluctuations,” *Living Reviews in Relativity* **22** no. 1, (Oct, 2019) 6. <https://doi.org/10.1007/s41114-019-0022-2>.
- [554] K. Aki and P. G. Richards, *Quantitative Seismology, 2nd edition*. University Science Books, 2009.
- [555] M Coughlin, J Harms, N Christensen, and others, “Wiener filtering with a seismic underground array at the Sanford Underground Research Facility,” *Classical and Quantum Gravity* **31** no. 21, (2014) 215003.  
<http://stacks.iop.org/0264-9381/31/i=21/a=215003>.
- [556] G G Barnaföldi, T Bulik, M Cieslar, and others, “First report of long term measurements of the MGGL laboratory in the mátra mountain range,” *Classical and Quantum Gravity* **34** no. 11, (Apr, 2017) 114001. <https://doi.org/10.1088/1361-6382/aa69e3>.
- [557] Donatella Fiorucci, Jan Harms, Matteo Barsuglia, Irene Fiori, and Federico Paoletti, “Impact of infrasound atmospheric noise on gravity detectors used for astrophysical and geophysical applications,” *Phys. Rev. D* **97** (Mar, 2018) 062003.  
<https://link.aps.org/doi/10.1103/PhysRevD.97.062003>.
- [558] J. A. Elliott, “Microscale pressure fluctuations measured within the lower atmospheric boundary layer,” *Journal of Fluid Mechanics* **53** no. 2, (1972) 351–384.
- [559] John A. McDonald and Eugene Herrin, “Properties of pressure fluctuations in an atmospheric boundary layer,” *Boundary-Layer Meteorology* **8** no. 3, (Apr, 1975) 419–436.  
<https://doi.org/10.1007/BF02153561>.
- [560] John D. Albertson, Gabriel G. Katul, Marc B. Parlange, and William E. Eichinger, “Spectral scaling of static pressure fluctuations in the atmospheric surface layer: The interaction between large and small scales,” *Physics of Fluids* **10** no. 7, (1998) 1725–1732,  
<https://doi.org/10.1063/1.869689>. <https://doi.org/10.1063/1.869689>.
- [561] EFR Bollaert, P Manso, and AJ Schleiss, “Dynamic pressure fluctuations at real-life plunge

- pool bottoms,” in *Proc. Int. Conf. Hydraulics of Dams and River Structures*, pp. 117–124. 2004.
- [562] Alois Schaffarczyk and Andreas Jeromin, “Measurements of high-frequency atmospheric turbulence and its impact on the boundary layer of wind turbine blades,” *Applied Sciences* **8** no. 9, (Aug, 2018) 1417. <http://dx.doi.org/10.3390/app8091417>.
- [563] M. J. Lighthill, “On Sound Generated Aerodynamically. I. General Theory,” *Proceedings of the Royal Society of London A: Mathematical, Physical and Engineering Sciences* **211** no. 1107, (1952) 564–587.
- [564] M. J. Lighthill, “On Sound Generated Aerodynamically. II. Turbulence as a Source of Sound,” *Proceedings of the Royal Society of London A: Mathematical, Physical and Engineering Sciences* **222** no. 1148, (1954) 1–32.
- [565] K. Träumner, Th. Damian, Ch. Stawiarski, and A. Wieser, “Turbulent structures and coherence in the atmospheric surface layer,” *Boundary-Layer Meteorology* **154** no. 1, (Jan, 2015) 1–25. <https://doi.org/10.1007/s10546-014-9967-6>.
- [566] Jürgen Neumeyer, “Superconducting Gravimetry,” in *Sciences of Geodesy - I*, Guochang Xu, ed., pp. 339–413. Springer Berlin Heidelberg, 2010. [http://dx.doi.org/10.1007/978-3-642-11741-1\\_10](http://dx.doi.org/10.1007/978-3-642-11741-1_10).
- [567] Teviet Creighton, “Tumbleweeds and airborne gravitational noise sources for LIGO,” *Classical and Quantum Gravity* **25** no. 12, (2008) 125011. <http://stacks.iop.org/0264-9381/25/i=12/a=125011>.
- [568] Peter Alan Davidson, *Turbulence: An Introduction for Scientists and Engineers*. Oxford University Press, 2004.
- [569] Fabric Matichard and Matthew Evans, “Review: Tilt-Free Low-Noise Seismometry,” *Bulletin of the Seismological Society of America* **105** no. 2A, (2015) 497–510. <https://doi.org/10.1785/0120140200>.
- [570] Jon R. Peterson, “Observation and modeling of seismic background noise,” 1993. <http://pubs.er.usgs.gov/publication/ofr93322>.
- [571] Sophocles J Orfanidis, *Optimum signal processing: an introduction*. Macmillan publishing company, 2007.
- [572] Jan Harms and Krishna Venkateswara, “Newtonian-noise cancellation in large-scale interferometric GW detectors using seismic tiltmeters,” *Classical and Quantum Gravity* **33** no. 23, (2016) 234001. <http://stacks.iop.org/0264-9381/33/i=23/a=234001>.
- [573] M. Coughlin and J. Harms, “Seismic topographic scattering in the context of gw detector site selection,” *Class. Quantum Grav.* **29** (2012) 075004.
- [574] David N. Green, “The spatial coherence structure of infrasonic waves: analysis of data from International Monitoring System arrays,” *Geophysical Journal International* **201** no. 1, (02, 2015) 377–389,

- <http://oup.prod.sis.lan/gji/article-pdf/201/1/377/17367674/ggu495.pdf>.  
<https://dx.doi.org/10.1093/gji/ggu495>.
- [575] J. A. Elliott, “Instrumentation for measuring static pressure fluctuations within the atmospheric boundary layer,” *Boundary-Layer Meteorology* **2** no. 4, (Jun, 1972) 476–495.  
<https://doi.org/10.1007/BF00821550>.
- [576] Kristoffer T. Walker and Michael A.H. Hedlin, “A review of wind-noise reduction methodologies,” in *Infrasound Monitoring for Atmospheric Studies*, Alexis Le Pichon, Elisabeth Blanc, and Alain Hauchecorne, eds., pp. 141–182. Springer Netherlands, 2009.  
[http://dx.doi.org/10.1007/978-1-4020-9508-5\\_5](http://dx.doi.org/10.1007/978-1-4020-9508-5_5).
- [577] John M. Noble, W.C. Kirkpatrick Alberts, Richard Raspet, Sandra L. Collier, and Mark A. Coleman, “Infrasonic wind noise reduction via porous fabric domes,” *Proceedings of Meetings on Acoustics* **21** no. 1, (2014) 045005,  
<https://asa.scitation.org/doi/pdf/10.1121/2.0000307>.  
<https://asa.scitation.org/doi/abs/10.1121/2.0000307>.
- [578] Tianfeng Chai, Ching-Long Lin, and Rob K. Newsom, “Retrieval of Microscale Flow Structures from High-Resolution Doppler Lidar Data Using an Adjoint Model,” *Journal of the Atmospheric Sciences* **61** no. 13, (2004) 1500–1520,  
[https://doi.org/10.1175/1520-0469\(2004\)061<1500:ROMFSF>2.0.CO;2](https://doi.org/10.1175/1520-0469(2004)061<1500:ROMFSF>2.0.CO;2).  
[https://doi.org/10.1175/1520-0469\(2004\)061<1500:ROMFSF>2.0.CO;2](https://doi.org/10.1175/1520-0469(2004)061<1500:ROMFSF>2.0.CO;2).
- [579] Andreas Behrendt, “Temperature measurements with lidar,” in *Lidar: Range-Resolved Optical Remote Sensing of the Atmosphere*, Claus Weitkamp, ed., pp. 273–305. Springer New York, New York, NY, 2005. [https://doi.org/10.1007/0-387-25101-4\\_10](https://doi.org/10.1007/0-387-25101-4_10).
- [580] Jennifer C. Driggers, Jan Harms, and Rana X. Adhikari, “Subtraction of Newtonian noise using optimized sensor arrays,” *Phys. Rev. D* **86** (Nov, 2012) 102001.  
<http://link.aps.org/doi/10.1103/PhysRevD.86.102001>.
- [581] Tianshou Ma, Ping Chen, and Jian Zhao, “Overview on vertical and directional drilling technologies for the exploration and exploitation of deep petroleum resources,” *Geomechanics and Geophysics for Geo-Energy and Geo-Resources* **2** no. 4, (Dec, 2016) 365–395.  
<https://doi.org/10.1007/s40948-016-0038-y>.
- [582] Stefano Bagnasco, Ian Bird, Peter Couvares, and others, “Gravitational-wave data analysis computing challenges in the 3g era,” tech. rep., Gravitational Wave International Committee (GWIC), 2020. <https://gwic.ligo.org/3Gsubcomm/documents.shtml>.
- [583] “Pycbc.” <https://pycbc.org/>.
- [584] E. Belgacem, Y. Dirian, S. Foffa, and others, “Cosmology and dark energy from joint gravitational wave-grb observations,” *Journal of Cosmology and Astroparticle Physics* **2019** (2019) 015–015.
- [585] Helge Meinhard, Bernd Panzer-Steindel, Servesh Muralidharan, and others, “Trends in computing technologies and markets,” in *Proceedings of the 24th International Conference on*

---

*Computing in High Energy & Nuclear Physics, Adelaide, South Australia, 4-8 November, 2019.* 2020. to appear.

- [586] Elena Cuoco et al., “Enhancing Gravitational-Wave Science with Machine Learning,” arXiv:2005.03745 [astro-ph.HE].
- [587] Daniel George and E.A. Huerta, “Deep learning for real-time gravitational wave detection and parameter estimation: Results with advanced ligo data,” *Physics Letters B* **778** (2018) 64 – 70. <http://www.sciencedirect.com/science/article/pii/S0370269317310390>.
- [588] Johannes Albrecht, Antonio Augusto Alves, Guilherme Amadio, and others, “A roadmap for hep software and computing r&d for the 2020s,” *Computing and Software for Big Science* **3** no. 1, (Mar, 2019) 7. <https://doi.org/10.1007/s41781-018-0018-8>.
- [589] Peter Mell and Timothy Grance, “The nist definition of cloud computing,” Tech. Rep. 800-145, National Institute of Standards and Technology (NIST), Gaithersburg, MD, September, 2011. <http://csrc.nist.gov/publications/nistpubs/800-145/SP800-145.pdf>.
- [590] “The lhc open network environment (lhcone).” <https://lhcone.web.cern.ch/>.
- [591] “European science cluster of astronomy & particle physics esfri research infrastructures (escape).” <https://projectescape.eu/>.
- [592] Derek Weitzel, Marian Zvada, Ilija Vukotic, and others, “Stashcache: A distributed caching federation for the open science grid,” in *Proceedings of the Practice and Experience in Advanced Research Computing on Rise of the Machines (Learning)*, PEARC ’19. Association for Computing Machinery, New York, NY, USA, 2019. <https://doi.org/10.1145/3332186.3332212>.
- [593] “Gofair.org.” <https://www.go-fair.org/>.
- [594] “The gravitational-wave open science center.” <https://www.gw-openscience.org/>.